Thèse

présentée

devant l'Université d'Orsay, Paris 11

pour obtenir

le grade de Docteur de l'Université d'Orsay, Paris 11
Mention Physique

par

A.D. Chepelianskii

Équipe d'accueil : Groupe de physique mésoscopique
Laboratoire d'accueil : Laboratoire de Physique des solides

Non equilibrium transport and chirality in mesoscopic physics

Transport hors d'équilibre et chiralité en physique mésoscopique

Soutenue le 24 Septembre 2010 devant la commission d'examen.
Composition du jury :

Président		
Geert	Rikken	Directeur de Recherche
Rapporteurs		
Markus	Büttiker	Professeur
Bernard	Plaçais	Directeur de Recherche
Examinateur		
Dominique	Vuillaume	Directeur de Recherche
Hélène	Bouchiat	Directeur de Recherche (Directrice de thèse)
Sophie	Guéron	Chargé de Recherche (Co-directrice de thèse)

Table des matières

Chapitre 1

Introduction

Dans cette thèse je m'intéresse à deux aspects physiques fondamentaux de systèmes nanoscopiques et moléculaires : la chiralité et la non-linéarité. Un système ou un objet tridimensionnel est dit chiral s'il ne peut pas être superposé à son image miroir. Un système est non-linéaire si les équations qui le gouvernent n'obéissent pas au principe de superposition. Cette définition mathématique se prête mal à une étude expérimentale, on est donc tenté de donner une définition plus concrète : un système est non-linéaire si soumis à une excitation monochromatique à fréquence f, il produit une réponse non-linéaire à une fréquence distincte f'. Ces définitions ne sont en fait pas équivalentes, puisque l'apparition d'une réponse non-linéaire n'est souvent possible que lorsque des symétries spatiales ou temporelles le permettent. Un des problèmes que j'ai abordé dans cette thèse est de caractériser une molécule chirale : l'Acide-Desoxyriboso-Nucléique (ADN) à travers des mesures de transport électroniques. Cette problématique m'a conduit à examiner en détail le lien subtil entre chiralité et non linéarité. Je commencerai donc cette introduction en décrivant plusieurs exemples de systèmes chiraux, avant de me concentrer sur le transport non-linéaire. En particulier je chercherai à déterminer s'il est possible de détecter la chiralité avec une mesure de transport électronique.

1.1 Chiralité

Probablement l'exemple le plus familier où la chiralité joue un rôle est le problème des gants. Il est en effet impossible de mettre un gant droit sur la main gauche même en tournant le gant dans tout les directions. Pour mieux représenter graphiquement la différence entre un objet chiral et non chiral on peut comparer les deux dessins de feuilles d'arbre sur la Figure 1.1, une seule des feuilles est chirale malgré les similitudes entre les deux motifs.

Un composé chiral peut donc exister sous deux formes distinctes reliées par une symétrie miroir, on parle alors de formes énantiomères d'une même molécule. Le biologie est un domaine ou la chiralité joue un rôle clef puisque, les principales molécules biologiques sont chirales. En général une seule des formes énantiomères possibles intervient dans les réactions

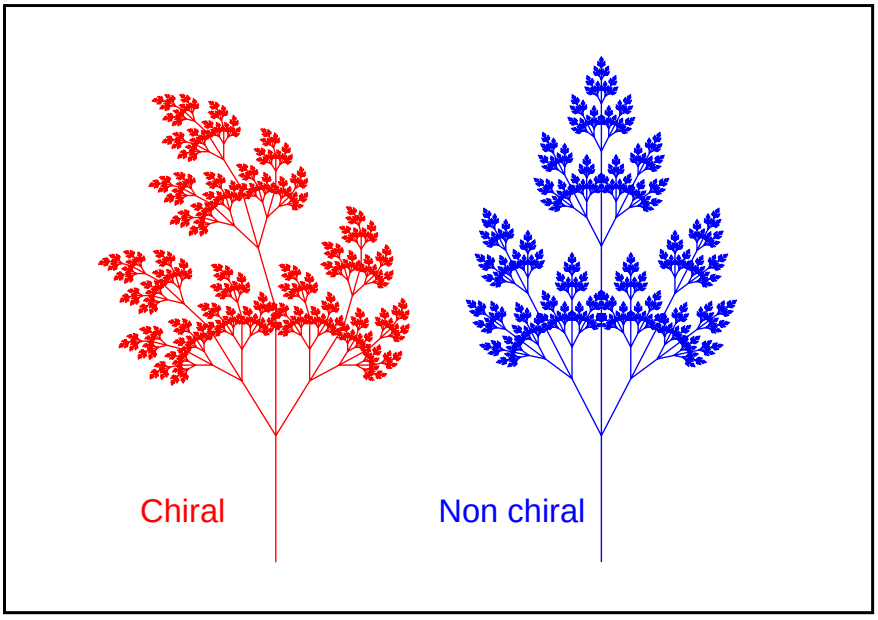

FIG. 1.1 – Un seul de ces deux dessins de feuille d'arbre est chiral malgré les similitudes entre les deux motifs. La figure rouge est chirale seulement si le plan de la feuille n'est pas un plan de symétrie du motif (ce qui est vrai en pratique car l'image n'est imprimé que d'un seul côté du papier !)

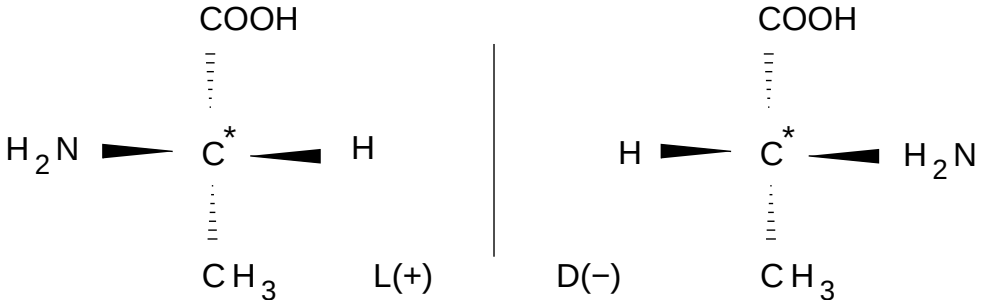

FIG. 1.2 – Formules stéreochimiques des deux formes énantiomères de l'alanine. La désignation L ou D (Lévogyre/Dextrogyree) se réfère au pouvoir rotatoire de chaque énantiomère.

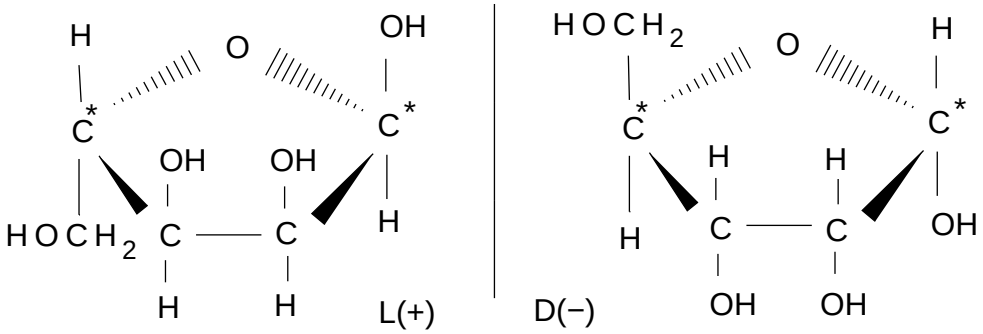

FIG. 1.3 – Formules stéreochimiques de deux formes énantiomères du ribose.

biochimiques au sein d'un organisme vivant. Je vais en donner ici plusieurs exemples :

- **Acides aminés :** A part la glycine, les vingt acides aminés présents dans le code génétique sont chiraux. Sur la figure 1.2 j'ai représenté les deux formes énantiomères possibles de l'alanine, seule la forme L est présente dans les protéines [1, 2]. On remarquera qu'au niveau chimique la chiralité provient de la présence d'atomes de carbone asymétriques en liaison covalente avec quatre groupes chimiques différents.
- **Sucres :** Le ribose qui intervient dans la formation de l'acide désoxyribonucléique (ADN) et de l'acide ribonucléique (ARN) est également chiral. Seule la forme D de cette molécule apparaît dans les organismes vivants, sa forme miroir ne peut être obtenue que de manière synthétique.
- **Acide désoxyribonucléique (ADN) :** L'ADN, une molécule d'une importance fondamentale en biologie, est en forme de double hélice ; sur la Figure 1.4 j'ai représenté un modèle simplifié qui permet d'en illustrer la structure. L'ADN est donc une molécule chirale.

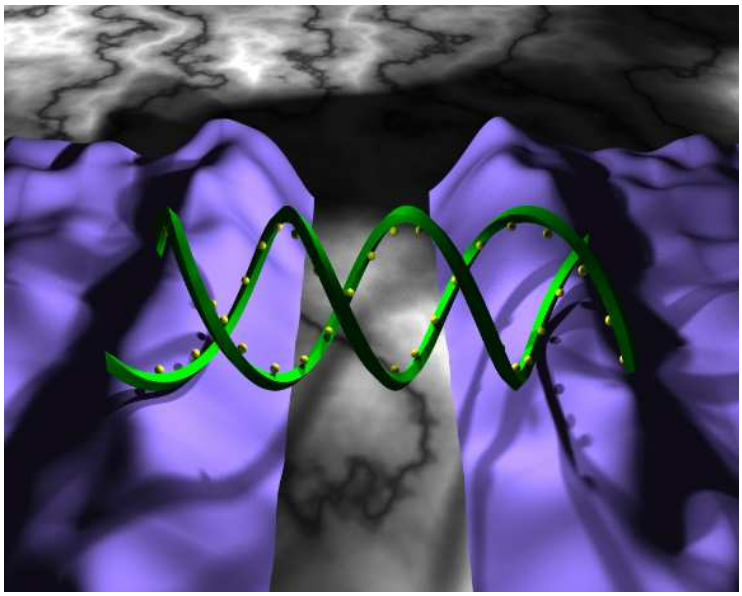

FIG. 1.4 – Représentation schématique d'une structure en double hélice similaire a celle de l'ADN placée entre deux électrodes.

La découverte de l'importance de la chiralité a été rendue possible par des expériences optiques utilisant de la lumière polarisée. En effet des solutions contenant une seule des formes énantiomères font tourner le plan de polarisation d'un faisceau de lumière polarisée. Cette propriété a été observée pour la première fois par Jean-Baptiste Biot en 1815 sur des solutions de sucre. En effet, comme souligné plus haut les sucres obtenus de manière naturelle sont sous forme dextrogyre : au passage à travers la solution le plan de polarisation tourne donc dans le sens des aiguilles d'une montre pour un observateur qui reçoit la lumière. Cette propriété d'un milieu de faire tourner la polarisation de l'onde qui le traverse s'appelle activité optique. Le lien avec la structure à l'échelle moléculaire ne fut fait que plus tardivement grâce au travaux de Louis Pasteur, qui a montré le lien entre le pouvoir rotatoire d'une solution d'acide tartrique et la chiralité des cristaux formés par celui ci. Les expériences d'optique sont donc une méthode privilégiée pour étudier la chiralité.

Cependant il est intéressant d'un point de vue fondamental de se demander s'il existe d'autres méthodes en physiques sensibles à la chiralité. Ces méthodes doivent par exemple être capables de distinguer entre les deux formes énantiomères d'une molécule ou d'un système physique. Plusieurs domaines ont contribué à une meilleure compréhension des différents effets de la chiralité au niveau microscopique à commencer par d'autres sources de radiation comme les rayons X ou les neutrons. Par exemple la structure en double hélice de l'ADN à été proposée grâce à des expériences de diffraction aux rayons X [3].

La formation de structures supra-moléculaires à été observée dans des cristaux liquides composés de molécules chirales, par exemple la phase cholesterique est formée de plans de molécules orientées dans une même direction la direction d'orientation tournant d'un

plan à l'autre [4]. L'étude des films de Langmuir a également mis en évidence l'apparition de structures chirales [5]. Cependant elle a également montré que la formation de motifs chiraux n'est pas forcement reliée à une chiralité au niveau moléculaire, une rupture dynamique de la symétrie chirale étant possible [6, 7].

Il est également important de souligner que la symétrie chirale n'est en réalité qu'approximative puisqu'elle n'est pas respectée par les interactions faibles [8, 9] importantes à l'échelle subatomique. Des effets liés à ce non respect fondamental de la parité, ont pu être montrés dans des expériences de physiques atomique. Cependant il semblerait que cette asymétrie soit trop faible pour qu'il existe un lien avec la chiralité privilégiée observée pour les molécules biologiques [2].

Dans cette description certainement incomplète j'ai volontairement omis la physique du transport électronique, sur laquelle je vais me concentrer à partir de maintenant. Je commencerai par décrire les systèmes chiraux les plus simples qui apparaissent en physique du solide.

- **Électrons en champ magnétique :** Les électrons dans un champ magnétique uniforme H décrivent des cercles à la fréquence cyclotron $\omega_c = \frac{eH}{m}$ où $-e$ est la charge de l'électron et m est sa masse, les trajectoires sont illustrées sur la Figure 1.5. La base $(\mathbf{i}, \mathbf{j}, \mathbf{H})$ est une base directe l'angle orienté $(\mathbf{i}, \mathbf{j})$ donne le sens de rotation de l'électron dans le plan.

En généralisant cet exemple, il est clair qu'un milieu homogène soumis à un champ magnétique devient "magnéto-chiral" (l'ensemble système avec le champ magnétique est chiral) et donc optiquement actif. Ceci donne lieux à des effets physiques célèbres comme l'effet Faraday (mesure optique en transmission à travers un milieu soumis à un champ magnétique) ou l'effet Kerr magnéto-optique (mesure en réflexion sur des systèmes aimantés). Cependant la signature de cette chiralité induite reste une mesure optique.

Il est important de souligner qu'un champ magnétique brise le renversement par le sens du temps, l'analogie avec l'activité optique liée à la chiralité est en ce sens trompeuse. Ainsi le sens de rotation de la polarisation dans l'effet Faraday change de signe selon si la lumière se propage dans la direction du champ magnétique où dans la direction opposée. Néanmoins il existe une connection entre "magnéto-chiralié" et chiralité intrinsèque, ainsi la constante diélectrique d'un liquide constitué de molécules chirales acquiert une composante en $\mathbf{Bk}$ dont le signe change pour les deux formes énantiomères, $\mathbf{k}$ étant la direction de propagation de la lumière. [10].

- **Effet Hall :** L'effet Hall permet de distinguer entre deux champs magnétiques uniformes de signes opposés, il s'agit donc d'une mesure sensible à la chiralité. Cette propriété peut se voir directement à partir de la géométrie de la mesure (voir Figure Fig. 1.6). En effet pour les deux signes du champ magnétique le trièdre formé par les vecteurs $(\mathbf{I}, \mathbf{V}, \mathbf{H})$ forme une base directe. Ici le vecteur $\mathbf{I}$ relie les contacts de courant de la sonde de Hall (orientée dans le sens du courant), $\mathbf{V}$ est le vecteur qui relie les sondes de tension (orienté dans le sens des potentiels croissants) et B est le champ magnétique.

L'utilisation d'une mesure quatre fils peut paraître superflue pour déterminer le signe du champ magnétique. En effet du point de vue des symétries spatiales la magnéto-résistance

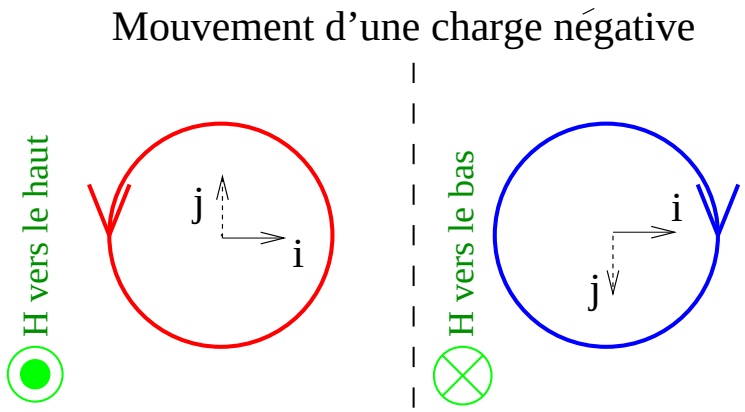

FIG. 1.5 – Trajectoire d'un électron (bidimensionel) soumis à un champ magnétique en l'absence de désordre. L'angle orienté $(\mathbf{i}, \mathbf{j})$ donne le sens de rotation de l'électron dans le plan

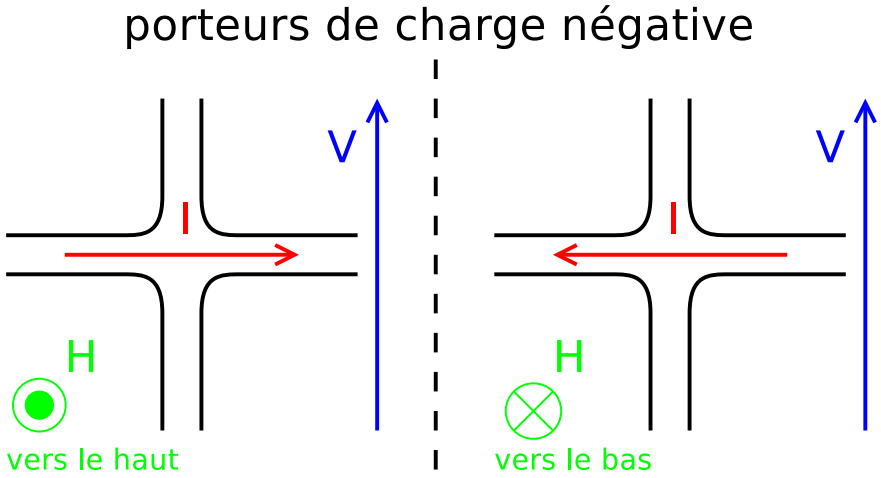

FIG. 1.6 – Géométrie d'une mesure de champ magnétique par effet Hall.

deux fils d'un échantillon chiral peut également contenir une composante impaire en champ magnétique. Cependant ce raisonnement qui s'appuie uniquement sur les symétries spatiales ne tient pas compte d'une autre symétrie des systèmes à l'équilibre thermodynamique : l'invariance par renversement du sens du temps. En effet si on remonte en arrière dans le temps les trajectoire soumises à un champ magnétique $\mathbf{H}$, la trajectoire obtenue est une solution des équations du mouvement pour un champ magnétique de direction opposée $-\mathbf{H}$. Cette propriété se voit facilement pour le cas des électrons libres Figure 1.5 : parcourir les trajectoires en arrière change le sens de rotation à l'instar d'un changement de signe du champ magnétique. D'après les relations fluctuation dissipation la résistance deux fils est reliée à une propriété à l'équilibre du système : par exemple le coefficient de diffusion dans la relation d'Einstein. Or le coefficient de diffusion ne dépend pas de la direction dans laquelle on parcourt les trajectoires et donc du signe du champ magnétique. La résistance deux fils est donc une fonction symétrique du champ magnétique.

Cette propriété est en fait un cas particulier des relations d'Onsager aux quelles nous nous intéresserons en détail pendant cette thèse. Au niveau expérimental, les relations d'Onsager sont souvent vérifiées avec une très bonne précision pour des conducteurs macroscopiques et même pour des échantillons mésocopiques cohérents où les fluctuations quantiques jouent un rôle. Cependant tout comme le principe de bilan de balance détaillé, il n'est pas un principe fondamental (comme la conservation de l'énergie) et il existe des systèmes où les relations d'Onsager ne sont pas valables : par exemple les bicouches de gaz bidimensionel electron-trou [11]. Pour l'heure la compréhension physique des causes derrière la non validité des relations d'Onsager dans ces systèmes reste limitée.

En conclusion, des mesures à plusieurs contacts peuvent être sensibles au signe du champ magnétique même pour des milieux qui n'ont pas de chiralité intrinsèque (par exemple de chiralité topologique reliée à la symétrie spatiale des molécules du milieux). Des mesures de magnéto-résistance deux fil, ne permettent pas de caractériser un objet chiral puisque la symétrie par renversement du sens du temps conduit à une magnéto-résistance symétrique en champ magnétique et masque l'effet de la chiralité. Cependant dans des régimes hors d'équilibre la symétrie par renversement du sens du temps est brisée. On peut donc espérer observer des signatures de la chiralité dans des expériences de transport non linéaire.

1.2 Transport non-linéaire

Des mesures de transport non linéaire consistent à étudier l'effet d'une irradiation à fréquence f_{ext} sur une observable mesurée à une fréquence distincte f_{mes}. Dans un contexte de physique des solides cette observable peut par exemple être la tension continue aux bornes de l'échantillon ou sa résistance à basse fréquence, on parle alors d'effet photovoltaique ou de photo-conductivité.

Au cours de ma thèse j'ai étudié la photo-conductivité de plusieurs systèmes : le gaz d'électrons bidimensionel (2DEG), des molécules d'ADN contactées à des électrodes ainsi que des nanofils/cristaux massifs de silicium. Dans ce chapitre je commencerai donc par

discuter les propriétés de symétrie de la photo-conductivité, pour aborder ensuite l'effet photovoltaique que j'ai surtout regardé sur le 2DEG. Enfin je discuterai l'effet de l'illumination sur d'autres observables telles que la polarisabilité ou le moment magnétique orbital.

Les semi-conducteurs sont en général photo-conductifs : lorsqu'ils sont soumis à une irradiation lumineuse, les photons d'énergie supérieure au "gap" entre la bande de valence et la bande de conduction sont absorbés pour créer des paires électrons-trou qui participent au transport et augmentent la conductivité. Nous avons essayé d'utiliser ce mécanisme dans nos expériences pour sonder le transport électronique dans l'ADN et les nanofils de silicium. Les résultats sont exposés en détail dans la seconde partie du manuscrit, et résumés dans le Chapitre 1.2. Dans ces systèmes la photo-conductivité repose sur un changement de la densité des porteurs sous l'effet de l'illumination, et n'exige pas la rupture de symétries spatiales. Elle peut donc être observée dans des cristaux macroscopiques homogènes, et n'apporte pas d'information directe sur la chiralité. Elle fait cependant intervenir des processus de relaxation irréversibles telle que la relaxation des paires électron trou qui fixe le nombre de porteurs total à l'équilibre, la photo-conductivité brise en ce sens la symétrie par renversement du sens du temps. Néanmoins si la photo-conductivité ne fait que changer la conductance effective du milieu en augmentant sa densité de porteurs, les relations de réciprocité restent valables tout comme à l'équilibre masquant l'effet de l'irréversibilité de la dynamique microscopique.

Des déviations aux relations de réciprocité sur la photo-conductance peuvent en revanche apparaître dans des systèmes où la description par un milieu continu de conductance effective n'est plus valable, par exemple les systèmes balistiques dans les quelles le désordre joue un rôle extrêmement faible ou encore les conducteurs quantiques cohérents dans lesquels les effets non locaux peuvent exister même en présence de désordre. Dans les gaz d'électrons bidimensionel GaAs/GaAlAs les électrons peuvent avoir des longueurs de libre parcours moyen très grandes de plus de 10 μm à basse température ($T \sim 4.2$ K). En étudiant le comportement d'une sonde de Hall balistique sous irradiation micro-onde non homogène nous avons ainsi pu montrer que la photo-conductivité ne vérifie plus les relations de réciprocité une fois que la fréquence d'excitation dépasse un seuil relié au temps de parcours des électrons à travers la sonde de Hall (voir Figure 1.7) . Ces mesures montrent que la rupture de la symétrie par renversement du temps intervient seulement si la fréquence d'excitation est suffisamment grande devant les temps de réponse du système. On peut donc avoir une photoconductance non nulle dans un système invariant par renversement du sens du temps.

Dans les paragraphes précédents j'ai abordé la photo-conductivité dans une limite ou la fréquence d'excitation est élevée (fréquences optiques pour la photo-conductivité dans les semi-conducteurs). Il est également instructif d'envisager cet effet dans une limite ou l'excitation se fait à basse fréquence. Considérons le cas d'un transistor à effet de champ, dont la conductance dépend de manière non linéaire de la tension de grille :

$$G(V_g) = G_0 + G_1 V_g + G_2 V_g^2 + ... \tag{1.1}$$

Lorsqu'une tension sinusoïdale $V_g(t) = V_0 \cos \omega t$ est appliquée sur la grille, la conductance

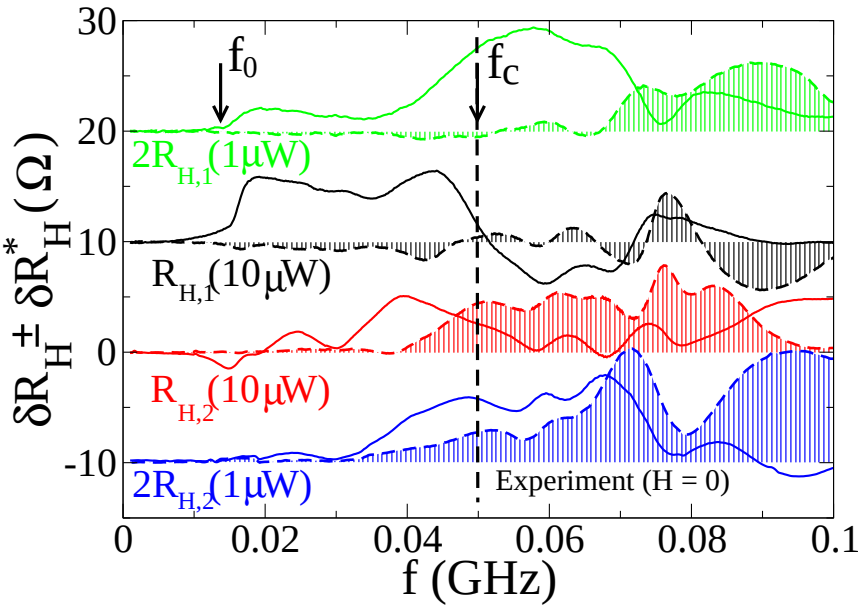

FIG. 1.7 – Changement de la résistance de Hall pour deux sonde de Hall sous une irradiation micro-onde non homogène en fonction de la fréquence micro-onde à champ magnétique nul (un champ magnétique résiduel faible pouvait être présent du fait du champ magnétique terrestre ou de courants résiduels piégés dans la bobine supraconductrice). La résistance de Hall est mesurée dans deux configurations où les sources de courant et les sondes de tension sont interverties, ce qui donne deux valeurs R_H et R_H^*. En l'absence de champ magnétique les relations d'Onsager impliquent que ces valeurs sont égales $R_H = R_H^*$ (à champ magnétique nul la résistance 4-fil en géométrie Hall mesure une composante de la résistance longitudinale de la sonde de Hall liée à ses imperfections géométriques). Les quantités δR_H et δR_H^* représentent le changement de la résistance de Hall dans les deux configurations du fait de l'irradiation micro-onde. Les courbes continues représentent la somme $\delta R_H + \delta R_H^*$ alors que la différence $\delta R_H - \delta R_H^*$ est représentée par les traits discontinus. Cette différence serait nulle, si les relations d'Onsager s'appliquaient à la photo-conductance. Dans ces données expérimentales nous avons changé la fréquences d'excitation pour deux sondes de Hall et deux valeurs de la puissance micro-onde. L'écart $\delta R_H - \delta R_H^*$ s'annule pour des fréquences inférieures à $f \leq f_c \simeq 50$ MHz, alors que la partie symétrique $\delta R_H + \delta R_H^*$ reste non nulle. La composante symétrique finit par s'annuler également à plus basse fréquence $f \leq f_0$ car le couplage capacitif employé devient inefficace. Ces données montrent que dans un régime basse fréquence (adiabatique) la photo-conductance ne brise pas la symétrie par renversement du sens du temps, cependant cette symétrie est brisée à plus haute fréquence. Les relations d'Onsager ne peuvent alors plus s'appliquer. Cette expérience est discutée en détail dans le Chapitre 2.11 de la première partie du manuscrit.

change également dans le temps. A des fréquences suffisamment basses, la variation de la conductance suit la tension de grille, dans cette approximation la conductance moyennée dans le temps prend la forme suivante :

$$< G >= G_0 + G_2 V_0^2/2 + ... \tag{1.2}$$

On remarquera que le terme linéaire $G_1 V_g(t)$ n'intervient pas dans la valeur de la photo-conductance $\delta G =< G > -G_0$ puisque sa moyenne sur le temps est nulle. Dans cette limite adiabatatique la symétrie par renversement du sens du temps n'empêche l'apparition d'une photo-conductance qui provient de la dépendance non linéaire de la conductance en la tension de grille $G(V_g)$ qui est définie à l'équilibre thermodynamique ou plus précisément en régime de réponse linéaire. Néanmoins à haute fréquence l'approximation adiabatique n'est en général plus valable et des effets qui violent la symétrie par renversement du sens du temps apparaissent.

En somme la photo-conductance donne accès à des informations précieuses sur la dynamique et la densité des porteurs photo-induits. Cependant elle apporte assez peu d'information sur les symétries spatiales du système étudié, qu'en est-il de l'effet photovoltaique ?

L'effet photovoltaique consiste en l'apparition d'une tension V_{pv} ou d'un courant stationnaire i_{pv} en réponse à une irradiation à fréquence finie. Dans le cas le plus simple ces deux quantités sont reliées à travers la résistance R de l'échantillon $V_{pv} = Ri_{pv}$. Le dispositif de mesure détermine la quantité mesurée (par exemple si on utilise un amplificateur de tension ou un amplificateur de courant) ; même si expérimentalement on préfère souvent mesurer la tension photovoltaique la quantité i_{pv} se prête plus facilement à une interprétation théorique.

La source d'excitation peut être par exemple un champ électrique micro-onde $\mathbf{E}\cos\omega t$ ou une tension alternative aux bornes de l'échantillon $V_{ac}\cos\omega t$. Puisque sa moyenne sur le temps est nulle, elle ne fixe en général pas d'orientation privilégiée dans l'espace pour le courant photovoltaique stationnaire. Un échantillon qui présente de l'effet photovoltaique ne peut donc pas avoir de symétrie par inversion ($\mathbf{r} \rightarrow -\mathbf{r}$) et contient une asymétrie intrinsèque qui fixe la direction de i_{pv}. Bien sur il y a des exceptions, par exemple dans l'effet "photon drag" la direction du courant est fixée par le vecteur d'onde du champ électromagnétique ; pour simplifier je ne vais pas aborder pour l'instant les cas où l'irradiation brise elle même la symétrie spatiale. Le courant moyen i_{pv} est également proportionnel à la vitesse de dérive moyenne des porteurs. Cette vitesse change de signe par renversement du sens du temps, l'effet photovoltaique brise donc la symétrie par renversement du sens du temps et dépend donc a-priori des processus irréversibles qui assurent le retour à l'équilibre du système.

Pour étudier plus en détail les propriétés de symétrie de l'effet photovoltaique, je vais me concentrer sur un système modèle assez simple constitué d'un réseau de semi-disques orienté dans une même direction (voir Figure 1.8 et insert sur la Figure 1.9). Remarquons que ce système n'est pas chiral puisque l'axe des x est un axe de symétrie du système. Dans ce modèle théorique les électrons suivent des trajectoires classiques obtenues par intégration des équations de Newton en présence d'un champ magnétique H perpendiculaire au plan

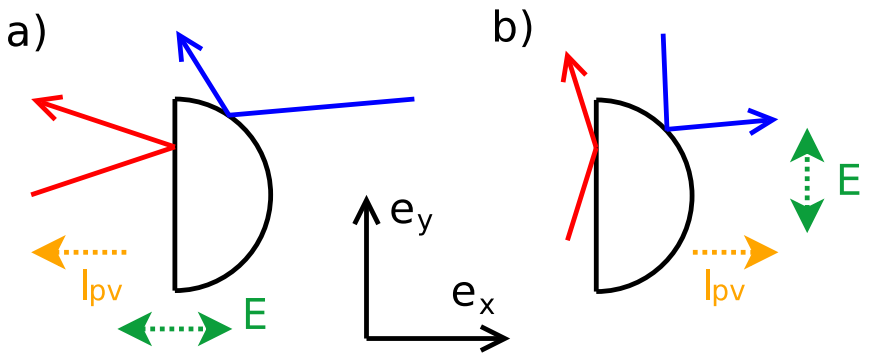

FIG. 1.8 – Cette figure représente des trajectoires typiques pour deux polarisation du champ électrique alternatif $\mathbf{E}$. Lorsque la polarisation est orientée le long l'axe de symétrie des semidisques (cas a), les trajectoires se propageant dans la direction $-\mathbf{e}_x$ sont favorisées. Une polarisation le long de l'axe $\mathbf{e}_y$ (cas b), conduit au contraire à un courant de particules photovoltaique I_{pv} dans le sens $\mathbf{e_x}$. Dans cette représentation le champ magnétique H est supposé nul, les trajectoires sont donc des lignes droites.

des électrons et d'un champ électrique oscillant $\mathbf{E}\cos\omega t$ dans le plan. Les collisions avec les parois sont supposées spéculaires. Dans ce système le mécanisme responsable de la rectification est illustré sur la Figure 1.8. Lorsque les électrons sont soumis à un champ électrique alternatif, les trajectoires se déplaçant dans la direction de la polarisation $\mathbf{E}$ sont favorisées. Après une réflection sur un semidisque ces trajectoires sont en majorité orientées dans la direction $-\mathbf{e}_x$ quand la polarisation est alignée le long de l'axe $\mathbf{e}_x$ qui fixe l'orientation des semidisques. Si la polarisation tourne de 90 degré, ce sont au contraire les trajectoire qui se propagent dans le sens $\mathbf{e}_x$ qui sont majoritaires.

La dépendance du courant photovoltaique du temps τ_H de relaxation irréversible des électron vers la distribution à l'équilibre a été étudié numériquement par [13]. Les simulations ont montré que le courant photovoltaique ne dépend pas de τ_H dans un large domaine de valeur de ce paramètre. Ceci peut sembler surprenant car en l'absence de relaxation (c'est à dire dans la limite $\tau_H \to \infty$) l'effet photovoltaique disparaît puisque la dynamique devient invariante par renversement du sens du temps. Cette disparition des taux de relaxation intervient aussi pour la résistance linéaire qui est déterminée par les collisions élastiques même si elle correspond à un effet dissipatif. Pour le transport classique elle peut être justifiée en remarquant que la puissance libérée par effet Joule $P = V^2/R$ est un effet d'ordre supérieur par rapport au courant continu induit $I = V/R$. Cependant cet argument n'est plus valable pour le transport non linéaire qui dépend de manière quadratique de la tension/champ alternatif. Les cellules photovoltaique solaires fournissent d'ailleurs un contre exemple naturel puisque le taux de recombinaison électron-trou est un paramètre important de ces dispositifs [12]. Il me semble donc que l'origine et la généralité de l'indépendance de i_{pv} vis à vis du taux de relaxation irréversible τ_H reste encore mal comprise.

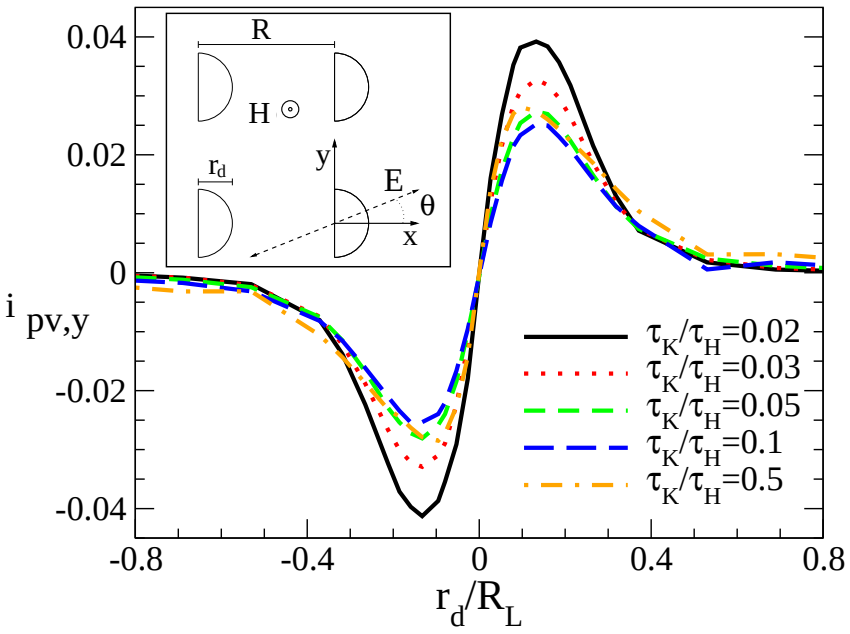

FIG. 1.9 – Cette figure décrit la dépendance en champ magnétique de l'effet photovoltaique dans un réseau constitué de semidisques. L'insert montre la géométrie du motif sur lequel se réfléchissent les électrons. L'axe des x qui fixe l'orientation des semi-disques est un axe de symétrie du réseau, en revanche la symétrie miroir est brisée le long de l'axe des y. La figure principale montre le courant photovoltaique calculé pour la configuration expérimentale M1 (voir tableau 1.1). Le quotient entre le rayon des semidisques r_d et le rayon de Larmor R_L est porté en abscisse, alors que le courant photovoltaique le long de l'axe y en unités arbitraires est porté en ordonnée. Puisque le rayon de Larmor est inversement proportionnel au champ magnétique, la quantité r_d/R_L est en fait proportionnelle au champ magnétique H. Comme le courant est mesuré selon l'axe de la polarisation micro-onde, une telle mesure peut être réalisée dans une expérience à deux contacts. Les simulations montrent que dans cette configuration de mesure, le courant photovoltaique est antisymétrique en champ magnétique même en l'absence d'interaction entre porteurs. Dans ces simulations l'interaction est décrite par le paramètre τ_K/τ_H qui est le rapport entre le temps moyen de parcours τ_K entre deux semidisques et le temps τ_H de libre parcours moyen associé aux interactions entre électrons. Les simulations montrent que dans cette géométrie de mesure, l'interaction modifie peu le courant photovoltaique. Dans ces simulations la fréquence est fixée à $\omega\tau_H = 1$.

Passons maintenant à l'analyse des propriétés de symétrie en champ magnétique. Je note $\mathbf{j}_{pv}$ la densité de courant photovoltaique à travers le réseau constitué par les semidisques, elle peut être décomposée en une partie symétrique $\mathbf{j}_s$ et antisymétrique $\mathbf{j}_a$ en champ magnétique : $\mathbf{j}_{pv} = \mathbf{j}_s + \mathbf{j}_a$. Les symétries du système imposent la forme suivant pour $\mathbf{j}_s$ et pour $\mathbf{j}_a$:

$$\mathbf{j}_s = f_2(H)\,(\mathbf{e}_x \cdot \mathbf{E})\,\mathbf{E} + f_1(H)(\mathbf{E}^2)\mathbf{e}_x \tag{1.3}$$

$$\mathbf{j}_a = g_2(H)\,(\mathbf{e}_x \cdot \mathbf{E})\,(\mathbf{H} \wedge \mathbf{E}) + g_1(H)(\mathbf{E}^2)\,(\mathbf{H} \wedge \mathbf{e}_x) \tag{1.4}$$

Dans cette expression seulement les termes quadratiques en $\mathbf{E}$ ont été gardés car ce sont les termes d'ordre le plus bas qui résistent à la moyenne sur le temps. Les vecteurs qui interviennent dans le résultat sont la polarisation $\mathbf{E}$, la direction $\mathbf{e_x}$ dans laquelle sont orienté les semi-disques et le champ magnétique H. Les fonctions $f_1(H), f_2(H), g_1(H), g_2(H)$ sont paires en champ magnétique. Nous pouvons remarquer d'ores et déjà que même si le réseau de semi-disques n'est pas chiral une composante antisymétrique en champ magnétique du courant photovoltaique est possible : le rayonnement micro-onde polarisé induit en effet un sens de rotation privilégié dans le système.

L'existence d'une partie antisymétrique en champ magnétique du courant photovoltaique a été prédite théoriquement en physique mésoscopique dans les articles pionniers : [14, 15, 16]. Plusieurs travaux théoriques et expérimentaux dans ce domaine ont montré que dans un système mésoscopique, comme un anneau Aharanov-Bohm désordonné, la composante antisymétrique de l'effet photovoltaique résulte des interactions entre électrons pour des fréquences d'irradiation faibles devant l'énergie de Thouless (à des fréquences plus élevées la composante antisymétrique devient du même ordre de grandeur que la composante symétrique indépendamment du paramètre d'intéraction ; voir par exemple Chap. 2.3). Cette conclusion est en un sens surprenante, car l'interaction entre électrons ne change pas le groupe de symétrie de l'Hamiltonien du système. Il est donc intéressant d'étudier la dépendance en interaction de $\mathbf{j}_a$ dans le système modèle constitué par le réseau de semi-disques où l'origine de l'asymétrie est plus contrôlée que le potentiel désordonné aléatoire dans les échantillons mésoscopiques [17].

L'équation Eq. 1.4 suggère deux géométries de mesures qui permettent de déterminer les coefficients $g_1(H)$ et $g_2(H)$ de manière indépendante.

La dépendance du courant photovoltaique en champ magnétique dans les deux configurations de mesures M1/M2 est représentées respectivement sur les Figures. (1.9,1.10) pour plusieurs valeurs du paramètre d'interaction entre particules. Dans la configuration M1, le courant photovoltaique dépend de manière antisymétrique ne le champ magnétique même dans la limite d'interactions faibles. Par contre dans la configuration M2, le courant photovoltaique est symétrique en champ magnétique en l'absence d'interactions : l'asymétrie n'apparaît que lorsque les interactions deviennent suffisamment fortes. Il semble donc d'après ces données que $i_{pv,a}$ peut dépendre ou non de l'interaction en fonction de la géométrie de la mesure.

Tournons nous un moment vers l'interprétation du terme qui ne dépend pas des interactions : $g_1(B)(\mathbf{E}^2)\,(\mathbf{H} \wedge \mathbf{e}_x)$. Sa valeur ne dépend pas de la polarisation du champ

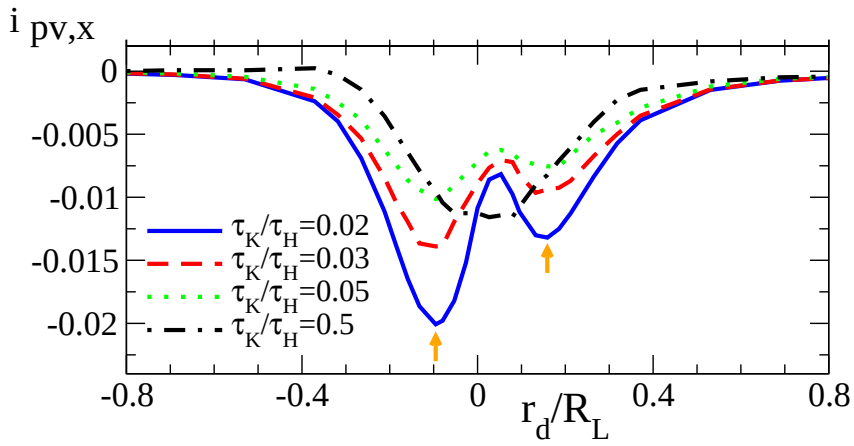

FIG. 1.10 – Courant photovoltaique pour la configuration expérimentale M2 (voir tableau 1.1). L'axe des ordonnées représente en unités arbitraires le courant photovoltaique $i_{pv,x}$ mesuré le long de l'axe des x fixé par l'orientation des semi-disques. Pour rompre la symétrie miroir le long de cet axe, la polarisation micro-onde $\mathbf{E}$ est légèrement incliné de $\pi/20$ radians par rapport à $\mathbf{e}_x$. Remarquons que cette géométrie est également compatibles avec une mesure deux fils puisque la direction du champ et la direction de la mesure du courant sont pratiquement les mêmes. L'axe des abscisse est proportionnel au champ magnétique, et les différentes courbes correspondent à de différentes valeurs du paramètre d'interaction (les définitions des symboles sont données dans la légende de la Figure 1.9). Les simulations montrent que la présence d'interactions est nécessaire pour observer une asymétrie en champ magnétique dans cette géométrie. La courbe noire (continue) sans interactions reste en effet symétrique alors que les courbes en présence d'interactions (en tirets) deviennent asymétriques en champ magnétique, l'asymétrie devenant de plus en plus importante avec la force des interactions. La fréquence de l'irradiation est $\omega\tau_H = 1$.

mesure	dépendance spatiale	description de la mesure sélective
M1	$g_1(B)(\mathbf{E}^2)\,(\mathbf{H}\wedge\mathbf{e}_x)$	mesure de i_{pv} le long de l'axe y $\mathbf{E}$ polarisé selon l'axe y
M2	$g_2(H)\,(\mathbf{e}_x\cdot\mathbf{E})\,(\mathbf{H}\wedge\mathbf{E})$	mesure de i_{pv} selon l'axe x $\mathbf{E}$ polarisation arbitraire

TAB. 1.1 – Ce tableau décrit les géométries de mesure qui permettent de séparer la contribution des deux termes antisymétriques en champ magnétiques possibles pour l'effet photovoltaique dans le réseau de semi-disques.

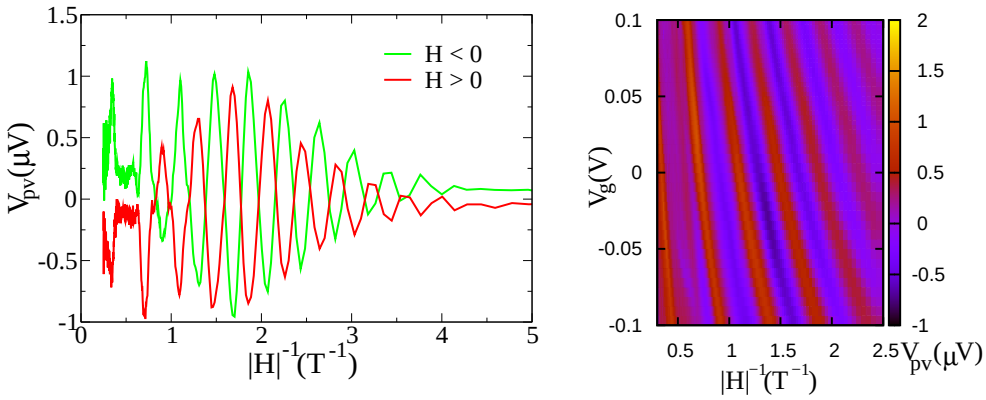

FIG. 1.11 – L'image de gauche montre montre la dépendance en le champ magnétique inverse de l'effet photovoltaique dans l'expérience décrite dans le Chapitre 2.9. Elle montre que l'effet photovoltaique peut être antisymétrique en champ magnétique dans une configuration de mesure bien choisie. Les oscillations de Shubnikov-de Haas sont clairement visibles sur l'effet photovoltaique (même si leur phase est décalée de $\pi/2$ par rapport au transport linéaire). La figure de droite montre comment la période, des oscillations est changée par une tension de grille qui module la densité des porteurs.

micro-onde, il peut être interprété comme le courant Hall associé au photo-courant induit le long de la direction privilégiée dans la quelle sont orientés les semi-disques : $\mathbf{e_x}$. Même si les échantillons mésoscopiques n'ont pas d'axe de symétrie, ils ne définissent pas explicitement de direction privilégiée car un potentiel désordonné est proche d'être isotrope. Ce terme est donc probablement négligeable dans les échantillons mésoscopiques, ce qui conduit à basse fréquence à une composante asymétrique proportionelle à la constante d'interaction [14, 15]. Expérimentalement nous avons confirmé que dans une géométrie de mesure bien choisie, l'effet photovoltaique peut être antisymétrique en champ magnétique (voir données expérimentales sur la Figure 1.11) comme prédit par les données de la Figure. 1.9 validant ainsi le mécanisme d'effet Hall induit par les courants photovoltaiques que je viens de décrire.

En somme l'effet photovoltaique exige (contrairement à la photo-conductance) une rup-

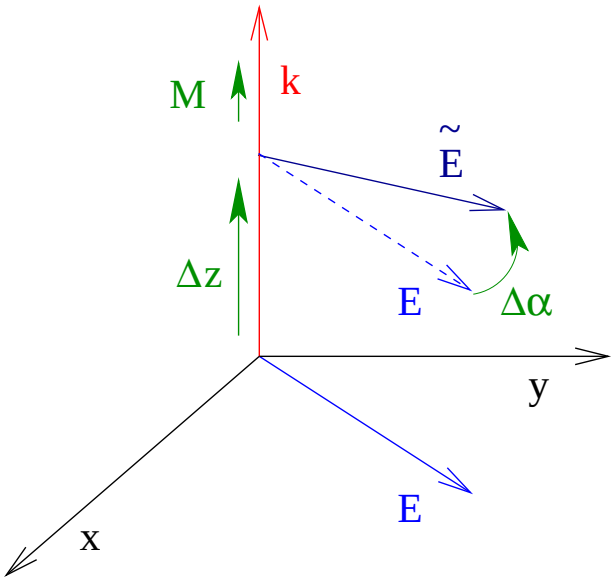

FIG. 1.12 – Dans un milieu chiral la polarisation **E** tourne d'un angle $\Delta\alpha$ lorsque l'onde parcourt une distance Δz le long de sa direction de propagation k. La symétrie spatiale du système formé par le vecteur **k** et le sens de rotation privilégié dans le plan (x, y) déterminé par l'angle $\Delta\alpha$ permet l'apparition d'une magnétisation $\mathbf{M} \propto \frac{\Delta\alpha}{\Delta z}\mathbf{k}$.

ture de symétrie spatiale qui se traduit par l'existence d'au moins une direction privilégiée, et une rupture de la symétrie par renversement du sens du temps par les effets de relaxation vers l'équilibre qui sont en principe importants (même si souvent le résultat n'en dépend pas). L'asymétrie en champ magnétique de l'effet photovoltaique ne donne a priori pas accès à une information directe sur la chiralité du conducteur puisque la présence du champ d'excitation peut également induire une chiralité dans l'échantillon. Cette asymétrie peut avoir plusieurs causes : la présence d'interactions, l'effet Hall sur les boucles de courant photoinduit, la fréquence finie de l'irradiation et le champ magnétique généré par les boucles de courant dans l'échantillon. Parmi ces mécanismes seul ce dernier est directement sensible à la chiralité, cela a été montré par G. Rikken dans des expériences sur des conducteurs chiraux macroscopiques en forme de spirale [18]. Cependant dans une expérience sur des conducteurs de faible dimension il est difficile de prévoir quel mécanisme sera dominant et donc d'obtenir une signature fiable de la chiralité.

Il semble donc difficile de proposer une mesure de transport électronique qui soit sensible à la chiralité du conducteur. Une solution envisageable est la détection du magnétisme orbital induit par une onde linéairement polarisé dans un milieu constitué de molécules chirales d'orientations aléatoires. L'apparition d'un magnétisme orbital sous une irradiation polarisé elliptiquement est connue sous le nom d'effet Faraday inverse [19, 20, 21], dans des milieux non chiraux cet effet disparaît pour des polarisations rectilignes. Cependant dans un milieu chiral un sens de rotation privilégié existe même pour une polarisation rectiligne

comme le montre la construction géométrique en Figure 1.12. A ma connaissance peu de choses sont connues concernant les ordres de grandeur de cet effet pour des systèmes composés de molécule chirales d'orientations aléatoires. Pendant la thèse je me suis penché sur le problème de la modélisation de cet effet pour des systèmes de gaz d'électrons bidimensionel [22] pour lesquels des prévisions théoriques sont plus faciles à obtenir. Pour conclure, les travaux expérimentaux et théoriques inspirés des idées que je viens de développer m'ont permis de proposer une théorie prometteuse pour expliquer les états de résistance nulle induits par une irradiation micro-onde dans des gaz d'électrons bidimensionel de très haute pureté. Les résultats que j'ai obtenus sur les gaz d'électrons bidimensionels sont décrits en détail dans la première partie de la thèse.

1.3 Mesures de transport sur des molécules d'ADN et les nanofils de silicium

Je vais maintenant passer à la description des mesures de transport sur les molécules d'ADN et les nanofils de silicium sur lesquels nous avons essayé de mettre en applications les concepts développés ci dessus. L'étude systématique des propriétés de symétrie du transport non linéaire n'a pas été possible sur les molécules d'ADN, du fait de la difficulté de fabriquer des échantillons conducteurs.

Pour tenter de résoudre ces problèmes nous avons réalisé des échantillons où des molécules d'ADN sont déposées au travers d'une fente isolante gravée dans un film de platine de 5nm d'épaisseur. Ces fentes ont été réalisées grâce à une technique de gravure au faisceau d'ion focalisé avec contrôle in-situ de la conductance développée dans notre groupe. Leur longueur est d'environ 50 micromètres pour une largeur de moins de 100 nm. Les dépôts de molécules ont ensuite été effectués grâce à un traitement qui permet d'accrocher les molécules d'ADN sur des électrodes recouvertes de carbone qui semble assurer un bon contact avec les molécules d'ADN. Des images par microscopie à force atomique de molécules sur nos échantillons, traversant les fentes isolantes sont montrées sur la Figure 1.13.

Les échantillons conducteurs, qui ont pu être mesurés à basse température, ont permis de montrer un comportement avec des corrélations supraconductrices à des températures inférieures à 4 Kelvins même si les contacts (en Platine) ne sont pas supraconducteurs. Ces mesures complétées par des caractérisations poussées au microscope électronique à balayage, et au microscope à force atomique (cAFM) suggèrent que les molécules sont fortement dopées par la présence de nanoparticules supraconductrices à l'intérieur de la fente. Ce sont ces nanoparticules qui induisent des corrélations supraconductrices à l'intérieur des molécules d'ADN à basse température.

Ces résultats ouvrent de nouvelles perspectives pour permettre la conduction de l'ADN à des échelles de plusieurs centaines de manomètres. Néanmoins même si plusieurs indices expérimentaux convergent en ce sens, nous n'avons pas pu démontrer que la conduction est effectivement assurée par les molécules d'ADN. En effet puisque des résidus métalliques

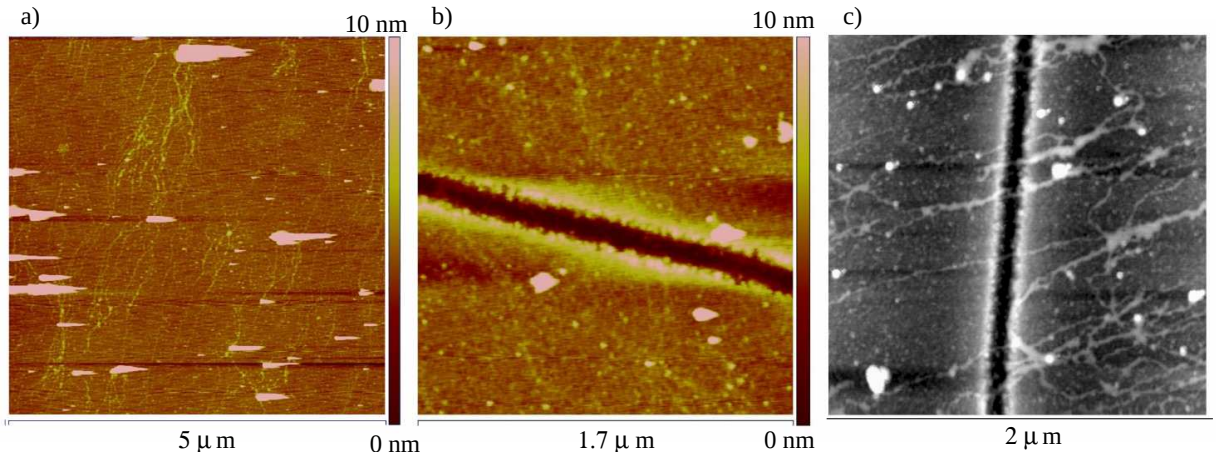

FIG. 1.13 – Panneaux a,b : Images par microscopie à force atomique sur un échantillon conducteur. L'image a) a été prise loin des fentes isolantes et montre l'étalement des molécules loin de la région exposé au faisceau d'ions. L'image b) montre des molécules d'ADN qui traversent une fentes isolante creusées au faisceau d'ions focalisé. Cet échantillon à été détruit au cours des tentatives pour le contacter afin de réaliser des mesures à basse température, sa résistance à température ambiante était de 1.8 kΩ après le dépôt des molécules d'ADN (avant le dépôt des molécules la jonction était ouverte). L'image c. a été prise par D. Klinov et montre également des molécules traversant une fente isolante (probablement sur le même substrat).

sont présents dans la fente isolante, il est possible qu'ils soient réorganisés par le dépôt des molécules d'ADN en phase liquide. Dans les expériences témoin sans molécules d'ADN aucune conduction n'a été observé ce qui rend cette hypothèse peu probable. Toutefois elles ne permettent pas de l'exclure complètement. Par ailleurs nous avons essayé de mener des expériences de photo-conductivité sous irradiation ultra-violette afin d'obtenir une signature spécifique du rôle de l'ADN dans la conduction, mais sur plusieurs échantillons la conduction a disparu à des échelles de temps trop rapides pour permettre une caractérisation fiable. Il est possible que l'irradiation ultraviolette ait endommagé les molécules d'ADN mais à cause du faible nombre d'échantillons conducteurs à notre disposition nous n'avons pas pu exclure que la conduction ait disparu à cause d'impulsions électriques ayant endommagé les échantillons.

Les expériences sur l'ADN sont décrites en détail dans la seconde partie de la thèse, je m'arrêterai donc à ce résumé succinct de nos expériences et des difficultés rencontrées pour passer à une description de nos mesures sans contact sur les nanofils de silicium. Au cours de ces mesures nous avons cherché à vérifier la possibilité de réaliser des mesures sans contacts sur un système de nanofils en mesurant leur contribution à la constante diélectrique du milieu. Ces mesures ont été faites grâce à des résonateurs supraconducteurs multimodes, les fréquences de résonance des différents modes et leurs facteurs de qualité dépendent respectivement de la partie réelle et imaginaire de la constante diélectrique de l'environnement. Les nanofils même s'ils sont placés à proximité immédiate du résonateur,

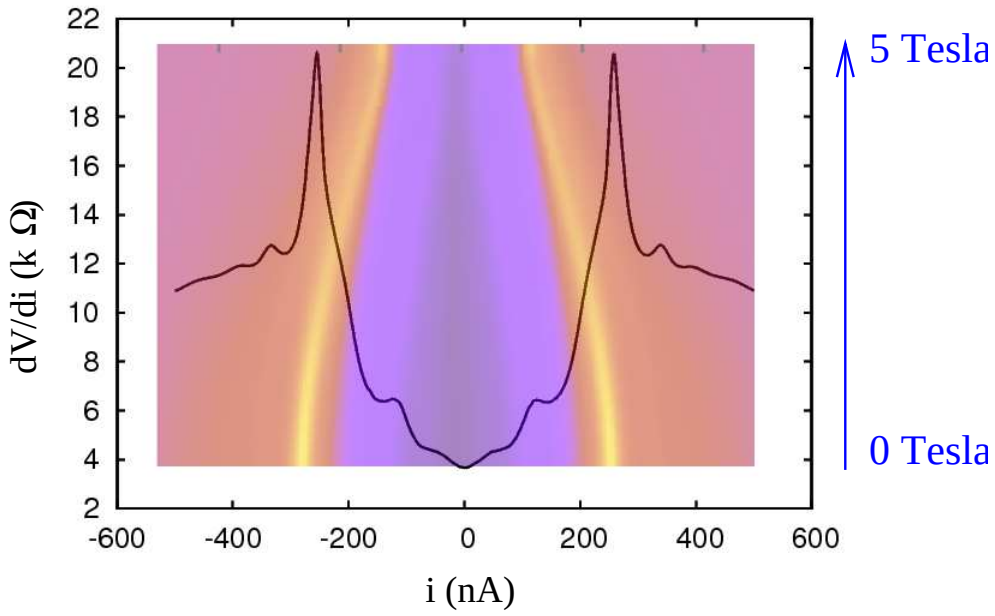

FIG. 1.14 – La courbe noire représente la résistance différentielle dV/di en fonction du courant DC atravers une jonction sur laquelle des molécules d'ADN ont été déposées. La température de mesure est de 100 mK. Cet échantillon est devenu conducteur après un dépôt de molécules d'ADN avec une résistance à température ambiante de 10 kΩ. Le transport à basse température, montre des signes de fluctuations supraconductrices. Le fond coloré montre la dépendance de la résistance différentielle représenté par le code couleur avec le courant en abscisse et le champ magnétique en ordonnée. Le jaune/violet représente la conductance différentielle maximale/minimale. Le champ magnétique varie de 0 à 5 Teslas et conduit à une diminution de la largeur du creux dans la dV/di sans pour autant détruire complètement la supraconductivité. Ces champs critiques élevés suggèrent l'influence de nanoparticules supraconductrices dont la présence a été confirmée par microscopie électronique et par microscopie à force atomique.

ne forment qu'une partie de son environnement électromagnétique : le résonateur repose par exemple sur un substrat qui contribue lui aussi à la constante diélectrique totale. Pour isoler la contribution des nanofils, une possibilité consiste à les éclairer avec de la lumière afin de créer des porteurs dans les nanofils. Le substrat en saphire avec un "gap" de 9.9 eV est en effet insensible à une lumière visible, alors qu'une lumière bleue d'énergie d'environ 2.5 eV peut exciter des porteurs dans des nanofils de silicium avec un "gap" $\Delta \simeq 1.2$ eV. Pour pouvoir effectuer cette mesure sur de l'ADN il faudrait en revanche avoir une radiation d'énergie plus élevée dans l'ultraviolet. Pour l'instant notre dispositif expérimental ne permet pas d'éclairer avec une lumière ultraviolette à basse température. Nous nous sommes donc concentrés sur le cas des nanofils de silicium, afin de valider notre technique de mesure et de mieux comprendre les informations qu'on peut en extraire.

Des résultats expérimentaux typiques sont montrés en Figure 1.15. Le résonateur supra-

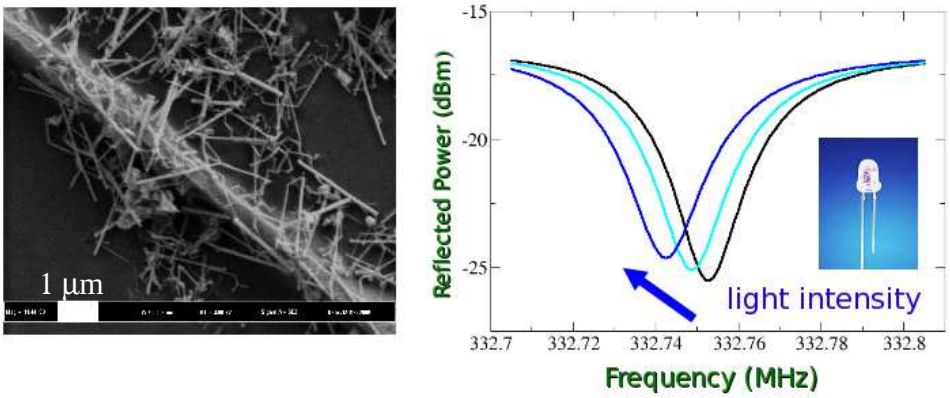

FIG. 1.15 – L'image de gauche obtenue par microscopie électronique à balayage montre les nanofils de silicium déposés sur un résonateur supraconducteur multimode. L'image de droite représente le décalage de la fréquence de résonance et la diminution du facteur de qualité en présence d'illumination par une lumière bleue. La température de l'expérience est 4.2 K. Le facteur de qualité est élevé (de l'ordre de 10^4) grâce à l'utilisation de matériaux supraconducteurs ce qui assure une grande sensibilité à la mesure.

conducteur recouvert de nanofils de silicium, est éclairé par une diode bleue. Sous l'effet de celle-ci on observe un décalage de la fréquence de résonance et une diminution du facteur de qualité de la raie. La diminution du facteur de qualité résulte de la création de paires électrons trou dans le silicium qui contribuent à dissiper l'énergie du champ micro-onde dans le résonateur. Ce signal photo-conductif existe également sur les échantillons de Silicium massifs. En revanche le décalage de la fréquence de résonance n'a été observé que pour les nanofils, en effet les porteurs photoinduits dans les nanofils sont très confinés et se polarisent donc facilement. La photo-polarisabilité observée dans nos expériences, peut permettre d'aborder sous un angle nouveau les propriétés des excitons dans les molécules. En effet ceux-ci ne participent pas au transport électronique mais peuvent se polariser sous une irradiation extérieure.

Les résultats sur les nanofils de silicium sont détaillés dans la seconde partie du manuscrit.

1.4 Application standard de Chirikov

Je vais conclure cette introduction par une description succincte d'un système non-linéaire très simple mais représentatif des phénomènes subtils qui peuvent apparaître dans d'autres systèmes non linéaires plus complexes : l'application standard de Chirikov. Ceci me permettra de faire le lien entre la présentation plutôt expérimentale du chapitre sur le transport non linéaire Chap. 1.2 et les concepts théoriques sous-jacents. En outre je montrerai dans ce manuscrit que ce système itératif décrit le transport le long des canaux de bord en présence d'irradiation micro-onde. Cette application est décrite par deux équations couplées :

$$\begin{cases} \bar{p} = p + K \sin x \\ \bar{x} = x + \bar{p} \end{cases} \tag{1.5}$$

Les quantités $\bar{p}$ et $\bar{x}$ dénotent les valeurs des variables p, x après une itération, K est un paramètre sans dimension qui décrit à quel point le système est proche d'un système intégrable ou d'un système chaotique. En raison de la périodicité de la fonction $\sin(x)$ la dynamique peut être représentée sur un tore en prenant $x = x(\mathrm{mod} 2\pi)$ et $p = p(\mathrm{mod} 2\pi)$.

L'application standard de Chirikov Eq. (1.5) décrit en fait la dynamique d'un système Hamiltonien :

$$H(p, x, t) = \frac{p^2}{2} - K \cos(x) \sum_n \delta(t - n) \tag{1.6}$$

où la somme parcourt tout les entiers. Cet Hamiltonien décrit une série de propagations libres, séparées par des à-coups réguliers qui changent l'impulsion p brutalement. En effet en intégrant par rapport au temps les équations Hamiltoniennes du mouvement

$$\begin{cases} \frac{dx}{dt} = \frac{\partial H}{\partial p} \\ \frac{dp}{dt} = -\frac{\partial H}{\partial x} \end{cases} \tag{1.7}$$

sur une période on retrouve l'application Eq. (1.5). Il s'en suit que la dynamique engendré par cette application conserve le volume dans l'espace phase. Cette propriété peut être verifiée directement par le calcul du Jacobien :

$$\frac{\partial(\bar{p}, \bar{x})}{\partial(p, x)} = \begin{vmatrix} \frac{\partial \bar{p}}{\partial p} & \frac{\partial \bar{p}}{\partial x} \\ \frac{\partial \bar{x}}{\partial p} & \frac{\partial \bar{x}}{\partial x} \end{vmatrix} = \begin{vmatrix} \frac{\partial(p + K \sin x)}{\partial p} & \frac{\partial(p + K \sin x)}{\partial x} \\ \frac{\partial(x + p + K \sin x)}{\partial p} & \frac{\partial(x + p + K \sin x)}{\partial x} \end{vmatrix} = 1 \tag{1.8}$$

Le comportement de cette application peut être exploré par des simulations numériques en représentant les valeurs successives par prises la suite (p, x) au cours de l'itération Eq. (1.5). Ceci revient en fait à construire une section de Poincaré de l'Hamiltonien Eq. (1.6), les résultats numériques sont représentés sur la Figure 1.16 pour plusieurs valeurs

du paramètre K. Pour $K \ll 1$ le comportement de l'application est proche de l'Hamiltonien d'un pendule :

$$H(p,x,t) = \frac{p^2}{2} - K\cos(x) \tag{1.9}$$

La durée entre les à-coups qui changent l'impulsion (1 dans les unités de l'Hamiltonien Eq. (1.6)) devient en effet très faible devant la période du pendule décrit par l'Hamiltonien Eq. (1.9) $T = 2\pi/\sqrt{\pi} \gg 1$, ce qui permet de remplacer les peignes de Dirac par leur valeur moyenne sur la période et conduit à l'Hamiltonien du pendule. L'espace phase pour $K \ll 1$ est donc séparé en plusieurs résonances 2π périodiques en impulsion p, chacune des résonances a une épaisseur maximale en impulsion de $\Delta p = 2\sqrt{2K}$. Cette quantité correspond à deux fois l'impulsion maximale pour laquelle le pendule Eq. (1.9) admet encore des solutions périodiques. Entre les résonances, la dynamique est proche de celle d'une particule libre d'Hamiltonien $H = \frac{p^2}{2}$. Ces deux régions sont séparées par des séparatrices dont l'équation pour $K \ll 1$ est bien décrite par l'équation de la séparatrice du pendule.

Lorsque la valeur du paramètre K augmente, des résonances secondaires apparaissent, ceci ce voit bien par exemple sur la Figure 1.16 pour $K = 0.2$. Néanmoins la dynamique reste périodique dans la plus grande partie de l'espace phase, sauf près des séparatrices où des régions stochastiques confinées apparaissent. Le confinement des régions stochastiques a en fait une origine mathématique très profonde, puisque la théorie Kolmogorov-Arnold-Moser (KAM) montre que les régions stochastiques creés par une perturbation suffisamment faible d'un Hamiltonien intégrable sont bornées par des courbes invariantes pour une valeur suffisamment faible de la perturbation. Dans le cas de l'application standard de Chirikov, l'Hamiltonien initial intégrable est $H_0 = \frac{p^2}{2}$ alors que le terme $V(x,t) = -K\cos(x)\sum_n \delta(t-n)$ joue le rôle de la perturbation.

Cependant lorsque la perturbation devient suffisamment forte la majorité des courbes invariantes est détruite (voir Figure 1.16 pour $K = 2$). Ceci crée une large région stochastique dans la quelle la variable p croit de manière diffusive et n'est plus bornée avec le temps. Au sein de cette région des îlots de stabilité subsistent encore autour de la position des résonances pour $K \ll 1$. Lorsque $K \simeq 1$, l'espace phase a une structure complexe où les régions stochastiques et régulières occupent approximativement la même surface et se mélangent entre elles.

La détermination de la valeur critique K_c du paramètre K pour laquelle des trajectoires diffusives non bornées apparaissent a une grande importance du point de vue fondamental et également en pratique. Par exemple si on imagine, que l'Hamiltonien décrit la dynamique dans un piège, alors le seuil où la diffusion apparaît correspond à une valeur des paramètres où le confinement dans le piège commence à être détruit par la diffusion. B. Chirikov a proposé un critère universel pour déterminer approximativement le seuil d'apparition du chaos : le critère de recouvrement des résonances. Sans rentrer dans une discussion de ce critère dans un cadre général, je vais juste montrer comment ce critère peut s'appliquer sur l'exemple de l'application standard. Selon le critère de recouvrement des résonances le chaos apparaît lorsque les résonances voisines séparées de 2π dans la direction des impulsions commencent à se recouvrir. L'épaisseur des résonances en impulsion est donnée dans

l'approximation du pendule par $\Delta p = 2\sqrt{2K}$, ceci conduit à une équation qui détermine K_c

$$\Delta p = 2\pi \;\rightarrow\; K_c = \pi^2/2 \simeq 4.93 \tag{1.10}$$

Les données de la Figure 1.16 confirment que le chaos se développe au fur et à mesure que les résonances se rapprochent, cependant déjà pour $K = 2$ l'espace des phases est chaotique hormis à l'intérieur des îlots de stabilité. Des études numériques et analytiques plus poussées ont montré que le seuil de transition vers le chaos se situe en réalité autour de $K_c \simeq 0.97$. Le critère de recouvrement entre résonances surestime donc le seuil d'apparition du chaos. Physiquement ceci est relié au fait que les résonances d'ordre supérieur n'ont pas été prises en compte dans le critère simple Eq. (1.10). Une extension du critère qui tient compte des harmoniques plus élevées conduit à $K_c \simeq 1.2$.

En conclusion, même si des méthodes analytiques plus sophistiquées ont été développées depuis, le critère de recouvrement entre résonances reste le critère physique le plus simple et universel pour décrire l'apparition du chaos. Un traitement approfondi des propriétés de l'application standard et du problème de la transition vers le chaos est présenté dans les références [23, 24, 25]. En physique mésoscopique, les états de bord en présence de micro-onde, semblent décrits par l'application standard de Chirikov dans le régime intégrable $K < K_c$, je ne discuterai donc pas des problèmes de transition vers le chaos dans la suite de ce manuscrit. Cependant je crois qu'il était important de récapituler ici les propriétés les plus simples de ce système très riche.

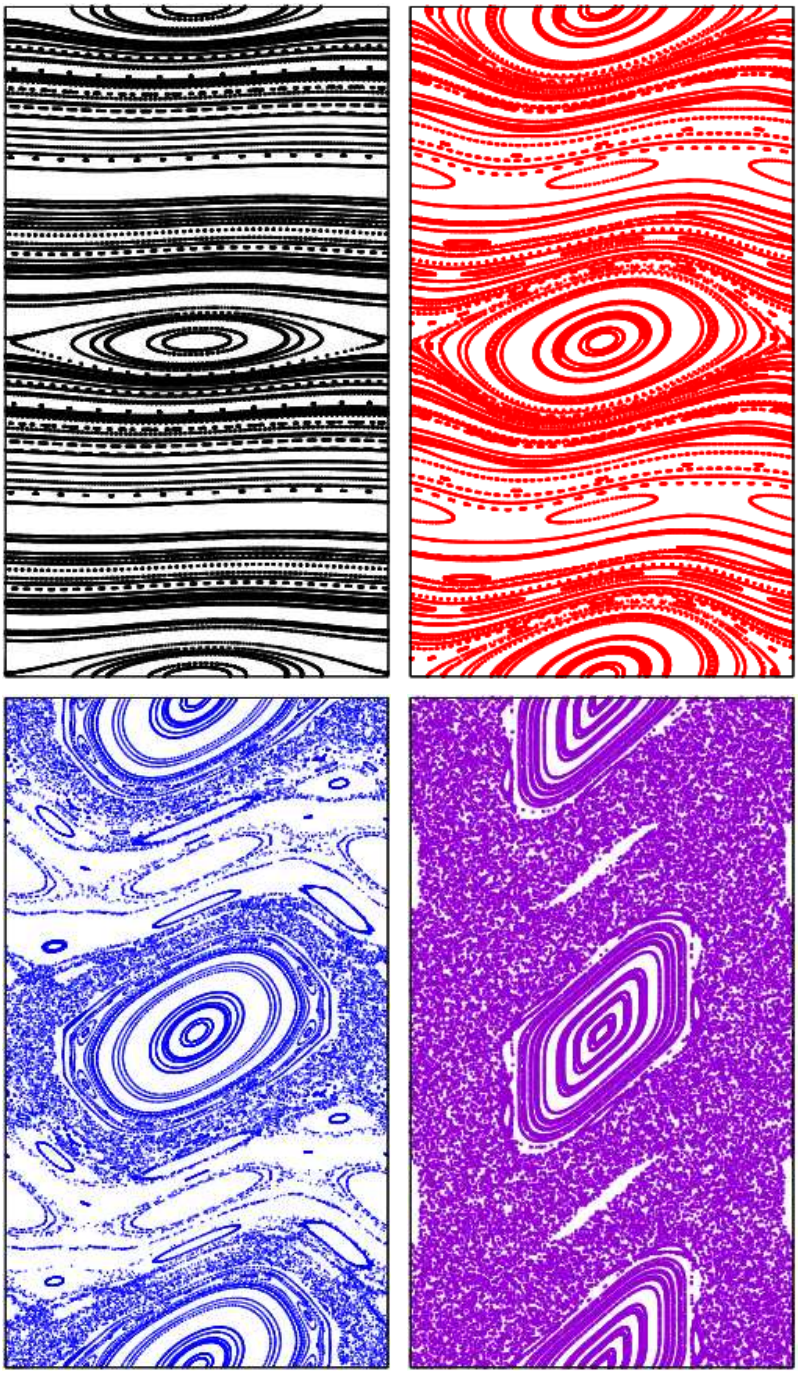

FIG. 1.16 – Sections de Poincaré de l'application standard de Chirikov dans l'intervalle $x \in (0, 2\pi) \mathrm{mod} 2\pi$ (en abscisse) et $p \in (0, 4\pi) \mathrm{mod} 4\pi$ (en ordonnée) pour $K = 0.1$ (figure noire), $K = 0.5$ (figure rouge), $K = 1.0$ (figure bleue), et $K = 2.0$ pour la figure violette. Deux périodes sont représentées sur l'axe des ordonnées afin d'illustrer l'idée d'interaction entres les résonances voisines.

Bibliographie

[1] *Amino acids and the asymmetry of life*, Uwe J. Meierhenrich, Springer, New York. ISBN 3540768858.

[2] *Physical causes of dissymetry in living systems*, V.A. Kizel, Science, Loscow, 1985 (in Russian)

[3] J.D. Watson, F.H.C. Crick, Nature **171**, 738 (1953)

[4] P.G. de Gennes, The physics of Liquid Crystals (Oxford Univ. Press, London, 1974)

[5] V. M. Kaganer, H. Möhwald, P. Dutta, Rev. Mod. Phys. **71**, 779 (1999)

[6] J. V. Selinger, Z.-G. Wang, R. F. Bruinsma and C. Knobler **70**, 1139 (1993)

[7] R. Viswanathan, J. A. Zasadzinski and D. K. Schwartz **368**, 440 (1994)

[8] T. D. Lee and C. N. Yang, Phys. Rev. **104**, 254 (1956)

[9] C.S. Wu, E. Ambler, R. W. Hayward, D. D. Hoppes, and R. P. Hudson, Phys. Rev. **105**, 1413 (1957)

[10] G.L.J.A. Rikken and E. Raupach, Nature **390** 494 (1997)

[11] A.F. Croxall, K.D. Gupta, C.A. Nicoll, M. Thangaraj, H.E. Beere, I. Farrer, D.A. Ritchie and M. Pepper, Phys. Rev. Lett. **101**, 246801 (2008)

[12] P. Wurfel, Physics of Solar Cells : From Principles to New Concepts, ISBN-13 : 978-3527404285, Wiley-VCH Verlag (2005)

[13] G.Cristadoro and D.L.Shepelyansky, Phys. Rev. E **71**, 036111 (2005)

[14] D. Sánchez and M. Büttiker, Phys. Rev. Lett. **93**, 106802 (2004)

[15] B. Spivak and A. Zyuzin, Phys. Rev. Lett. **93** 226801 (2004)

[16] M.L. Polianski and M. Büttiker, Phys. Rev. B **76**, 205308 (2007)

[17] L.Ermann, A.D Chepelianskii and D.L.Shepelyansky, *Magnetic field symmertry of ratchet transport* to be published 2010

[18] G.L.J.A. Rikken, J. Fölling and P. Wyder, Phys. Rev. Lett. **87** 236602 (2001)

[19] L. Landau and E. Lifshitz, *Electodynamics of Continuous Media* (Pergamon Press, New York, 1960)

[20] R. Hertel, J. Magn. Magn. Mater. **303**, L1 (2006)

[21] M. L. Polianski, Phys. Rev. B **80**, 241301(R) (2009)

[22] A. D. Chepelianskii and D. L. Shepelyansky, Eur. Phys. J. B **55**, p.261 (2007)

[23] B.V.Chirikov, *A universal instability of many-dimensional oscillator systems*, Phys. Rep. **52** : 263 (1979)

[24] A.J. Lichtenberg and M.A. Lieberman, (1992).*Regular and Chaotic Dynamics*. Springer, Berlin. ISBN 978-0-387-97745-4.

[25] B.Chirikov, D.Shepelyansky, *Chirikov standard map*, Scholarpedia, 3(3) :3550 (2008), www.scholarpedia.org/article/Chirikov_standard_map

Chapitre 2

Non linear dynamics in two dimensional electron gas

2.1 Transport models in classical and quantum mechanics

Macroscopic metallic electrical circuits are well described by the combination of Ohm and Kirchoff laws. Only when electron transport is studied at smaller scales do the details of scattering mechanisms become important due to the absence of self-averaging. For this purpose more complete models are required. Low temperature transport measurements proved very fruitful at introducing new concepts to solid state physics by investigating transport in previously unattainable regimes. A broad temperature regime is well described by the kinetic transport theory. In this models the electrons are described by the distribution function $f(\mathbf{p}, t)$ of their momentum $\mathbf{p}$ at time t. The time evolution of the distribution function is obtained from classical equations of motion and probability conservation in the phase space. Quantum mechanics which is necessary to describe scattering mechanisms on a microscopic level is introduced through collision integrals $I_{cc}(f)$ that describe the transition probabilities between states with different momenta. The transition rates can usually be obtained from the Fermi-Golden rule which keeps the quantum part of the calculations relatively simple. All these ingredients combine to yield the kinetic Boltzmann equation

$$\frac{\partial f}{\partial t} + q\mathbf{E}(\mathbf{t})\frac{\partial f}{\partial \mathbf{p}} = I_{cc}(f) \tag{2.1}$$

Here q is the carrier charge and $\mathbf{E}(\mathbf{t})$ is the electric field driving electron transport. In general $I_{cc}(f)$ is a non-linear functional of the distribution function f and the kinetic equation can not be solved explicitly. In order to obtain a solvable equation one notices that the collision integral vanishes on the equilibrium distribution function f_0. For small perturbations around equilibrium the collision integral can be linearized leading to the τ approximation $I_{cc}(f) = -(f - f_0)/\tau$. The time τ is an overall relaxation time, which usually depends on electron-impurity, and electron-phonon interactions. In this form the

kinetic equation can be solved through perturbation theory in the quantity $f - f_0$. In the above simple example, this entails the usual Drude value for conductivity :

$$\sigma(\omega) = \frac{q^2 n}{m} \frac{\tau}{1 + i\omega\tau} \tag{2.2}$$

where ω is the driving frequency and m is the carrier mass.

The kinetic equation describes successfully the temperature dependence of electrical resistance in a broad temperature range. It also explains some general relations between transport coefficients (for example the Wiedemann-Franz law). At last kinetic theory is the starting point for the quantitative description of transport in semiconductor structures where contrarily to metals extremely nonlinear current voltage $I(V)$ characteristics are observed. Despite its successes the kinetic theory usually breaks down at sufficiently low temperatures when quantum effects start to play a dominant role. A possible reason for the dramatic failure of kinetic theory, is that at very low temperatures the system occupies a nontrivial many-body ground state that can not be described as independent electrons anymore. Perhaps the most spectacular realization of this scenario is the superconductor transition discovered by Kamerlingh Onnes in 1911. To describe these behaviors theoretically innovative approaches had to be found, since no general method exists to establish the ground state directly from a many body Hamiltonian. The Bardeen, Cooper, and Schrieffer (BCS) theory is an historic example of a construction of this kind. Several other ground states play a central role in solid state physics, for example the fractional quantum Hall effect states in two dimensional electron gas and the Kondo ground state for metals with dilute magnetic impurities. The observation of these new ground states, spurred intense experimental and theoretical studies and theoretical understanding was often achieved years after the initial experiments.

Even when carriers can still be described as independent electrons, quantum interferences in a disordered potential can drastically modify the predictions of the kinetic theory. This occurs in the localization metal insulator transition discovered theoretically by P. W. Anderson. He showed that the random inference between waves scattered by random impurities lead to an exponential localization of the wave functions in real space. This in turn leads to an exponential suppression of classical diffusion which is responsible of the metal-insulator transition. This phenomenon is actually generic to wave propagation in disordered media and spreads well beyond the realm of solid state physics. Important efforts have been devoted to the observation of Anderson localization of light, and recently Anderson localization was also observed in cold atom physics. At last dynamical localization was a spectacular result in the field of quantum chaos.

Recently the intermediate regime where quantum fluctuations start to show up attracted considerable attention. These investigations, were made possible by the technological progress in fabrication of small electronic devices where the electron phase could remain coherent through the entire sample at low temperatures (typical devices have a size in the micrometer range). In these samples the quantum mechanical contribution is still a correction to the results of the kinetic theory, and an elegant description of electronic transport was developed to takes into account interference phenomena. The field devoted

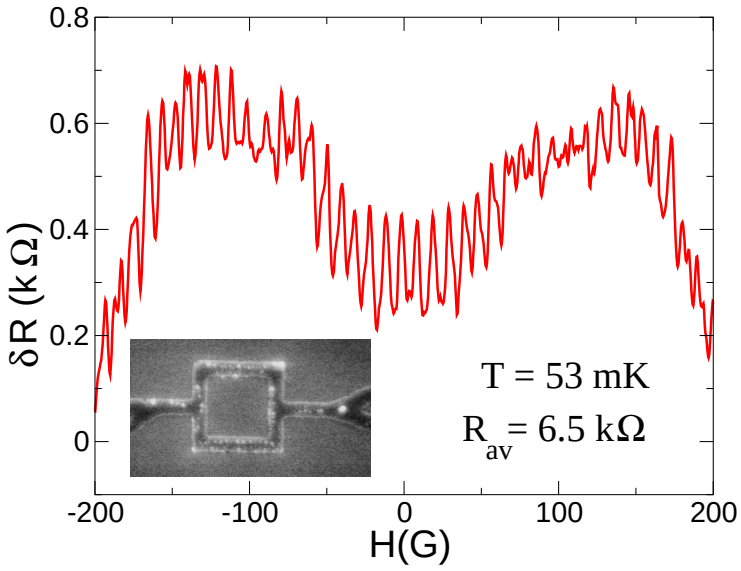

FIG. 2.1 – Measurement of Aharonov-Bohm oscillations in a two dimensional electron gas ring with perimeter of 6 μm

to study of this regime is called mesoscopic physics. One of the founding experiments of mesoscopic physics was the observation of the Aharonov-Bohm interference pattern in the magnetoresitance of small ring structures [1]. A typical experimental pattern measured at low temperature in a two dimensional electron gas ring (2DEG) is shown on Fig. 2.1. It has strikingly the features of an optical interference pattern. To describe this interference phenomenon one must renounce to the point of view of the kinetic theory where carriers are mainly treated as classical particles and include quantum mechanics directly into the transport theory. A simple way to achieve this goal is to use the semi-classical formalism, where conductance G is expressed as through the sum of the propagation amplitudes along all paths in the sample. Different paths acquire different phase and interference appear in a way similar to optical interferometers. In more formal terms, the expression for conductance reads :

$$G = \left| \sum_i A_i e^{i\phi_i} \right|^2 = \sum_i |A_i|^2 + \sum_{i \neq j} A_i^* A_j e^{i(\phi_j - \phi_i)} \tag{2.3}$$

Here A_i is the classical probability of the path i, while the term $e^{i\phi_i}$ represents the phase acquired during the propagation in the ring. The sum runs over all trajectories that span between the two contacts of the Aharonov-Bohm ring. An example of typical trajectories is shown on Fig. 2.2. This expression for G can be decomposed in two parts. The first part consists of terms with $i = j$, it is a classical term similar to Drude conductance (see Eq. (2.2)). The second term contains the contribution of the phase ϕ_i accumulated along

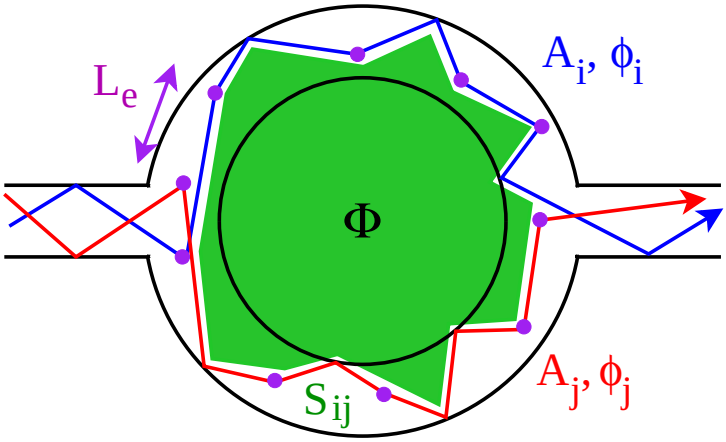

FIG. 2.2 – Two typical trajectories (i) and (j) in an Aharonov-Bohm ring of size L that link the two contacts of the ring. The area S_{ij} delimited by the two trajectories is approximately indicated in green. Purple disks represent elastic impurities with average distance L_e. The magnetic flux through the ring is noted Φ.

the classical path. In a semi-classical approximation this phase is given by :

$$\phi_i = \frac{S[r_i(t)]}{\hbar} = \frac{1}{\hbar}\int_{\tau_0}^{\tau_f} \mathcal{L}(\mathbf{r_i}(t), \mathbf{r}_i'(t), t)dt \tag{2.4}$$

where $S[r_i(t)]$ is the classical action acquired along trajectory $r_i(t)$ and $\mathcal{L}$ is the system's Lagrangian. I have also introduced the time τ_0 when the trajectory leaves the left contact and the time τ_f when it is absorbed in the reservoir on the right. To understand the magnetic field dependence in the Aharonov-Bohm effect, it is enough to consider only the magnetic field dependent part of the Lagrangian $\mathcal{L} = -e\mathbf{r}'(t)\cdot\mathbf{A}$. The vector potential $\mathbf{A}$ is related to the magnetic field through the relation $\mathbf{B} = \text{rot}\ \mathbf{A}$. With this simplification the phase difference between the two paths shown in Fig. 2.2 becomes :

$$\phi_i - \phi_j = \phi_{ij}^0 - \frac{e}{\hbar}\left(\int_{(i)} \mathbf{A}(\mathbf{r}_i(t), t)d\mathbf{r}_i - \int_{(j)} \mathbf{A}(\mathbf{r}_j(t), t)d\mathbf{r}_j\right) \tag{2.5}$$

$$= \phi_{ij}^0 - \frac{e}{\hbar}\int_{S_{ij}} \mathbf{B}\cdot\mathbf{dS} = \phi_{ij}^0 - \frac{e\Phi}{\hbar} \tag{2.6}$$

In the last step I have approximated the magnetic flux through the complicated domain S_{ij} enclosed between curves i and j by the average flux through the ring Φ, and I introduced the notation ϕ_{ij}^0 for the magnetic field independent par of the dephasing $\phi_i - \phi_j$. The terms in Eq. (2.3) can now be arranged in the approximate form :

$$G = G_0 + G_{AH}\cos\left(2\pi\frac{\Phi}{\Phi_0}\right)\ ,\ \Phi_0 = \frac{e}{h} \tag{2.7}$$

which shows that the magnetic field period of the Aharonov-Bohm oscillations is given by the field that induces a flux quantum $\Phi_0 = \frac{e}{h}$ in the ring. The conductance G_0 is equal to the

classical conductance and the amplitude G_{AH} is usually of the order of the conductance quantum $G_0 = e^2/h$ when temperature is low enough for the phase of the electrons to remain coherent across the sample on a length scale L_ϕ called phase coherence length and determined by inelastic interactions. At temperature $T \simeq 100$ mK, L_ϕ is of the order of a few micrometers. Another important characteristic length-scale is the mean free path L_e which is determined by elastic scattering. Elastic processes do not destroy phase coherence, since electron energy is conserved, but they blur the regular interference pattern predicted by Eq. (2.7) as can be seen from the experimental data in Fig. 2.1. Usually mesoscopic physics experiments take place in a regime the size L of the samples is in the range : $L_e < L < L_\phi$ (see Fig. 2.2).

The semi-classical model is very convenient to qualitatively understand interference phenomena in mesoscopic devices, but quantitative results are difficult to derive in this framework because it provides no rule to compute the sum over trajectories that appear in Eq. (2.3). These sums may be evaluated in more rigorous theoretical approaches based on Landauer-Buttiker or the Green function formalisms. However the accuracy is often achieved at the expense of the physical transparency of the calculations. Therefore sometime we will adopt an intermediate approach where a qualitative picture is obtained from the semi-classical formulas and the missing parameters are estimated from a more involved calculation.

The reduction of electrical devices to nanometric dimensions has revealed new exciting quantum effects (with Aharonov-Bohm oscillations being one of the examples). However some unexpected behaviors can still be understood from classical physics. An intuitive example is the quenching of the Hall effect in small ballistic junctions of size $L > L_e$. Classical mechanics suggests that Hall effect can be observed only when the electrons have time to describe at least one cyclotron orbit before leaving the junction (otherwise the effect of magnetic field can be neglected). This predicts that Hall effect should decrease in ballistic samples with channel size $L \ll v_F/\omega_C$ where v_F is the Fermi velocity and ω_C is the cyclotron frequency. This effect has indeed been observed by [72] however the theoretical explanation did not emerge immediately. Indeed first theoretical explanations attempted to model this effect in a purely quantum formulation. And the simple picture from classical physics does not emerge easily in these approaches.

In summary depending on the context transport can be described more naturally with different theoretical approaches. Kinetic theory is very successful when quantum mechanics is restricted to a microscopic scale smaller than the sample size. But note that even if this condition is satisfied kinetic-theory can break down for example if interactions among carriers are too strong or if the details of the classical dynamics must be taken into account more accurately. The Wigner crystal (formed for example by electrons trapped on a liquid Helium surface) is an example where both these situations are realized. In the mesoscopic regime quantum interferences start to play a role. These effects can be described only if electrons are treated as waves, instead of an ensemble of particles with a well defined momentum distribution function. However while the interferences appear naturally in these theories some aspects of classical mechanics may be hard to recover. As we will see non-linear transport often involves both aspects of quantum and classical physics and therefore

it will be important to choose the transport description most appropriate for the physical context.

2.2 Non linear high frequency transport experiments

The previous section focused on the stationary (low frequency) linear conductance. As can be seen straightforwardly from the Drude relation Eq. (2.2), the conductance $G(\omega)$ at a finite frequency ω probes the characteristic time-scales of the system. In the Drude formula only the elastic relaxation rate appears but in a mesoscopic samples additional time-scales set-in for e.g. the diffusion time across the sample and the information which could be extracted from $G(\omega)$ is very rich. However it is difficult to measure $G(\omega)$ directly in a low temperature dilution fridge environment. Indeed for a frequency $f = 1$ GHz, the electromagnetic wavelength is 30 cm. The high frequency measurement setup is located at room temperature outside the cryostat. It is connected to the sample by wires typically longer that 1 m, thus propagation becomes important. To actually measure $G(\omega)$ one needs a 50 Ω adapted transmission line down to the mesoscopic sample in a constraining dilution fridge environment. Although this direct approach allowed to obtain several key experimental results including the measurement of AC-conductance Aharaonv-Bohm oscillations [2] and the determination of mesoscopic capacitance [3], it is technologically very difficult to achieve in practice.

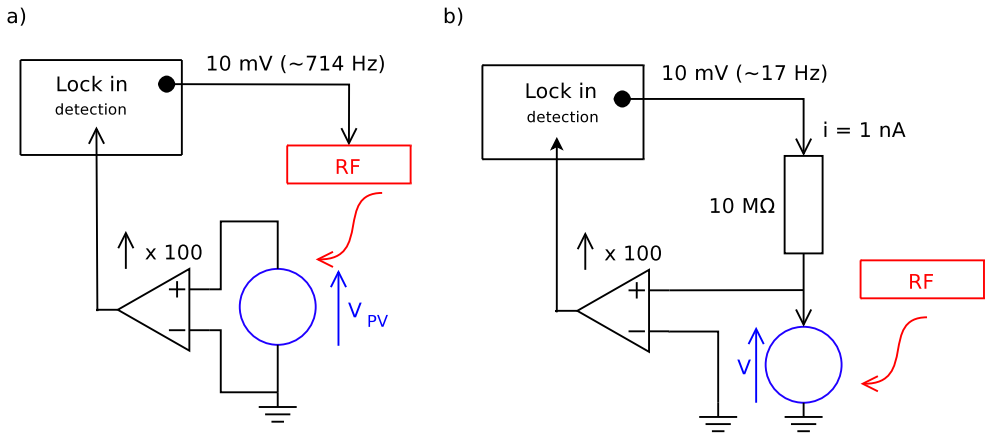

FIG. 2.3 – a) Typical measurement scheme for the microwave induced photovoltaic voltage V_{PV}. b) Measurement scheme for measuring the change of sample conductance under microwave irradiation.

Instead of attempting to measure the high frequency conductance $G(\omega)$ or $\sigma(\omega)$ directly, it is easier to measure the effect of microwave irradiation on low frequency quantities. Such experiments give access to information on the nonlinear response properties of mesoscopic samples and are therefore highly interesting from a fundamental point of view. Two simple experiments can be imagined in this direction. One can study the rectification proprieties of a sample by measuring the DC-voltage that develops under microwave irradiation.

By analogy with semiconductor photovoltaic cells that develop a voltage under light irradiation, we will call this behavior the photovoltaic effect (in the microwave frequency range). Another possibility is to measure the change of DC-conductance G in the presence of a microwave field. In the following I will call this a photoconductance measurement. Photovoltaic and photoconductive effects require some non-linearity in the sample because they measure the change of a DC quantity (voltage, conductance) under high frequency irradiation. In the case of the photovoltaic effect a directed current appears in presence of a zero mean force, such a behavior has attracted strong interest recently in connection with transport in bio-systems where this phenomenon became known as ratchet [4, 5, 6]. Thus understar ead to interesting insi

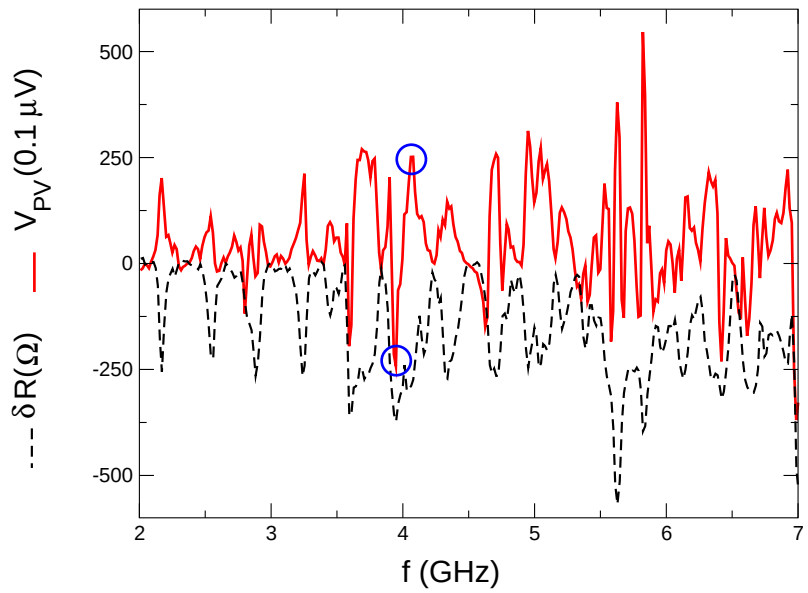

FIG. 2.4 – Dependence of photovoltaic voltage and of photo-resistance on the microwave frequency for the Ahoronov-Bohm ring from Fig. 2.1. As it is highlighted by the blue circles, V_{PV} can change sign as a function of frequency while δR is always negative.

A possible measurement of photovoltaic and photoconductive effects on an Aharonov-Bohm ring is sketched in Fig. 2.3. For a photovoltaic effect measurement the sample is connected directly on a low noise voltage amplifier. Since DC-voltage measurements at low temperatures suffer from uncontrolled thermoelectric offsets, we need to measure photovoltaic effect at a low frequency. This is achieved by modulating the amplitude of the microwave field at a low frequency $f_0 \simeq 700$ Hz, a lockin detector then measures the component of the voltage V_{pv} across the ring at frequency f_0. Frequency f_0 is chosen small enough so that all the signal is in phase with the amplitude modulation (see Fig. 2.3.a). In photoconduction measurements, the sample is usually polarized with a small AC-current i and voltage across the ring is detected at the current frequency (Fig. 2.3.b). The conductance is determined by the ratio $G = i/V$, in the linear response regime where i is small

enough for this ratio to be independent of current amplitude. The photoconductivity is then the difference $\delta G = G_{RF} - G$ between the value of conductance G_{RF} in presence of microwaves and its equilibrium value G. In this case the amplitude of the microwave signal is not modulated (yet both current and microwave amplitude modulation may be used in a more sophisticated detection scheme). Sometimes it is more convenient to deal with the photo-resistance $\delta R = R_{PV} - R \simeq -\frac{\delta G}{G^2}$ where R_{PV} and R are sample resistances with and without microwaves.

Both photovoltaic and photoconductive effects are non linear signals since the exciting field and the measured signals vary at very different frequencies. Therefore compared to the high-frequency conductance $G(\omega)$ their theoretical interpretation is more challenging. A comparison between V_{PV} and photo-resistance δR measured on the Aharonov-Bohm ring from Fig. 2.1 is shown on Fig. 2.4. Both quantities show characteristic peaks as a function of microwave frequency. The origin of these resonances are mainly reflections along the transmission line which leads from the generator towards an antenna inside the dilution fridge. This antenna is a short wire connected at the end of the transmission cable and placed $\simeq$ 1 cm away from the sample. It ensures a capacitive coupling between the Aharonov-Bohm ring and the microwaves. Peaks correspond to wavelengths where a maximal ac-potential is applied to the antenna, zero signal is measured for wavelengths where this potential is zero.

An important feature of the results displayed on Fig. 2.4 is that the quantity δR is negative for all frequencies. This property can be understood as heating of the sample by the microwave irradiation. Indeed at sufficiently low temperature ($T \simeq 50$ mK in the experiment) the electrons in 2DEG start to localize. Therefore a small increase in electron temperature leads to a drop in sample resistance and $\delta R < 0$. On the contrary the sign of the photovoltaic voltage V_{PV} can change as a function of microwave frequency. This suggests that photovoltaic voltage is a mesoscopic effect.

2.3 Magnetic field symmetry of non-linear transport

Electron transport occurs in devices which are driven out of thermal equilibrium by an external potential V. Hence the current voltage characteristic $i(V)$ of the device can be found only when the out of equilibrium distribution function (or density matrix in a quantum description) has been determined. This can be achieved by solving the Kinetic equation Eq. (2.1), which usually has to be supplemented by a Poisson equation relating the potential distribution with the charge density distribution. In practise, the above approach has to be implemented numerically and sophisticated codes of this type have been created to describe semiconductor field effect transistors and diodes.

However at low enough bias V the external potential is a minor perturbation of the equilibrium state of the system. The voltage range where this condition is observed, is called the linear response regime. In this regime a simple linear current-voltage relation holds $i(V) = GV$. The conductance G does not dependent on the external voltage and can be found from an average over the equilibrium state of the system. This idea was

first proposed by A. Einstein in his fluctuation dissipation theorem that relates mobility and diffusion coefficients. The diffusion coefficient is invariant under the change of sign of the magnetic field, which is a consequence of time reversal symmetry of the underlying microscopic dynamics. Indeed the diffusion coefficient does not depend on whether we travel forward or backward in time along a trajectory. As a result two terminal resistance is symmetric with respect to the magnetic field (see also experimental data from Fig. 2.1) :

$$G(H) = G(-H) \tag{2.8}$$

The argument described above relies on Einstein's relation, which is valid only in the simplest transport models. For example there is no direct relation between mobility and diffusion coefficient if interaction among carrier is taken into account. However it is also more general since the two main ingredients : a form of the fluctuation dissipation theorem and magnetic field symmetry of the underlying equilibrium quantity hold for very different transport models and regimes. Finally one may notice that Eq. (2.8) is a specific case of the Onsager relation, which will be discussed in more detail later on in this thesis.

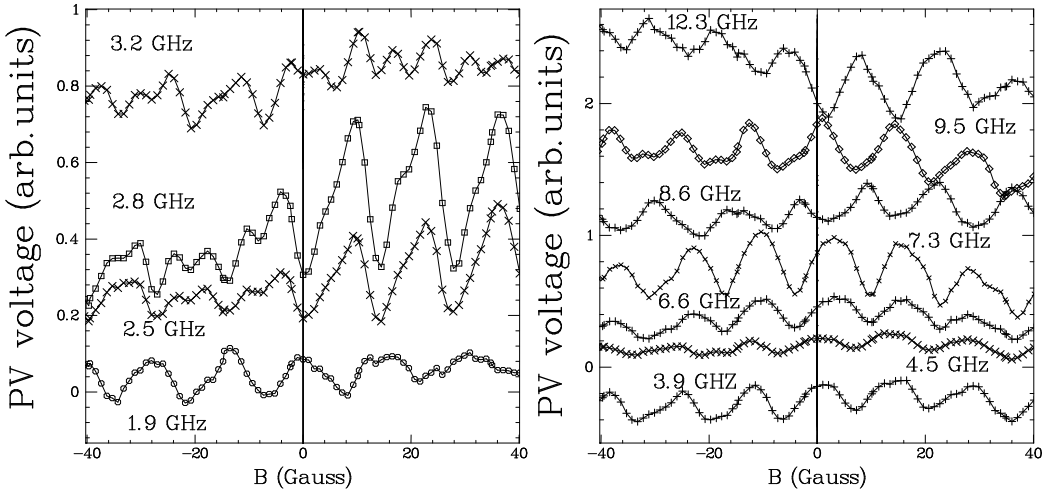

FIG. 2.5 – Low field dependence of the photovoltaic voltage at several RF frequencies. Left : $\omega \leq 1/\tau_D$ the phase of the AB oscillations remains pinned to 0 or π at $B = 0$. Right $\omega \geq 1/\tau_D$ the phase of the AB oscillations take any value between 0 and π. The vertical line in the plots corresponds to zero magnetic field. The curves have been shifted vertically for clarity. Even for low excitation frequencies $\omega \leq 1/\tau_D$, a magnetic field asymmetry appears when the magnetic field becomes larger than 10 Gauss. This effect is probably due to electron-electron interactions.

As we stressed in the previous paragraph Eq. (2.8) holds only in the linear response regime, but it is interesting to understand physically why non linear transport may start to deviate from this rule. For this reason we have studied the magnetic field symmetry properties of the rectified voltage V_{pv} in an Aharonov-Bohm ring. In the previous section we showed the behavior of V_{pv} as a function of microwave frequency at zero magnetic field.

We now choose several frequencies corresponding to peaks of the photovoltaic effect and measure their dependence on magnetic field. The experimental results are summarized on Fig. 2.5. The photovoltaic (PV) voltage varies both in sign and amplitude with magnetic field around a zero average value. This clearly indicated the mesoscopic origin of this PV Voltage. The magnetic field dependence of the PV voltage is reproducible for a given frequency but strongly differs from one frequency to the other. One may see that V_{pv} presents Aharonov-Bohm oscillations similar to those observed on the magnetoresistance (aperiodic fluctuations also appear because of the flux entering inside the 2DEG channels of the ring). These results show that mesoscopic systems behave as diodes which polarity depends on quantum interferences and can be thus inverted by applying a magnetic field or changing the RF frequency. The typical amplitude of the photovoltaic signal is 100 times larger than on metallic rings [44]. This difference can be easily related to the value of the resistance of GaAs samples, of the order of 6 kΩ, to be compared to several tens of Ω for metallic samples. The maximum amplitude measured at the resonances of our experimental setup is of the order of 0.3 Re/τ_D and only slightly varies with frequency for a given injected power on the resonances of our experimental set-up.

We now turn to the analysis of the magnetic field symmetry of the PV-voltage. For low frequencies $f < 3$ GHz the dependence on magnetic field is mainly symmetric $V_{pv}(H) = V_{pv}(-H)$, while at higher frequencies a completely asymmetric dependence is observed. In the low frequency regime the Aharonov Bohm oscillations of the PV voltage exhibit either a maximum or a minimum at zero field up to $f = f_c/2$, i.e. their phase is either equal to 0 or π. On the other hand this phase takes random values at higher frequencies. We attribute these effects to the time reversal symmetry breaking induced by the high frequency electric field experienced by an electron diffusing around the ring. However this can occur only at high enough frequencies, otherwise the microwave effect is similar to local electrostatic gating and does not break microscopic time reversal symmetry.

The typical time scale for electron transport across the ring in the diffusive transport regime is the diffusion time across the sample $\tau_D = L^2/D$. Here L is the distance between contacts (half a perimeter) and D is the diffusion rate. In Table 2.1 we summarize the main characteristics of the sample and give the value of the diffusion time. We find that the transition to a magnetic field asymmetric PV voltage indeed occurs for frequencies higher than $f_c = 1/(2\pi\tau_D) = 3.5$ GHz. The energy $E_c = hf_c = \hbar/\tau_D$ that is obtained from the diffusion rate is called the Thouless energy. It plays a central role in mesoscopic physics and sets the typical energy scale for quantum transport phenomena. In our experiment this energy $E_c \simeq 170$ mK is very small compared to the Fermi energy $E_F \simeq 150$ K that determines classical conductance (for example through the Drude formula). This regime where the energy scales are clearly separated $E_c \ll E_F$ corresponds physically to a semi-classical regime with weak disorder (no strong localization). From a theoretical point of view this allows to treat the disorder potential using perturbation theory. Diagrammatic techniques allow to sum the contributions of the disorder potential to all orders, which leads to highly accurate theoretical predictions on weak localization and universal conduction fluctuations in mesoscopic samples.

In the next section we present a semiclassical analysis which explains the dependence

Mean perimeter of the ring $2L$	6 μm
Width W=	0.2μm
l_e	2μm
$D = v_F l_e/2$	$0.2 m^2 s^{-1}$
$\tau_D = L^2/D$	0.45 10^{-10}s
$f_c = 1/(2\pi\tau_D)$	3.5GHz
$E_c = \hbar D/L^2$	170mK
Phase coherence time τ_ϕ	10^{-10}s

TAB. 2.1 – Characteristics of the ring. W, l_e are deduced from weak localization measurements on wires etched in the same heterojunction with the same width. Note that the investigated frequency range between 2 and 20 GHz corresponds to to a range of temperature between 0.1K and 1K.

of magnetic field symmetric and anti-symmetric components of the PV-voltage as a function of microwave frequency. This analysis allows to understand why the Thouless energy determines the frequency scale for the transition from the symmetric to asymmetric regime.

2.4 Semi-classical model for the origin of magnetic field asymmetry

In this section, we derive approximate expressions for the photovoltage across a 1D mesoscopic conductor starting from the semi-classical expression of conductance. I will note I_{pv+} and I_{pv-} the magnetic field symmetric and antisymmetric components of the photovoltage respectively.

In the semi-classical approximation ($k_f l_e >> 1$) it is possible to express the conductance at zero temperature in terms of interferences using Eq. 2.3. To describe the effect of the magnetic field, it is useful to write this expression in a form that directly leads to Onsager relations $G(B) = G(-B)$ in the absence of microwave driving.

$$G = \sum_{i,j} A_i A_j (\cos(\phi_j - \phi_i) + \cos(\phi_{-j} - \phi_{-i})) \tag{2.9}$$

In this expression the sum is taken on all possible classical trajectories leading from contact A to contact B. The trajectory $-i$ is obtained by moving along the trajectory i in the opposite direction, and the phases ϕ_i and ϕ_{-i} are defined as the integral of the system's

Lagrangian $\mathcal{L}(\mathbf{v},\mathbf{r},\tau)$:

$$\phi_i = \frac{1}{\hbar}\int_i \mathcal{L}(\mathbf{v}(\tau),\mathbf{r}(\tau),\tau)d\tau \tag{2.10}$$

$$= \frac{1}{\hbar}\int_i \left(\frac{m\mathbf{v}^2(\tau)}{2} - e\mathbf{A}(\mathbf{r}(\tau),\tau)\mathbf{v}(t) + eV(\mathbf{r}(\tau),\tau)\right)d\tau \tag{2.11}$$

$$\phi_{-i} = \frac{1}{\hbar}\int_i \mathcal{L}(-\mathbf{v}(\tau_i-\tau),\mathbf{r}(\tau_i-\tau),\tau)d\tau \tag{2.12}$$

Here $V(\mathbf{r},\tau),\mathbf{A}(\mathbf{r},\tau)$ are the scalar and vector potentials and τ_i is the time needed to reach contact A starting from contact B along the trajectory i. In the case where the external fields are stationary, the particle energy is conserved and only trajectories at the Fermi energy contribute to the conductance. If we assume now that the potential in the leads is stationary and that only the mesoscopic ring is exposed to microwave field, the particle energy is conserved inside the leads, but the initial energy in contact A can differ from the final energy in contact B. In the following, we will assume for simplicity that as in the stationary case the initial and final energy are both equal to the Fermi Energy E_F. This approximation is questionable at very high frequency $\omega\tau_D \gg 1$

In the presence of a static magnetic field $\mathbf{B} = \mathbf{rot}\mathbf{A} = \mathbf{rot}\frac{\mathbf{B}\times\mathbf{r}}{2}$, the phases are given by :

$$\phi_i = \phi_i^0 + \alpha_i B, \quad \phi_{-i} = \phi_i^0 - \alpha_i B \tag{2.13}$$

where $\phi_i^0 = \frac{1}{\hbar}\int_i \frac{m\mathbf{v}^2(\tau)^2}{2}d\tau$. $\alpha_i = \frac{e}{2\hbar}\int_i \mathbf{v}(\tau)\times\mathbf{r}(\tau)d\tau$. By inserting these expression in Eq. 2.9, one can show that

$$G(V) = 2\sum_{i,j} A_i A_j \cos(\phi_{ij}^0)\cos(\alpha_{ij}B) \tag{2.14}$$

with $\phi_{ij}^0 = \phi_i^0 - \phi_j^0$ and $\alpha_{ij} = \alpha_i - \alpha_j = 2\pi S_{ij}/\phi_0$.

Under the influence of a radiofrequency field, the values of the phases are changed by time dependent quantities $\delta\phi_i$, $\delta\phi_{-i}$ which are proportional to the amplitude of the RF field

$$\phi_i = \phi_i^0 + \alpha_i B + \delta\phi_i \tag{2.15}$$

$$\phi_{-i} = \phi_i^0 - \alpha_i B + \delta\phi_{-i} \tag{2.16}$$

At finite frequency the increments $\delta\phi_i$ and $\delta\phi_{-i}$ are different, leading to the appearance of a nonlinear component in the conductance that is odd upon the inversion of magnetic field. The time dependent conductance $G(t)$ can then be decomposed in a symmetric $G_+(t)$ and antisymmetric $G_-(t)$ part as a function of magnetic field :

$$\begin{aligned} G(t) &= G_+(t) + G_-(t) \\ &= \sum_{i,j} A_i A_j \left(\cos(\phi_{ij}^0 + \delta\phi_{ij}) + \cos(\phi_{ij}^0 + \delta\phi_{-ij})\right)\cos(\alpha_{ij}B) \\ &- \left(\sin(\phi_{ij}^0 + \delta\phi_{ij}) - \sin(\phi_{ij}^0 + \delta\phi_{-ij})\right)\sin(\alpha_{ij}B) \end{aligned}$$

After averaging the time dependent current $I(t) = G(t)V\cos(\omega t)$ over an oscillation period, we find the symmetric I_{pv+} and antisymmetric I_{pv-} components of the photovoltaic current $I_{pv} =< I(t) >_t$. These quantities are respectively equal to $I_{pv+} =< G_+(t)V\cos(\omega t) >$ and to $I_{pv-} =< G_-(t)V\cos(\omega t) >$. First we will estimate the amplitude of the photovoltaic current I_{pv+} even in magnetic field. In the limit of small phase shifts $\delta\phi_i$, $\delta\phi_{-i}$ we have

$$I_{pv+} =< G_+V\cos(\omega t) >_t = -2V < \sum_{i,j} A_iA_j \sin(\delta\phi^0_{ij})(\delta\phi_i + \delta\phi_{-i})\cos(\alpha_{ij}B)\cos(\omega t) >_t$$

On has to estimate terms of the form :

$$< \delta\phi_i \cos(\omega t) >_t =< \frac{e}{\hbar}\cos(\omega t)\int_t^{t+\tau_i} E_x\cos(\omega\tau)x_i(\tau)d\tau >_t \tag{2.17}$$

$$= -\frac{e}{2\hbar}\int_0^{\tau_i} E_x\cos(\omega\tau)x_i(\tau)d\tau \tag{2.18}$$

$$\sim \frac{eV}{\hbar}\frac{\sin(\omega\tau_i)}{\omega} \tag{2.19}$$

Where $x_i(\tau)$ is the x coordinate of the i-th trajectory, τ_i the time needed to go from point A to point B and $V = E_x|AB|$ is the AC-voltage. A similar estimate holds for $\delta\phi_{-i}$ leading to

$$I_{pv+} \sim \frac{eV^2}{\hbar}\sum_{i,j} A_iA_j\sin(\phi_j - \phi_i)\cos(\alpha_{ij}B)\frac{\sin(\omega\tau_i)}{\omega} \tag{2.20}$$

In the high frequency region $\omega\tau_D \gg 1$, $\sin(\omega\tau_i)$ is essentially a random phase, and leads (similarly to $\cos(\alpha_{ij}B)$) to conductance fluctuations of the order $\frac{e^2}{\hbar\sqrt{\omega\tau_D}}$ at high frequency. This property will be derived in the next section using a more sophisticated theoretical approach.

Hence

$$I_{pv+} \sim \frac{e^3V^2}{\hbar^2\omega\sqrt{\omega\tau_D}} \quad (\omega\tau_D \gg 1) \tag{2.21}$$

In the low frequency regime the quantity $\sin(\omega\tau_i)/\omega \sim \tau_i$ has fluctuations of the order τ_D around its average value, and the conductance fluctuations are of the order $\frac{e^2}{\hbar}$ therefore

$$I_{pv+} \sim \frac{e^3V^2\tau_D}{\hbar^2} \quad (\omega\tau_D \ll 1) \tag{2.22}$$

The term antisymmetric in B is zero in the absence of rf-field :

$$G_- = \sum_{i,j} A_iA_j\cos(\phi_{j,i,0})\sin(\alpha_{j,i}B)(\delta\phi_{j,i} - \delta\phi_{-j,-i}) \tag{2.23}$$

$$= 2\sum_{i,j} A_iA_j\cos(\phi_{j,i,0})\sin(\alpha_{j,i}B)(\delta\phi_j - \delta\phi_{-j}) \tag{2.24}$$

In the presence of an RF-field the component of the photovoltaic current antisymmetric in field is calculated from :

$$I_{pv-} =< G_- V\cos(\omega t) >_t =< 2V\sum_{i,j} A_i A_j \cos(\phi_{j,i,0})\sin(\alpha_{j,i}B)(\delta\phi_i(t) - \delta\phi_{-i}(t))\cos(\omega t) >_t$$

$$\delta\phi_i(t) - \delta\phi_{-i}(t) = \frac{-eE_x}{\hbar}\int_0^{\tau_i} d\tau x(\tau) \times (\cos(\omega\tau + \omega t) - \cos(\omega(\tau_i - \tau) + \omega t))$$

This leads to a term in $\sin(\omega t)$ and a term in $\cos(\omega t)$. When calculating $I_{pv-} =< \delta G_-(V(t))V\cos(\omega t) >_t$ we keep only the term in $\cos(\omega t)$. This means that we have neglected the imaginary component of the linear conductance induced at finite frequency by quantum interferences [2].

$$< (\delta\phi_i - \delta\phi_{-i})\cos(\omega t) >_t \tag{2.25}$$
$$= \frac{eE_x}{\hbar}\sin(\omega\tau_i/2)\int_0^{\tau_i} d\tau x(\tau)\sin(\omega(\tau - \tau_i/2)) \tag{2.26}$$
$$\sim \sin(\omega\tau_i/2)\sqrt{(\delta\phi)^2} \tag{2.27}$$

Bellow follow the calculation of the mean square phase difference $< (\delta\phi)^2 >$ inspired by reference [8].

$$< (\delta\phi)^2 > \tag{2.28}$$
$$= \frac{(eE_x)^2}{\hbar^2}\int_0^{\tau_i}\int_0^{\tau_i} d\tau_1 d\tau_2 \times \sin(\omega(\tau_1 - \tau_i/2))\sin(\omega(\tau_2 - \tau_i/2)) < x(\tau_1)x(\tau_2) > \tag{2.29}$$
$$= \frac{(eE_x)^2}{\hbar^2}\int_0^{\tau_i}\int_0^{\tau_i} d\tau_1 d\tau_2 \times \sin(\omega(\tau_1 - \tau_i/2))\sin(\omega(\tau_2 - \tau_i/2)) Dmin(\tau_1, \tau_2) \tag{2.30}$$
$$= \frac{(eE_x)^2 D}{\hbar^2}\frac{2\omega\tau_i(2 + \cos(2\omega\tau_i)) - 3\sin(2\omega\tau_i)}{2\omega^3} \tag{2.31}$$

In the low frequency limit $\omega t \to 0$ we recover the result of reference [8]. In the high frequency regime, $\omega t \gg 1$, $< \delta\phi^2 >$ decays $\propto 1/\omega^2$:

Omitting numerical factors, we can estimate the induced dephasing by a microwave field :

$$< (\delta\phi)^2 > \sim \frac{(eE_x\omega)^2 D\tau_D^5}{\hbar^2},\ \omega\tau_D \ll 1 \tag{2.32}$$
$$< (\delta\phi)^2 > \sim \frac{(eE_x)^2 D\tau_D}{\omega^2\hbar^2}, \omega\tau_D \gg 1 \tag{2.33}$$

where τ_D is the mean diffusion time in the ring. We then have :

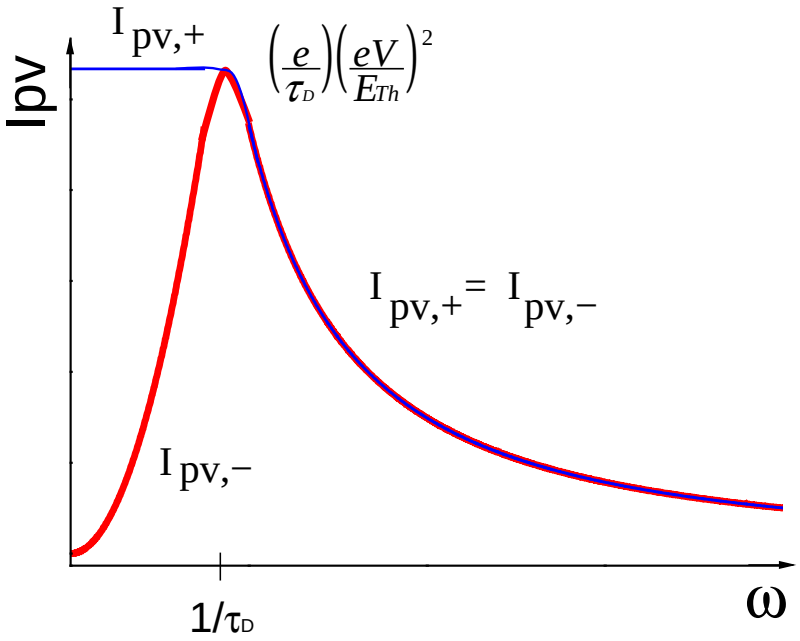

FIG. 2.6 – Qualitative dependence on frequency of the magnetic field symmetric : I_{pv+} and antisymmetric : I_{pv-} components of the PV current.

In the low frequency regime :

$$I_{pv-} \sim V\frac{e^2}{\hbar}\omega\tau_D\sqrt{\frac{(eV\omega)^2\tau_D^4}{\hbar^2}} \sim \frac{e^3V^2}{\hbar^2}\omega^2\tau_D^3 \tag{2.34}$$

In the high frequency regime :

$$I_{pv-} \sim V\frac{e^2}{\hbar\sqrt{\omega\tau_D}}\sqrt{\frac{(eV)^2}{\omega^2\hbar^2}} \sim \frac{e^3V^2}{\hbar^2\omega\sqrt{\omega\tau_D}} \tag{2.35}$$

The expected qualitative behavior is summarized on Fig. 2.6. According to our calculations the photovoltaic current tends to an even function of magnetic field in the zero frequency limit. This however is not true and it was shown both theoretically [9, 10, 11] and experimentally [12] that a finite asymmetry survives even in the zero frequency limit due to the presence of electron-electron interactions. Of course this effect is not captured in our semiclassical model that does not take electron-electron interactions into account. An extension of the semiclassical approach that includes electron-electron interactions is described in [12].

2.5 Universal conductance fluctuations at finite frequency

In the previous section I used the dependence of the amplitude of the universal conductance fluctuations as a function of frequency to obtain the typical value of the sum over classical classical paths $\sum_i A_i e^{i\phi_i}$ where A_i are classical probability amplitudes and ϕ_i are quantum phases. This allowed to derive the scaling relations that led to the qualitative picture Fig. 2.6 where even and odd components of the typical photovoltaic current are shown as a function of microwave frequency.

In this section I develop in more detail the calculation of the amplitude of the Universal conductance fluctuation at finite frequency ω using the Green function formalism and deriving the scaling relation :

$$< (\delta \mathrm{Re} G(\omega))^2 > \propto \frac{e^4}{\hbar^2}\frac{E_c}{\hbar\omega} \tag{2.36}$$

The calculation described in this chapter is a finite frequency extension of the zero frequency universal conductance fluctuation (UCF) theory. An excellent introduction to UCF theory can be found in [13], hence I mainly focus on the steps of the calculation where the frequency enters explicitly and highlight the differences with the static case that is treated in detail in [13]. The starting point of the calculation is the Kubo formula for conductivity $\sigma(\omega)$ as a function of the Green functions of a diffusive wire.

$$\sigma(\omega) = s\frac{\hbar}{2\pi\Omega}\int d\epsilon \frac{f(\epsilon) - f(\epsilon - \hbar\omega)}{\hbar\omega}\mathrm{Tr}[\mathrm{j_x G^R_\epsilon j_x G^A_{\epsilon-\hbar\omega}}] \tag{2.37}$$

Here $G^{R,A}$ are the retarded/advanced Green functions, that are defined through the relation

$$\hat{G}^{R,A}(\epsilon) = \frac{1}{\epsilon - \hat{H} \pm i0} \tag{2.38}$$

where $\hat{H}$ is the Hamiltonian of a one dimensional wire with a disorder potential $V(x)$

$$\hat{H} = -\frac{\hbar^2}{2m}\frac{\partial^2}{\partial x^2} + V(x) \tag{2.39}$$

while the current operator operator in Eq. (2.37) reads $\hat{j}_x = (ie\hbar/m)\partial/\partial x$. Note that the system volume Ω is present in the denominator and s is the spin degeneracy.

One can check easily that the conductance obtained from the Kubo formula obeys the relation

$$\sigma(\omega)^* = \sigma(-\omega) \tag{2.40}$$

Indeed

$$\sigma(\omega)^* = s\frac{\hbar}{2\pi\Omega}\int d\epsilon \frac{f(\epsilon)-f(\epsilon-\hbar\omega)}{\hbar\omega}(\mathrm{Tr}[\mathrm{j_x G^R_\epsilon j_x G^A_{\epsilon-\hbar\omega}}])^* \tag{2.41}$$

$$= s\frac{\hbar}{2\pi\Omega}\int d\epsilon \frac{f(\epsilon)-f(\epsilon-\hbar\omega)}{\hbar\omega}\mathrm{Tr}[\mathrm{G^R_{\epsilon-\hbar\omega} j_x G^A_\epsilon j_x}] \tag{2.42}$$

$$= s\frac{\hbar}{2\pi\Omega}\int d\epsilon \frac{f(\epsilon)-f(\epsilon-\hbar\omega)}{\hbar\omega}\mathrm{Tr}[\mathrm{j_x G^R_{\epsilon-\hbar\omega} j_x G^A_\epsilon}] \tag{2.43}$$

$$= s\frac{\hbar}{2\pi\Omega}\int d\epsilon \frac{f(\epsilon')-f(\epsilon'+\hbar\omega)}{-\hbar\omega}\mathrm{Tr}[\mathrm{j_x G^R_{\epsilon'} j_x G^A_{\epsilon'-\hbar\omega}}] \tag{2.44}$$

$$= \sigma(-\omega) \tag{2.45}$$

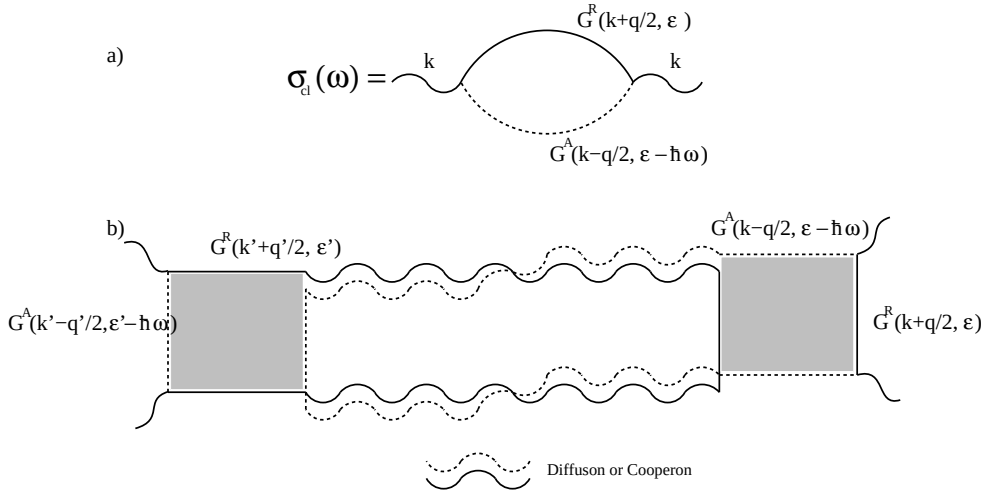

FIG. 2.7 – a) Diagrammatic representation of the Drude conductance, straight lines are retarded disordered averaged Green functions while dotted lines are advanced Green functions (see Eq. 2.47). b) Diagrammatic representation of a contribution to the correlator $< \delta\sigma(\omega,\epsilon)\delta\sigma(\omega',\epsilon') >_T$, neighboring dotted and continuous line represent a Diffuson or a Cooperon term and squares represent Hikami boxes.

The Green function in the Kubo formula depends on a random potential and can not be obtained analytically. However it is possible to derive the statistical properties of the conductance by calculating disorder averaged quantities directly. For example in order to find the disorder averaged Green function $< G^R >$, one can average the series expansion of the Green function as a function of the disorder potential.

$$< G^{R,A} > = < G_0^{R,A} + G_0^{R,A} V G_0^{R,A} + G_0^{R,A} V G_0^{R,A} V G_0^{R,A} + ... > \tag{2.46}$$

In this expansion G_0^R is the Green function defined by Eqs. (2.38,2.39) in the absence of disorder potential $V = 0$. The average of each term over disorder can be done explicitly

in the case of a Gaussian-delta correlated disorder, then the dominant terms in E_c/E_F are resumed leading :

$$G^{R,A}(\mathbf{k},\epsilon) = \frac{1}{\epsilon - \epsilon_{\mathbf{k}} \pm i\frac{\hbar}{2\tau_e}} \tag{2.47}$$

In this expression $\epsilon_{\mathbf{k}} = \frac{\hbar^2 k^2}{2m}$ is the carrier dispersion relation and τ_e is the mean free path.

With the disorder averaged Green functions it is possible to calculate the classical contribution to conductance. This is achieved by neglecting the correlation terms in the Kubo Formula Eq. (2.37) :

$$< j_x G^R_\epsilon j_x G^A_{\epsilon-\hbar\omega} > \simeq j_x < G^R_\epsilon > j_x < G^A_{\epsilon-\hbar\omega} > \tag{2.48}$$

The resulting approximation can be conveniently represented in a diagram shown on Fig. (2.7.a) , since the disorder averaged Green functions are diagonal in the plane wave basis (translational invariance is recovered after disorder average) the trace in the Kubo formula can be readily calculated, and one recovers the Drude formula Eq. (2.2). However by keeping cross correlation terms in the product $j_x G^R_\epsilon j_x G^A_{\epsilon-\hbar\omega}$, the Green function method can keep track the contributions resulting from quantum interferences that lead to weak localization and universal conductance fluctuations while this is not possible in the Kinetic theory.

I will now proceed to the calculation of the correlators

$$< \delta\sigma(\omega,\epsilon_F)\delta\sigma(\omega',\epsilon'_F) >_T \tag{2.49}$$

where the average is taken over all disorder realization and the thermal distributions at temperature T, ω and ω' are the frequencies while ϵ_F and ϵ'_F represent the position of the Fermi-level.

One of the possible contributions to this correlator is shown as a diagram on Fig. (2.7.b), note that these calculations are very similar to UCF calculations at zero frequency and for this reason I will not explain in detail the calculations corresponding to diagrams such as Fig. (2.7.b).

The final expression for the conductance correlator can be cast in the following form

$$< \delta G(\omega,\epsilon_F)\delta G(\omega',\epsilon'_F) >_T = \int \frac{d\Omega}{T} G(\frac{\omega}{T},\frac{\omega'}{T},\frac{\Omega}{T}) F(\omega,\omega',\Omega+\epsilon'_F-\epsilon_F) \tag{2.50}$$

(in order to simplify notations we have set $\hbar = 1$, and measure frequency in energy units).

In this expression the function G arises from integration over the Fermi-distributions

$$\frac{1}{T}G(\frac{\omega}{T},\frac{\omega'}{T},\frac{\Omega}{T}) \tag{2.51}$$

$$= \int d\epsilon \frac{f(\epsilon)-f(\epsilon-\omega)}{\omega}\frac{f(\epsilon+\Omega)-f(\epsilon+\Omega-\omega')}{\omega'} = \tag{2.52}$$

$$= \frac{e^{\Omega/T}}{\omega\omega'}\left(\frac{\Omega - e^{\omega/T}(\Omega+\omega-e^{\Omega/T}\omega)}{(-1+e^{\Omega/T})(-1+e^{(\Omega+\omega)/T})} + \frac{\Omega-\omega'}{e^{\Omega/T}-e^{\omega'/T}} + \frac{e^{\omega/T}(\Omega+\omega-\omega')}{-e^{(\Omega+\omega)/T}+e^{\omega'}}\right) \tag{2.53}$$

and has the property

$$G(\omega,\omega',\Omega) = G(\omega',\omega,-\Omega) \tag{2.54}$$

which can easily be checked from the integral representation of G.

The function F stems from the Diffuson and Cooperon terms inside the diagrams similar to Fig. (2.7.b) :

$$F(\omega,\omega'\Omega) = 4\left(\frac{se^2D}{hL^2}\right)^2\left(2\sum_{\mathbf{q}}(P_d(\mathbf{q},-\Omega+\omega')P_d(\mathbf{q},\Omega+\omega)+\sum_{\mathbf{q}}\frac{P_d(\mathbf{q},-\Omega+\omega')^2+P_d(\mathbf{q},\Omega+\omega)^2}{2}\right) \tag{2.55}$$

I remind that in the Diffusion term only the average along identical diffusion paths is kept in the correlators $< G^AG^R >$ whereas the Cooperon term retains only the contribution of trajectories that are conjugated by time reversion symmetry. As a consequence, the Cooperon contribution tends to vanish in presence of a magnetic field because it breaks time reversal symmetry. The function $P_d(\mathbf{q},\omega)$ is the inverse of the diffusion operator in Fourier space, its expression is derived in [13] and reads :

$$P_d(\mathbf{q},\omega) = \frac{1}{-i\omega+Dq^2} \tag{2.56}$$

In the equations Eqs. (2.55,2.56) D is the diffusion constant, L is the wire length and $s=2$ is the spin-degeneracy.

In the case of a one dimensional wire the expression for F can be cast in a more explicit form :

$$\begin{aligned}&F(\omega,\omega',\Omega) = \\ &= 4s^2\left(\frac{e^2}{h}\right)^2\sum_{n>0}2\frac{1}{i\frac{\Omega-\omega'}{E_c}+\pi^2n^2}\frac{1}{-i\frac{\Omega+\omega}{E_c}+\pi^2n^2}+\frac{1}{2}\left(\frac{1}{i\frac{\Omega-\omega'}{E_c}+\pi^2n^2}\right)^2+\frac{1}{2}\left(\frac{1}{-i\frac{\Omega+\omega}{E_c}+\pi^2n^2}\right)^2\end{aligned} \tag{2.57}$$

By inserting Eqs. (2.53,2.57) inside the expression of the correlator from Eq. (2.53) it is possible to calculate numerically the behavior of the correlator as a function of various system parameters. Figure Fig. (2.8) shows the behavior of the correlation function at zero temperature and for $\epsilon_F = \epsilon'_F$, it represents the amplitude of real/imaginary conductance fluctuations as a function of frequency. At frequencies $\omega \ll E_c$, the conductance has mainly a real part hence UCF mainly appear on the real part of conductance with a typical value $< (\delta \mathrm{Re}G)^2 > \simeq \frac{2}{15}(se^2/h)^2$ which is known from zero frequency calculations. In this low frequency regime, the amplitude of the fluctuations on the imaginary conductance decays as a power law which is well approximated by the relation $< (\delta \mathrm{Im}G)^2 > \simeq 2\times 10^{-3}(se^2/h)^2(\omega/E_c)^2$. This decay actually follows the behavior of the mean value of the imaginary resistance than scales like ImG $\propto \tau_e\omega$ at low frequencies. However the cutoff

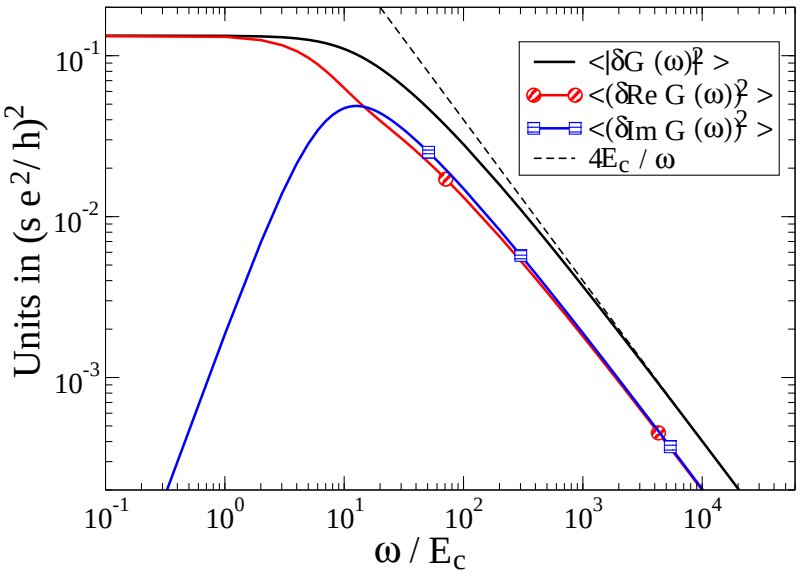

FIG. 2.8 – Amplitude of universal conductance fluctuations for real/imaginary part of conductance as a function of frequency at zero temperature.

	$\omega \ll 10E_c$	$\omega \gg E_c$
$< (\delta \, \mathrm{Re}G)^2 >$	$\frac{2}{15}\left(\frac{se^2}{h}\right)^2$	$\simeq 2\left(\frac{se^2}{h}\right)^2 \frac{E_c}{\omega}$
$< (\delta \, \mathrm{Im}G)^2 >$	$\simeq 2\times 10^{-3}\left(\frac{se^2}{h}\right)^2\left(\frac{\omega}{E_c}\right)^2$	$\simeq 2\left(\frac{se^2}{h}\right)^2 \frac{E_c}{\omega}$

TAB. 2.2 – Possible regimes for real/imaginary universal conductance fluctuation amplitude as function of frequency. The sign $\simeq$ indicates that the numerical constant was determined from a fit to the numerical data from Fig. 2.8 in the asymptotic regime.

frequency is the Thouless energy E_c for universal conductance fluctuations while it given by the elastic rate for the mean Drude conductance. At high frequencies $\omega \gg E_c$ the fluctuation amplitude of real and imaginary components of conductance are equal and their dependence on frequency is well described by the relation $< (\delta \mathrm{Im}G)^2 > = < (\delta \mathrm{Re}G)^2 > \simeq 2(se^2/h)^2(E_c/\omega)$. Hence our numerical data shows that the typical UCF amplitude decays as $\delta G \propto \sqrt{E_c/\omega}$ at high frequency, note that the same dependence is observed as a function of temperature $\delta G \propto \sqrt{E_c/T}$ when temperature is low enough for phase coherence to be preserved across the entire sample. In this respect frequency and temperature play a similar role in UCF amplitude damping. Finally note that the transition from the low to high frequency regime occurs at $\omega \simeq 10E_c$. The results of this section are summarized in Table 2.2.

2.6 Photo-magnetism in closed mesoscopic samples

In the previous sections we considered non linear transport in connected samples. It was shown that due to the asymmetry of the disorder potential inside a mesoscopic sample, an AC electromagnetic field can create a stationary current across the sample. In the case where the sample is not connected to an external electrical circuit two scenarios are possible. The current created by the microwave field can be compensated by a potential drop across the sample which causes the total current to cancel. However it is also possible that the photo-induced currents start to forms closed loops inside the sample. In this hypothesis a stationary orbital momentum develops in the sample even at zero applied magnetic fields. This effect is very different from equilibrium persistent currents, which are a purely quantum mechanical effect. Indeed it is well known that a magnetic field gives no magnetization in a classical system at thermal equilibrium (see e.g. [15]). However in presence of microwave driving the sample may reach an out of equilibrium state, where a stationary magnetization exists even in a classical regime.

The physical origin of this dynamical magnetization can be seen already from a simple model of two decoupled dissipative oscillators for which a monochromatic driving leads to a certain degree of synchronization with the driving phase [14]. This phenomenological approach was proposed by Magarill and Chaplik [16] who gave first estimates for photoinduced magnetism in ballistic nanostructures.

In this approach the electron dynamics inside a two-dimensional (2D) dot is described by a the classical Hamiltonian

$$H = \frac{p_x^2 + p_y^2}{2m} + U(x,y) - x f_x \cos\omega t - y f_y \cos\omega t \tag{2.58}$$

where m is electron mass and $p_{x,y}$ and x, y are conjugated momentum and coordinate. An external force $f_{x,y}$ is created by a linear-polarized microwave field with frequency ω. The polarization angle θ and the force amplitude f are defined by relations $f_x = f\cos\theta$, $f_y = f\sin\theta$. For simplicity we consider the case of an harmonic potential

$$U(x,y) = \frac{m(\omega_x^2 x^2 + \omega_y^2 y^2)}{2} \tag{2.59}$$

where $\omega_{x,y}$ are oscillation frequencies in x, y directions (generally non equal).

The component of a magnetic moment along a system symmetry plane vanishes In presence of irradiation, this holds when both the mesoscopic sample and the microwave field are invariant under the plane symmetry. For a two dimensional system the 2DEG surface is a natural symmetry plane and the momentum must be perpendicular to the 2DEG surface. When the microwave field is not oriented along x or y directions, this is the only existing symmetry plane and momentum is not forbidden by spacial symmetries.

However magnetic moment changes sign under time reversion $t \to -t$, and a time reversal symmetric microscopic dynamics can not lead to the onset a stationary magnetic moment. Time reversal symmetry can be broken by dissipative processes, that introduce

irreversibility in the microscopic dynamics For this reason we assume that electrons experience an additional friction force $\mathbf{F} = -\gamma \mathbf{p}$ where γ is a relaxation rate. The dynamical equations of motion in this case are linear and read :

$$\begin{cases} x'' + \gamma x' + \omega_x^2 x = \frac{f_x}{m} \cos(\omega t) \\ y'' + \gamma y' + \omega_y^2 y = \frac{f_y}{m} \cos(\omega t) \end{cases} \tag{2.60}$$

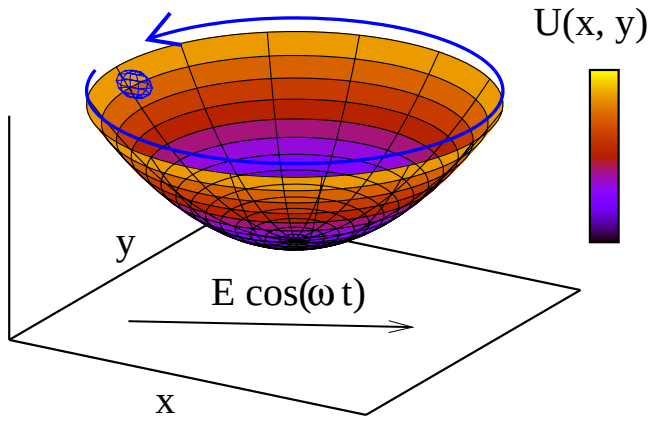

FIG. 2.9 – Electron motion in the potential $U(x, y) = m(\omega_x^2 x^2 + \omega_y^2 y^2)/2$ described by equations of motion : Eq. 2.60.

At times $t \gg 1/\gamma$, the solutions is found easily using the complex representation

$$\begin{cases} x(t) = \Re \frac{e^{i\omega t} f_x/m}{\omega_x^2 - \omega^2 + i\gamma\omega} = \Re\, X(t), \\ y(t) = \Re \frac{e^{i\omega t} f_y/m}{\omega_y^2 - \omega^2 + i\gamma\omega} = \Re\, Y(t), \end{cases} \tag{2.61}$$

where $\Re$ marks the real part. In general, it corresponds to an elliptic rotations of the electron inside the harmonic trap.A typical trajectory is shown on Fig. 2.9.

The kinetic momentum associated with these trajectories is obtained as :

$$\begin{aligned} & L = m \left\langle x(t) v_y(t) - y(t) v_x(t) \right\rangle \\ = \quad & \Re \frac{1}{m^2} \frac{-i\omega f_x f_y}{(\omega_x^2 - \omega^2 + i\gamma\omega)(\omega_y^2 - \omega^2 - i\gamma\omega)} \quad . \end{aligned} \tag{2.62}$$

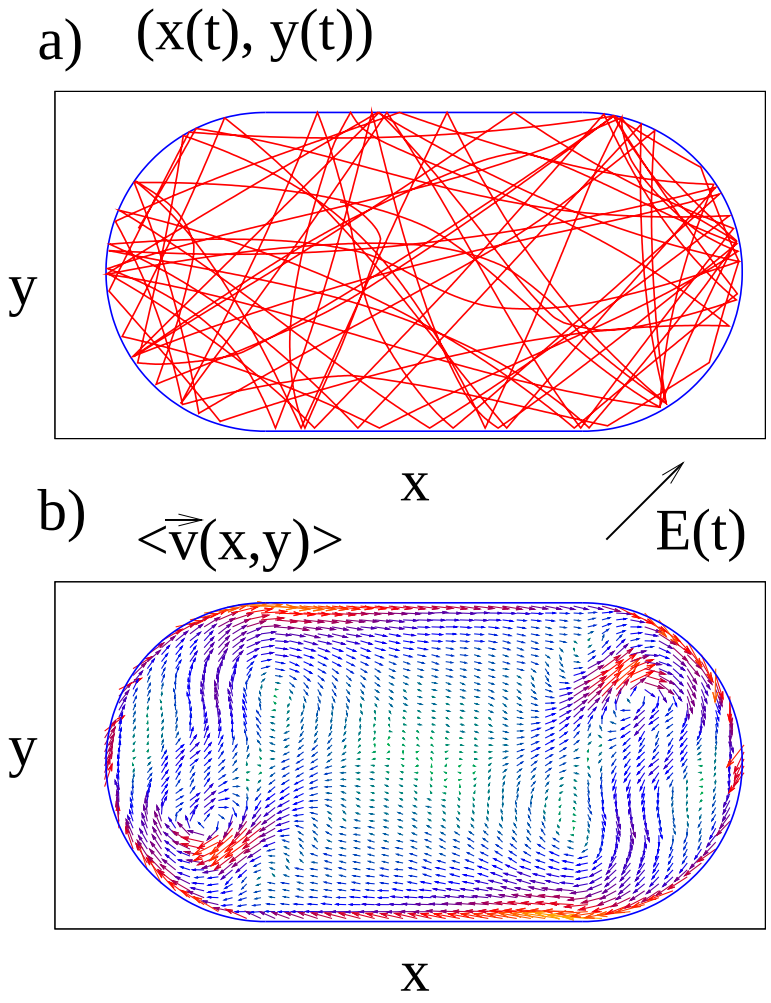

FIG. 2.10 – a) Chaotic trajectory inside a billiard with specular walls in presence of a microwave field and dissipation. b) Average flow inside the billiard under microwave irradiation. While the trajectory seems completely chaotic in the (x, y) plane, the average flow shows a rotating (turbulent) structure with a finite orbital moment.

From a physical viewpoint an average momentum appears due to a phase shift between oscillator phases induced by dissipation and an orbit takes an elliptic form with rotation in one direction. In some sense, due to dissipation the two oscillators become synchronized by external force [14]. As usual [15], an average orbital momentum L for one electron gives a total magnetic moment $M = NLe/2mc$ where N is a number of electrons in a quantum dot.

The photomagnetic effect that I presented above share some common features with the inverse Faraday effect where a medium is magnetized by a beam of circularly polarized radiation [17, 18, 19]. However the inverse Faraday effect vanishes for linear polarizations [17], while the geometrical asymmetry of the confining potential dot makes possible the

onset of a finite magnetization for linearly polarized microwave radiation even at zero magnetic fields (the analogy between inverse Faraday and photomagnetic effects was put forward in [20]) . In this respect the photomagnetic effect, is also distinct from non-linear quantum coherence effects in driven mesoscopic systems where a photo-induced magnetic moment was predicted only at non zero magnetic fields [21].

The rather phenomenological approach based on dissipative classical dynamics can be extended to the case of quantum electrons inside an harmonic confining potential where the electron distribution is governed by a Fermi-Dirac distribution [22]. In this case the effects of microwave field on the quantum dot can be considered in the frame of the Kubo formalism for the density matrix (see e.g. [13]). This analysis essentially confirms the above results.

At last the above example is completely integrable and one may wonder if these stationary orbital currents exist in the more generic case of a chaotic dot. In order to understand this case we have studied numerically the case of a Bunimovitch stadium under the driving of an external AC field (see Fig. 2.10). In this model we have assumed specular collisions on the wall, and the presence of a (Metropolis) thermostat equilibrating the electron distribution function to the Fermi-Dirac distribution (for more detail [22]). A typical trajectory inside the stadium is chaotic and fills ergodically the interior of the stadium (see for e.g. Fig. 2.10). Hence the onset of a magnetization in this model, can not be understood in term of simple elliptic trajectories. Yet Fig. 2.10.b reveals that there is a an average electron current circulating inside the stadium and hence a finite magnetization.

The amplitude of the circulating orbital current I can be estimated as :

$$I \sim \frac{me^3E^2L^3}{\hbar^3\sqrt{n}} \sim \frac{ev_F}{L}\left(\frac{eEL}{E_{th}}\right)^2 \ , \ E_{th} = \hbar v_F/L \tag{2.63}$$

In this expression m is the carrier mass, E is the AC-electric field and L is the typical size of the dot. Note that the orbital current can be cast in two equivalent forms, depending if it is expressed as a function of the 2DEG carrier density n or of the Fermi-velocity v_F. In the later case, the current can be interpreted as the equilibrium persistent current increased by the square of the ratio between the external AC potential drop eEL and effective Thouless energy $E_{th} = \hbar v_F/L$. This expression assumes that the mean free path is larger than the dot size and that transport in the dot is ballistic. We have also assumed that the induced orbital current does not depend on the energy relaxation rate (for e.g. γ in the harmonic oscillator model). Note that the latter assumption is not fully consistent with monte-carlo simulations of the dot dynamics.

Using the Biot-Savar law we can estimate the magnetic field H seen by a detector at distance $\sim L$ from the quantum dot.

$$H \sim \mu_0 \frac{I}{L} \sim \frac{\mu_0 me^3E^2L^2}{\hbar^3\sqrt{n}} \tag{2.64}$$

For typical parameters $n \simeq 10^{11}$ cm^{-2}, $L \simeq 10$ μm and $E \simeq$ Volt/cm we can estimate the induced magnetic field $H \simeq 75$ mGauss. A magnetic field of this amplitude can be detected

with a 2DEG Hall probe. The advantage of this setup is that both the quantum dot and Hall detector are can be fabricated in the same material which greatly simplifies on-chip integration.

2.7 Fabrication of the Hall Probes

In this chapter I describe the fabrication steps which allow to prepare a ballistic billiard coupled to a Hall detector in a two dimensional $GaAs/GaAlAs$ electron gas (2DEG). For our experiments on photo-magnetism we used a $GaAs/GaAlAs$ heterostructure with electron density $n_e \simeq 1.2 \times 10^{11}$ cm^{-2} and mobility $\mu \simeq 1.2 \times 10^2$ m^2/Vs grown at Laboratoire de Photonique et Nanostructures by A. Cavanna and B. Etienne.

A crucial step is to make Ohmics contacts to 2DEG. An Au/Ge film is evaporated onto the areas dedicated for contacts. The sample is then heated to a temperature of 440 °C in an argon atmosphere during a few minutes. This leads to diffusion of Au/Ge inside the substrate down to the GaAs/GaAlAs interface where the electrons are confined at low temperatures, for our samples the 2DEG was confined at about 200 nm below the wafer surface. The contact quality is strongly decreased if an oxide layer is present at the sample surface, in this case the contacts are not Ohmic at low temperature and can present a gap of a few eV. In these conditions the sample can not function as a Hall probe, hence the oxide layer must be carefully removed. We achieved this by cleaning the sample in a 20% HCl solution for a few minutes just before evaporation of Au/Ge.

A pattern defining the shape of the billiard and of the Hall probe is created using a computer aided design (CAD) software (see Fig. 2.11). Electron beam lithography allows to transpose this pattern on a polymer film composed typically of a bilayer of methyl methacrylate (MMA)/poly-methyl methacrylate (PMMA) which is about 300 nm thick. After development in methyl isobutyl ketone (MIBK) an aluminum film about 100 nm thick is evaporated to mask 2DEG from chemical etching. After lift-off the Al remains only on the areas we want to protect from chemical etching.

The 2DEG was etched in a mixture of H_3PO_4, H_2O_2 and water (see Table. 2.3 for exact composition). Wet chemical processing was favored over plasma etching since it is known that chemical etching tends to follow existing defects in the sample and creates a more specular edge potential for electrons at low temperature. The total etching time was around 5 minutes with an etch rate of approximately 30 nm/min. After this procedure the protecting Al mask was removed by cleaning the sample in an NaOH solution with pH $\simeq$ 12 for 6 minutes. An atomic force microscopy (AFM) image of a 2DEG sample after etching and removal of the Al mask is shown on Fig. 2.12. It shows a topography image of the billiard which is placed between the Hall probe and a lateral gate. The AFM measurements confirm that the 2DEG was etched at a depth of around 150 nm.

Once the pattern inside 2DEG is defined we evaporate a copper top-gate (thickness $\simeq$ 100 nm) over the Hall bar using another step of electron beam lithography. The top-gate was designed to shield the Hall bar from microwave irradiation, it also allows to modulate carrier density. A complete optical microscope image of the sample is shown on

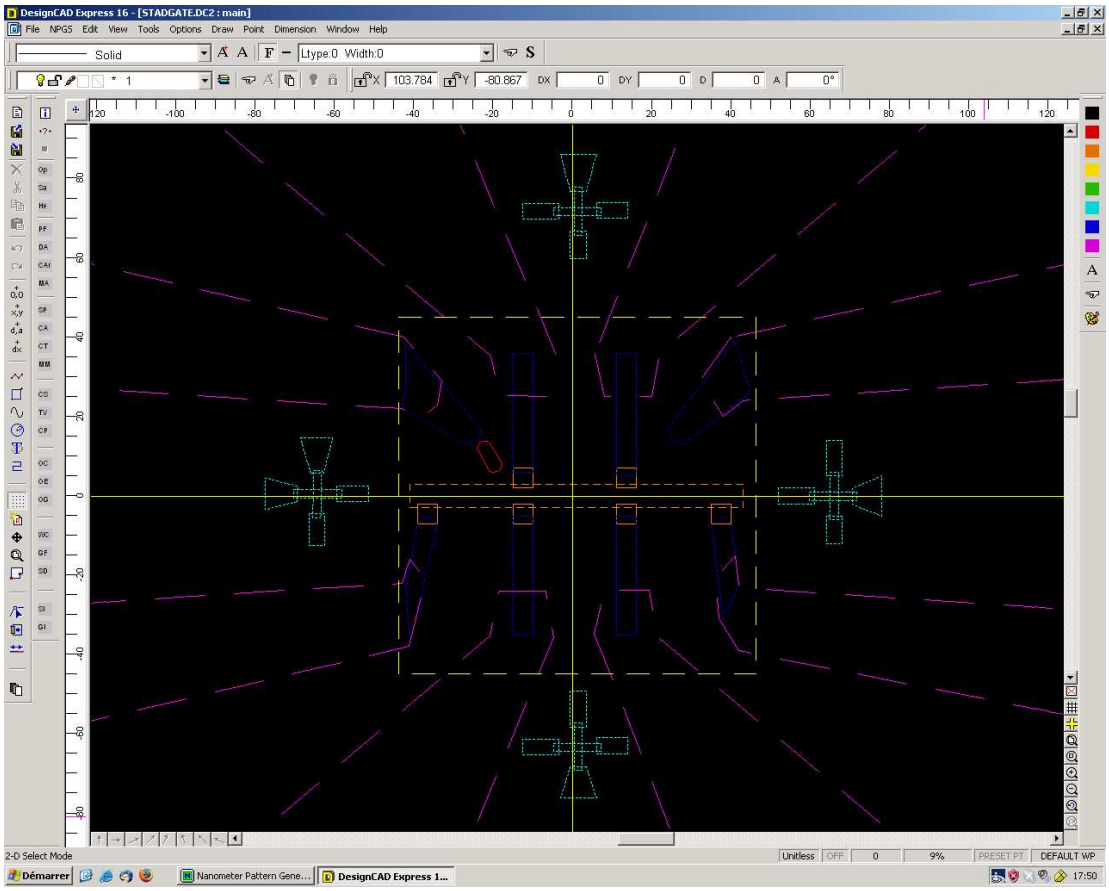

FIG. 2.11 – NPGS layout for the fabrication of the Hall bar and of the billiard.

Fig. 2.13. The leftmost image is a large scale view where contacts and alignment marks appear clearly. The Hall bar is located at the center of the sample, the layout of our Hall bars is shown on Fig. 2.13.b,c. The 2DEG edges are clearly visible and appear as black lines. The region where the 2DEG was covered by the Al mask is cleaner since it was not contaminated during the chemical etching procedure. The copper top-gate covers the active region of the Hall bar and gives an orange color. In a last batch of samples lateral copper split-gates were also deposited (see Fig. 2.13.c), they were used to create a more controlled microwave field around the billiard. The latter is highlighted with red circles. It is positioned in a way to interact only with the left Hall probe. The probe on the right serves as a control reference.

The sample is then mounted on a sample holder that provides macroscopic connectors that allow to connect the sample with the circuitry inside the dilution refrigerators. We have prepared a customized sample holder that allows to connect up to two SMA transmission cables on the sample, additionally it provides many other contacts suitable for low frequency signals. The link between the connection pads of the sample holder and the small

H_3PO_4	6 mL	84-87%
H_2O_2	2 mL	33%
H_2O	160 mL	

TAB. 2.3 – Solution used for etching of 2DEG.

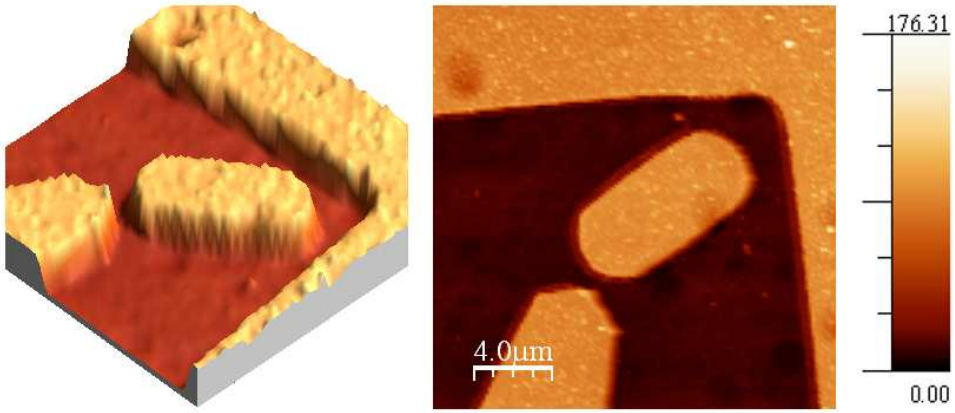

FIG. 2.12 – AFM image of the billiard after etching of 2DEG with the solution from Table 2.3.

contacts on the sample is obtained with ultrasound bonding procedure which solders thin AlSi wires onto both contacts. This allows to contact the six contacts of the Hall bar, the two 2DEG gates and the top gate. The 2DEG gates did not have a very good coupling to our device, but they allowed to check that 2DEG etch was successful and that the etched areas were insulating at low temperature.

2.8 Measurement of photo-induced orbital magnetism with a Hall probe

In this chapter we describe our experiments aimed at establishing the existence of photoinduced magnetization inside the billiard. When we want to measure an unknown magnetic field with a Hall probe some care must be taken because of the residual geometrical defects of the Hall probe which add a longitudinal resistivity component to the measured resistance. For this reason the relation between Hall resistance R_H and magnetic field reads

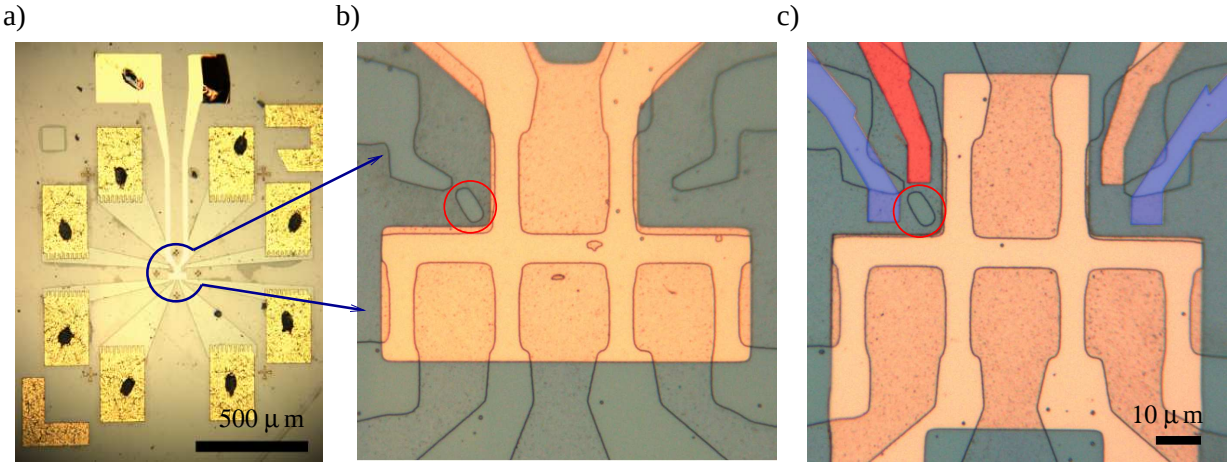

FIG. 2.13 – Optical microscope image of the Hall bar samples fabricated during this thesis. a) Large scale image sample showing Au/Ge contacts and 2DEG wires connecting the Hall bar at the center of the sample b) Detailed view of the Hall bar region. The position of the billiard is highlighted by a red circle. The copper top-gate with orange color screens the microwave field from the Hall bar and allows to tune carrier density. c) In another sample, two additional copper split gates were deposited near the billiard. They are colored in blue/red for visibility.

$$R_H = \frac{H}{ne} + \alpha R_{xx} \tag{2.65}$$

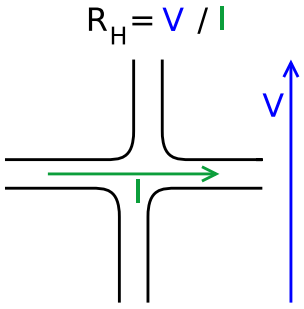

where H is the magnetic field n the carrier density. The coefficient α gives the contribution of longitudinal resistivity to the transverse resistance that arises due to geometric imperfections of the Hall probe (see sketch on the right). In order to determine the magnetic field one must find a way to remove the contribution of longitudinal resistance. One way to do this is to measure R_{xx} independently and subtract it from measured R_H. Another approach is to measure the Hall resistance in two different configurations where the role of current and voltage probes is interchanged (see Fig. 2.14) leading to two values R_H and R_H^* for the Hall resistance One then uses the Onsager-Casimir symmetry that provides a relation between R_H and R_H^* :

$$R_H(H) = R_H^*(-H) \tag{2.66}$$

Combining Eq. (2.65) and Eq. (2.66) we can express the unknown magnetic field as a function of the difference :

$$H = ne(R_H - R_H^*) \tag{2.67}$$

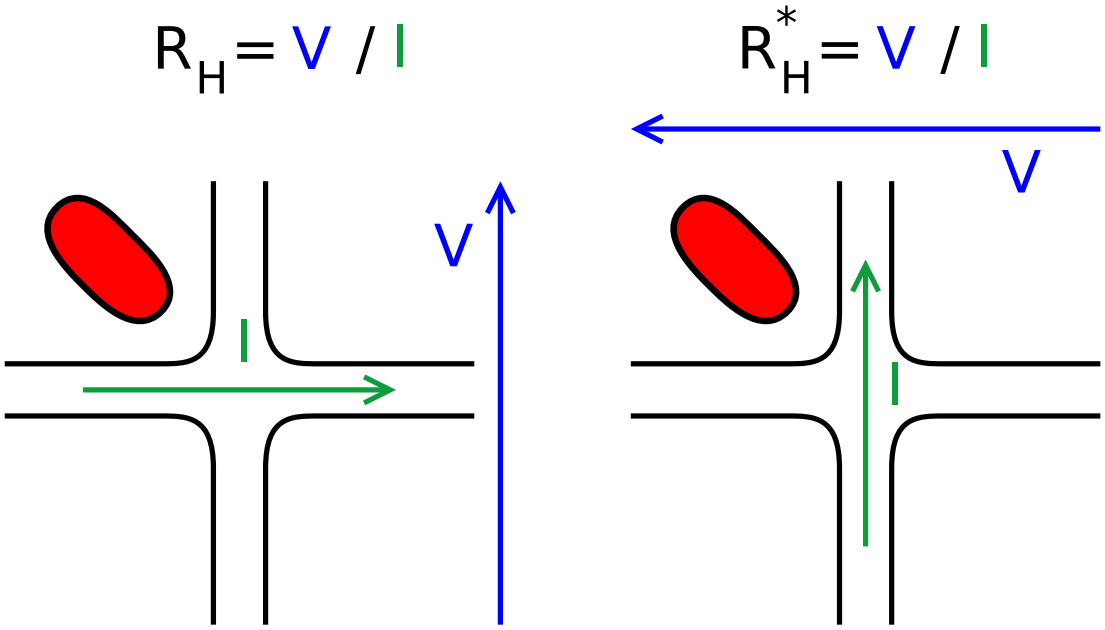

FIG. 2.14 – Two different configurations for measurement of the Hall resistance where the role of current and voltage probes is interchanged. We call R_H and R_H^* the values of the Hall resistance measured in these two experiments.

Note that in the derivation of the above relation we assumed that $R_{xx}(H) = R_{xx}(-H)$.

Following this logic, the signature of photo-induced orbital magnetism in the billiard is a shift of the Hall resistance under irradiation of the probe coupled to the billiard. The observed change of Hall resistance must have the symmetry of a magnetic field under exchange of current and voltage leads. However this implicitly assumes that Onsager-Casimir relations are still valid in a Hall probe under microwave irradiation. Although quite natural this assumption must be verified experimentally. This can be done by applying a local RF field on the Hall bar and looking at the deviations from Onsager-Casimir relation under driving. The outcome of these experiments can determine whether the Hall bar is a good detector of magnetic fields under microwave driving.

2.9 Time reversal symmetry breaking in the Hall bar

In a four terminal sample microscopic time-reversibility leads to symmetry relations between resistance measurements where the role of current and voltage leads are exchanged. These reciprocity relations are a manifestation of general Onsager-Casimir symmetries in equilibrium systems. We investigate experimentally the validity of time reversal symmetry in a $GaAs/Ga_{1-x}Al_xAs$ Hall bar irradiated by an external AC field, at zero magnetic field. For inhomogeneous AC fields we find strong deviations from reciprocity relations and show that their origin can be understood from the the billiard model of a Hall junction.

Under homogeneous irradiation the symmetry is more robust, indicating that time-reversal symmetry is preserved.

The Onsager-Casimir relations are a consequence at a macroscopic scale of microscopic time-reversal symmetry [23, 24]. In mesoscopic physics, these relations proved crucial in the understanding of magnetotransport properties when the reciprocity relation between resistances R and R^* measured in experiments which exchange the current and voltage leads : $R(H) = R^*(-H)$ was derived [25] and verified experimentally [26]. Since then the possibility to extend the reciprocity relation to out-of equilibrium conductors has attracted considerable attention. In the special case where the conductor has only two contacts the reciprocity relation implies that the transport is symmetrical with magnetic field H : $R(H) = R(-H)$. In the nonlinear transport regime, it was predicted theoretically that two terminal transport can be asymmetric with magnetic field [9, 10, 27], providing a signature of time-reversal symmetry breaking. This fact was later confirmed in several experiments [28, 29, 30, 31, 32], and lead to new theoretical proposals for the generalization of reciprocal relations to nonlinear transport [33, 34]. Recently it was proposed that time-reversal symmetry breaking can be analyzed from linear dc-magnetotransport of a system coupled to non-equilibrium baths [35], however in this model the presence of a magnetic field is necessary to reveal the breaking of reciprocity relations. Other manifestations of time-reversal symmetry breaking in non-equilibrium conductors at zero magnetic fields were predicted including commensurability effects in the frequency domain [36] and generation of stationary orbital magnetism [22]. However to our knowledge these effects have not yet been observed experimentally. In this Chapter we directly probe experimentally time-reversal symmetry in zero magnetic field by measuring deviations from the four terminal reciprocity relations in a Hall geometry. We interpret our results using a billiard model initially developed by Beenakker *et.al* [37]. to describe dc-magnetic field behavior. We extended this model to investigate the influence of an inhomogeneous time dependent potential.

We have investigated two Hall bars fabricated in a GaAs/$Ga_{1-x}Al_xAs$ two dimensional electron gas (2DEG) with density $n_e \simeq 1.2 \times 10^{11}$ cm^{-2} and mobility $\mu \simeq 1.2 \times 10^2$ m^2/Vs. The two samples, (A) and (B), were fabricated using wet etching and an aluminum mask. They have six Au/Ge ohmic contacts to 2DEG labeled (1)−(6) (see Fig. 2.15). Both samples are covered by a copper top-gate allowing to modulate carrier density. On sample (A) we have also fabricated a local split gate $[S]$ connected to a high frequency transmission line ; this gate can produce an AC field inhomogeneous on the micron scale. We define the four terminal resistances $R_{ij,kl}$ as $R_{ij,kl} = (V_k - V_l)/I_i$ where V_k and V_l are the voltages on the leads k and l and $I_i = -I_j$ is the current injected through the source lead i. The resistance measured in the configuration where current and voltage leads are interchanged is noted $R^*_{ij,kl} = R_{kl,ij}$. With this notations the reciprocity relation reads $R^*_{ij,kl}(H) = R_{ij,kl}(-H)$ [25]. As expected the magnetic field dependence of the Hall resistances $R_{H,1} = R_{14,26}$, $R_{H,2} = R_{14,35}$, and of the longitudinal resistance $R_{xx} = R_{14,23}$ exhibits quantum Hall effect plateaux and Shubnikov-de Haas oscillations at high magnetic fields $H > 0.5$ T. The resistances were measured at temperature $T = 0.3$ K with an excitation current $I = 1\ \mu A$ modulated at 67 Hz. Voltages were detected with a low noise amplifiers and standard lock-in technique. At lower magnetic field we observe magneto-size peaks, which occur when

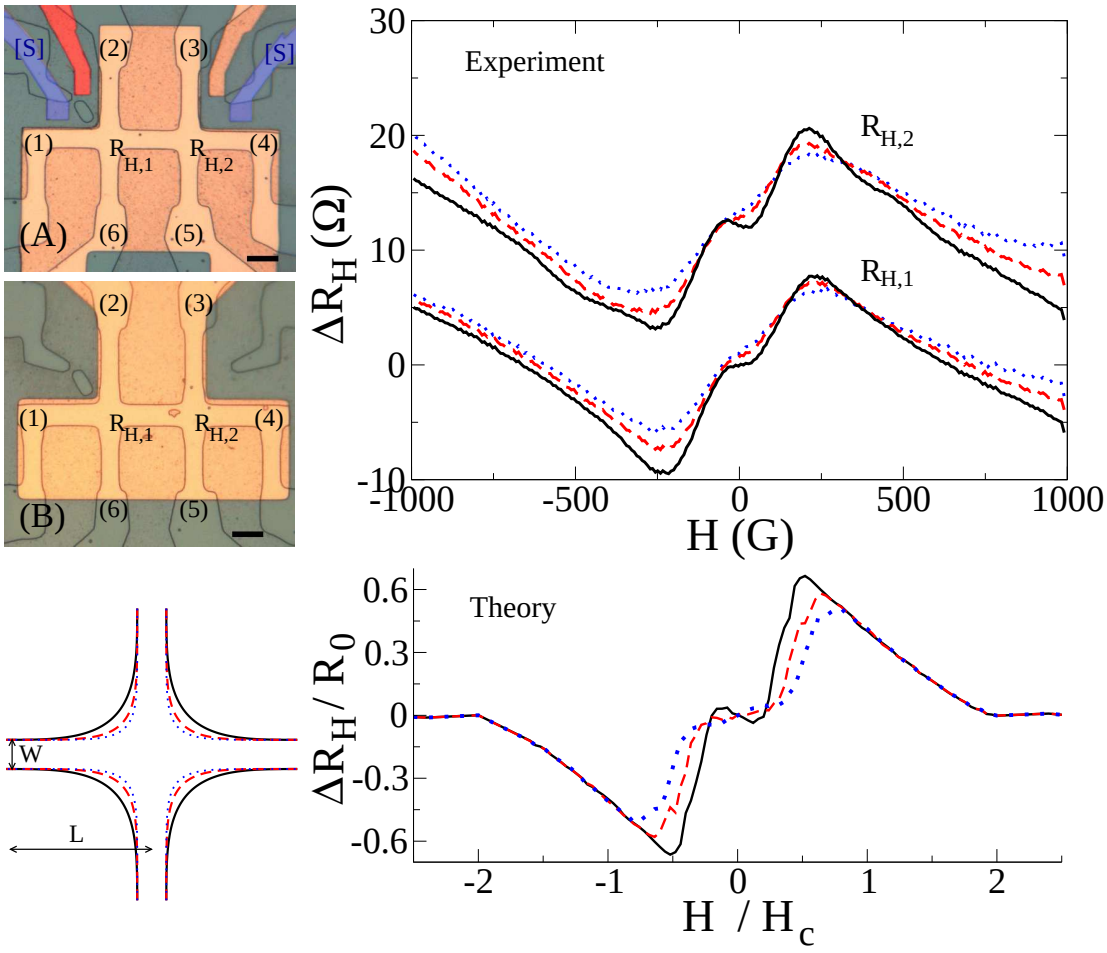

FIG. 2.15 – Left panel, optical micrograph of samples (A) and (B). The black scale line correspond to 10 μm. Right panel, on the top we show the experimental behavior of : $\Delta R_H = R_H - \frac{H}{ne}$ as a function of magnetic field for different top gate voltages $V_g = 0.1, 0.2, 0.4$ (doted , dashed and continuous line respectively), on the bottom theoretical predictions for ΔR_H for Hall junctions with increasing curvatures (doted, dashed and continuous line). The specular walls are sketched on the bottom left panel. Temperature was 0.3 K.

the size of cyclotron orbits matches the width of the 2DEG sample, on both Hall and longitudinal resistance for magnetic fields $H \simeq 200$ G. These observations confirm that our samples are in a ballistic regime (the mean free path in our Hall bar is $l_e \simeq 10$ μm).

The magneto-size peaks on the Hall resistance are analyzed in more detail in Fig. 2.15 for different top-gate voltages. To emphasize the magneto-size peaks, we have subtracted the classical Hall resistance $\Delta R_H = R_H - \frac{H}{n_e e}$ where n_e is the 2DEG density determined by a linear fit to the Hall resistance at fields above the magneto-size peak. An additional cusp appears in ΔR_H at low magnetic fields for higher gate voltages $V_g = 0.4$ V. This can be understood from the billiard model of a Hall junction [37]. In this model the Hall junction is treated as a classical billiard with specular walls and four contact channels of width W with absorbing boundary conditions at the reservoirs distant by $L > W$ (possible theoretical geometries are sketched on the left of Fig. 1). The classical probabilities $P_{i,j}$ of propagating from lead (j) to lead (i) are then determined numerically by injecting a large number of classical particles (typically 10^5) at Fermi velocity v_F into lead j and monitoring them until they reach one of the leads i. The propagation is determined by classical equations of motion in constant field H. The exit probabilities are then normalized to $\sum_j P_{i,j} = 1$, and the conductance matrix is calculated from :

$$G_{ij} = \frac{1}{R_0}\left[(1 - P_{ii})\delta_{ij} + P_{ij}(1 - \delta_{ij})\right] \tag{2.68}$$

Here $R_0 = \frac{h}{2e^2 N} \simeq \frac{h}{2e^2}\frac{\pi}{k_F W}$ where N is the channel number and k_F the Fermi wavevector. The characteristic magnetic field scale in this model is $H_c = \frac{m v_F}{eW}$, where m is the carrier effective mass in 2DEG. From the conductance matrix all four terminal resistances can be calculated including the Hall resistance R_H. On the bottom panel of Fig. 2.15, we show theoretical magneto-resistances ΔR_H of Hall junctions with different central curvatures. For the largest curvature, a cusp appears that is very similar to the behavior observed at higher positive gate voltages. When the curvature radius is decreased the cusp disappears, as in the magnetoresistance curves at lower gate voltages. These observations suggest that positive gate voltage favor larger curvature radius, which is reasonable since higher gate voltages are likely to reduce depletion at the sample boundaries. While there is a very good qualitative agreement between the billiard model and our data, the agreement is not quantitative. For example for $V_g = 0.4$ V with electron gas density $n_e \approx 2.8 \times 10^{11}\mathrm{cm}^{-2}$ and estimated channel width $W \simeq 5$ μm we find $H_c = \frac{m v_F}{eW} \simeq 170$ G (we used $v_F = \hbar\sqrt{2\pi n_e}/m$) . This leads to a predicted magneto-size peak at $H \simeq 100$G whereas experimentally the peak appears at $H \simeq 250$ G.

We now address the question of the influence of an external time dependent potential on the Hall resistance, in zero magnetic field. This problem can be treated theoretically if we generalize the billiard model and introduce a local oscillating potential $U(\mathbf{r})\cos\omega t$. As previously the transmission probabilities $P_{i,j}$ are determined by integrating the classical equations of motion (see typical particle trajectory inset in Fig. 2.16). In the static limit $\omega = 0$, an external potential creates a contribution to the Hall resistance by deforming the electronic trajectories. However time reversal symmetry implies that the relation $P_{i,j} = P_{j,i}$ is preserved, and reciprocity relation holds $R_H = R_H^*$. Our numerical simulations show

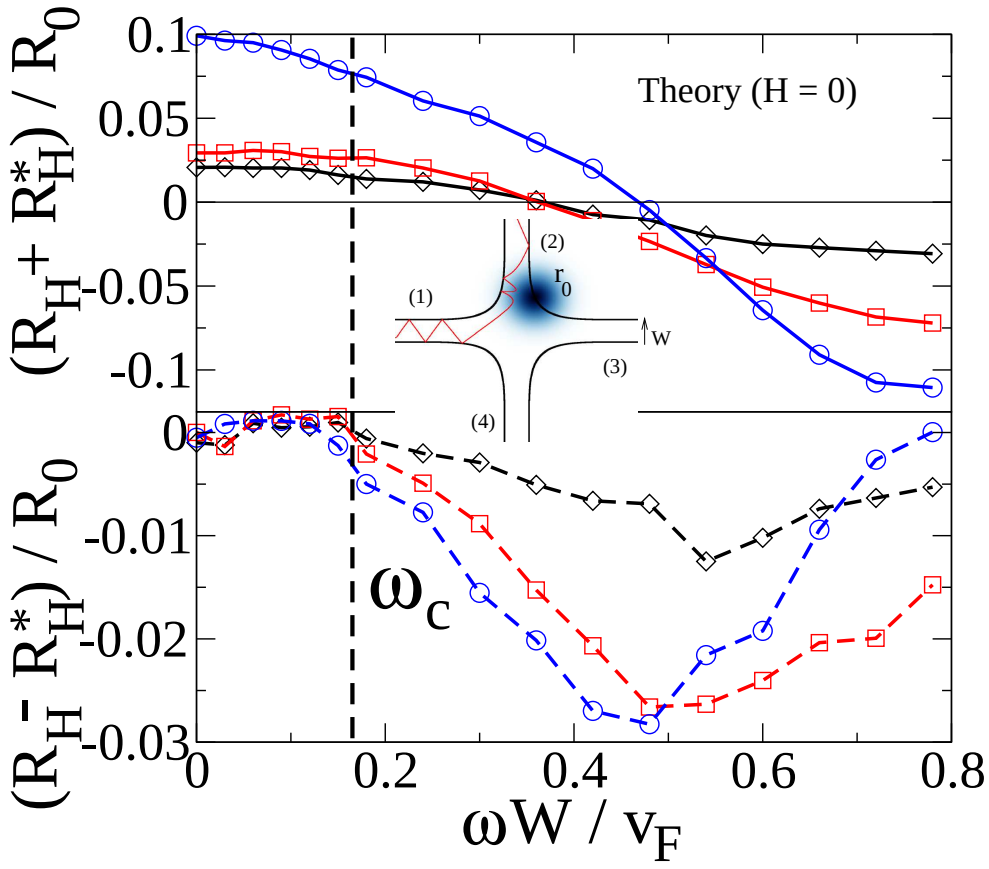

FIG. 2.16 – Calculated dependence of the Onsager-Casimir symmetric and anti-symmetric components of the Hall resistance R_H as a function of the reduced AC-potential frequency $\omega W/v_F$. Inset shows a ballistic trajectory in presence of an external potential of the form $U(r,t) = U_0 \exp(-k^2r^2/2)\cos\omega t$ centered around $\mathbf{r}_0$ inside the Hall junction with $kW = 1$ (colored circle). The anti-symmetric component appears only for $\omega > \omega_c$. Symbols represent different potential amplitudes : circles $U_0 = 0.7\epsilon_F$, squares $U_0 = 0.5\epsilon_F$ and diamonds $U_0 = 0.35\epsilon_F$.

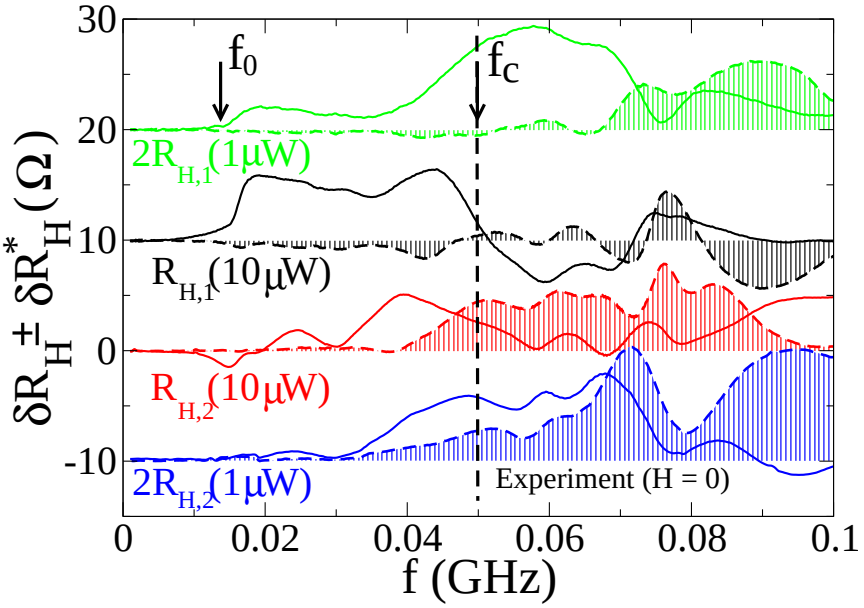

FIG. 2.17 – Change of Hall resistance on sample (A) under microwave irradiation on the local split-gate S as a function of microwave frequency. Continuous curves represent the Onsager-symmetric part of the Hall resistance $\delta R_H + \delta R_H^*$, while the dashed curves show the anti-symmetric part $\delta R_H - \delta R_H^*$. The data was obtained on the two Hall probes $\delta R_{H,1}$ and $\delta R_{H,2}$ at injected microwave powers of 1μW and 10μW. The origin of the different curves is shifted by an arbitrary offset for clarity (δR_H vanishes at low frequencies $f < 1$ MHz) and the values of δR_H at power 1μW are scaled up by a factor 2.

however that when the driving frequency ω is increased the probabilities $P_{i,j}$ and $P_{j,i}$ are no longer equal. This causes a difference between R_H and R_H^* even at zero magnetic field. For frequencies larger than a certain threshold ω_c the difference $R_H - R_H^*$ becomes of the order of the symmetric contribution $R_H + R_H^*$. We compare the amplitude of these two components as a function of frequency on Fig. 2.16. Our simulation shows that this frequency is nearly independent on the amplitude of the external potential. We note that trajectories that are absorbed in the reservoirs after a single scattering on $U(\mathbf{r})$ do not break time reversal symmetry. Indeed in this case it is possible to choose the phase of the external field in a way that the time reversed trajectory is also solution of the equations of motion. As a result the difference between $P_{i,j}$ and $P_{j,i}$ must stem from trajectories that scatter several times on the potential $U(\mathbf{r})$ centered around $\mathbf{r}_0$. This allows us to associate the frequency ω_c with the average return time to $\mathbf{r}_0$. Interestingly we find in the simulations that the frequency ω_c is several times smaller than the characteristic frequency associated with the size of the channels v_F/W. This points to the role of long trajectories with many reflections on the edges of the sample with typical length $L_c = \frac{v_F}{\omega_c}$ which can be much larger than W, of the order of the distance between reservoirs L.

Our theoretical model predicts that the onset of time-reversal symmetry breaking by

an ac-radiation can be probed directly by measurements of the difference $R_H - R_H^*$ as a function of ac-frequency without introducing an external magnetic field. We have checked this prediction experimentally by applying a high frequency potential on the split gate $[S]$ on sample (A). In order to remove the contribution of geometrical imperfections of our Hall junctions that lead to non-zero R_H even in the absence of magnetic field we now focus on the difference δR_H between the Hall resistance with AC-driving and its equilibrium value. We have measured the change of Hall resistances for the two Hall junctions of the sample, polarized in the two reciprocal configurations : $\delta R_{H,1}, \delta R_{H,1}^*, \delta R_{H,2}$ and $\delta R_{H,2}^*$ as a function of microwave frequency f for fixed injected microwave power. The data, shown on Fig. 2.17, indicate the following scenario. At very low driving frequencies $f < f_0 \simeq 10$MHz both symmetric and anti-symmetric components $\delta R_{H,i} + \delta R_{H,i}^*$ and $\delta R_{H,i} - \delta R_{H,i}^*$ are zero $(i = 1, 2)$, we attribute this to the fact that our capacitive coupling is not efficient at so low frequencies and the amplitude of the AC potential is very small in this limit. For higher frequencies, a change of Hall resistance due to microwave irradiation is observed, however as expected from our model the reciprocity relations is still valid $\delta R_{H,i} \simeq \delta R_{H,i}^*$. It is only for $f > f_c \simeq 50$ MHz that the anti-symmetric component becomes significant, and for higher frequencies (we measured up to $f = 10$ GHz) we observe that the symmetric and anti-symmetric components are of the same order of magnitude. We find that that the critical frequency f_c is similar for both Hall junctions and weakly depends on injected microwave power. This is consistent with our simulations where the threshold ω_c did not depend on the potential amplitude U_0. We note that as in our theoretical results on Fig. 2.16, $\delta R_H + \delta R_H^*$ scales proportionally to power (U_0^2) for $f < f_c$. At higher higher frequencies a more complicated behavior is observed since $\delta R_H + \delta R_H^*$ may change sign as a function of frequency. We showed that in a ballistic sample the length $L_c = \frac{v_F}{\omega_c}$ is of the order of the distance between reservoirs L, in a diffusive sample with mean free path l_e (we estimate $L \simeq 65$ μm and $l_e \simeq 10$ μm for our samples) we expect that the relevant length scale is determined by $L_c \simeq L^2/l_e \simeq 400$ μm. Such a value for L_c is consistent with a critical frequency $f_c = 50$ MHz as observed in the experiment. We remark that the onset of the difference $\delta R_H - \delta R_H^*$ could also be caused by the appearance of stationary orbital magnetism under microwave irradiation, an effect that was predicted theoretically in Ref. [22]. Indeed the quantity $R_H - R_H^*$ is proportional to the induced magnetic field. However the magnetic field required to change the value of Hall resistance by $\delta R_H \simeq 10\ \Omega$ as observed on Fig. 2.17 is $H \simeq 30$ G. This is several orders of magnitudes larger than the effect predicted in [22], which under our experimental conditions should create magnetic fields of the order of $H \simeq 10^{-2}$ G.

We now show that the spatial inhomogeneity of the alternating electric field is essential in order to observe strong deviations from Onsager symmetries. We prove this experimentally by irradiating sample (B) with an external electromagnetic field homogeneous on the sample scale emitted with a macroscopic antenna. For the Hall junction $R_{H,1}$ the presence of a quantum dot a few microns away from the sample (see Fig. 2.15) is expected to deform the external potential creating inhomogeneities in the electric field. On the contrary for $R_{H,2}$ we expect an homogeneous irradiation. On Fig. 2.18, we compare the variation of Hall resistances $\delta R_{H,2}, \delta R_{H,2}^*$ with frequency f at fixed power. We find that the Onsager

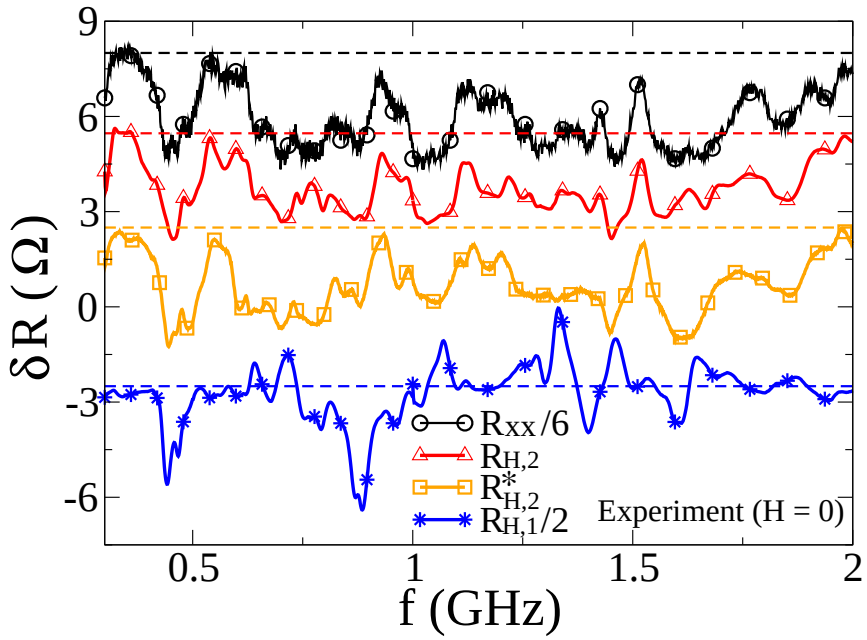

FIG. 2.18 – Change of Hall and longitudinal resistance under homogeneous microwave irradiation of sample (B) as a function of microwave frequency at injected microwave power of 10 μW and $T = 0.3$ K. The curves are marked with circles for $\delta R_{xx}/6$, triangles for $\delta R_{H,2}$, squares for $\delta R^*_{H,2}$ and stars for $\delta R_{H,1}/2$. The origin ($\delta R = 0$) is indicated by the dashed lines and is shifted for clarity. Note that the signal measured on $R_{H,2}$ closely follows R_{xx}.

relations are verified even in the limit of very high frequencies $f \simeq 1$ GHz compared to our previous experiment, and the relation $\delta R_{H,2} \simeq \delta R^*_{H,2}$ is valid. We also note that $\delta R_{H,2}$ is proportional to the change of sample resistance, δR_{xx} which is negative at all frequencies. The sign of δR_{xx} corresponds to heating, since we are in a regime where the sample resistivity decreases with temperature ($T \simeq 0.3$ K). The proportionality between δR_{xx} and $\delta R_{H,2}$ can be explained as a geometrical offset in $R_{H,2}$ proportional to R_{xx}. In fact, such a simple proportionality relation is a good indication of the external electric field homogeneity in the Hall junction. It does not hold for inhomogeneous irradiation, as shown by our measurements on $R_{H,1}$. In this case the proportionality to δR_{xx} is not observed and we find $\delta R_{H,1} \neq \delta R^*_{H,1}$ (data not shown) as in sample (A).

In this chapter we have addressed the validity of reciprocity relations in a Hall bar under AC driving. We have established that the magnetotransport in our samples is well described by the billiard model of [37]. We have generalized this model to include the effect of an AC field. With this model we predicted the onset of deviations from reciprocity relations at high enough AC frequencies even at zero magnetic field. We have checked this prediction experimentally by applying an inhomogeneous AC-field on the Hall bar. The transition from the low frequency regime where reciprocity symmetry holds to the asymmetric regime at high frequencies was clearly observed. Finally by irradiating a Hall bar with a macroscopic antenna, we established that the reciprocal relations are more robust under homogeneous irradiation. Intriguingly the signal we observe : $R_H - R^*_H$ resembles a static magnetic field except for its very large amplitude. This raises the question of a detector that can discriminate between inhomogeneous AC-electric fields and a small static magnetic field. As a consequence a direct measurement of the photomagnetic effect at zero magnetic field is not possible with a Hall probe, however we will show in Chapter 2.11 a signature of stationary photo-induced orbital currents at high magnetic fields.

2.10 Quantum theory for microwave induced time reversal symmetry breaking

In this section we propose another interpretation of the origin of the deviations from Onsager-Casimir symmetries under microwave driving. It is based on a scattering approach to conductance in quantum devices. Here electrons are treated as waves which are scattered by the potential distribution inside the Hall probe. The model geometry is shown on Fig. 2.19, we assume that the junction is described by a stationary 4×4 S-matrix with transmission/reflection coefficients t^0_{ij}, r^0_{ij}. In one of the leads a time dependent potential $V(x,t) = \alpha\delta(x)\cos(\omega t)$ creates additional scattering that can be described by a 2×2 scattering matrix with transmissions/reflections given by $t_V(\tau), r_V(\tau)$. Since this potential is not stationary the transmission/reflection coefficients depend explicitly on time.

The transmission from contact $1 \rightarrow 2$ can be expressed as a sum of over all paths after

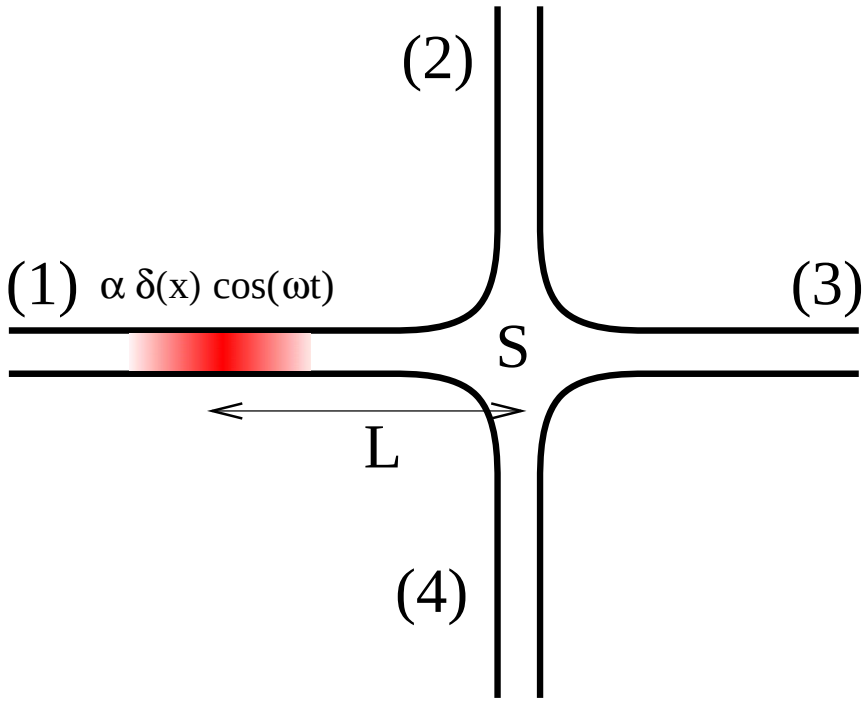

FIG. 2.19 – Schematic geometry of a four terminal sample where the scattering is described by a 4×4 stationary S matrix. An additional time dependent is applied locally inside the lead number (1).

multiple reflections at the junction and at the time dependent potential :

$$t_{1,2}(\tau) = t_V(\tau)e^{ikL}t^0_{1,2} + e^{i3kL}t_V(\tau)r^0_{1,1}r_V(\tau+\tau_D)t^0_{1,2} + \\ e^{i5kL}t_V(\tau)r^0_{1,1}r_V(\tau+\tau_D)r^0_{1,1}r_V(\tau+2\tau_D)t^0_{1,2} + ... \tag{2.69}$$

The terms In this expression e^{ikL} represent the phase accumulated during the trip from the potential $V(x,t)$ to the center of the junction. The delay τ_D in the reflection amplitude $r_V(\tau+\tau_D)$ takes into account the time τ_D it takes to the wave to travels from the potential to the junction and return backward.

A similar expression holds for the reciprocal transmission coefficient $t_{2,1}$

$$t_{2,1}(\tau) = t^0_{2,1}e^{ikL}t_V(\tau) + e^{i3kL}t^0_{2,1}r_V(\tau)r^0_{1,1}t_V(\tau+\tau_D) + \\ e^{i5kL}t^0_{2,1}r_V(\tau)r^0_{1,1}r_V(\tau+\tau_D)r^0_{1,1}t_V(\tau+2\tau_D) + ... \tag{2.70}$$

In this sum we have assumed that $r^0_{1,1} \ll 1$ so that only the first two terms can be kept to lower non trivial order in $r^0_{1,1}$, in general the sum over all possible reflections should be considered in a way very similar to a Fabry-Pérot interferometer in optics.

A deviation from Onsager-Casimir symmetry is expected to appear when the time average $< |t_{1,2}(\tau)|^2 - |t_{2,1}(\tau)|^2 >_\tau$ is non-zero. For this purpose we expand the transmission probability keeping only the lowest order terms :

$$|t_{1,2}(\tau)|^2 = |t_V(\tau)t^0_{1,2}|^2 + 2\ \mathrm{Re}\ \left[e^{i3kL}t_V(\tau)r^0_{1,1}r_V(\tau+\tau_D)t^0_{1,2}\ \times\ (t^0_{1,2}e^{ikL}t_V(\tau))^*\right] + ... \tag{2.71}$$

$$|t_{2,1}(\tau)|^2 = |t_V(\tau)t^0_{2,1}|^2 + 2\ \mathrm{Re}\ \left[e^{i3kL}t^0_{2,1}r_V(\tau)r^0_{1,1}t_V(\tau+\tau_D)\ \times\ (t^0_{2,1}e^{ikL}t_V(\tau))^*\right] + ... \tag{2.72}$$

The transmission and reflection coefficients $t_V(\tau), r_V(\tau)$ can be found directly from the Schrödinger equation in presence of a potential $V(x) \propto \alpha\delta(x)$ (see for e.g. Ref. [58])

$$t_V(\tau) = \frac{2}{2+i\alpha\cos\omega\tau}, r_V(\tau) = \frac{-i\alpha\cos\omega\tau}{2+i\alpha\cos\omega\tau} \tag{2.73}$$

The time averaged transmission coefficients involve $< |t_{1,2}(\tau)|^2 >_\tau$ and $< |t_{2,1}(\tau)|^2 >_\tau$ involve the correlators

$$< t_V(\tau)r_V(\tau+\tau_D)t^*_V(\tau) >_\tau = -\frac{\alpha^2}{8} + O(\alpha^4) \tag{2.74}$$

and

$$< r_V(\tau)t_V(\tau+\tau_D)t^*_V(\tau) >_\tau = -\frac{\alpha^2}{8}\cos\omega\tau_D + O(\alpha^4) \tag{2.75}$$

This yields

$$< |t_{1,2}(\tau)|^2 - |t_{2,1}(\tau)|^2 > = -\frac{\alpha^2}{4}|t_{1,2}|^2\ \mathrm{Re}\left[e^{i2kL}r^0_{1,1}(\cos\omega\tau_D - 1)\right] \tag{2.76}$$

Physically this finite difference originates from the interference between the direct path with a single passage across the time dependent potential $V(x,t)$ and an indirect path were a reflection occurred before the transmission. For a trajectory going from contact (1) to contact (2) the transmission across the potential V occurs at the same time in both cases. However for trajectories from (2) to (1), the transmission is delayed for a reflected trajectory compared to the scenario where the particle directly passes through $V(x,t)$. This explains the difference in the structure of the correlators in Eq. (2.74) and Eq. (2.75).

A more complete and rigorous treatment of the origin of TRS symmetry breaking in mesoscopic samples was recently proposed by M. Polianski [20]. In this article calculations are done explicitly in the Landau-Bütttiker formalism for a coherent quantum dot. The asymmetric contribution to resistance is found in second order perturbation theory versus applied AC-voltages on the sample, the theoretical prediction derived by M. Polianski for a small number of channels then reads :

$$\delta R_{-} \sim \frac{h}{e^2}\left(\frac{eV_{AC}}{\epsilon}\right)^2,\ \epsilon = \max(E_c, \hbar\omega) \tag{2.77}$$

where E_c is the Thouless energy, ω is the AC driving frequency and V_{AC} is the amplitude of the AC potential. This asymmetric contribution to sample 4-terminal resistance has random sign which is typical for a quantum effect. Since a magnetic flux of order Φ_0 inside the sample induces an asymmetric fluctuation of order h/e^2 the above formula can be cast in the form of an effective flux :

$$\phi_{eff} \simeq \phi_0\left(\frac{eV_{AC}}{\epsilon}\right)^2,\ \epsilon = \max(E_c, \hbar\omega) \tag{2.78}$$

A fundamental question is whether this effective flux can be interpreted as a magnetic flux created by microwave induced orbital magnetism inside the quantum dot. A priori an explicit calculation of the induced magnetic moment in the quantum regime is needed in a spirit similar to the calculations in Section 2.6. However a direct calculation of magnetization is not possible in the frame of Landauer-Büttiker formalism and new approaches must be found. To answer this question experimentally, one must find a magnetometer which is not sensitive to microwave irradiation. Possible candidates include NS SQUID, or optical magnetometers (for e.g. Kerr magnetometry). We have tried to prepare NS SQUID samples in order to check whether they provide a reliable measurement of magnetic field under microwave irradiation However the technology involved in the fabrication is not well controlled at the moment, and our samples did not display a SQUID behavior. Therefore the determination of photomagnetic effects in mesoscopic samples is still an open question from both experimental and theoretical points of views.

In the next section we describe an indirect detection of microwave induced orbital currents, through measurements of rectified voltage across the Hall bar in an evanescent wave geometry. We show that unexpectedly the currents can be detected using the Hall resistance not as a magnetic field detector but as a measurement of the current in the sample.

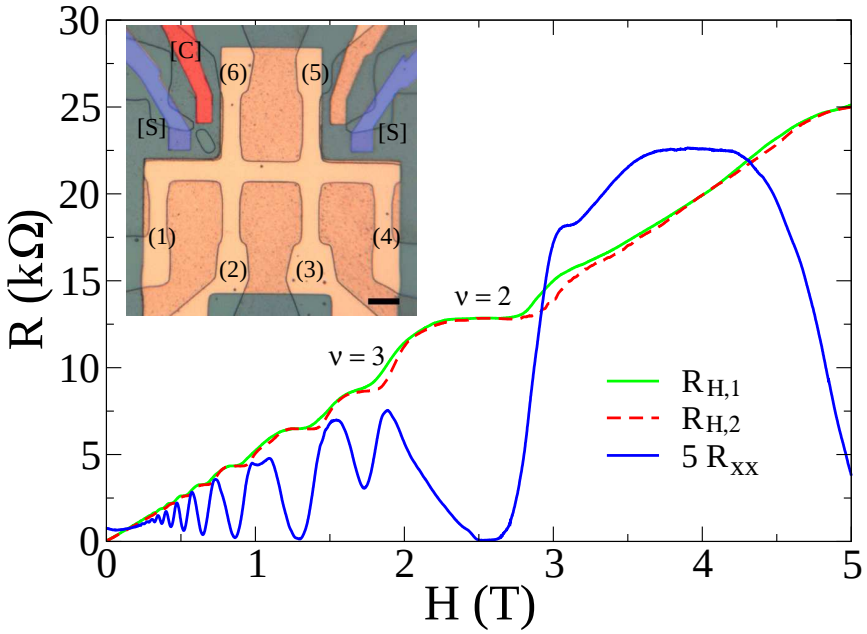

FIG. 2.20 – Magneto-transport properties of the Hall bar. The dashed and neighbor curves represent respectively the Hall resistances $R_{H,2} = R_{14,35}$ and $R_{H,1} = R_{14,26}$ (see text). The oscillating curve represents the longitudinal resistance $R_{xx} = R_{14,23}$. The data was acquired with a 100 nA excitation and lock-in detection at frequency 67 Hz at a temperature of 300 mK. The inset is an optical image of the sample, the leads $(1) - (6)$ form the contacts of the Hall bar, while the electrodes $[S]$ and $[C]$ are local gates connected to a high frequency 50 Ω transmission line. The (orange) copper shield on top of the Hall bar can be used as a top gate to change the carrier density in the 2DEG. The black scale bar corresponds to 10 μm.

2.11 Antisymmetric photovoltaic effect

Coherent mesoscopic samples present remarkable rectification properties, related to the absence of spatial inversion symmetry of the disorder potential. In particular when submitted to a radio-frequency radiation they develop a dc voltage. The dependence on magnetic field of this photovoltaic (PV) effect, gives rise to random but reproducible fluctuations that were predicted theoretically [38, 39] and observed experimentally in references [40, 41]. In contrast with universal conductance fluctuations that obey Onsager symmetry rules [42, 25], the fluctuations of the PV-voltage do not have a well defined magnetic field symmetry [43]. At high frequency this can be understood from the violation of time inversion symmetry by the microwave radiation [44, 45, 32]. At low frequencies, this behavior was explained through a mechanism involving electron-electron interactions [28, 29, 30, 31, 46, 47]. Recently the PV effect was studied in asymmetric antidot super-lattices where magnetic field asymmetry was also present [48, 49]. In all these cases however, the anti-symmetric component of the PV voltage was never larger than the symmetric one (see e.g. [50]). In

this Chapter we investigate the regime where the spatial symmetry of the system is broken by a non homogeneous high frequency potential. This potential is screened in the region of the sample where the photovoltaic voltage is measured by a copper shield evaporated on the surface of the Hall bar. This reduces the mesoscopic fluctuations of the PV-voltage, revealing a PV-voltage with a dominant anti-symmetric contribution.

The system consists of a Hall bar in a GaAs/$Ga_{1-x}Al_xAs$ two dimensional electron gas (2DEG) with density $n_e \simeq 1.2 \times 10^{11}$ cm^{-2} and mobility $\mu \simeq 1.1 \times 10^2$ m^2/Vs. The sample was fabricated using wet etching and an aluminum mask using the procedure described in Chap. 2.7. It was used for the measurements described in Chap. 2.9, in the present chapter however we investigate the high magnetic field behavior. The six contacts of the Hall bar are numbered $(1)-(6)$ (see photograph inset in Fig. 2.20). The four terminal resistances with source (i) and drain (j) and voltage probes k and l are defined by the usual relation $R_{ij,kl} = (V_k - V_l)/I_i$ where V_k and V_l are the voltages on the leads (k) and (l) and $I_i = -I_j$ is the current injected in the source lead. We measure simultaneously the Hall resistances $R_{H,1} = R_{14,26}$, $R_{H,2} = R_{14,35}$, and the longitudinal resistance $R_{xx} = R_{14,23}$ as a function of magnetic field H. As shown on Fig. 2.20 our samples exhibit quantum Hall effect plateaux [51] for the Hall resistances $R_{H,1}, R_{H,2}$ and Shubnikov-de Haas (SdH) oscillations [52] in the transverse resistance R_{xx} . We notice that the carrier density in our system is homogeneous since $R_{H,1} \simeq R_{H,2}$.

In the following, we excite the system with a high frequency potential $V_{ac}\cos(2\pi ft)$ applied on a symmetrical split gate $[S]$ shown in the inset of Fig. 2.20. This potential is screened by a 100nm thick copper top-gate deposited over the Hall bar device and therefore the induced potential is spatially non homogeneous and vanishes exponentially inside the Hall bar. We note that while the topgate ensures a good shielding of the AC electric potential on the Hall probe, this is not the case for AC magnetic fields at frequencies below 10GHz such that the skin depth is larger than 100nm. However we expect the effect of those fields to be negligible because of the electrostatic coupling between the RF lines and the Hall probe. We measure the PV voltage drop $V_{pv} = V_3 - V_2$ induced by the irradiation. In order to determine this voltage with a high precision we modulate the high frequency signal at a low frequency below 1.5 kHz. The voltage V_{pv} is then amplified by a low-noise amplifier and measured by a lock-in detector working at the frequency of the amplitude modulation. In Fig. 2.21, we have studied the dependence of V_{pv} on magnetic field and microwave power at fixed frequency $f = 2.5$ GHz. The photovoltaic voltage displays oscillations as a function of magnetic field reminiscent of SdH oscillations in the longitudinal resistance R_{xx} (Fig. 2.21 left panel), except that the PV voltage oscillates around a zero mean value which is not the case for the longitudinal resistance. We also notice that the oscillations of V_{pv} are quenched in the quantum Hall plateau region around $H = 2$ Tesla (filling factor $\nu = 2$), in contrast to oscillations in longitudinal resistance (see Fig. 2.20). The amplitude of these oscillations increases with the injected microwave power P. Since the microwaves are transmitted through a $Z_0 = 50\ \Omega$ adapted line, P is related to the high frequency potential amplitude through $V_{ac}^2 = \alpha Z_0 P$. Here α is a frequency dependent coefficient taking into account the attenuation and reflection in the transmission line. We estimate that $\alpha \simeq 0.1$ for frequencies in the GHz range. On the

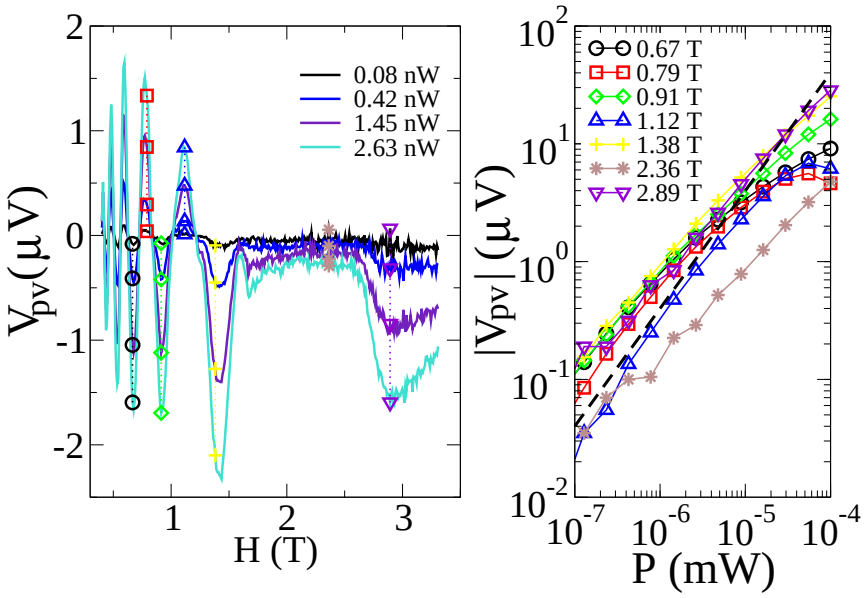

FIG. 2.21 – Left panel : Magnetic field dependence of the photovoltaic voltage V_{pv} for different microwave powers, namely $0.08, 0.42, 1.45$ and 2.63 nW in the direction of increasing oscillation amplitude. Right panel : Dependence of the photovoltage amplitude V_{pv} as a function of microwave power for different values of the magnetic field (the symbols correspond to different magnetic fields and are indicated on both the right and left panel). The dashed line represents the dependence $V_{pv} \propto P$. Temperature is 300 mK, and frequency $f = 2.5$ GHz.

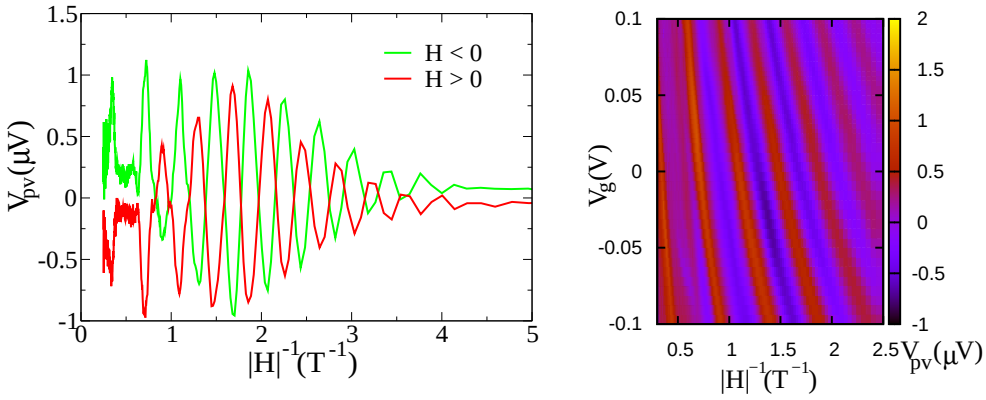

FIG. 2.22 – Left panel : Comparison of the PV voltage V_{pv} as a function of inverse magnetic field for positive and negative magnetic fields. Frequency was $f = 2.5$ GHz and injected microwave power of 1 nW. On the right panel, a color diagram showing the PV voltage as a function of both top-gate voltage and applied magnetic field.

right panel of Fig. 2.21 we show the dependence of the rectified voltage on power more quantitatively at selected values of magnetic field. We find that the photovoltaic voltage is well described by $V_{pv} \propto P$, the deviations at higher power are attributed to heating effects. We have also performed experiments with asymmetric irradiation on the electrode $[C]$, with the electrode opposite to $[C]$ floating. These experiments lead to a similar behavior with the difference that the oscillations of the PV voltage are no longer centered around zero. For this reason we focus on the case of symmetric irradiation on the local gate $[S]$ in the rest of this chapter.

The Shubnikov-de Haas (SdH) oscillations of resistivity in metals and in 2DEG are symmetric with magnetic field. Indeed SdH oscillations are well described by the classical relation [52, 53]

$$\frac{\delta R(H)}{R_0} = 4D_T \exp\left(-\frac{\pi}{\omega_c \tau_e}\right) \cos\left(2\pi \frac{h n_e}{2e} \frac{1}{H}\right) \tag{2.79}$$

which shows that relative amplitude of the SdH oscillations $\delta R(H)/R_0$ is an even function of magnetic field. In this expression n_e is the electron density, ω_c the cyclotron frequency and τ_e is the elastic time. The prefactor $D_T = \gamma/\sinh\gamma$ with $\gamma = 2\pi^2 k_B T/(\hbar\omega_c)$ describes the temperature damping of the oscillations on the scale of $\hbar\omega_c/(2\pi^2 k_B)$. In contrast as illustrated on the left panel of Fig. 2.22, we find that the oscillations of the photovoltage are mostly anti-symmetric with magnetic field. On this figure, in order to make the connection with SdH oscillations more obvious we have shown the photovoltage V_{pv} as a function of the inverse absolute value of the magnetic field. The photovoltage displays periodic oscillations with inverse magnetic field with the exception of a missing half-period at $H^{-1} \simeq 0.5$ Tesla^{-1} in the quantum-Hall plateau regime (filling factor $\nu = 2$). The right panel shows that the period of the oscillations of the photovoltage can be modified by changing the density n_e

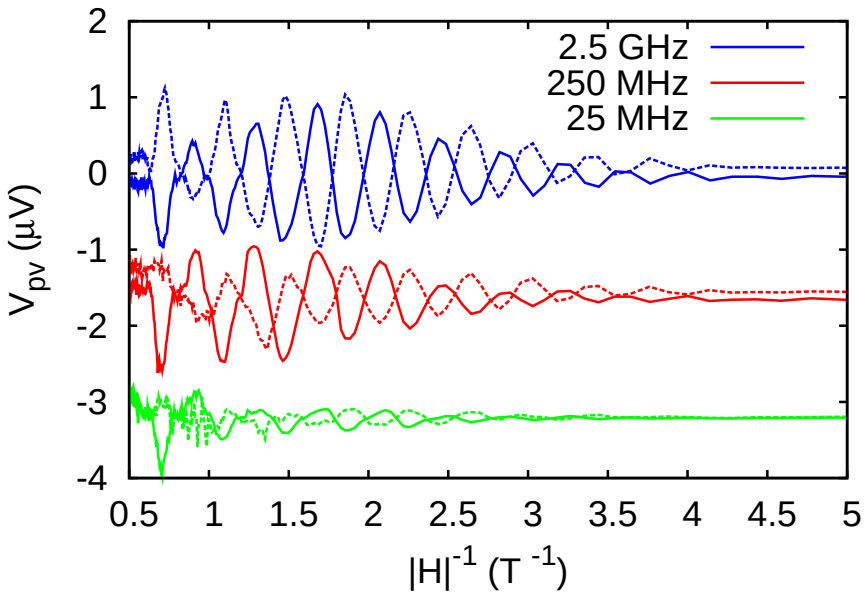

FIG. 2.23 – Dependence of the PV voltage on inverse magnetic fields for different excitation frequencies. Continuous/dashed curves correspond to positive/negative values of the magnetic field respectively. The curves at different are shifted vertically for clarity, the excitation frequencies are from top to bottom : $f = 2.5$ GHz, 250 MHz and $f = 25$ MHz. The microwave power was 1 nW.

of the Hall probe with a top-gate voltage V_g. This further supports the connection with SdH oscillation of resistivity whose period τ_H is related to electron density through $\tau_H = e/(\pi\hbar n_e)$. We have also checked the anti-symmetry of the photovoltage at different gate voltages. The data shown on Fig. 2.22 was obtained for $f = 2.5$GHz, at lower microwave frequencies the photovoltage decreases and vanishes around $f \simeq 10$MHz while remaining mostly anti-symmetric (see experimental data on Fig. 2.23). We attribute this decrease to the inefficiency of our capacitive coupling at so low frequencies. We note that we are always in the regime $2\pi f < \omega_c$ where ω_c is the cyclotron frequency, therefore we do not expect the frequency to play an important role in contrast with recent experiments where a sharp frequency dependent PV effect was investigated around $\omega = \omega_c$ [54] in relation with microwave induced resistance oscillations and zero resistance states [55, 56, 57].

Under homogeneous irradiation the photovoltage also displays $1/H$ oscillations with the period τ_H as shown on Fig. 2.24. However these oscillations contain a large symmetric component as a function of magnetic field in contrast with our data for evanescent irradiation. This is consistent with the previous experimental results reported in [44, 45, 32] where high frequency photovoltoaic effect did not exhibit a well defined magnetic field symmetry.

The SdH oscillations of longitudinal resistance R_{xx} as a function of inverse magnetic field have a well defined phase, which is given by the expression $R_{xx}(H^{-1}) = R_0(H^{-1}) +$

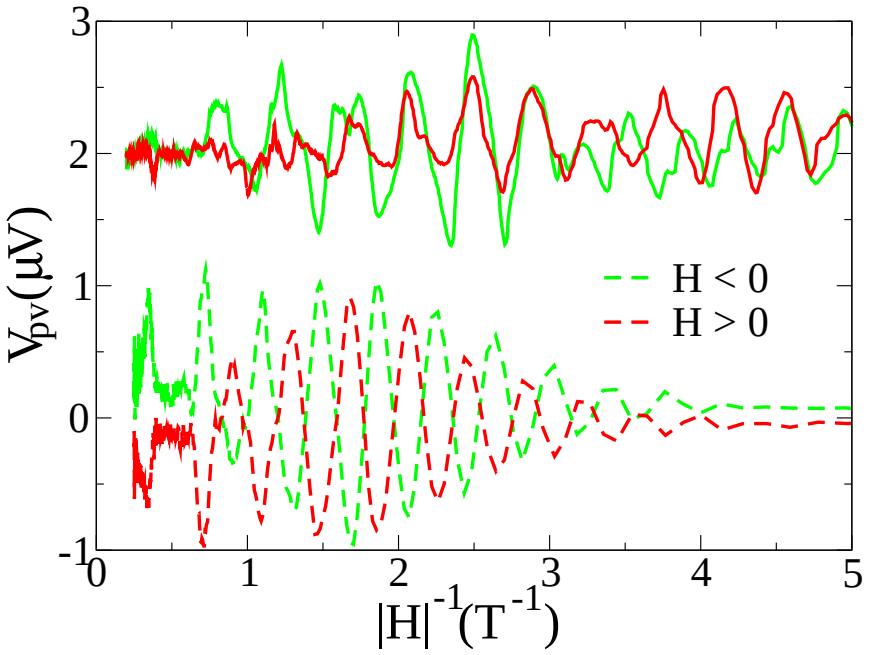

FIG. 2.24 – Comparison of the PV voltage V_{pv} dependence on the inverse magnetic field for homogeneous and evanescent microwave excitations. For the continuous curves microwave irradiation was sent using an external 3mm long antenna terminating a 50 Ω cryogenic coaxial cable. The dashed curves reproduce for comparison our data of Fig. 2.22 obtained by applying a high frequency potential directly on the local split gate. In both cases frequency was $f = 2.5$ GHz. The continuous curves are shifted for clarity by 2 μV. An asymmetric behavior is detected for homogeneous (antenna) excitation, whereas antisymmetric dependence is observed in the case of evanescent excitation (spit gate).

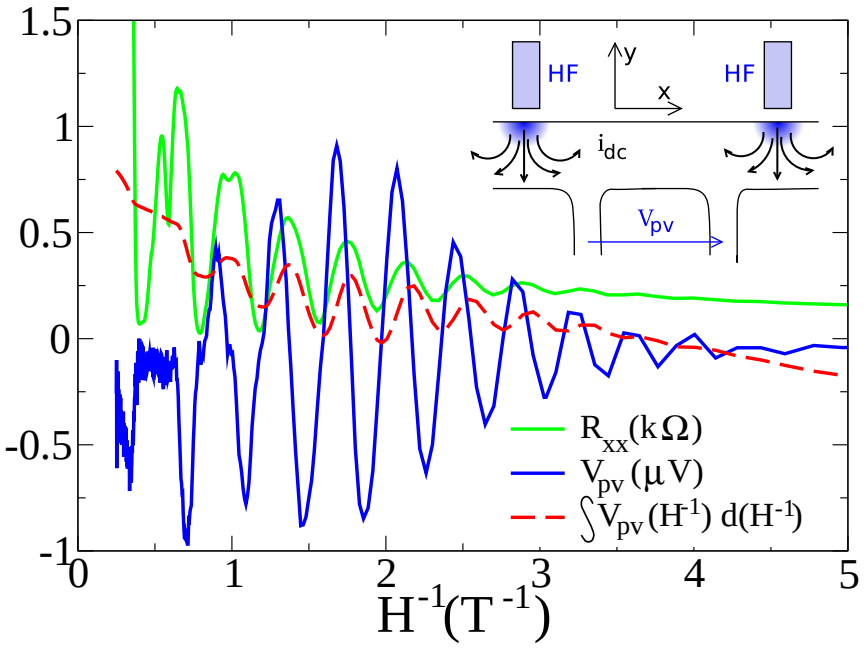

FIG. 2.25 – Comparison between the behavior of R_{xx} (kΩ) (green/gray curve), V_{pv} (μV) (blue/black curve) and $\int V_{pv}(H^{-1})dH^{-1}$ (red dashed curve). The inset shows a simplified sample geometry with schematic representation of induced stationary currents i_{dc}, and density modulation (colored semi-disks). Frequency is $f = 2.5$ GHz and $P = 1$ nW.

$R_1(H^{-1})\cos(\frac{2\pi^2 n_e \hbar}{eH})$, where $R_0(H^{-1})$ and $R_1(H^{-1})$ are envelope functions weakly depending on the magnetic field on the scale of one SdH oscillation period τ_H [52]. On Fig. 2.25 (main figure) we compare the phase of the oscillations of V_{pv} and the phase of the oscillations in R_{xx}. Our results demonstrate that the oscillation of the photovoltage are dephased by $\pi/2$ compared to the oscillations of R_{xx}. We check this by calculating numerically the integral $\int V_{pv}(H^{-1})dH^{-1}$ from the experimental data. We find that oscillations of this quantity are in phase with the oscillations of $R_{xx}(H^{-1})$ (a theoretical argument justifying this comparison is given below).

In summary we find that the SdH oscillations of the PV voltage are anti-symmetric with magnetic field and are out of phase with the usual SdH oscillation of resistivity as a function of H^{-1}. These oscillations are quenched in the plateau regions of the quantum Hall effect. The main lines of our explanation are the following. The high frequency potential applied on the local gate $[S]$ creates a stationary current distribution i_{dc} inside the sample mostly along the y axis. A possible current distribution is shown in the inset of Fig. 2.25 with a simplified sample geometry. This current leads to the appearance of a static Hall voltage drop $V_{pv} \simeq R_H i_{dc}$ along the x axis perpendicular to i_{dc}. For this expression to be valid, the applied potential V_{ac} must vanish in the region where V_{pv} is measured. Otherwise an additional contribution appears from mesoscopic fluctuations induced by the alternating potential. This contribution has a large symmetric component. In this respect, the

evanescent potential geometry used in our experiment is crucial, and we have checked that under an homogeneous irradiation we recover an essentially symmetric photovoltage.

It is possible to derive more quantitative estimates from this heuristic scenario. The potential V_{ac} on the local gate creates a modulation of the electronic density δn in the Hall bar. We assume that for high magnetic fields this density modulation occurs in a region of typical Larmor radius $r_l = v_F m^*/eH$ inside the sample, where $v_F = \hbar\sqrt{2\pi n_e}/m^*$ is the Fermi velocity and m^* the electron mass in 2DEG (colored regions in the sketch of Fig. 2.25). Indeed in this regime most electronic trajectories are localized on cyclotron orbits of radius r_l, which is therefore the natural length scale. The total charge induced on the Hall bar is given by CV_{ac} where C is the capacitance between the local gate and the Hall bar, hence the amplitude of δn can be estimated as : $\delta n \simeq \frac{C}{r_l^2} V_{ac}\cos(2\pi f t)$. An approximate value of the capacitance is ϵD, where ϵ is the permittivity and D is the typical distance between the gate and the Hall bar. In the SdH regime, the amplitude of the rectified current i_{dc} is given by :

$$i_{dc} \simeq < \frac{\partial G_{yy}}{\partial n_e} \delta n \; V_{ac}\cos(2\pi f t) > \tag{2.80}$$

where $< \; . \; >$ denotes time averaging, and G_{yy} is the conductance in y direction of the sample. Up to a geometrical factor we have $G_{yy} \simeq G_{xx}$ and in the regime where $R_{xx} \ll R_H$, G_{xx} is given by $G_{xx} \simeq R_{xx}/R_H^2$. As noted above, $R_{xx} = R_0 + R_1\cos(\frac{2\pi^2 n_e \hbar}{eH})$ where R_0 and R_1 are slow functions of density and inverse magnetic field. This allows us to take into account only the oscillating term in the density derivative, which yields : $i_{dc} \simeq \frac{\hbar}{eH}\frac{R_1 \sin(\frac{2\pi^2 n_e \hbar}{eH})}{R_H^2} < \delta n V_{ac}\cos(2\pi f t) >$. By injecting in this formula the expression of δn as a function of V_{ac}, and using the relation $V_{pv} = i_{dc} R_H$ with the approximation $R_H = H/(en_e)$ that is accurate below 1 T, we obtain

$$V_{pv} \simeq \frac{eC}{\hbar} R_1(H) \sin\left(\frac{2\pi^2 n_e \hbar}{eH}\right) V_{ac}^2 \tag{2.81}$$

In this expression $R_1(H)$ is the typical SdH oscillation amplitude that is symmetric with magnetic field. Consequently this expression reproduces the main features observed in our experiment : V_{pv} is anti-symmetric with magnetic field, with a phase given by $\sin\left(\frac{2\pi^2 n_e \hbar}{eH}\right)$, and an amplitude that scales proportionally to microwave power $V_{pv} \propto V_{ac}^2 \propto P$. This expression also leads to the right order of magnitude for the observed photovoltaic voltage, indeed for $C \simeq \epsilon_0 D$ with $D \simeq 1$ μm, $V_{ac}^2 = 1$ nW $\times\, 50\ \Omega$ and $R_1(H) \simeq 1$ kΩ at $H \simeq 1$ T we find that $V_{pv} \simeq 0.1$ μV (experimental amplitude is shown on the right panel of Fig. 2.21). Further comparison is possible by noting that the product $R_1(H)\sin\left(\frac{2\pi^2 n_e \hbar}{eH}\right)$ is proportional to $dR_{xx}(H^{-1})/dH^{-1}$. In our approximation, this leads to the simple prediction :

$$\int V_{pv}(H^{-1}) dH^{-1} \propto R_{xx}(H^{-1}) \tag{2.82}$$

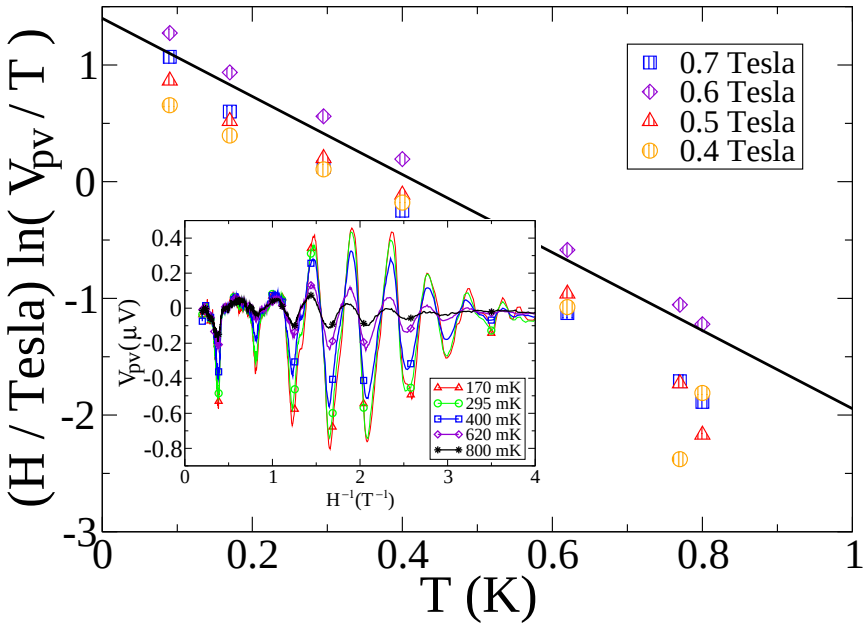

FIG. 2.26 – Dependence of the photovoltage on temperature for several magnetic fields in semi-logarithmic scale. The data for different magnetic fields can be rescaled on a single linear curve as predicted by Eq. (2.83). The inset shows the photovoltage dependence on inverse magnetic fields for different temperatures for $f = 2.5$ GHz and $P = 1$ nW.

On figure Fig. 2.25, we show that this relation is well verified as long as $H^{-1} \geq 1.5$ T^{-1}. Deviations are observed for higher magnetic fields, specially at $H^{-1} \simeq 0.5$ T^{-1} where a plateau appears in V_{pv} that is not present in R_{xx}. We attribute this deviation to other quantum effects which are not taken into account in our simple model and become relevant at higher magnetic field. Specially the physics of the quantum Hall effect is important, while our model is based on a Shubnikov-de Haas approximation for conductivity.

We have also measured the temperature dependence of photovoltaic effect. Our results, summarized on Fig. 2.26, show that the amplitude of the photovoltaic oscillations strongly decreases with temperature in the 100 mK-1 K range, in a similar way to SdH oscillations on the linear resistance. To achieve a more quantitative comparison we have tried to extract the carrier effective mass from the temperature dependence of the amplitude of the SdH oscillations of the photovoltage. As shown on Fig. 2.25 this dependence is well described by a relation of the form

$$\ln \frac{|V_{pv}|}{T} = -A\frac{T}{B} + \text{ const} \tag{2.83}$$

For SdH oscillations of the resistivity the coefficient A is equal to $A_0 = \frac{2\pi^2 k_B m^*}{e\hbar}$. In the case of photovoltage oscillations of resistivity we find a higher value $A \simeq 3.5A_0$. While detailed studies as a function of both temperature and microwave power are needed to establish

the origin of this discrepancy, this most likely indicates that there is an additional energy scale in the problem which is related to microwave power.

In conclusion we have investigated the photovoltaic effect in high mobility two dimensional electron gas under irradiation by an evanescent microwave potential. We have found that the photovoltaic voltage exhibits zero centered oscillations as a function of inverse magnetic field. These oscillations are anti-symmetric with magnetic field and are out of phase with the well known Shubnikov-de Haas oscillations in resistivity as a function of inverse magnetic field. The amplitude of these oscillations is proportional to microwave power. Our experimental findings can be understood from a simple model that predicts the creation of stationary orbital currents in the sample under microwave driving. In this model the stationary voltage across the sample appears as a Hall effect detection of the orbital currents.

2.12 Summary on out of equilibrium experiments in 2DEG

We can now summarize the experimental and theoretical results on out of equilibrium transport in 2DEG that we have obtained so far. A graphical representation of the results is shown on Fig. 2.27. On the theoretical side we have shown that microwave irradiation can create a stationary magnetic moment in an isolated mesoscopic sample. This effects can appear only if the system formed by the sample and microwave irradiation does not have mirror symmetries. It also requires a sample with weak disorder. We have attempted to detect this magnetic moment with a Hall bar detector coupled to a ballistic billiard located near one of the Hall probes of our detector. We expected that the irradiation would change the value of the Hall resistance and create a deviation from Onsager reciprocity relations. This behavior was indeed observed in our experiments however the magnetic fields needed to create a comparable shift of Hall resistance ($\simeq$ 10 Gauss) were much stronger that those predicted by theory $\simeq$ 0.1 Gauss.

In order to understand these results we proposed an alternative theoretical explanation for the onset of deviations from Onsager reciprocity relations in Hall bar. It consists in a dynamical time reversal symmetry breaking by inhomogeneous microwave fields. These effect can be captured in a simple semiclassical transport model where the conductance matrix is determined from the transmission probabilities from one contact to another in the Hall bar. This model was shown to reproduce magneto-size effects in our Hall probe that appear when the Larmor radius is of the order of the wire width. Note that dynamical time reversal symmetry breaking can also be understood in the framework of the Landauer-Büttiker quantum transport theory.

Signatures of stationary orbital currents inside the sample could be seen at higher magnetic fields where an effective Hall geometry allows to detect currents inside the sample through the Hall voltage they induce. In this experiment the evanescent field geometry used in our samples was crucial and allowed to detect a magnetic field anti-symmetric photovoltoaic voltage. However the current geometry used in our samples did not allow a precise control of the flow of the induced current. On figure Fig. 2.28 we show a sample geometry where the current can be channeled more effectively inside the structure. However the fabrication of such a sample requires the ability to make very small Ohmic contacts to 2DEG, which is possible only for 2DEG samples closer to the sample surface. The latter constraint however is hardly compatible with a large mean free path since high mobility 2DEG tends to be buried deep under the sample surface (e.g. $\simeq$ 200 nm for the heterostructrue we used in our experiments).

In the next chapters, I will show describe a new theory that applies the ideas we developed to interpret our experiments on phototransport in Hall probes to understand the physical origin of microwave induced zero resistance states that attracted a strong interest in the 2DEG community.

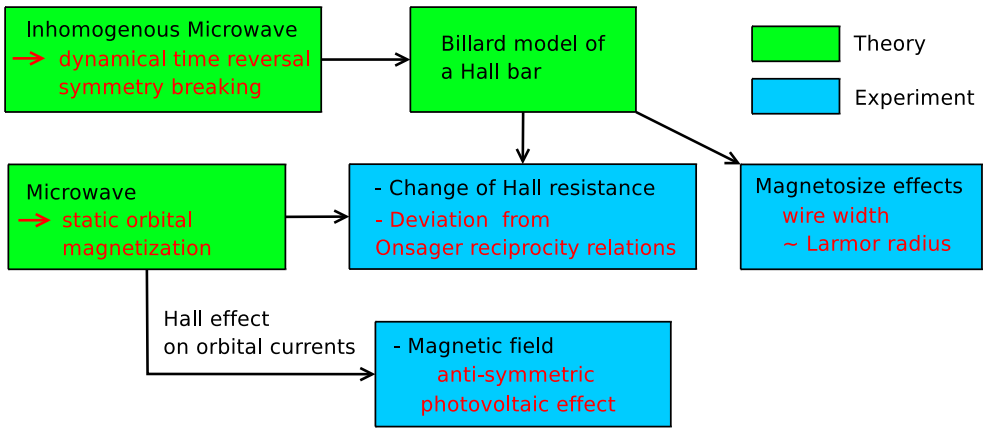

FIG. 2.27 – Graphical representation of the theoretical and experimental results obtained on non equilibrium transport in 2DEG.

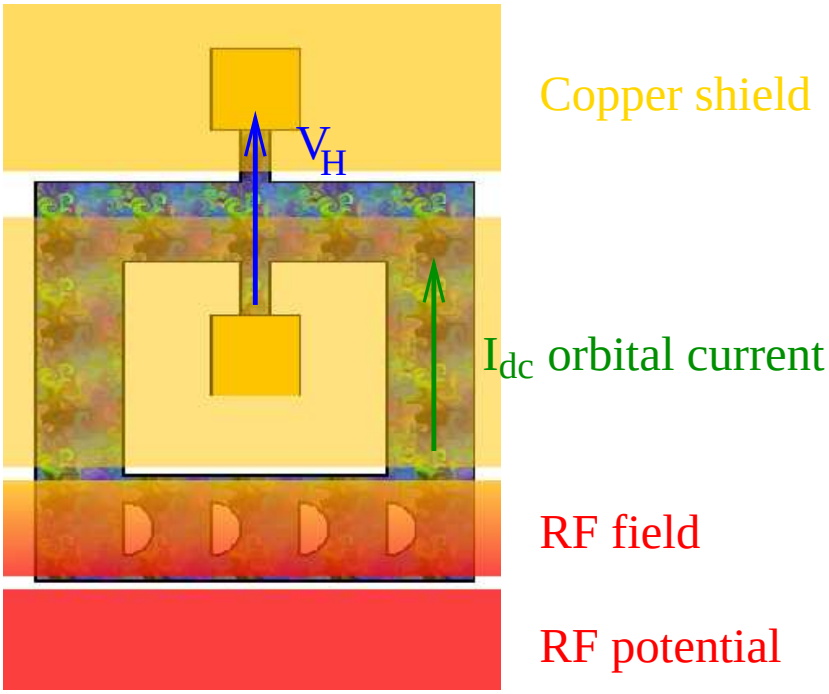

FIG. 2.28 – Stationary orbital current excited by a localized microwave field in a ring geometry. Asymmetric antidots (semi-disks) define an orientation for the rectified current, which flows through the ring and induces a Hall voltage on the opposite side of the ring. The microwave field must be screened completely in the region where the Hall voltage is measured.

2.13 Microwave induced zero-resistance states

The samples we used in this thesis had mobility $\mu \simeq 1.1 \times 10^2$ m^2/Vs. However progress in molecular beam epitaxy (MBE) growth have allowed to prepare ultra-low disorder 2DEG with mobilities exceeding 35×10^2 m^2/Vs [59]. In these samples several new types of low magnetic $1/B$ periodic oscillations have been detected in the sample magnetoresistance. They appear at magnetic fields smaller than the characteristic magnetic field at which the Schubnikov-de Haas oscillations start to show up $\simeq$ 2 kGauss. The possible source of these oscillations include electron-phonon coupling [60] and interaction static electric field induced by passing strong DC currents through the sample [61]. For these oscillations however the oscillation amplitude represented only a small fraction of the longitudinal resistance R_{xx}.

In 2002-2003 two independent experimental groups announced the discovery of a new class of low magnetic field resistance oscillations where the oscillation amplitude could become of the order of the mean R_{xx} [62, 63]. In these experiments a high mobility 2DEG sample was irradiated with an electromagnetic field at frequencies $f \simeq 50$ GHz (see Fig. 2.29 for a sketch of the experimental setup). The four terminal resistance R_{xx} in presence of magnetic field irradiation displays a spectacular behavior which is mainly governed by the dimensionless ratio j between the microwave and cyclotron frequencies :

$$j = \frac{\omega}{\omega_c} \ , \ \omega_c = \frac{eB}{m} \tag{2.84}$$

As shown on Fig. 2.30, the magnetoresistance under irradiation presents a maximum when j is an integer. Surprisingly when j is of the form $j = n + \delta$ with n an integer and $\delta \simeq 1/4$ the four terminal resistance R_{xx} vanishes. The plateaux where $R_{xx} = 0$ vanishes are called zero resistance states. The experimental observation of microwave induced zero resistance states (ZRS) attracted great experimental and theoretical interest.

λ_{Fermi}	$<$	λ_T (at 1 K)	$\ll$	r_c	$\ll$	Mean free path
$\simeq 50$ nm		$\frac{\hbar}{\sqrt{mT}} \simeq 100$ nm		$\frac{v_F}{\omega_c} \simeq 1\mu$m		$l_e \simeq 100\ \mu$m

TAB. 2.4 – This table summarizes the relevant length scales at equilibrium in an ultra-high mobility 2DEG sample at low temperature.

In order to understand the theoretical challenge raised by zero-resistance states let us assume for a moment that carriers move freely without disorder and interactions. When electrons (classical or quantum) move in the presence of a magnetic field they behave as an harmonic oscillator with cyclotron frequency ω_c. The harmonic oscillator has only a single resonance frequency at $\omega = \omega_c$, all higher harmonics $\omega = n\omega_c$ are not resonant. This is easily seen in the classical oscillator. Quantum mechanics does not change this qualitative picture and the above property takes the form of selection rules well known from atomic physics. The coupling to the microwave radiation is dipolar and the interaction Hamiltonian can be cast in the form $\hat{H}_{int} = -(\hat{a}+\hat{a}^+)DE_{rf}$ where $\hat{a}^+$ and $\hat{a}$ are creation/annihilation operators,

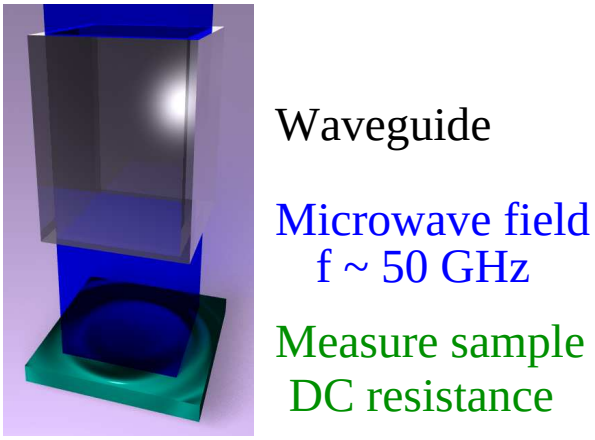

FIG. 2.29 – A simple sketch of an experimental setup, where irradiation is sent through a waveguide onto a sample.

D is the dipolar moment and E_{rf} is the microwave field. Hence even if Landau levels are equally spaced the irradiation can create transitions only between neighbor Landau levels and the transitions at frequencies $j\omega_c$ (j integer ¿ 1) are forbidden. Therefore both in quantum and classical mechanics a source of nonlinearities is needed to explain the origin of high order resonances observed in the experiments. If the disorder is smooth on the scale of a Larmor radius, it just creates an additional mean force on the oscillator that shifts the position of the resonance center without introducing high harmonics. In conclusion one of the main theoretical challenge raised by the discovery of ZRS is to understand the origin of high frequency harmonics in very clean samples with smooth disorder.

2.14 Edge channel theory of zero-resistance states

In this chapter we apply some of the ideas we developed to understand our photo-transport experiments in Hall bar samples with lower mobilities to the context of ZRS. An important property that played a role in our experiments is that guiding along sample edges influences the magnetoresistance even in the semi-classical regime where Landau-levels are smeared by disorder [72, 73]. This effects explains the appearance of magnetosize peaks and negative magnetoresistance observed in clean Hall bar samples. All these effects are naturally captured in the frame of the billiard model [73]. Due to the presence of disorder guiding is not perfect and resistance can not vanish completely. For this reason it is usually thought that ballistic transport along edges occurs only in the quantum regime with low filling factors where a gap appears in the 2DEG density of states. In this chapter we show that a microwave field can stabilize edge trajectories even in the semiclassical regime leading to a vanishing longitudinal resistance. This mechanism gives a clear physical interpretation for observed zero-resistance states.

Before explaining our model in detail, we review the theoretical explanations that have

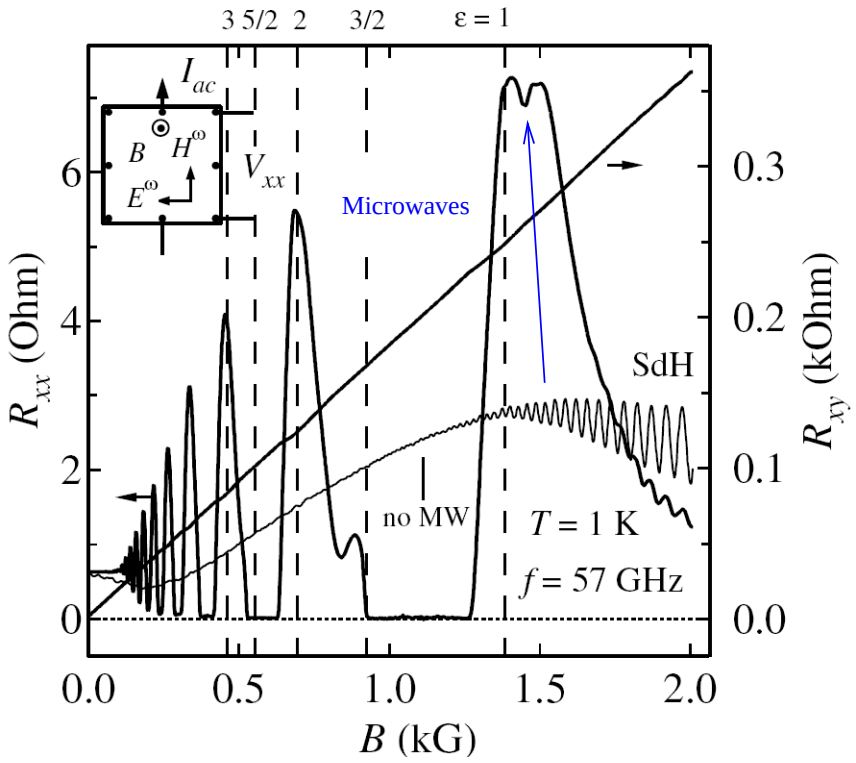

FIG. 2.30 – Experimental results from Ref. [63] on magnetoresistance of utra-high mobility 2DEG under microwave irradiation (Fig. 1, from condmat cond-mat/0210034). *Thick lines represent R_{xx} (left axis) and R_{xy} (right axis) under microwave irradiation with frequency $f = 57$ GHz at $T \simeq 1$ K. Thin lines shows R_{xx} without microwave irradiation. Inset depicts the sample layout, contacts, DC current orientation, magnetic field B and electromagnetic fields E^ω and H^ω.*

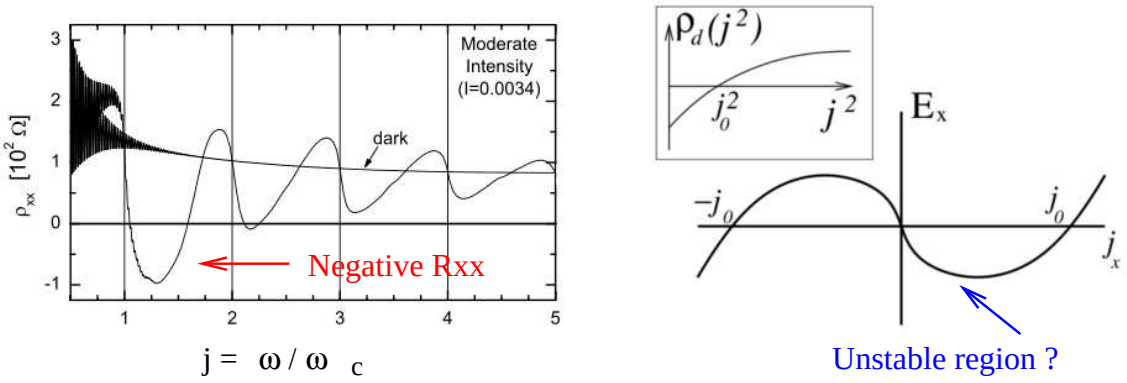

FIG. 2.31 – (Left pannel) Figure from [65] predicting negative resistance states. (Right pannel) Figure from [70] illustrating the possible formation of an unstable region corresponding to negative resistance states.

been proposed so far, which mainly rely on scattering mechanisms inside the bulk of 2DEG. The "displacement" mechanism originates from the effect of microwaves on disorder elastic scattering in the sample [64, 65, 66, 67], while the "inelastic" mechanism involves inelastic processes that lead to a modified out-of equilibrium distribution function [68, 69]. Even if these theories reproduce certain experimental features we believe that the physical origin of ZRS is still not captured. Indeed several arguments can challenge those approaches. The above theories naturally generate negative resistance states and one has to rely on an uncontrolled out of equilibrium compensation of all currents [70] to produce ZRS as observed in experiments (see Fig. 2.31). This instability mechanism predicts a switching to a zero resistance state as soon as microwave power is strong enough to generate negative resistances, for stronger power the resistance should remain zero independently on the power value. For example a similar behavior can be observed in a normal-superconductor transition that occurs due to an instability of the Fermi-liquid state : once temperature is smaller than the critical temperature, resistance is zero independently on temperature value. However in ZRS experiments no switching is observed and the experimental dependence on power is well described by an exponential decay [81].

Also ZRS is observed in very clean samples, therefore in the bulk the electron moves like an oscillator where selection rules allow transitions only between nearby oscillator states. Hence resonant transitions are possible only at cyclotron resonance where the ratio j between microwave frequency ω and cyclotron frequency ω_c is unity. However experiments show that the onset of ZRS occurs also for high $j = \omega/\omega_c$ approximately at $j = 1 + 1/4, 2 + 1/4, ...$ High j resonances could appear due to nonlinear effects, however the microwave fields are relatively weak giving a ratio ϵ between oscillating component of electron velocity and Fermi velocity v_F of the order of few percents. Therefore the appearance of high j ZRS in "displacement" models with weak disorder seems problematic. In the "inelastic" models one assumes that 2DEG evolves in a far from equilibrium state

due to small energy relaxation rates. However since the microwave frequency is high compared to the elastic rate, the 2DEG has mainly imaginary high frequency conductivity and should not significantly absorb microwave power. This can be seen very clearly in [62] where the amplitude of the Shubnikov-de Haas oscillations is not changed by the presence of microwave radiation even when power is strong enough to generate ZRS. Hence it seems unlikely that 2DEG actually reaches the out of equilibrium states needed for the "inelastic" theories.

In order to develop a theory for ZRS we note that they occur when the mean free path l_e is much larger than the cyclotron radius $r_c = v_F/\omega_c$. In usual 2DEG samples with lower mobilities this regime corresponds to strong magnetic fields and quantum Hall effect. In this case it is known that propagation along sample edges is ballistic and plays a crucial role in magnetotransport. It leads to quantization of the Hall resistance R_{xy} and to the disappearance of four terminal resistance R_{xx} strikingly similar to ZRS [71]. This occurs at low filling factors ν when a gap forms in the 2DEG density of states due to discreetness of Landau levels. In contrast ZRS appear at $\nu \simeq 50$ where Landau levels are smeared out by disorder. Even in this semiclassical regime, edge trajectories are still important for transport. Guiding along sample edges can lead to a significant decrease of R_{xx} with magnetic fields giving a negative magnetoresistance and singularities in R_{xy} [72, 73] (note that negative magnetoresistance is also observed in ZRS samples [62, 63, 74]). This behavior can be understood theoretically from the transmission probability T between neighbor sample contacts [73]. The drop in R_{xx} is linked to increased T, but transmission remains smaller than unity due to disorder and R_{xx} remains finite. Recently this model was extended to understand experimental deviations from Onsager reciprocity relations in samples under microwave driving [75]. But the impact of microwaves on stability of edge channels was never considered before.

In this chapter we show that microwave radiation can stabilize guiding along sample edges leading to a ballistic transport regime with vanishing R_{xx} and transmission exponentially close to unity. It was established experimentally that edge channels are very sensitive to irradiation [76] and recent contact-less measurements in the ZRS regime did not show a significant drop of R_{xx} [77] that supports our edge transport mechanism for ZRS. Our model also relies on the fact that scattering occur on small angles in 2DEG [62, 78]. This contrasts with other ZRS models which do not rely on specific physical properties of 2DEG.

Since filling factors are large we study classical dynamics of an electron at the Fermi surface [73] propagating along a sample edge modeled as a specular wall. The motion is described by Newton equations :

$$d\mathbf{v}/dt = \omega_\mathbf{c} \times \mathbf{v} + \epsilon \cos \omega t - \gamma(v)\mathbf{v} + I_{wall} + I_S \tag{2.85}$$

where $\epsilon = e\mathbf{E}/(m\omega v_F)$ describes microwave driving field $\mathbf{E}$, velocity is measured in units of Fermi velocity v_F, and $\gamma(v) = \gamma_0(|\mathbf{v}|^2 - 1)$ describes relaxation processes to the Fermi surface. The last two terms account for elastic collisions with the wall and small angle scattering. Disorder scattering is modeled as random rotations of $\mathbf{v}$ by small angles in the interval $\pm\alpha$ with Poissonian distribution over microwave period. Examples of electron

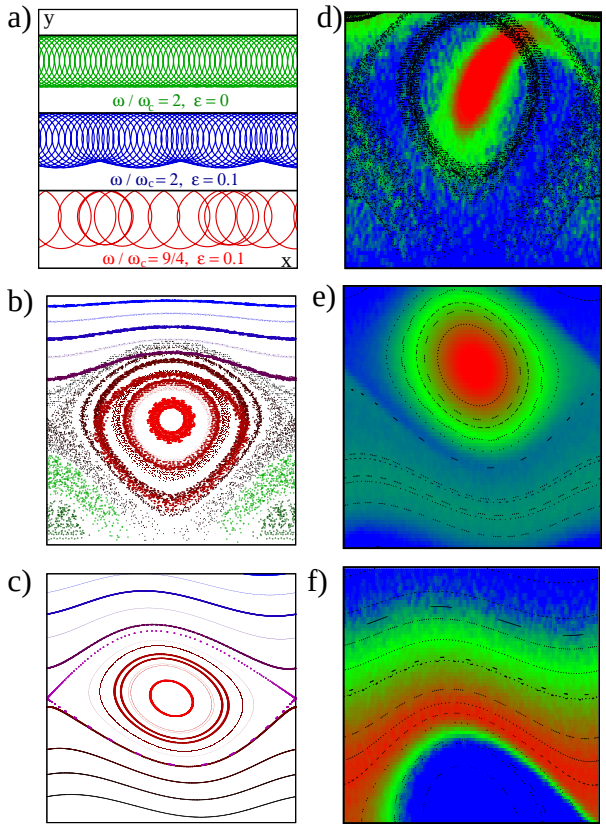

FIG. 2.32 – a) Examples of electron trajectories along sample edge for several values of ω/ω_c and y-polarized field ϵ. b) Poincaré section of (2.85) for $\omega/\omega_c = 9/4$ at y-polarized $\epsilon = 0.02$ drawn in the region $0 < v_y < 0.7$ and $-\pi < \phi < \pi$. c) Poincaré section in the same region for the Chirikov standard map (2.86) giving approximate description of dynamics in b). In a,b,c) dissipation and impurity scattering angle are zero. d,e,f) Density of propagating particles on the Poincaré section in presence of noise and dissipation (red/gray for maximum and blue/black for zero; v_y range is $0 < v_y < 0.5$), black points show trajectories without noise and dissipation. For $\omega/\omega_c = 9/4$ particles are trapped inside the nonlinear resonance (d,e) while for $\omega/\omega_c = 2$ microwave repels particles from the edge (f). Here $\gamma_0 = 10^{-3}$ (d) and $\gamma_C = 10^{-2}$ (e,f) and $\alpha \simeq 5 \times 10^{-3}$.

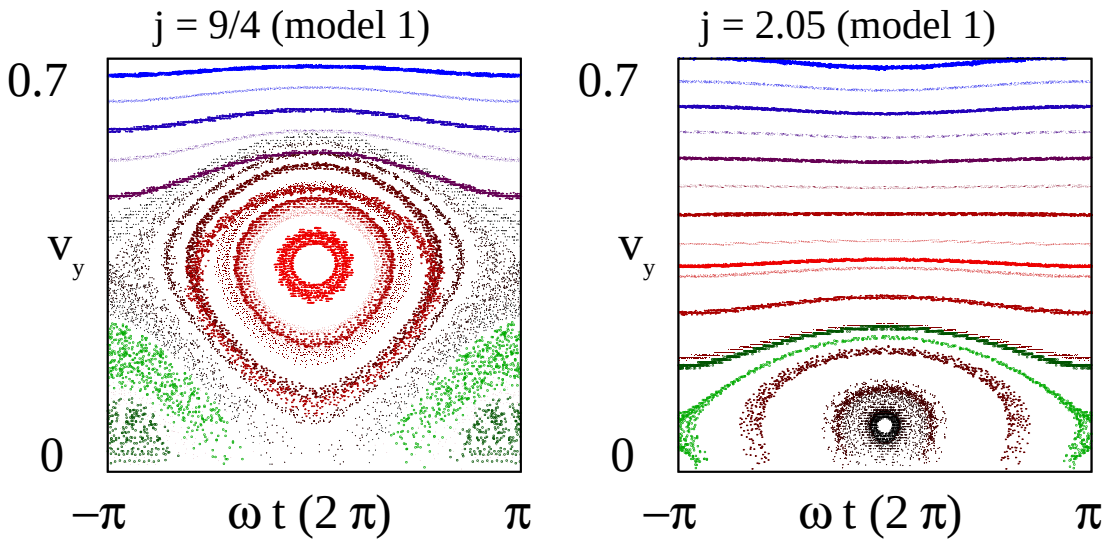

FIG. 2.33 – Poincaré section of (2.85) for $j = \omega/\omega_c = 9/4$ (left) and $j = 2.05$ (right) at y-polarized $\epsilon = 0.02$ drawn in the region $0 < v_y < 0.7$ and $-\pi < \phi < \pi$. For $j = 2.05$ the resonance has an overlap with the region $v_y < 0$, whereas for $j = 9/2$ only the separatrix touches the line $v_y = 0$.

dynamics along the sample edge for $\gamma_0 = 0$ and $\alpha = 0$ are shown in Fig. 2.32a. They show that even a weak field $\epsilon = 0.1$ has strong impact on dynamics along the edge. A more direct understanding of the dynamics can be obtained from the Poincaré sections constructed for the microwave field phase $\phi = \omega t (\mathrm{mod} 2\pi)$ and the velocity component $v_y > 0$ at the moment of collision with the wall. The system (2.85) has two and half degrees of freedom and therefore the curves on the section are only approximately invariant (Figs. 2.32b, 2.33). The main feature of this figure is the appearance of a nonlinear resonance. We assume for simplicity that 2DEG is not at cyclotron resonance and polarization is mainly along y axis. Since Eq. (2.85) is linear outside the wall, one can go to the oscillating frame where electron moves on a circular orbit while the wall oscillates in y with velocity $\epsilon \sin \omega t$. Hence collisions change v_y by twice the wall velocity. For small collision angles the time between collisions is $\Delta t = 2(\pi - v_y)/\omega_c$. This yields an approximate dynamics description in terms of the Chirikov standard map [79] :

$$\bar{v}_y = v_y + 2\epsilon \sin\phi + I_{cc}, \;\; \bar{\phi} = \phi + 2(\pi - \bar{v}_y)\omega_/\omega_c \tag{2.86}$$

The additional term $I_{cc} = -\gamma_c v_y + \alpha_n$ describes dissipation and noise, bars denote values after map iteration ($-\alpha < \alpha_n < \alpha$). Damping from electron-phonon and electron-electron collisions contribute to γ_c. The Poincaré sections for Eqs. (2.85,2.86) are compared in Figs. 1b,c showing that the Chirikov standard map gives a good description for edge dynamics under microwave driving. A phase shift by 2π does not change the behavior of map (2.86) and hence the phase space structure is periodic in $j = \omega/\omega_c$ with period unity

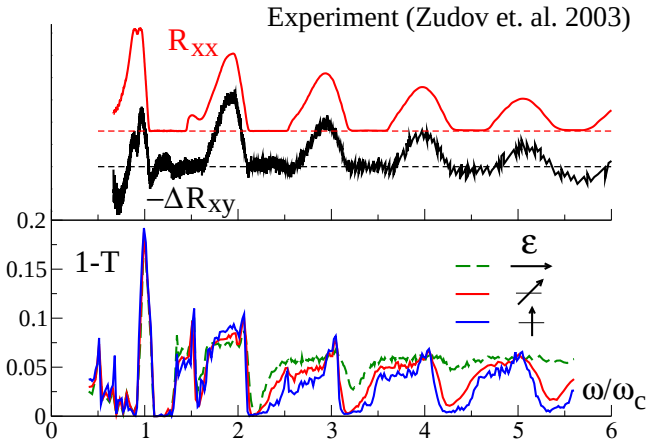

FIG. 2.34 – Top panel : dependence of R_{xx} and $-\Delta R_{xy}$ (in arbitrary units) on ω/ω_c from [63]. ΔR_{xy} is obtained from measured Hall resistance by subtracting a linear fit to R_{xy}. Bottom panel : calculated transmission along sample edge for three microwave polarizations. Microwave field is $\epsilon = 0.05$, relaxation $\gamma_0 = 10^{-3}$ and noise amplitude $\alpha = 3 \times 10^{-3}$. Transmission without microwaves is $T \simeq 0.95$.

which naturally yields high harmonics. The resonance is centered at $v_y = \pi(1 - m\omega_c/\omega)$ where m is the integer part of ω/ω_c. The chaos parameter of the map is $K = 4\epsilon\omega/\omega_c$ and the resonance separatrix width $\delta v_y = 4\sqrt{\epsilon\omega_c/\omega}$. The energy barrier of the resonance is given by $E_r = (\delta v_y)^2/2 = 8\epsilon\omega_c/\omega$.

In presence of weak dissipation the center of resonance acts as an attractor for trajectories inside the resonance. The presence of small angle scattering leads to a broadening of the attractor but trajectories are still trapped inside. If the center is located near $v_y = 0$ particles are easily kicked out from the edge, transmission T drops and R_{xx} increases. On the other hand, if the resonance width δv_y does not touch $v_y = 0$ then orbits trapped inside propagate ballistically with $T \to 1$ and $R_{xx} \to 0$. The trapping is confirmed in Figs. 1d,e for both models at $\omega/\omega_c = 9/4$ with propagating trajectories concentrated inside the resonance, whereas for $\omega/\omega_c = 2$ in Fig. 2.32f the region inside the resonance does not propagate (propagating orbits concentrate on the unstable separatrix and their number is much smaller).

In order to compare our theory with experiment we calculate the transmission T for model (2.85). An ensemble of $N = 5000$ particles are thrown on the wall at $x = 0$ with random velocity angle. They propagate in positive x direction but due to noise some trajectories detach from the wall, we consider that a particle is lost in the bulk when it does not collide with the wall for time $20\pi/\omega_c$. These particles do not contribute to transmission which is defined as the fraction of particles that reaches $x = 250v_F/\omega$, that can be viewed as a distance between contacts. For $l_e \gg r_c$ the billiard model of a Hall bar [73, 75] gives $R_{xx} \propto 1 - T$ and a deviation from the classical Hall conductance $\Delta R_{xy} = R_{xy} - B/ne \propto -(1 - T)$. The data in Fig. 2.34 show calculated $1 - T$ and experimental R_{xx} and ΔR_{xy} [63]. One can see a good agreement between results of model (2.85) and

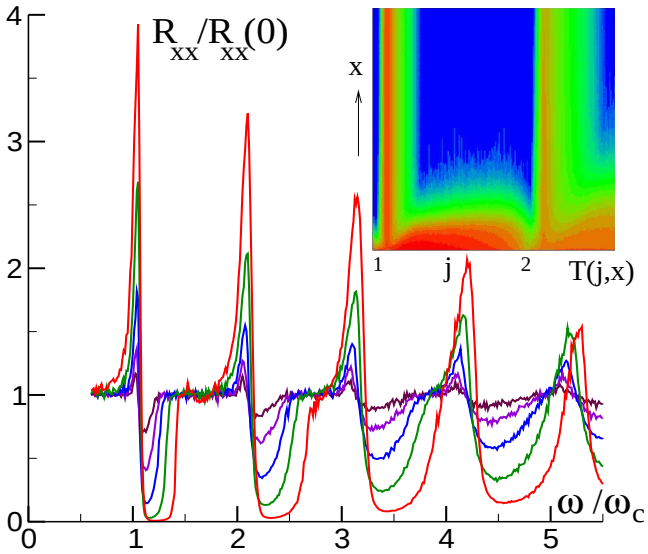

FIG. 2.35 – Dependence of rescaled R_{xx} in model (2.86) on ω/ω_c for microwave field $\epsilon = 0.00375, 0.0075, 0.015, 0.03, 0.06$ (curves from top to bottom at $j = \omega/\omega_c = 4.5$). Here $\gamma_c = 0.01$, $\alpha = 0.03$. Average is done over 10^4 particles and 5000 map iterations. Insert shows transmission probability $T(j, x)$ at distance x along the edge for $\epsilon = 0.02$ (red/gray is for maximum, blue/black for zero, $0 < x < 10^3 v_F/\omega$).

experimental data. Both show R_{xx} peaks at integer j and zeros around $j = 5/4, 9/4, ...$ We also reproduce peaks and dips for "fractional" ZRS around $j = 3/2, 1/2$ [80]. Our specular wall potential is specially suited for the cleaved samples from [63] where edges should follow crystallographic directions but peak positions can be shifted for other edge potentials. We also note that the possibility to observe ZRS on ΔR_{xy} was discussed in [81]. Finally our data show weak polarization dependence which supports the Chirikov standard map model (2.86).

This approximation is more accessible to analytical analysis and numerical simulations. In this model a particle is considered lost in the bulk as soon as $v_y < 0$. The displacement along the edge between collisions is $\delta x = 2v_y\omega/\omega_c$ and an effective "diffusion" along the edge is defined as $D_x(\epsilon) = (\Delta x)^2/\Delta t$ where Δx is a total displacement along the edge during the computation time $\Delta t \sim 10^4/\omega$. In numerical simulations D_x is averaged over 10^4 particles homogeneously distributed in phase space. We then assume that $R_{xx} \propto 1/D_x$ and present the dependence of the dimensionless ratio $R_{xx}/R_{xx}(\epsilon = 0)$ on ω/ω_c in Fig. 3. The computation of transmission T (shown in Fig. 3 inset) gives similar results but is less convenient for numerical analysis. The dependence on $j = \omega/\omega_c$ is similar to those shown in Fig. 2.34. Both peaks and dips grow with the increase of microwave field ϵ.

The dependence on ϵ can be understood from the following arguments. Due to noise a typical spread square width in velocity angle during the relaxation time $1/\gamma_c$ is $D_s = \alpha^2/\gamma_c$. The resonance square width is $(\delta v_y)^2 = 16\epsilon\omega_c/\omega$ and therefore the probability to escape

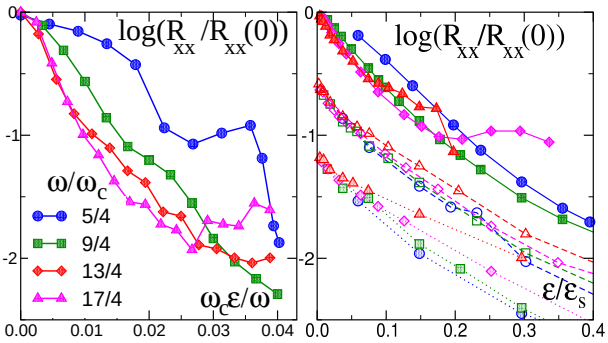

FIG. 2.36 – Dependence of rescaled R_{xx} on rescaled microwave field ϵ for models (2.85) (left) and (2.86) (right). Left : parameters as in Fig. 2.34 and ϵ is varied. Right : $\gamma = 0.01$, $\alpha = 0.02$ (full curves), $\gamma = 0.01$, $\epsilon = 0.03$ (dashed curves), $\epsilon = 0.03$, $\alpha = 0.02$ (dotted curves) ; symbols are shifted for clarity and $\epsilon_s = \omega D_s/\omega_c$.

from the resonance is

$$W \sim \exp(-(\delta v_y)^2/D_s) \sim \exp(-A\epsilon\omega_c/(D_s\omega)) \tag{2.87}$$

Edge transport is ballistic for exponentially small W and $R_{xx}/R_{xx}(0) \sim 1 - T \sim W$. The above estimate gives the numerical coefficient $A = 16$ while numerical data presented in Fig. 2.36 for model (2.86) give $A \approx 12$, and confirm dependence Eq. (2.87) on all model parameters. It holds when edge transport is stabilized by the presence of the nonlinear resonance which corresponds to regions around $j = 5/4, 9/4, ...$ Deviations appear when the parameter $K = 4\epsilon\omega/\omega_c$ approaches the chaos border $K \approx 1$ and trapping is weakened by chaos. The numerical data for model (2.85) based on transmission calculation also confirm the scaling dependence $\log R_{xx}/R_{xx}(0) \propto -\omega_c\epsilon/\omega$ as shown in Fig. 4. This dependence is consistent with the power dependence measured in [62]. A detailed analysis of the power dependence may be complicated due to heating and out of equilibrium effects at strong power, but the global exponential decay of R_{xx} with power was confirmed in [81].

The billiard model used in our studies focuses on dynamics of an electron on the Fermi surface which corresponds to a zero temperature limit. In order to include the effect of temperature one needs to account for the thermal smearing of the electrons around the Fermi surface. The relaxation rate to the Fermi surface that we introduced in our model is also likely to depend on temperature. This makes rigorous analysis of temperature dependence challenging. A simple estimate can be obtained in the frame of Arrhenius law with activation energy equal to the energy height of the nonlinear resonance $E_r = 16\epsilon\omega_c E_F/\omega$ where E_F is the Fermi energy. This dependence appears as an additional damping factor in ZRS amplitude in a way similar to temperature dependence of Shubnikov-de Hass oscillations leading to

$$R_{xx} \propto \exp(-A\epsilon\omega_c/(D_s\omega)) \exp(-16\epsilon\omega_c E_F/\omega T) \tag{2.88}$$

Our prediction on activation energy E_r is in a good agreement with experimental data and reproduces the proportionality dependence on magnetic field observed in [62, 63].

For a typical $\epsilon = 0.01$ we obtain $E_r \sim 20$ K at $j = 1$. The proposed mechanism can find applications for microwave induced stabilization of ballistic transport in magnetically confined quantum wires [82].

In summary we have shown that microwave radiation can stabilize edge trajectories against small angle disorder scattering. For propagating edge channels a microwave field creates a nonlinear resonance well described by the Chirikov standard map. Dissipative processes lead to trapping of particle inside the resonance. Depending on the position of the resonance center in respect to the edge the channeling of particles can be enhanced or weakened providing a physical explanation of ZRS dependence on the ratio between microwave and cyclotron frequencies. In the trapping case transmission along the edges is exponentially close to unity, naturally leading to an exponential drop in R_{xx} with microwave power. Our theory also explains the appearance of large energy scale in temperature dependence of ZRS. A complete theory should also take into account quantum effects since about ten Landau levels are typically captured inside the resonance. A microscopic treatment of dissipation mechanism is also needed for further theory development.

2.15 Screening in 2DEG

In the context of our theory for ZRS the microwave field must be present only in a small region around the sample edges with thickness approximately equal to a Larmor radius hence it was reasonable to neglect screening in a first approximation. However for bulk theories the microwave field must penetrate inside the 2DEG bulk and screening becomes important. In this Chapter we review some results on screening of an external electric field by 2DEG. In general screening effects are important in 2DEG in spite of its two dimensional nature which makes screening less efficient than in three dimensional metals. Here we develop a systematic description founded on an effective continuum media approximation, which describes the penetration of a microwave field in a sample. This approximation is of course valid only for length-scales larger than microscopic parameters such as Fermi and Thomas-Fermi wavelengths.

In order to describe the penetration of an external field E_{ext} with wavelength much larger than the sample size we consider the special case of a 2DEG stripe, that is infinite in y direction. In the x direction the stripe is the region $-b < x < b,\ (z = 0)$. Let $\lambda(x)$ the line-charge density in the stripe. The electric field then reads :

$$E(x) = E_{ext} + \frac{1}{2\pi\epsilon} \int \frac{\lambda(x')}{x - x'} dx' \tag{2.89}$$

Note that for $-b < x < b$ the integral is singular, a well defined equation is obtained if the integral is taken in term of Cauchy its principal values.

We introduce $Q(x) = \int_{-b}^{x} \lambda(x)$ the charge on the left of x, which allows us to write the

continuity equation :

$$i\omega Q(x) = -\sigma(\omega)E(x) \tag{2.90}$$

$$i\omega Q(x) = -\sigma(\omega)\left(E_{ext} + \frac{1}{2\pi\epsilon}\int \frac{1}{x-x'}dx'\frac{dQ}{dx'}\right) \tag{2.91}$$

where $\sigma(\omega)$ is the 2DEG conductivity, which in absence of magnetic field read in a Drude approximation

$$\sigma(\omega) = \frac{q^2 n\tau}{m(1+i\omega\tau)} \tag{2.92}$$

The integro-differential equation Eq. 2.91 also requires a boundary condition at stripe edges, which we take as $Q(-b) = Q(b) = 0$. This amounts to assume that $\lambda(x)$ has at most an integrable singularity at the sample edges.

In the static limit the field E_{ext} is completely screened inside the sample, an integral equation on λ follows directly from Eq. 2.89

$$\frac{1}{2\pi}\int_{-b}^{b}\frac{\lambda(x')}{x-x'}dx' = -\epsilon E_{ext} \tag{2.93}$$

by rescaling λ and x this equation can be cast in the dimensionless form :

$$\frac{1}{2\pi}\int_{-1}^{1}\frac{\lambda(x')}{x-x'}dx' = 1 \tag{2.94}$$

Equations of this type are well-known in integral equation theory [83]. In particular Eq. (2.94) has the analytic solution

$$\frac{1}{2\pi}\int_{-1}^{1}\frac{dx'}{x-x'}\left(\sqrt{\frac{1-x'}{1+x'}} - \sqrt{\frac{1+x'}{1-x'}}\right) = 1 \tag{2.95}$$

Actually the solution of Eq. (2.94) is not unique and we have chosen the solution with gives an antisymmetric charge distribution $\lambda(x) = -\lambda(-x)$, alternatively it is the only solution with only integrable singularities. This leads to the charge distribution $\lambda(x)$ on the stripe in the static limit :

$$\lambda(x) = \epsilon E_{ext}\left(\sqrt{\frac{b+x}{b-x}} - \sqrt{\frac{b-x}{b+x}}\right) \tag{2.96}$$

From the charge distribution we can calculate quantities such as induced dipolar momentum (per length unit of the stripe)

$$P(x) = \int_{-b}^{b} x\lambda(x)dx = \epsilon E_{ext}\pi b^2 \tag{2.97}$$

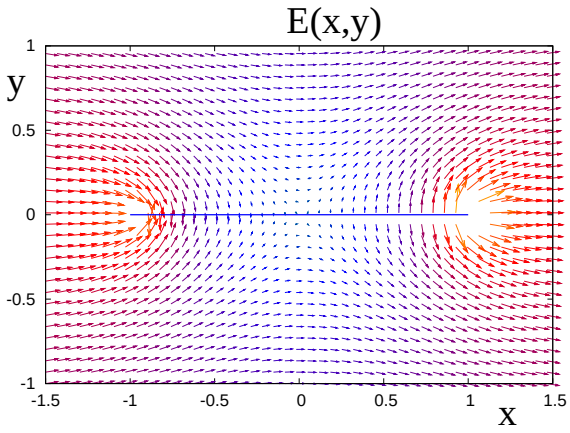

FIG. 2.37 – Distribution of the electric field $\mathbf{E}(x, y)$ in the static limit where the field is completely screened inside the 2DEG stripe. The charge distribution on the stripe (thick blue line) is given by Eq. (2.96).

The induced electric field distribution is shown on Fig. 2.96, far from the sample the field coincides with the external field but close to the sample the field lines are strongly distorted and perpendicular to the stripe surface.

At higher frequencies the electric field starts to penetrate inside 2DEG, for utra-high mobility 2DEG samples $\tau_i \simeq 1$ nanosec. and for frequencies $\omega/(2\pi) > 1$ GHz one can neglect the real part of the Drude conductance $\sigma \simeq \frac{q^2 n}{im\omega}$ and Eq. (2.91) reduces to :

$$Q(x) - \frac{q^2 n}{m\omega^2}\left(E_{ext} + \frac{1}{2\pi\epsilon}\int_{-b}^{b}\frac{1}{x-x'}\frac{dQ}{dx'}dx'\right) = 0 \tag{2.98}$$

The substitutions $x \to b\tilde{x}$, $Q(x) \to 2\pi\epsilon b E_{ext}\tilde{Q}(x)$ brings this equation to a dimensionless form :

$$Q(x) - \lambda\left(1 + \int_{-1}^{1}\frac{1}{x-x'}\frac{dQ}{dx'}dx'\right) = 0\ ,\ \lambda = \frac{q^2 n}{2\pi\epsilon m\omega^2 b} \tag{2.99}$$

(in the above equation we have omitted the tildes on the dimensionless variables). There is no known analytic solution for this integro-differential equation, and we have found the solutions numerically using a method developed in detail in [84]. The field distribution inside the stripe is shown on Fig. 2.38 in the limit of large $\lambda \gg 1$ we recover the static limit where the field is almost completely screened inside the sample. Fog $\lambda \ll 1$ the electric field penetrates inside the sample and oscillates around the value of the external electric field. The electric field around the stripe for $\lambda = 0.02$ is represented on Fig. 2.39 where oscillations of the electric field are clearly visible.

The wavelength of the oscillations and the mean electric field inside the sample can be estimated by looking for an approximate solution in the form :

$$Q(x) = A + B\cos kx \tag{2.100}$$

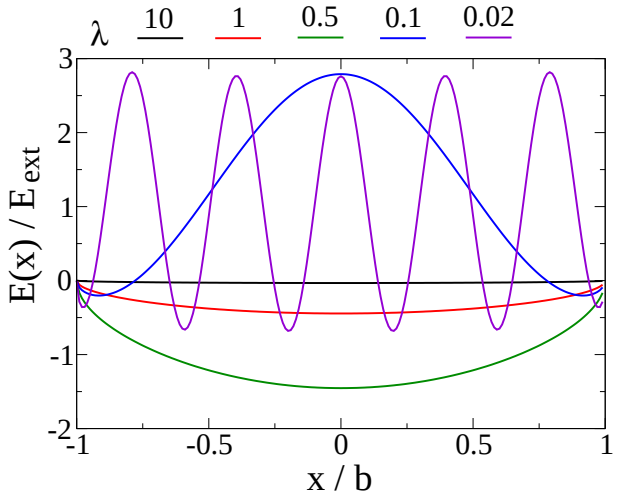

FIG. 2.38 – Electric field inside the 2DEG stripe for different values of $\lambda = \frac{q^2 n}{2\pi\epsilon m\omega^2 b}$.

where k is the (so far unknown) wave number and A and B are amplitudes to be determined. Physically A is the amplitude is proportional the mean electric field inside the stripe whereas B gives the amplitude of the oscillating component.

The oscillating term gives rise to an integral of the form

$$-\lambda \int_{-1}^{1} \frac{1}{x-x'} \frac{dQ}{dx'} dx' = \lambda k B \int_{-1}^{1} \frac{\sin(kx')}{x-x'} dx' \tag{2.101}$$

The asymptotic value of the integral can be derived in the limit $k \gg 1$,

$$\int_{-1}^{1} \frac{\sin(kx')}{x-x'} dx' = \sin kx \left[-\int_{(1+x)k}^{\infty} \frac{\cos y}{y} dy + \int_{(1-x)k}^{\infty} \frac{\cos y}{y} dy \right] - \cos kx \int_{(-1+x)k}^{(1+x)k} \frac{\sin y}{y} dy \tag{2.102}$$

$$\simeq -\pi \cos kx + \frac{2\cos k}{k} \frac{1}{1-x^2} + \ldots \,, \; k \gg 1 \tag{2.103}$$

this equations holds for x far enough from the sample borders. The above result implies that the oscillating component in Eq. (2.99) for a trial solution of the form Eq. (2.100) vanishes only if

$$k = \frac{1}{\pi\lambda} \tag{2.104}$$

Restoring dimensions this leads the following expression for the plasmon wavenumber in agreement with the results from the literature [85, 86].

$$k_P = \frac{2\epsilon m b}{q^2 n} \omega^2 \tag{2.105}$$

The above calculation can be extended to determine the amplitude of the mean electric field inside the stripe :

$$\lambda\left(1+\int_{-1}^{1}\frac{1}{x-x'}\frac{dQ}{dx'}dx'\right)=A+B\cos(\frac{x}{\pi\lambda})-\lambda\left(1+Bk[\pi\cos kx-\frac{2\cos k}{k}\frac{1}{1-x^2}]\right)$$
$$-\lambda(A+B\cos k)\int_{-1}^{1}\frac{dx'}{x-x'}\left(\delta(x'+1)-\delta(x'-1)\right)+O(k^{-2}) \tag{2.106}$$
$$=A-\lambda-\lambda\frac{2A}{1-x^2}+O(k^{-2}) \tag{2.107}$$

In this calculation we have used the function form Eq. (2.100) for $Q(x)$ and the asymptotic expansion Eq. (2.103). The important step here is to account for the discontinuities of $Q(x)$ at $x=\pm1$ which originate from the incompatibility between the boundary conditions $Q(-1)=Q(1)=0$ and the approximate form Eq. (2.100). Physically the δ functions represent the contribution of the charges accumulated at the edge of the sample. By requiring that the field vanishes in the middle of the sample we derive the leading order correction to the mean field inside the sample

$$\frac{<E(x)>}{E_{ext}}=1+2\lambda+O(\lambda^2)\simeq1+\frac{q^2n\omega^2}{\pi\epsilon mb} \tag{2.108}$$

This derivation of the plasmon correction to the mean field is possible because the amplitude of plasmon oscillations cancels in Eq. (2.107) due to a compensation between the field created by the oscillating charge density inside the stripe and the charges accumulated on the sample edge. As a counterpart the analytical estimation of the oscillation amplitudes proved difficult.

The situation is somewhat simpler when $\cos^2 k\simeq1$ and in this case it was possible to derive an approximation for the oscillating component of the electric field and for the whole field distribution inside the stripe. This approximation reads

$$Q(x)\simeq-\frac{3}{2\cos k}(\cos kx-\cos k)-\frac{k}{2\cos k}g(x)\quad[\text{ for }\cos^2k\simeq1,k\gg1\text{ }] \tag{2.109}$$
$$g(x)=\frac{\cos k-\cos kx}{k}-\frac{1}{\pi k}\int_{-1}^{1}dy\sqrt{\frac{1-x^2}{1-y^2}}\frac{\sin ky}{x-y} \tag{2.110}$$

where we have defined the axillary function $g(x)$ which does not contain any oscillating component. The case $\cos^2 k\simeq1$ is easier because in this case the second term in the asymptotic expansion Eq. (2.103) is maximal and a good approximation can be obtained by attempting to compensate for this term. The opposite limit $\cos k\to0$ is in this respect more complicated since on the level of approximation used in Eq. (2.103) $Q(x)=\cos kx$ appears as an eigenfunction of the integral equation kernel introducing artificial divergences.

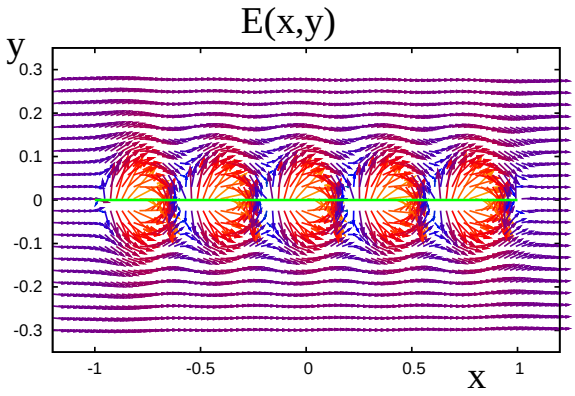

FIG. 2.39 – Distribution of the electric field $\mathbf{E}(x, y)$ in the high frequency limit $\lambda = 0.02$ where the field penetrates inside the 2DEG stripe. The stripe is represented by the thick green line.

Numerical simulations suggest that the problem is still well defined for $\cos k \simeq 0$, hence a proper treatment of the equation at the stripe edges should yield the correct solution.

To summarize the screening in 2DEG rises non-trivial problems of two dimensional electrostatics. In the regime where the plasmon wavelength $\lambda_P = \frac{\pi q^2 n \omega^2}{\epsilon m b}$ is smaller than the stripe width, a high frequency electric field starts to penetrate in 2DEG in the form of plasmon waves. In ZRS the experiments the plasmon wavelength $\lambda_P \simeq 100$ μm is smaller than the sample size (few millimeters) but larger than the cyclotron radius which is around 1 μm. Hence plasmons should create a slow modulation of the microwave field amplitude inside the sample bulk but the model developed in the previous section still applies since it only depends on the eclectic field at the sample edge. It is worth to mention that in general bulk ZRS theories do not take plasmon oscillations into account and assume an uniform electric field in the sample. I will conclude this chapter by noting that a similar integral equation describes the distribution of the Hall field in a 2DEG stripe in the integer quantum Hall effect [87]. In this case also no exact analytical solution is known and the asymptotic analysis of the solution properties is difficult.

Bibliographie

[1] R. A. Webb, S. Washburn, C. P. Umbach, and R. B. Laibowitz, Phys. Rev. Lett. **54** 2696 (1985)

[2] J.B. Pieper and J.C Price, Phys. Rev. Lett. **72**, 3586 (1993)

[3] J. Gabelli, G. Fève, J.-M. Berroir, B. Plaçais, A. Cavanna, B. Etienne, Y. Jin, D. C. Glattli, Science **313** 499 (2006)

[4] R.P. Feynman, R.B. Leighton, M. Sands, *The Feynman lectures on physics* (Addison Wesley, Reading MA, 1963)

[5] R.D. Astumian, P. Hänggi, Physics Today **55**, 33 (2002)

[6] R. Reimann, Phys. Rep. **361**, 57 (2002)

[7] H. Linke, T.E. Humphrey, A. Löfgren, A.O. Sushkov, R. Newbury, R.P. Taylor, P. Omling, Science **286**, 2314 (1999)

[8] B.L. Altshuler, A.G. Aronov and D.E. Khmel'nistskii, Solid State Commun. **39**, 619 (1981)

[9] D. Sánchez and M. Büttiker, Phys. Rev. Lett. **93**, 106802 (2004)

[10] B. Spivak and A. Zyuzin, Phys. Rev. Lett. **93** 226801 (2004)

[11] M.L. Polianski and M. Büttiker, Phys. Rev. Lett. **96** 156804 (2006)

[12] L. Angers, E. Zakka-Bajjani, R. Deblock, S. Gueron, A. Cavanna, U.Gennser, H.Bouchiat, Phys. Rev. B **75**, 115309 (2007).

[13] E. Akkermans and G. Monatambaux *Mesoscopic Physics of Electrons and Photons*, Cambdrige University Press, 2007

[14] A. Pikovsky, M. Rosenblum and J. Kurths, *Synchronization : a universal concept in nonlinear sciences*, Cambridge University Press, Cambridge (2001).

[15] J.E. Mayer and M. Goeppert-Mayer, *Statistical mechanics*, John Wiley & Sons, N.Y. (1977)

[16] L.I. Magarill, and A.V. Chaplik, JETP Lett. **70**, 615 (1999) [Pis'ma Zh. Eksp. Teor. Fiz. **70**, 607 (1999)].

[17] L. Landau and E. Lifshitz, *Electrodynamics of continuous media* (Pergamon Press, New York, 1960)

[18] R. Hertel, J. Magn. Magn. Mater. **303**, L1 (2006)

[19] V. M. Edelstein, Phys. Rev. Lett. **95**, 156602 (2005)

[20] M. L. Polianski, Phys. Rev. B **80**, 241301(R) (2009)

[21] V.E. Kravtsov, *Nonlinear Quantum Coherence Effects in Driven Mesoscopic Systems*, Proceedings of LXXXI Les Houches School on "Nanoscopic quantum transport", Les Houches, France, June 28-July 30, 2004 (arXiv :cond-mat/0504671).

[22] A. D. Chepelianskii and D. L. Shepelyansky, Eur. Phys. J. B **55**, p.261 (2007)

[23] L. Onsager, Phys. Rev. **38**, 2265 (1931).

[24] H.B.G. Casimir, Rev. Mod. Phys. **17**, 343 (1945)

[25] M. Büttiker, Phys. Rev. Lett. **57**, 1761 (1986)

[26] A.D. Benoit, S. Washburn, C.P. Umbach, R.B. Laibowitz and R. A. Webb , Phys. Rev. Lett. **57**, 1765 (1986)

[27] M.L. Polianski and M. Büttiker, Phys. Rev. B **76**, 205308 (2007)

[28] J. Wei, M. Shimogawa, Z. Wang *et al.* Phys. Rev. Lett. **95**, 256601 (2005)

[29] R. Leturcq, D. Sánchez, G. Götz *et al.* Phys. Rev. Lett. **96**, 126801 (2006).

[30] D. M. Zumbühl, C. M. Marcus, M. P. Hanson *et al.* Phys. Rev. Lett. **96**,206802 (2006).

[31] L. Angers, E. Zakka-Bajjani, R. Deblock S. Gueron, A. Cavanna *et al.* Phys. Rev. B **75**, 115309 (2007)

[32] L. Angers, A. Chepelianski, R. Deblock, B. Reulet and H. Bouchiat Phys. Rev. B **76**, 075331 (2007)

[33] H. Förster and M. Büttiker, Phys. Rev. Lett. **101**, 136805 (2008)

[34] R.D. Astumian, Phys. Rev. Lett **101**, 046802 (2008)

[35] D. Sánchez and K. Kang, Phys. Rev. Lett. **100**, 036806 (2008)

[36] V.E. Kravtsov, Pramana **58** 0304 (2002)

[37] C.W.J. Beenakker and H. van Houten, Phys. Rev. Lett. **63**, 1857 (1989)

[38] B.L. Altshuler and D.E. Khmel'nitskii JETP Lett. **42**, 359 (1985). A.I. Larkin and D.E. Khmel'nitskii JETP**64**, 1075 (1986).

[39] V. Fal'ko and D. Khmel'niskii, Zh. Eksp. Teor. Fiz. **95,** 328–337 (1989). [Sov. Phys. JETP **68**(1), 186 (1989)].

[40] R. A. Webb, S. Washburn, and C. P. Umbach, Phys. Rev. B **37** 8455 (1988), P. G. N. de Vegvar, G. Timp, P. M. Mankiewich *et al.* Phys. Rev. B **38**, 4326 (1988)

[41] A. Bykov, G. Gusev, and Z. Kvon, Pis'ma Eksp. Teor. Fiz. **49,** 13 (1989) [JETP Lett. **49**(1), 13 (1989)].

[42] S. Washburn and R. A. Webb, Adv. Phys. **35**, 375 (1986)

[43] D. Sanchez and M. Büttiker, Phys. Rev. Lett **93**, 106802 (2004)

[44] R. Bartolo, N. Giordano, X. Huang, and G. Bernstein, Phys. Rev. B **55,** 2384 (1997)

[45] DiCarlo, C.M.Marcus, and J.S.Harris, Phys. Rev. Lett.**91**, 246804 (2003).

[46] B.Spivak, F.Zhou and M.T.Beal Monod Phys. Rev. B **51,** 13226 (1995).

[47] M. Moskalets and M. Büttiker,Phys. Rev. B **69,**, 205316 (2004).

[48] S. Sassine, Yu. Krupko, J.-C. Portal, Z. D. Kvon, R. Murali, K. P. Martin, G. Hill and A. D. Wieck, Phys. Rev. B **78,** 045431 (2008)

[49] A. D. Chepelianskii1, M. V. Entin, L. I. Magarill and D. L. Shepelyansky, Euro. Phys. J. B **56,** 1434 (2007)

[50] J-Q. Zhang, S. Vitkalov, Z. D. Kvon, J. C. Portal, A. Wieck, Phys. Rev. Lett. **97**, 226807 (2006)

[51] K. v. Klitzing, G. Dorda and M. Pepper, Phys. Rev. Let. **45**, 494 (1980)

[52] D. Shoenberg, *Magnetic oscillations in metals*, Cambrdige University Press (1984) ISBN 052122480

[53] I.M. Lifshitz and A.M. Kosevich, Sov. Phys. JETP **2**, 636 (1956)

[54] A.A. Bykov, JETP Lett. **87**, 233 (2008)

[55] M.A. Zudov, R.R. Du, J.A. Simmons, and J.R. Reno, Phys. Rev. B **64**, 201311(R) (2001).

[56] R.G. Mani, J.H. Smet, K. von Klitzing, V. Narayanamurti, W.B. Johnson, and V. Umansky, Nature **420**, 646 (2002).

[57] M.A. Zudov, R.R. Du, L.N. Pfeiffer, and K.W. West, Phys. Rev. Lett. **90**, 046807 (2003).

[58] S. Datta, *Electronic transport in mesoscopic systems*, Cambridge Univ. Press, Cambridge, UK (1995).

[59] V. Umansky, M. Heiblum, Y. Levinson, J. Smet, J. Nübler and M. Dolev, Journal of Crystal Growth **311**, 1658 (2009)

[60] M.A. Zudov, I.V. Ponomarev, A.L. Efros, R.R. Du, J.A. Simmons and J.L Reno, PRL **86**, 3614 (2001)

[61] C.L. Yang, J. Zhang, R.R. Du, J.A. Simmons and J.L. Reno, PRL **89**, 076801 (2002)

[62] R.G. Mani, J.H. Smet, K. von Klitzing, V. Narayanamurti, W.B. Johnson, and V. Umansky, Nature **420**, 646 (2002).

[63] M.A. Zudov, R.R. Du, L.N. Pfeiffer, and K.W. West, Phys. Rev. Lett. **90**, 046807 (2003).

[64] V.I. Ryzhii, Sov. Phys. Solid State **11**, 2078 (1970).

[65] A.C. Durst, S. Sachdev, N. Read, and S.M. Girvin, Phys. Rev. Lett. **91**, 086803 (2003).

[66] M.G. Vavilov and I.L. Aleiner, Phys. Rev. B **69**, 035303 (2004).

[67] J. Iñarrea and G. Platero, Phys. Rev. Lett. **94**, 016806 (2005).

[68] I.A. Dmitriev, A.D. Mirlin, and D.G. Polyakov, Phys. Rev. Lett. **91**, 226802 (2003).

[69] I.A. Dmitriev, M.G. Vavilov, I.L. Aleiner, A.D. Mirlin, and D.G. Polyakov, Phys. Rev. B **71**, 115316 (2005).

[70] A.V. Andreev, I.L. Aleiner and A.J. Millis, Phys. Rev. Lett. **91**, 056803 (2003)

[71] B.I. Halperin, Phys. Rev. B **25**, 2185 (1982) ; M. Büttiker, Phys. Rev. B **38**, 9375 (1988).

[72] M.L. Roukes, A. Scherer, S.J. Allen, Jr., H.G. Craighead, R.M. Ruthen, E.D. Beebe and J.P. Harbison, Phys. Rev. Lett. **59**, 3011 (1987).

[73] C.W.J. Beenakker and H. van Houten, Phys. Rev. Lett. **63**, 1857 (1989).

[74] A.A. Bykov, A.K. Bakarov, D.R. Islamov and A.I. Toropov, JETP Lett. **84**, 391 (2006).

[75] A. Chepelianskii and H.Bouchiat, Phys. Rev. Lett. **102**, 086810 (2009).

[76] R. Merz, F. Keilmann, R.J. Haug and K. Ploog, Phys. Rev. Lett **70**, 651 (1993).

[77] I.V. Andreev, V.M. Murav'ev, I.V. Kukushkin, J.H. Smet, K. von Klitzing and V. Umanskii, JETP Lett. **88**, 616 (2008).

[78] T. Ando, A.B. Fowler and F. Stern, Rev. Mod. Phys. **54**, 437 (1982).

[79] B.V. Chirikov, Phys. Rep. **52**, 263 (1979).

[80] M.A. Zudov, R.R. Du, L.N. Pfeiffer and K.W. West, Phys. Rev. B **73**, 041303(R) (2006).

[81] R.G. Mani, V. Narayanamurti, K. von Klitzing, J.H. Smet, W.B. Johnson and V. Umansky Phys. Rev. B **69**, 161306(R) (2004) ; **ibid. 70**, 155310 (2004).

[82] A. Nogaret, J.-C. Portal, H.E. Beere, D.A. Ritchie and C. Phillips, J. Phys. Cond. Mat. **21**, 025303 (2009).

[83] H. Hochstadt, *Integral Equations*, A Wiley-Interscience publication ISBN 0-471-40165-X

[84] Waves avec Michael

[85] F. Stern, Phys. Rev. Lett. **18**, 546 (1967)

[86] E. Vasiliadou, G. Müller, D. Heitmann, D. Weiss, K.v. Klitzing, H. Nickel, W. Schlapp and R. Lösch , Phys. Rev. B. **48**, 17145 (1993)

[87] A. H. MacDoanld, T. M. Rice, W.F. Brinkman, Phys. Rev. B. **28**, 3648(R) (1983)

Chapitre 3

Mesoscopic transport in DNA molecules

3.1 Structure of DNA molecules and possibilities for electron transport

DNA is a double stranded molecule, with diameter 2 nanometer and length that can vary from a few nanometers to centimeters for mammal DNA. It is rather stiff compared to other polymers and polyelectrolytes with a persistence length of 50 nanometers. DNA has a double helix structure, each strand contains four possible bases : adenine (abbreviated A), cytosine (C), guanine (G) and thymine (T). The bases C-G and A-T are paired through hydrogen-bonds and appear on complementary strands of the double helix. The backbone of DNA is formed by sugar and negatively charged phosphate groups. The chemical structure of DNA is summarized on Fig. 3.1, which shows the phosphate-desoxyribose backbone of DNA, and the four possibles bases. In solution, these charged groups are surrounded by a cloud of positively charged counter-ions which screens part of the negative charge. As a result the effective charge of DNA in solution is still negative with average charge density $e/0.7$ nm instead of $e/0.34$ nm for the bare chemical charge. (0.7 nm is the Bjerrum length in water at room temperature).

The possibility of electronic transport through DNA molecules is motivated by the existence of an overlap between π orbitals between bases stacked along the DNA backbone. The stacking-distance between neighbor basepairs is around 0.34 nm [1], close to the distance between atomic planes in graphite. Hence the overlap between the molecular orbitals could create delocalized electronic states along the DNA chain. The theoretical modeling of electron delocalization along the helix is challenging due to the presence of a complicated environment, where sugar, phosphates, water and counterions play an important role. Most calculations however agree on the presence of a HOMO (highest occupied molecular orbital) - LUMO (lowest unoccupied molecular orbital) gap of a few eV (see Fig. 3.2). The overlap between HOMO/LUMO orbitals localized on neighboring basepairs gives an electronic coupling of the order of 0.1 eV. This value must be compared to the

ionization potential between adjacent basepairs which is for example 0.6 eV between guanine and thymine [2]. These values suggest that electronic states are mainly localized on a single basepair. However this picture can be strongly modified if the molecule is strongly doped/depleted due to interaction with the metallic contacts.

-

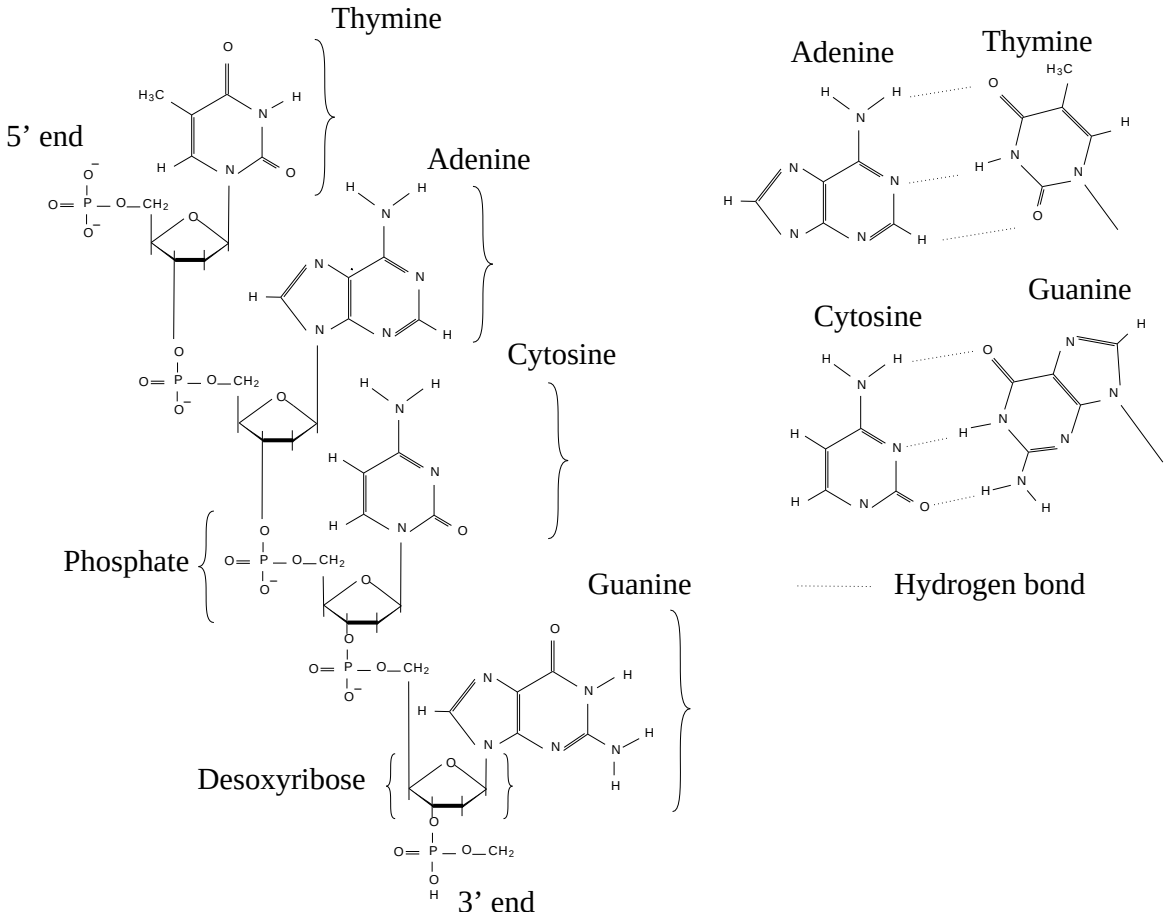

FIG. 3.1 – Chemical structure of DNA. Hydrogen bonds between basepairs A-T and G-C are shown as dotted lines.

Practical interest in conducting DNA molecules is related to their self-assembly properties which allow to create nanostructures of a specific shape with a 'bottom-up' approach [3]. It is now possible to manufacture both two dimensional [4] and three dimensional structures [5, 6] of well defined shape and chemical properties. It is also conjectured that conduction inside DNA may play a role in DNA repair mechanisms, whose efficiency is not well understood yet.

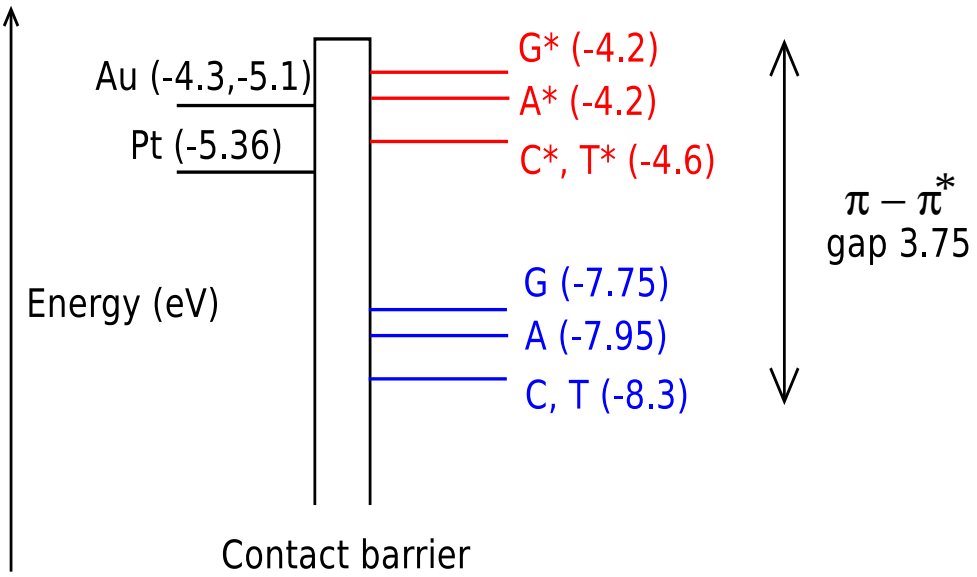

FIG. 3.2 – Work functions of platinum and gold, and ionization potential of the DNA bases, HOMO and LUMO orbitals are separated by a gap of approximately 3.75 eV.

3.2 Past experiments on DNA transport and outline of our experiments

Many experiments were designed to probe transport properties of DNA molecules leading to a controversial history that spans across the past decade. Conceptually an experiment to measure conduction of a DNA molecule is rather simple (see Fig. 3.3). Nevertheless many contradictory behaviors were reported primarily owing to the difficulty of controlling electrode fabrication and the interactions between the molecule and its environment on a substrate.

Here I will give a brief overview of the experiments in the field referring to [2] for a more thorough review (see also introduction in French). Probably the first experiment providing direct evidence of electron transport in DNA molecules was reported by Fink and Schönenberger [7] in 1999. Previous spectroscopy experiments also showed charge transfer on distances larger than 4 nm [8, 9], however DNA resistivity was not measured directly.

This experiment was followed by [10] where semiconducting behavior was observed on poly(G)-poly(C) DNA molecules inserted in a platinum nanogap with separation between electrodes around 8 nanometers. The gap reported in [10] was in the electron-Volt range. The best conduction properties were reported by A. Yu. Kasumov [11] where conduction was observed at cryogenic temperatures. The observation of the superconducting proximity effect suggested that electron transport could be coherent over distances larger than 100 nm.

Controversy emerged rapidly after the first experiments indicating transport in DNA molecules. The experiment [7] was heavily criticized in Ref. [13] where conduction was at-

tributed to the formation of a carbon contamination layer under electron beam irradiation. Absence of transport in DNA on the 100 nm scale was reported by several other groups, [14, 15, 16] for DNA on mica and silicon dioxide substrates. Conduction was probed with DC transport, using gold or platinum electrodes [14, 15] or with electric force microscopy [16].

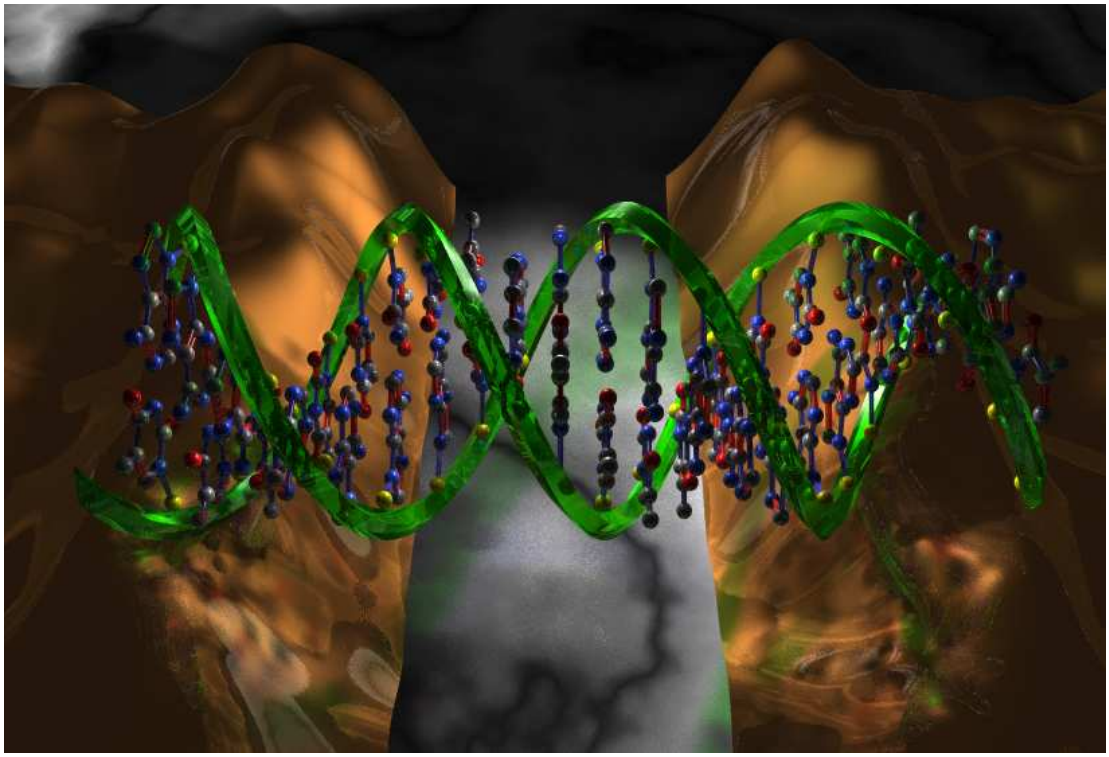

FIG. 3.3 – Schematic representation of an experiment for the measurement of DNA conduction. A small DNA molecule is connected to conducting electrodes separated by an insulating gap.

In view of these results, it appeared that the key ingredient for observation of long range transport in DNA molecules [11] resides in the control of molecule substrate interactions. In the experiment by A. Yu. Kasumov *et. al.* where conduction could be observed on a 100 nm scale an organic film (pentylamine) was deposited onto the substrate before the deposition of DNA and separated molecules from the insulator/electrode surface [11, 12]. The key role of the organic film was confirmed in electrostatic mode AFM charge delocalization experiments [17] but direct conduction measurements failed at detecting long range conduction [18].

Recently several experiments observed conduction of short fragments of DNA (with length of a few nanometers). By repeatedly forming DNA junctions in aqueous buffer solution [19] concluded that resistance was proportional to the molecule length for poly(G)-poly(C) whereas insertion of A-T bases led to an exponential decrease of conductance with a decay constant of 0.43 Å. Using a scanning tunnel microscope operating at cryogenic

temperatures [20] determined the excitation spectrum of Poly(C)-Poly(G) molecules which exhibited a clear gap further supporting the semiconductor model of DNA from Ref. [10]. At last both biological characterization and transport measurements were combined in Ref. [21] in an experiments where the conduction of a short DNA sequence (15 basepair or 4.5 nm) could be destroyed/restored by introducing/correcting mismatches in the DNA sequence. Notwithstanding these recent advances for short molecules, the ability of DNA to transport current on length scales of the order of 100 nm with rather low resistances around 100 kΩ per molecule is still debated.

In order to clarify the regime where DNA can transport charge on a relatively long length-scale we have tried to reproduce the experiment from Ref. [12]. The description of our experiments will be organized as follow :

- **Chap. 3.3** we describe the buffer solutions we use and deposition of λ-DNA onto mica
- **Chap. 3.4** we describe the deposition of λ DNA molecules on Pt electrodes, without the pentylamine organic film. In this experiment molecules are found to be insulating.
- **Chap. 3.5** we describe deposition of DNA molecules on a substrate with pentylamine. We argue that the presence of carbon atoms is necessary to stabilize the pentylamine layer and to bind DNA molecules.
- **Chap. 3.6** we explain how λ DNA molecules can be combed across electrodes functionalized with pentylamine. Unfortunately all samples where we deposited pentlyamine/molecules ourselves exhibited insulating behavior.
- **Chap. 3.7** gives a description of the fabrication of the insulating gaps with a focused ion beam. Starting from this chapter deposition of DNA molecules was done by D. Klinov who deposited molecules as in the samples from [11, 12]. Some of the structures became conducting after deposition of DNA molecules by D. Klinov.
- **Chap. 3.8** describes transport measurements on the samples where conduction was observed down to a low temperatures.
- **Chap. 3.9** gives an overview of our atomic force microscopy/electron microscopy data on the gaps. We attempt to establish a correlation between conduction and presence of DNA molecules across the slits.
- **Chap : 3.10** summarizes the content of the previous chapters (that are rather technical), and attempts to draw some conclusions on the possibility of long range transport in DNA molecules. An important point is that due to the presence of metallic residues in the gap, conduction of DNA molecules may be actually probed on much smaller scales than the average size of the gap (for e.g. 10 nm instead of an average of 100 nm). Hence in all cases arguments for long range transport in DNA molecules are scarce.
- **Chap. 3.11** and **Chap. 3.12**. These two chapters are independent from the others. Chap. 3.11 describes a contactless experiment to probe photo-transport in nanowires that we plan to extend to DNA molecules. Chap. 3.12 is a theoretical discussion on counterion condensation around large (hydrophobic) molecules.

As I mentioned in the beginning of this chapter transport in DNA molecules seems strongly dependent on the molecule environment. Unfortunately even if very clean bulk

materials can now be synthesized, the surface structure and chemistry remain poorly controlled. For these reasons technological details become very important, however the understanding of how a certain process (electron beam lithography or ion beam etching) modifies the surface state of the sample is very limited. As a consequence, I will often just try to give a coherent interpretation to our empirical observations. Indeed if we had to prove the origin of all our empirical observation with the rigor required to experimentally prove a hypothesis, it would take us far from the goal of obtaining conducting DNA structures and take a prohibiting time.

3.3 Deposition of DNA on a mica substrate

In order to reproducibly deposit DNA molecules on metallic electrodes, a microscopy technique is needed to observe the molecules on the substrate. Two main microscopy techniques have sufficient resolution to properly image DNA molecules. Transmission electron microscopy (TEM) is the oldest technique which allows to study DNA molecules and still offers the best spacial resolution and chemical sensitivity. However it has the disadvantage that molecules have to be deposited on thin suspended carbon films on a TEM grid. A special surface treatment is required in order to capture DNA molecules on hydrophobic carbon films, and often molecules have to be "stained" with heavy metal salts (uranyl acetate) to improve contrast [22]. Recently atomic force microscopy emerged as an alternative technique for visualization of single DNA molecules [23], in liquid and in air. For this purpose DNA molecules must first be absorbed on a flat surface, which is usually mica because it can be easily cleaved in order to provide an atomically flat surface. In the past few years AFM resolution achieved incredible improvements. For example recently it was shown that it is possible to determine the chemical structure of organic molecules absorbed on a surface using an atomic force microscope in a mode where individual atoms can be resolved [24].

Mica and DNA are both negatively charged in a water solution and therefore there is no adsorption of DNA onto Mica when only monovalent salt is present in solution at neutral pH [25]. Binding sites can be created by adding a poly-valent salt such as $MgCl_2$. Table 3.1 gives the chemical composition of a a typical solution we used for deposition of lambda DNA molecules onto a mica substrate. The choice of the ammonium acetate buffer is unusual, it is chosen mainly for consistency with buffers used in [11, 12]. Historically this choice is also motivated by the use of ammonium acetate in some standard protocols from electron microscopy on DNA molecules [26]. The solution of Table 3.1 contains only a very small amount of ethylenediaminetetraacetic acid (EDTA) from the native solution, hence it is not suitable for DNA storage. EDTA neutralizes metallic ions such as Ca^{2+} or Fe^{3+} which are always present in small quantity in solution, and act as catalysts for metal-dependent enzymes which can damage DNA. For this reason we never used solutions from Tab. 3.1 for longer than a single day.

In order to achieve a reproducible deposition of λ-DNA onto mica the following protocol was suggested to us by D. Klinov. In order to obtain stable humidity conditions during

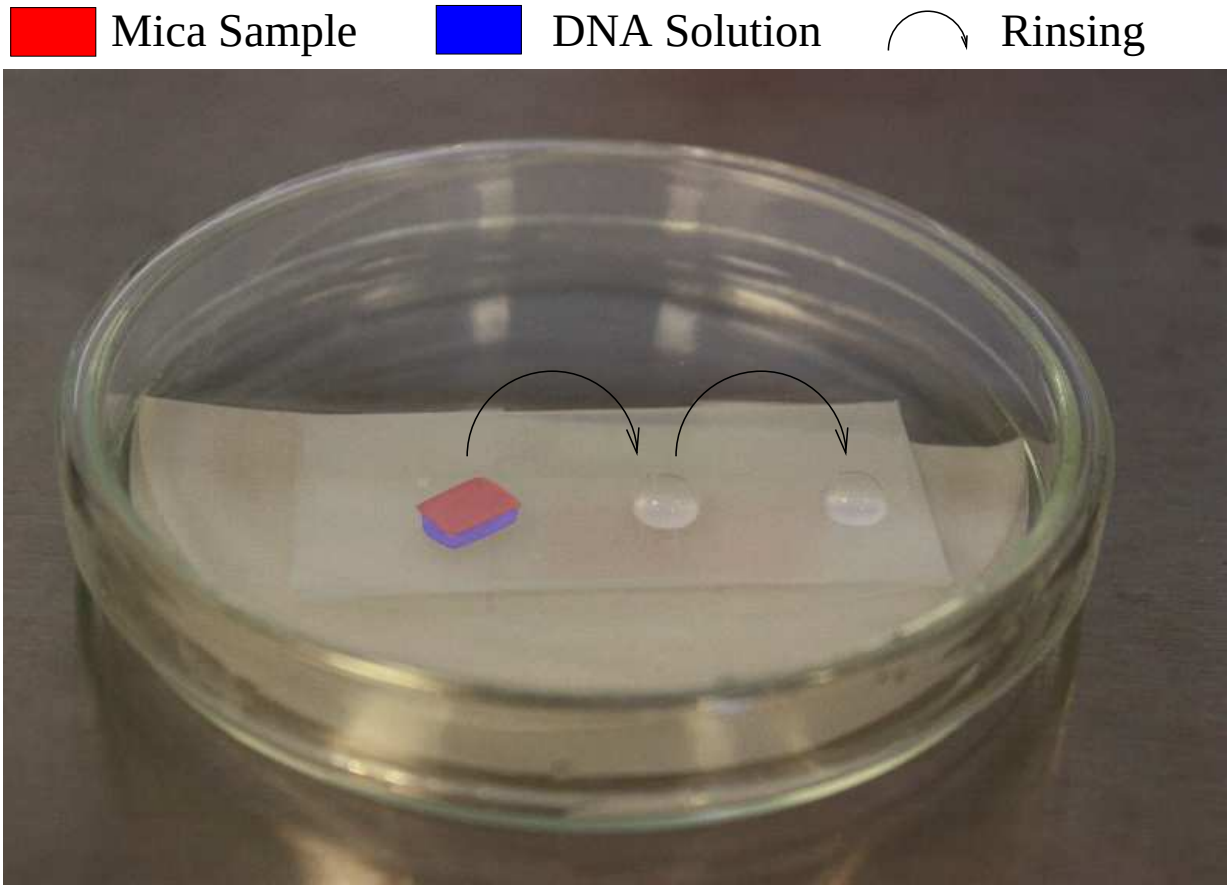

FIG. 3.4 – Setup for deposition of λ-DNA molecules onto mica. Inside the closed petri box, three 100 μL droplets are deposited on top of a parafilm film : one drop of λ-DNA, and two drops of purified water. The sample is deposited on top of the λ-DNA drop and is subsequently moved onto the water droplets for rinsing. During deposition the petri box is closed to ensure stable humidity conditions.

DNA deposition, the sample and DNA solution are kept in a closed petri box with wet filter paper at the bottom (see Fig. 3.4). A drop of DNA solution (volume $\simeq$ 100 μL) is deposited onto the clean side of a para-film sheet folded around a glass slide. The freshly cleaved mica sample is then deposited on top of the drop (clean side facing down). This reduces the area of the water-air interface during deposition and reduces the contamination of the drop. After 10 minutes, many λ-DNA molecules are attached to the mica surface at several anchoring points and the sample can be moved onto of a purified watter droplet where salt residues are left to dissolve for around 10 minutes. This rinsing process is repeated two times.

The above protocol allows to achieve reproducible DNA deposition due to several advantages. DNA molecules have the time to adsorb on the surface before they undergo the force of the meniscus during the drying of the sample, hence they are attached in

Ammonium acetate	$CH_3COO^- + NH_4^+$	15 mM
Magnesium chloride	$MgCl_2$	5 mL
λ-DNA	bought from Invitrogen Cat no. 25250-028	5 μg/ml
	Commercial DNA solution contains	
λ-DNA	48 502 base pairs	0.25-0.6 mg/ml
Tris-HCl	$(HOCH_2)_3CNH_2 + HCl$ (pH 7.4)	10 mM
Sodium chloride	NaCl	5 mM
EDTA		0.1 mM

Tab. 3.1 – Solution for deposition of DNA onto mica for AFM imaging

a state where they are not overstretched and keep their natural persistence length. Two AFM images from different samples are shown on Fig. 3.5, in both cases AFM shows long molecules undulating on a clean substrate with very little contamination. This deposition experiment allows us to check that our DNA solution has the right concentration and is not contaminated by undesired chemical substances.

The measured height of DNA is around 0.7 nm, which contrasts with measurements of DNA height on mica in liquid AFM cells where height around 2 nm can be observed [23]. Several explanations can be put forward to explain this discrepancy. It is possible that a water hydration layer forms near the DNA molecules reducing the apparent height of the molecules. Another hypothesis is that DNA may be strongly denaturated by the strong interaction with the surface when the sample is dry, which can create a transition from B-DNA to A-DNA. However we note that there is no significant difference in DNA diameter for A and B forms of DNA [27].

For overstretched molecules a transition to the Pauling's P-DNA form is possible and the molecule thickness may indeed be close to a nanometer since the phosphate backbones are tightly interwound and the bases are exposed to the exterior of the molecule [28]. After deposition of DNA we check that the molecules absorbed on the substrate have a persistence length close to their natural persistence length in solution. This ensures that we apply a very limited strain on the molecules and transition to P-DNA form seems unlikely in most of our experiments (see Fig. 3.5 for undulating molecules, examples of overstretched molecules are shown on Fig. 3.6).

3.4 DNA deposition onto metallic surfaces

For transport measurements DNA must be deposited on a metallic substrate. Many metals (for example Aluminum, Copper, ...) can form a thin insulating oxide layer on their surface in atmospheric conditions. While the oxide layer does not influence conduction properties in the bulk of the metallic film, it can prevent the formation of an electrical contact between DNA and the metallic electrodes. Hence the choice of material for electrode is limited to noble metals. For experiments on DNA mainly gold, platinum and rhenium

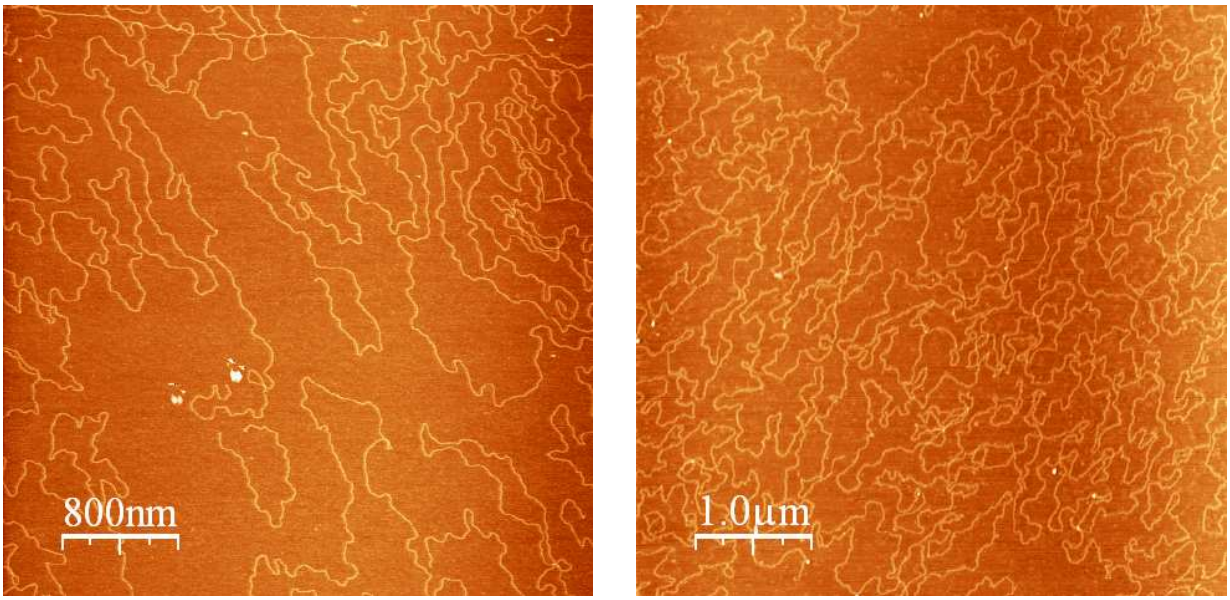

FIG. 3.5 – AFM image of λ-DNA molecules absorbed on a mica substrate using solution Tab. 3.1 and following deposition procedure explained in Fig. 3.4. Molecule height is around 0.7 nm.

have been used so far [2] although carbon based materials (carbon nanotubes, graphite) emerge as a promising material for contacting DNA electrically [21].

In our experiments we have used a thin Platinum metallic film of a few nanometers (typically between 3 and 5 nm) deposited by Argon DC-plasma sputtering on a freshly cleaved mica surface. Since platinum is deposited everywhere on the sample, no further chemical processing is needed and the obtained metallic surface is very clean and chemically inert. As a result there is in principle no binding sites to attach DNA molecules to the substrate, and we do not expect DNA adsorption. This is not completely true however since DNA molecules have active chemical end groups. For example it has been proposed that in certain pH ranges DNA ends can expose hydrophobic domains of the bases and bind to hydrophic surfaces [29]. Hence it is possible that DNA molecules bind to platinum through their extremities.

If the DNA solution is incubated a few minutes on the sample both ends of the molecule have in general enough time to attach to the substrate. Once the sample is dried the molecules are stretched by the water flow leading to a characteristic "U" shape of the molecules when the substrate is analyzed with an AFM (see Fig. 3.6.a). As molecules already present on the substrate create additional binding sites for the adhesion of other molecules in the solution, many ropes of DNA molecules can be observed on the Platinum substrate. Note that the formation of ropes is less likely if the sample is incubated for a shorter time (or rinsed under a continuous flow), in this case (see Fig. 3.6.b) AFM images show only a small number of stretched DNA molecules which are mainly attached through one of their extremities.

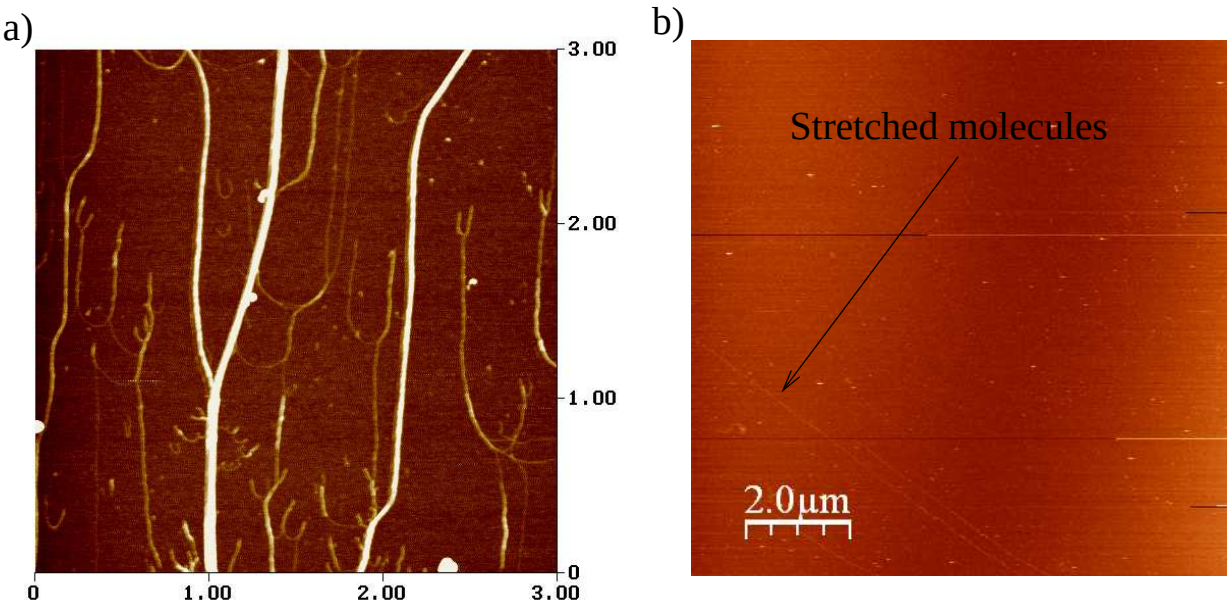

FIG. 3.6 – Deposition of DNA molecules on a Platinum substrate without treatment of the surface a) after an incubation time of a few minutes, combing was achieved with a water meniscus b) after rinsing under a flow before drying using the protocol described in Chap. 3.6.

In the above procedure the DNA molecules were deposited onto the platinum film directly after sputtering. Of course transport measurements can not be realized in this configuration. Transport measurements are possible only after electrodes have been patterned on the substrate. The simplest way to fabricate an insulating gap is to protect the regions where we do not want Pt deposition by a MMA/PMMA resist that can be patterned beforehand using usual electron-beam lithography techniques. After sputtering the resist is dissolved in hot acetone and a gap is formed. The presence of organic residues originating from imperfect removal of the PMMA film changes the adsorption properties of DNA molecules on the substrate. On this "contaminated" substrate it becomes possible to deposit molecules without over-stretching or creation of ropes (see Fig. 3.7) although the success rate is small since the surface state of these samples is rather poorly controlled (indeed in many cases DNA molecules do not bind at all to sample). These sample showed insulating behavior even if several DNA molecules crossed the gap between the Pt electrodes (see for e.g. Fig. 3.7, shortest distance between electrodes was around 500 nm in this sample). This insulating behavior is consistent with the experimental findings from [14], which indicated that DNA is an insulator when it is deposited on Silicon/and mica surfaces.

Because of the poor reproducibility of DNA deposition on bare metallic samples, and confirmed absence of conduction we subsequently focused onto deposition of DNA on metallic electrodes functionalized by a pentylamine plasma as proposed in Refs. [11, 12] where

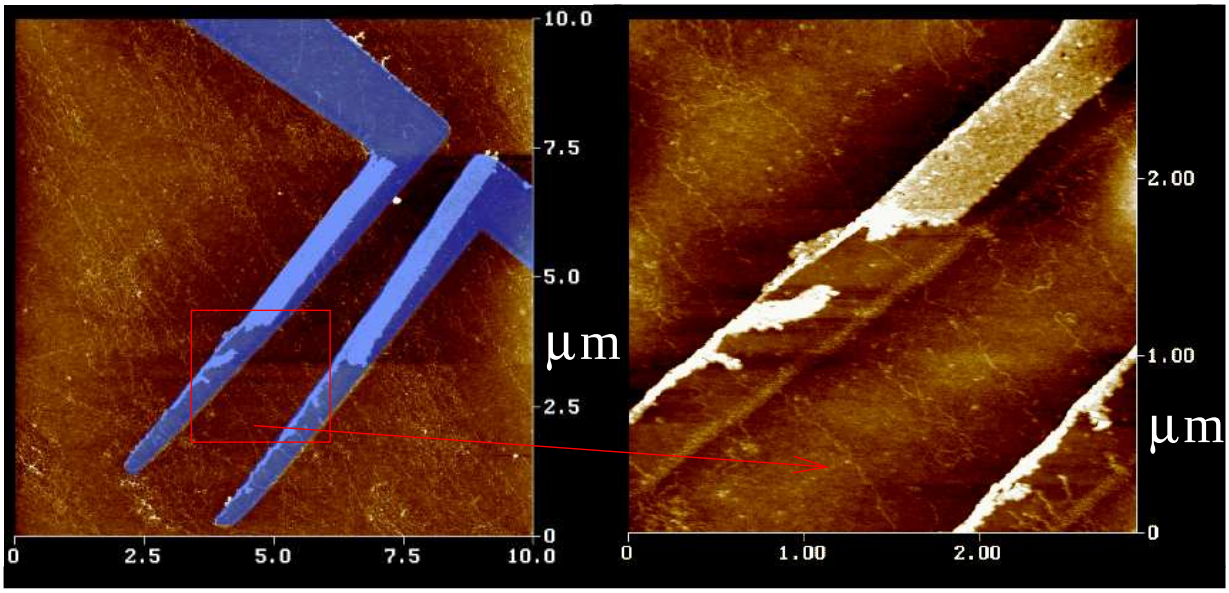

FIG. 3.7 – AFM image of DNA molecules deposited across Pt electrodes. The electrodes are highlighted in blue on the left image and their height is approximately $\simeq 3$ nm. They were fabricated with electron beam lithography on a SiO_2/Si substrate. The right image shows a magnified view of DNA molecules inside the gap. This sample displayed insulating behavior after deposition of DNA molecules. (This sample actually underwent a pentylamine plasma treatment, but due to the absence of a carbon film on the Pt substrate, this treatment was most likely ineffective, see Chap. 3.5 for a more detailed discussion).

conduction on samples with DNA was observed at low temperature.

3.5 Pentylamine plasma functionalization for deposition of DNA molecules

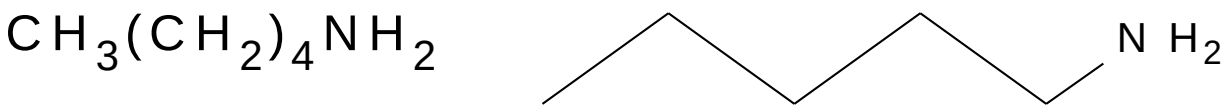

FIG. 3.8 – Chemical structure of the pentylamine molecule

The use of the pentylamine molecule (see Fig. 3.8) was introduced by Dubochet [30] as a mean to render carbon support films for electron microscopy hydrophilic in order to make possible adsorption of biological molecules. The sample is commonly placed between two parallel electrode plates in a vacuum chamber with weak pentylamine pressure (2.5 millibar). A high voltage (80 V) is then applied to the plates creating a glow discharge. The ionic species produced during the discharge are deposited on the substrate and create

Bond dissociation energy	kJ/mol
$H - NH_2$	450
$H - CH_3$	439
$CH_3 - CH_3$	376
$C_2H_5 - CH_2NH_2$	336
$C_6H_5CH_2 - NH_2$	297
Ionization energy	kJ/mol
H	1312
CH_3NH_2	826
$C_5H_{11}N$	726

TAB. 3.2 – Dissociation energies for bonds present in the pentylamine molecule, and ionization energies of methylamine (CH_3NH_2) and piperidine ($C_5H_{11}N$) [32]. The last two molecule are chemically close to pentylamine for which data is not available. Since the bond dissociation energies are all comparable and smaller than the typical ionization energies it seems very likely that all possible chemical species are present in the plasma.

a positively charged background favorable for DNA adsorption (typical discharge time was 30 s in our experiments, reported pressure and voltage values correspond to those used for the setup in the group "Microscopie moléculaire" at Institut Gustave Roussy).

The chemical structure of the deposited chemical species is not well characterized and is certainly complex (see also Table 3.2). For example it is known that a discharge of an CF_4/O_2 gas mixture, creates $CF_3^+, CF_2^+, O_2^+, O^-, F^-$ ions and CF_3, CF_2, O, F radicals [31] Note however that the fraction of dissociated species among the gas molecules is usually very small (of the order of 10^{-5}) in this discharges used for material processing, hence it is highly probable that not only dissociated molecules are deposited on the substrate.

The pentylamine discharge technique was adapted to attach DNA molecules to conducting electrodes in the experiments from Refs. [11, 12]. It constitutes the main difference with other studies where in most cases the substrate was silicon dioxide. Hence we dedicated considerable efforts to identify the substrate on which this treatment yields effective binding of DNA molecules. These studies led us to the conclusion that reproducible adsorption of DNA with pentylamine treatment occurs only on carbon coated substrates, which are similar to the carbon support films for electron microscopy. In this respect the analysis in [12] is somewhat misleading since it claims that pentylamine can form a polymer film on mica suitable for adsorption of DNA. Below we summarize the results of our DNA deposition experiments on different substrates using the pentylamine technique. In all cases the DNA deposition was attempted rapidly (at most one hour) after the glow discharge since we have observed that the efficiency of the pentylamine layer at binding DNA molecules decreases quickly once it is exposed to ambient air.

Our attempts to deposit DNA on a freshly cleaved mica substrate functionalized by pentylamine plasma were never successful. An example AFM image of the mica substrate after pentylamine plasma and DNA deposition is shown on the right. Only a single feature reassembling a DNA molecule can be distinguished inside the 3 μm $\times$ 3 μm scan area : this is much less than the number of molecules on the Figs. 3.5,3.7 which have similar scan size. The absence of molecules on the mica substrate is puzzling since DNA binds to both pentylamine functionalized surfaces and bare mica. A possible explanation is that in a first stage molecules bind to the pentylamine film on top of the mica surface. In a second stage this film is washed away from the surface when the sample is dried ripping away the DNA molecules on top of the pentylamine film. Indeed the pentylamine film must be destroyed at some stage of the deposition because the density of DNA molecules on the surface is extremely small compared to the densities achieved on the Pt/C surface with the same functionalization. It can not be destroyed immediately when the drop is deposited on the surface, otherwise DNA molecules would bind to the exposed mica surface. To summarize in the above scenario pentylamine masks the mica surface from the DNA solution and is at least partially removed when the sample is dried, carrying away the attached DNA molecules (this assumes that the layer formed during the plasma discharge is continuous).

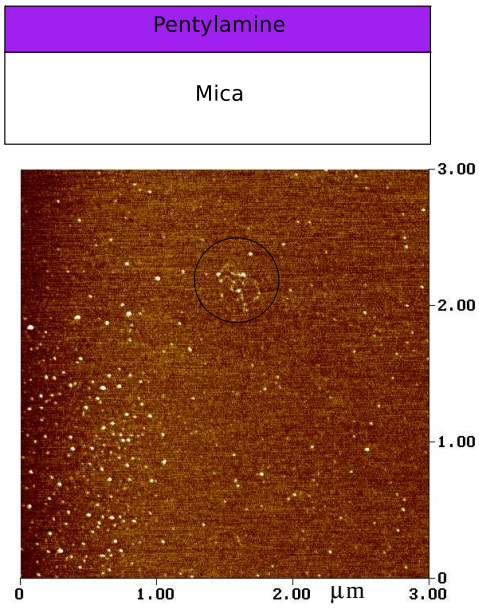

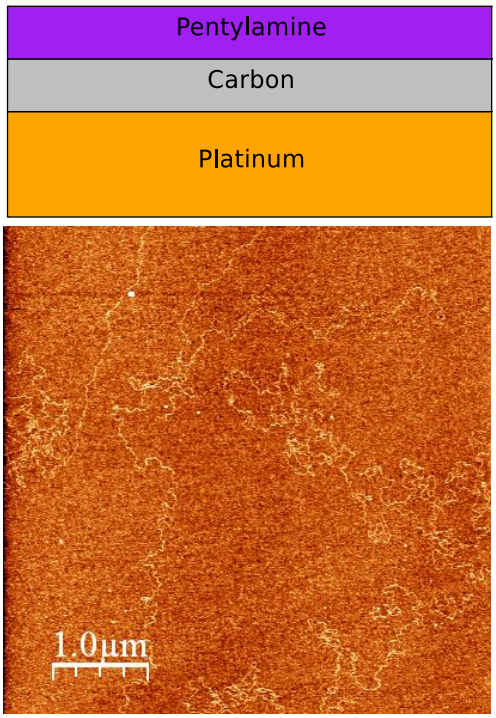

Deposition of DNA molecules on a platinum film coated with an evaporated layer of amorphous carbon (around 10 nm) were reproducible and successful. Most likely the free radicals created during the glow discharge react with the amorphous carbon on the surface, and anchor the pentylamine layer. As seen in this image the molecules are not overstretched, it may also seem that their persistence length is smaller than on the mica substrate (see Fig. 3.5). This observation is supported by other quantitative studies of DNA adsorption on positively charged surfaces [33]. Following Ref. [12] we have also tried to deposit DNA with the pentylamine treatment directly onto platinum without the carbon layer. For clean platinum films only a low density of overstretched molecules could be detected on the surface after DNA deposition. This most likely indicates that the pentylamine is removed during the DNA deposition and only a few molecules bind to the platinum surface through their ends with a mechanism similar to that described in Chap. 3.4. After discussions with D. Klinov, we found that the Platinum deposited in [12] actually contained a certain amount of carbon (around 10%) which allowed fixation of the pentylamine. In this regard also the presentation in Ref. [12] is misleading.

In conclusion the adhesion of the pentylamine is reliable only on surfaces with a high enough density of carbon atoms that can bind with the ions/radicals produced during the glow discharge sticking the pentylamine to the surface. In this case the deposition of DNA molecules is reproducible and molecules are not overstretched. The role of the carbon atoms is only to anchor the pentylamine layer. Hence it is not necessary to form a continuous carbon coating of the substrate. For example the Pt/C samples produced by D. Klinov were obtained by simultaneous evaporation of both Platinum and Carbon in unknown proportions. (However in the transport devices for measurement of DNA transport the nature of the substrate will not be relevant since the active region will be contaminated by carbon from the focused ion beam microscope).

3.6 Combing DNA molecules onto electrodes with the pentylamine technique

In the previous chapter we described how DNA molecules can be attached on a metallic film with the pentylamine plasma functionalization. From our experiments it seems that this procedure is successful at attaching DNA molecules only on carbon coated substrates. In this chapter the substrate will be a Platinum film (3 nm) sputtered on a cleaved mica surface and covered by a layer ($\simeq$ 10 nm of evaporated amorphous carbon).

We now describe how to orient DNA molecules perpendicularly to an insulating gap separating wide metallic electrodes. The possibility to orient individual DNA molecules with a moving air-liquid interface was first established experimentally in Ref. [34]. Figure 3.9 shows a photography of the deposition setup, and an AFM image of the molecules at the metal-insulator interface (both were covered by an amorphous carbon layer before deposition). Even if molecules are combed on the electrodes, they seem to turn around at the metal boundary avoiding the insulator. This guiding may be explained by pinning of the liquid air-interface at the border between the two regions. Moreover many molecules are overstretched which is to be avoided for transport measurements. For this reason we have chosen an alternative technique which consists in orienting the molecules with a flow. A macroscopic Poiseuille flow is not perturbed by defects and interfaces on the nanoscale, and regulation of the flow velocity allows in principle to control the elongation of the molecules.

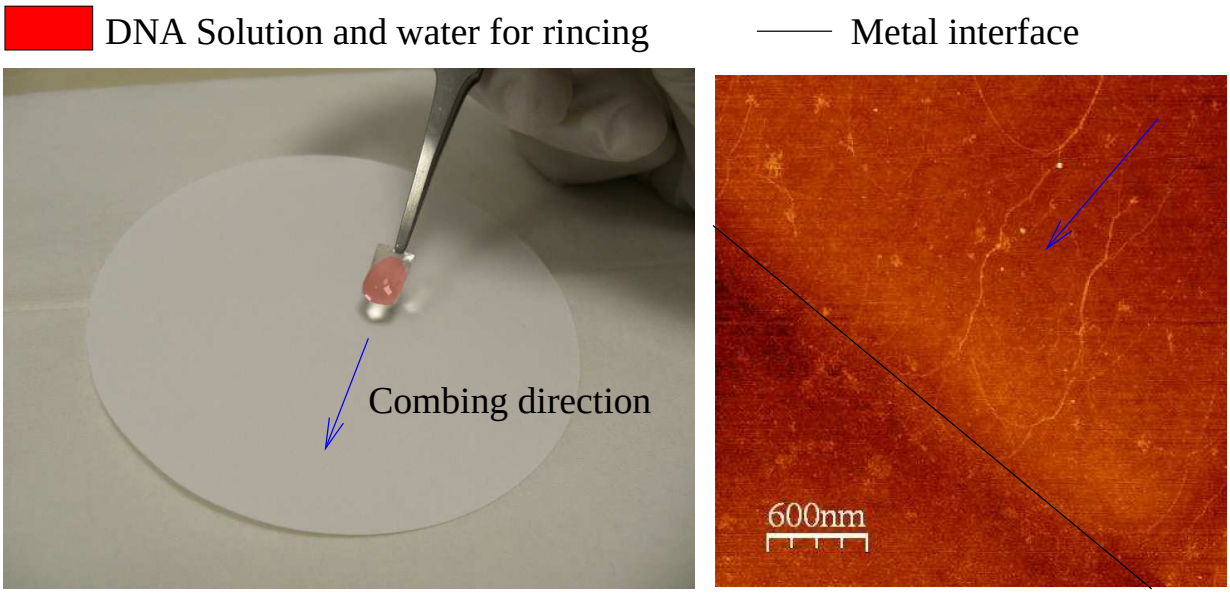

FIG. 3.9 – Combing of DNA molecules using a drying water air interface. A droplet of DNA ($\simeq$ 15 μL) is incubated on the functionalized surface for a minute. Afterward $\simeq$ 100 μL of water are added to the drop to avoid formation of salt crystals when the solution is dried. The combing is achieved by draining the liquid from the sample with a filter paper (combing direction indicated by blue arrows, see photography on the left). An AFM image of the molecules near metal-insulator interface is shown on the right. Molecules are combed on the metal electrodes but turn around near the interface, and no molecule crosses the interface in this picture.

In our deposition protocol (see Fig. 3.10 for a description of the setup) the droplet is first incubated on the sample surface for around a minute. This allows DNA molecules to bind to the surface at a few contact points without complete adsorption on the surface. Afterward the rinsing flow is turned on, it provides a flow rate of $\simeq$ 5 ml/min of pure water

on the sample. This flow has a double function of combing DNA molecules and rinsing salt residues that may form on the surface rendering AFM imaging difficult. It is interesting to know in which flow speed regime DNA molecules may start to be overstretched. A quantitative study of the dynamics of a tethered DNA molecules under a Poiseuille flow was performed recently [35] using fluorescence microscopy.

It was found that the elongation of the molecules was governed by a single dimensionless parameter, called the Weissenberg number $\mathrm{Wi} = \dot{\gamma}\tau$ where $\dot{\gamma}$ is the shear rate and τ is the longest relaxation time of the DNA molecule (it was found to be $\tau \simeq 0.4$ s for λ-DNA labeled with fluorescent beads [35]). Complete elongation of the molecules occurred only for $\mathrm{Wi} \simeq 100$, while an elongation of 25% occurs already for $\mathrm{Wi} \simeq 5$. The shear rate in our experiments can be estimated as follows : the outflow of liquid on the surface is $D_{flow} \simeq 5$ ml/min, for a cross section of the droplet of the order of $S = H \times (2R)$ where $H = 1.5$ mm is the droplet height and $R = 5$ mm is the droplet radius. The mean velocity in the fluid is $V = D/S$ and since the flow vanishes at the contact with the substrate the shear rate is $\dot{\gamma} = V/H \simeq 4\ \mathrm{s}^{-1}$ leading to $\mathrm{Wi} = 1.5$. This calculation shows that with our typical flow parameters we are far from the threshold $\mathrm{Wi} \simeq 100$ where molecules may start to be overstretched. As a result we have set the debit to a value around 5 ml/min where the flow on the sample was stable without risks of uncontrolled drying of the drop during the rinsing process.

AFM images of DNA molecules deposited with this technique on a carbon coated platinum surface are shown on Fig. 3.11. The extension of molecule depends on the number of active binding sites created during the glow discharge, the incubation time before rinsing and on the water flow rate. Since all these parameters are hard to fix in a reproducible way, sometimes molecules are more collapsed onto themselves (Fig. 3.11.a) and sometimes they are more extended (Fig. 3.11.c). However binding and orientation of the molecule (in the range suggested by the different cases of Fig. 3.11) was reproducible with this technique.

Now all ingredients are assembled to deposit DNA molecules across an insulating gap using the pentylamine technique. We have done this with electrodes produced with both electron beam lithography and focused ion beam etching (this technique was also used in [12] and will be described further on in Chap. 3.7). A cross section of the material layers constituting electrodes and the gap is sketched on Fig. 3.12, this structure is similar for both electron-and ion beam processed samples. The width of the gaps for these samples was between 100 and 400 nm. Molecules crossing the gap are clearly visible in Fig. 3.13 however all the gaps where we deposited molecules always remained insulating with resistances larger than Giga-Ohms despite presence of carbon and pentylamine layers. In order to verify that the surface of the electrodes is not insulating due to the formation of an oxide layer or due to organic contamination we have deposited HIPCO single wall carbon nanotubes (SWNT) from a dichloroethane solution across the electrodes. The resistance of the junction then dropped to values of the order of 100 kOhms suggesting that our electrodes were clean enough to make contacts to nanonotubes. However we will argue in the next chapters that the electrodes were probably covered by an insulating pentylamine layer during deposition of DNA molecules. The organic solvent of the SWNT may have cleaned the electrode surface thereby allowing the formation of an electrical contact.

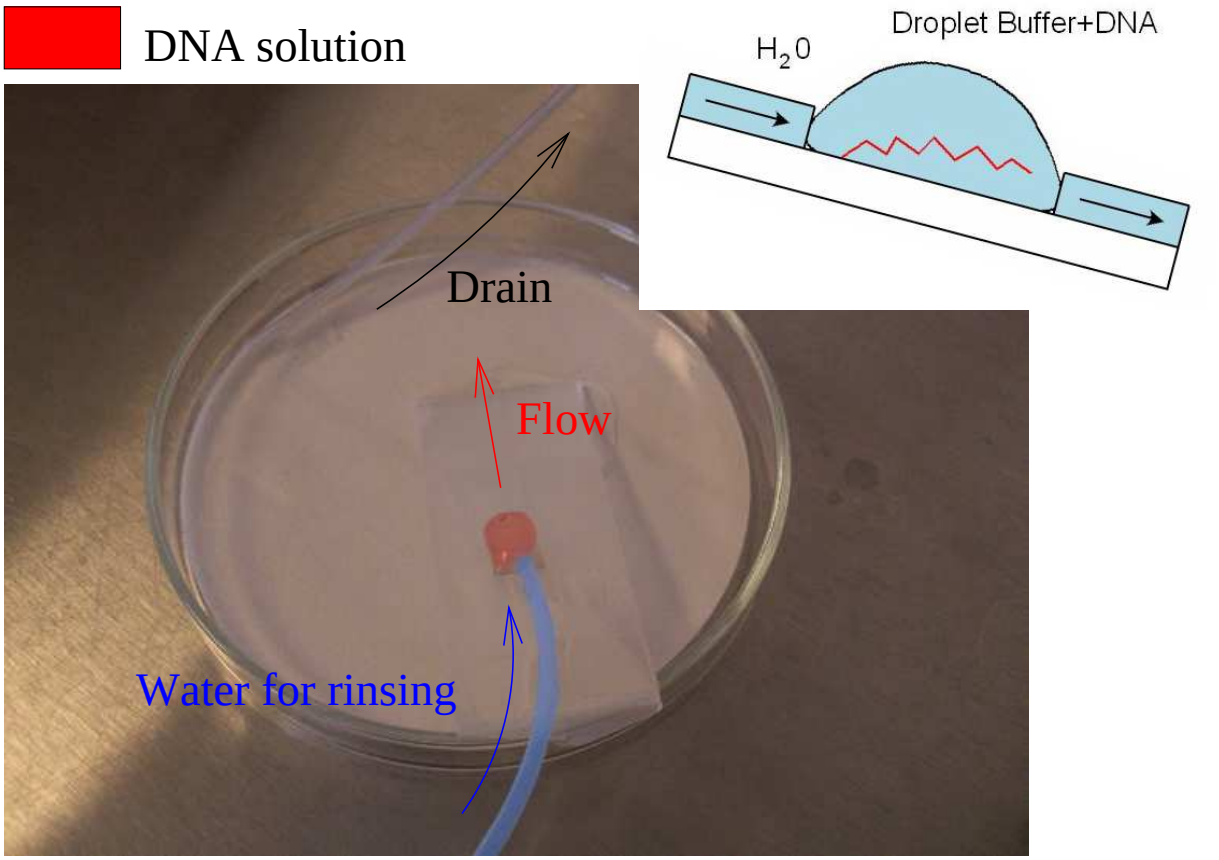

FIG. 3.10 – Combing of DNA molecules with a flow. A drop of DNA solution is deposited on the sample and incubated for a few minutes. The substrate is then rinsed with a flow of pure water injected by a peristaltic pump. The liquid regularly runs off the sample, which is tilted in the direction of the flow allowing to collect the excess liquid in a petri dish under the sample. The liquid is drained by the peristaltic pump thus keeping the water level constant.

These results are in disagreement with findings from [11, 12] which suggested that the presence of a pentylamine layer creates a suitable substrate where conduction of DNA molecules is possible. However the above experiments depend on many parameters which are often poorly defined. In the absence of any credible indication on the origin of this discrepancy we have asked D. Klinov to deposit DNA molecules with his setup on samples with insulating gaps prepared in our laboratory using a focused ion beam reproducing as accurately as possible the experiment from Ref. [12].

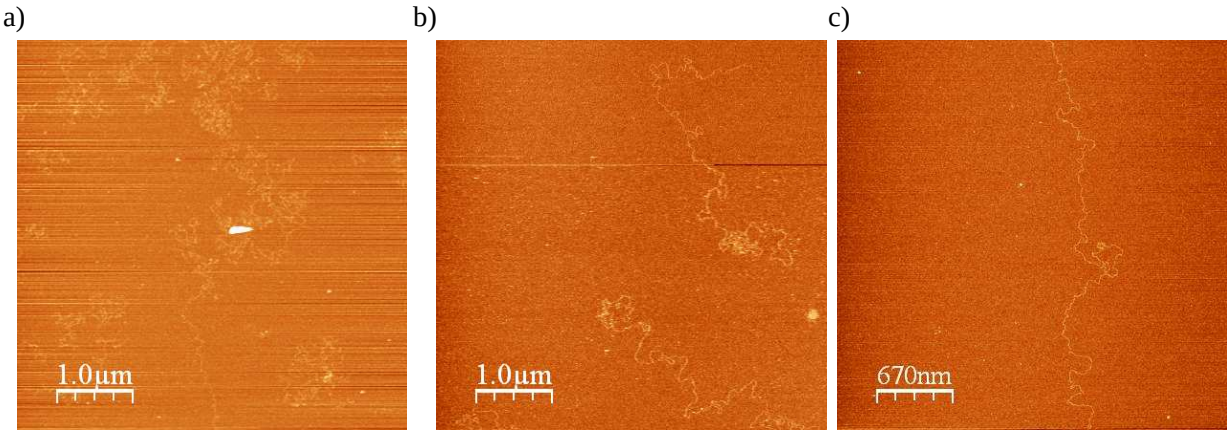

FIG. 3.11 – AFM images of DNA molecules combed on a platinum carbon pentylamine substrate with a liquid flow. Images from left to right correspond to increasing flow velocity.

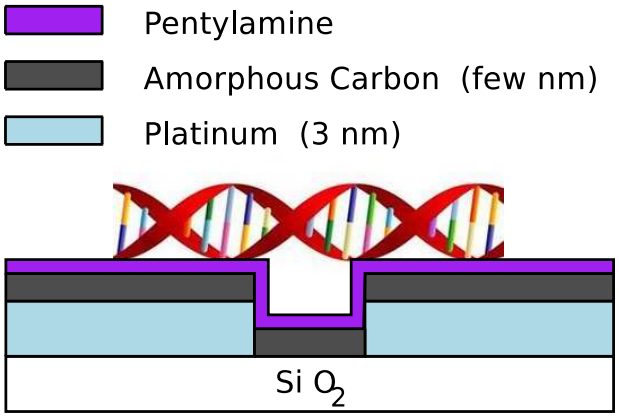

FIG. 3.12 – Schematic representation of the material layers for samples produced by electron beam lithography. Structure of the samples produced with the focused ion beam is similar except that the substrate is mica and will be discussed in more detail in Chap. 3.7.

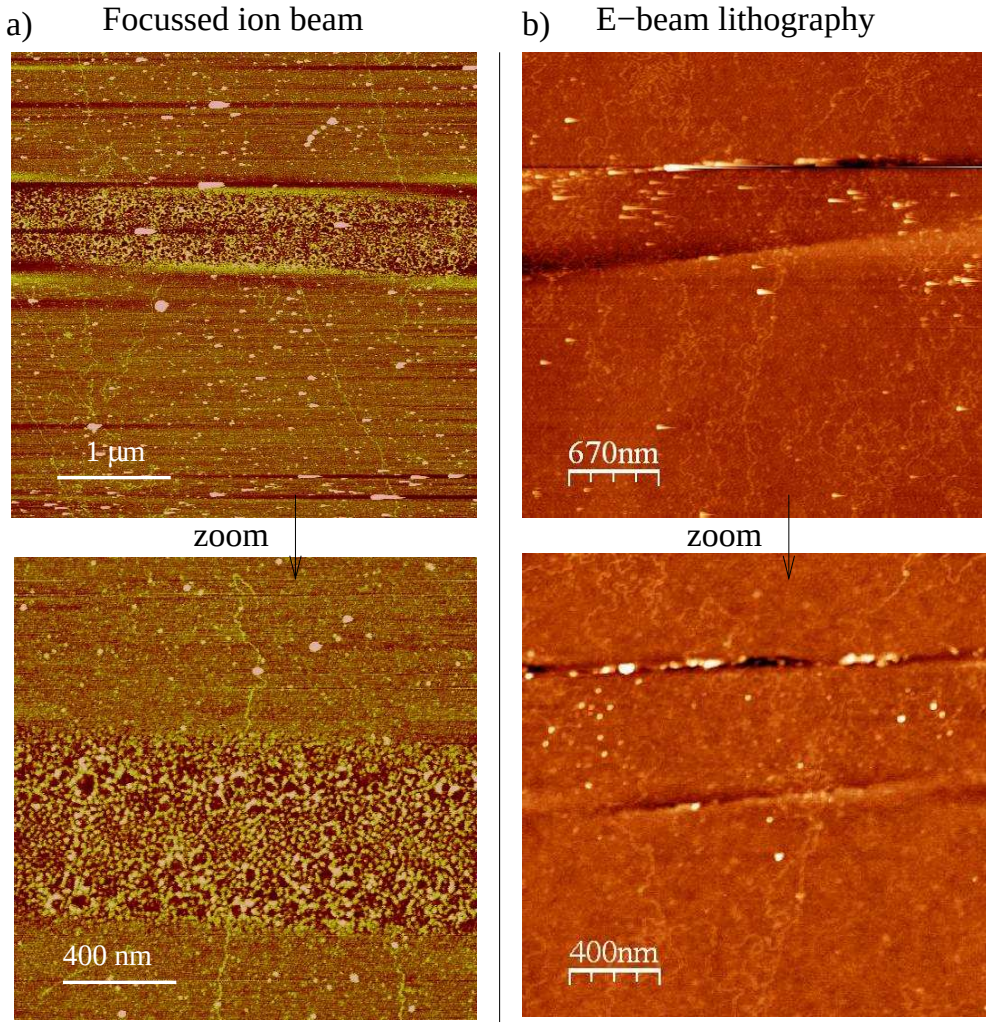

FIG. 3.13 – AFM image of DNA molecules deposited across insulating gaps using the flow combing technique. a) Shows a sample produced with focused ion beam etching. The insulating gap is actually around 100 nm wide, even if apparent width is around 400 nm. This occurs because the roughness of the Pt film is increased in a large area around the gap after FIB irradiation. b) Shows DNA molecules across a gap produced with electron beam lithography. Note that the gap realized with electron beam lithography is cleaner and one can follow the molecules inside the gap. This is not possible for the gap produced by focused ion beam etching due to the roughness of the substrate after etching (see also Chap. 3.7).

3.7 Fabrication of narrow insulating gaps using a focused ion beam

This method of fabrication of insulating gaps does not use electron beam lithography and therefore avoids the contamination of the surface by residues from organic resist. A thin layer of platinum carbon was deposited in D. Klinov's laboratory on a freshly cleaved mica substrate. This metal layer has an estimated thickness of at around 5 nm and a resistance per square of around 1 kΩ. A schematic representation of the sample layout after laser and focused ion beam (FIB) etching is shown on Fig. 3.14. In a first step thick gold ($\simeq$ 200 nm) contact pads were evaporated through a mechanical mask. We then cut long trenches in the metallic film using an ultraviolet focused laser with spot-size around 10 to 30 μm. The laser locally heats the surface and evaporates the metal layer creating holes in the metal of the order of the spot size. Programmable motors then allow to expose the metal in predefined patterns around the golden contacts leaving regularly spaced metal openings 60 μm long. These remaining metal stripes were opened with a Gallium FIB which can etch narrow 100 nm wide trenches. In order to determine the minimal dose of FIB irradiation required to produce a narrow insulating gap in the platinum film we have developed a technique for in-situ measurement of the film resistance inside the FIB microscope.

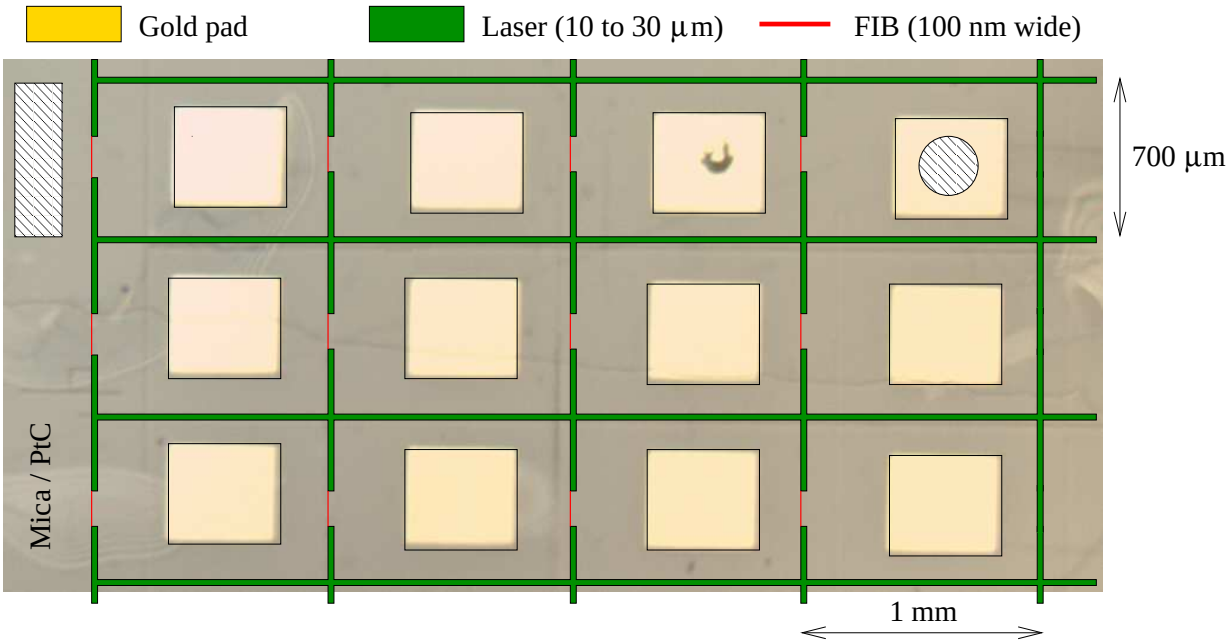

FIG. 3.14 – Sketch of a sample produced with FIB etching with a sample photography on the background. It shows the gold contact pads, the pattern exposed to laser irradiation (green line) and the small gaps etched with FIB at the last step (red line). The scales are not all preserved on this diagram : the red line (region etched with FIB) is in reality 50 μm long and 100 nm whereas the width of the lines etched with laser is roughly 10 μm.

This technique allows us to continuously monitor the resistance between several gaps contacted in series (for e.g. between the hatched regions on Fig. 3.14). First an estimate of the required etch time is obtained by cutting half of one gap and monitoring simultaneously the increase of resistance as a function of time. We estimate the optimum etching time of the PtC film from the value at which the resistance saturates. After this operation the measured resistance is still finite since only half of the gap is etched, this allows to repeat the operation and accumulate statistics on a few (typically 5) gaps. At the last step one of the gap is opened completely until resistance diverges, the resistance dependence on the etch time is shown on Fig. 3.15 for one of the junctions. This last measure gives a very precise estimate of the minimal dose. Considering possible fluctuations in the thickness of the film ıe same do

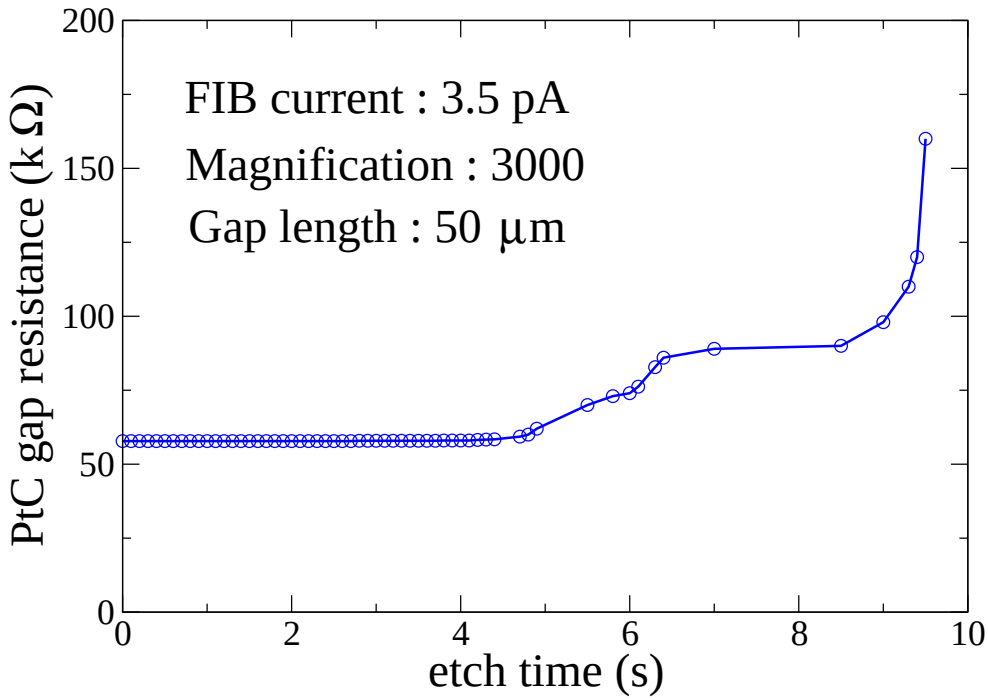

FIG. 3.15 – Resistance of a gap during FIB etching as a function of exposure time. The gap is etched in a single scan mode with a scan time of 0.1 s which allows to measure the resistance after each scan. After total time $t > 9.7$ s the resistance jumps and the gap becomes insulating. Usually at the beginning of the etching there is a short phase were conduction drops by a small amount that can not be seen on this scale. This surprising behavior will be discussed in Chap. 3.9.

Atomic force microscopy images of the gaps fabricated with the FIB are shown on Fig. 3.16. For the narrowest gap the height profile exhibits a characteristic peak with a small dip in the center where the gap is insulating. Certainly the dip is actually deeper than shown on the AFM image because of tip convolution effects. At higher irradiation

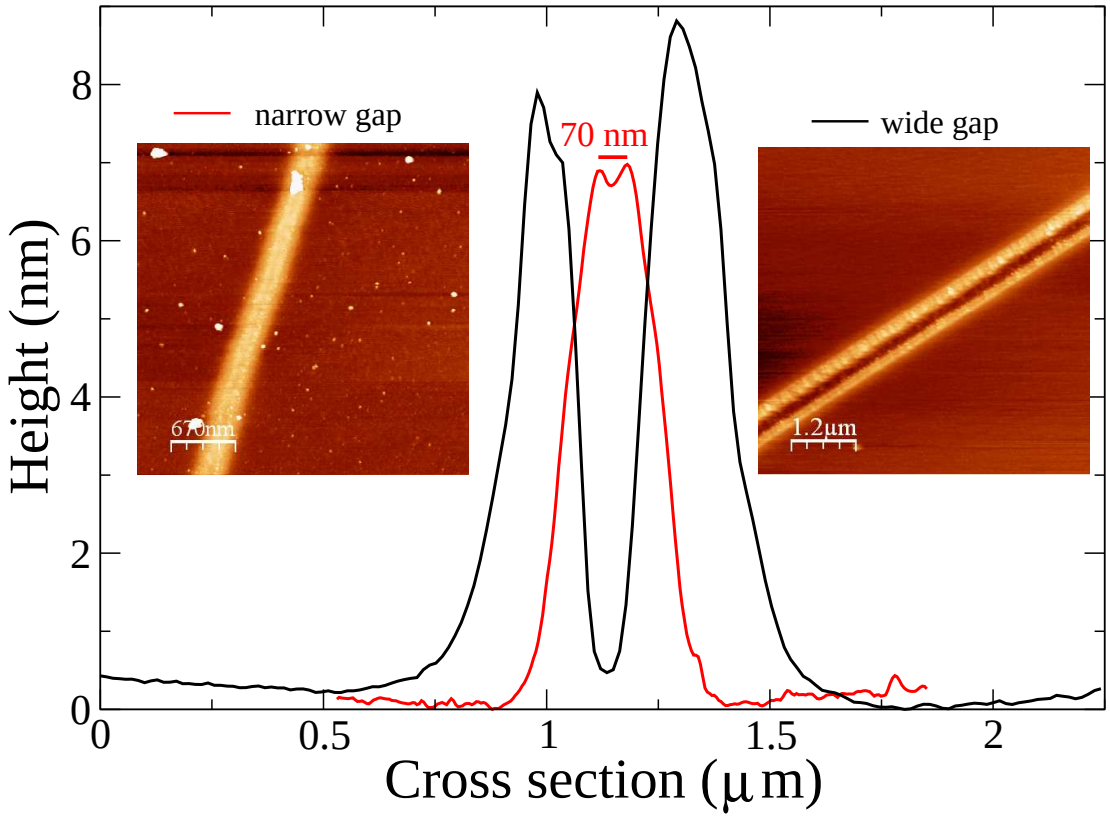

FIG. 3.16 – Averaged height profile from two gaps prepared using FIB, their AFM images are shown in the color insets. The narrow gap was obtained during the calibration resistance measurement from Fig. 3.15 while the wide gap was obtained with a larger exposure time. It is difficult to distinguish the insulating region from the main contrast that comes from the roughness near the edge of the gap produced during the FIB etching.

doses, the gap grows in size and more pronounced side peaks appear.

Surprisingly for the minimal etch time width of the insulating region is of the order of $\simeq$ 70 nm and is very slender compared to the contamination peak which extends over about 500 nm. The cross section of the peak for the narrow gap is $\Sigma = (250\text{ nm} - 70\text{ nm}) \times 7\text{ nm} \simeq 1260\text{ nm}^2$ where 7 nm is the gap height, 250 nm and 70 nm are respectively the bump and gap widths. Assuming that the thickness of the platinum film is around 5 nm we find that the cross section of the excavated platinum is sensibly smaller 70 nm $\times$ 5 350nm^2. It is possible that FIB dug also into mica providing the remaining material inside the bump. However since we stopped etching just when the gap became insulating, it is unlikely that we dug very deep into the mica surface. It is instructive to compare the number of atoms $\mathcal{N}$ inside this "bump" (we find that $\mathcal{N} = \Sigma \times 50\ \mu\text{m}/(0.25\text{ nm})^3 \simeq 4 \times 10^9$ where 50 μm is the gap length and 0.25 nm is the average distance between atoms for e.g. in a gallium crystal), with the number of gallium atoms $\mathcal{N}_{FIB}$ sent by the FIB. This number can be estimated from the FIB current and the etch time for the narrow gap on Fig. 3.15, it amounts to

$\mathcal{N}_{FIB} = 3.5$ pA $\times$ 10 s$/e \simeq 2 \times 10^8$ (e is the elementary charge). According to this calculation there is an almost two order of magnitude difference between the quantity of atoms in the bump $\mathcal{N}$ and the quantity of atoms emitted by the ion beam $\mathcal{N}_{FIB}$. Although these estimates are not very accurate they suggest that there may be a third origin for the peaks around the gap other than displacement of platinum and mica and injection of gallium atoms. It is possible that the metallic film dewets locally from the mica surface due to heating by FIB creating a bump (we have remarked adhesion of thin films is generally not very good on mica). In all cases AFM scans in the direction parallel to the gap show (see AFM images from Fig. 3.13.a) that the surface is very rough in a region extending across $\simeq$ 700 nm much wider than the insulating region ($\simeq$ 200 nm), indicating that the PtC film is damaged or contaminated in a large region outside the gap.

For the moment we stop here the analysis of the gap structure (but it continues in Chap. 3.9 !). In the discussion that follows it is enough to keep in mind that the structure of the gap may actually be quite complicated even if it is obtained by "physical" means without organic resists.

A total of about twelve substrates were sent to D. Klinov in Moscow for the deposition of DNA molecules, with about ten gaps opened by FIB on each sample. The deposition protocol used by D. Klinov seems similar to the protocol we used in our deposition experiments (see Chap. 3.6). The main difference seems that in D. Klinov's pentylamine setup a gas flow continuously refreshes the pentylamine gas in the discharge chamber. This procedure can reduce the probability of forming radicals/ions which require breaking several bonds or removing several electrons from the pentylamine molecule. But this probability is low anyway and it is not clear how it could influence the conduction of DNA.

The results on conduction after deposition of DNA molecules in D. Klinov's laboratory are summarized in Table 3.3. On three samples conduction was observed after deposition of DNA molecules across slits that were insulating before DNA deposition. The statistics on these three sample is very favorable since 11 out of 15 slits became conducting. Moreover the deposition protocol was repeated with a buffer solution without DNA on a control sample from the same batch as two of the conducting samples (the mica sample was cut in three pieces before the pentylamine treatment) and all the 14 gaps remained insulating. This statistic is strongly in favor of an interpretation in term of conduction through DNA molecules. However this statistical argument must be handled with care. If we consider all the samples were deposition of λ molecules was attempted, the conducting slits represent only around 10% of the prepared structures. On the other samples or no DNA molecules could be detected with AFM indicating that pentylamine functionalization was not effective or the molecules were insulating. Hence observation of conductivity after attempts of DNA deposition has actually a low success rate even when deposition is done by D. Klinov following the recipes used in [11, 12]. We have reached the conclusion that one of the reasons behind this irreducibility lies in the structure of the sample after etching which will be disused in more detail in Chap. 3.9. We now turn to transport measurements on the three samples where conduction was observed.

# of substrates	12
# of FIB slits	$\simeq$ 100
# of substrates with visible λ DNA	5
# of substrates with conducting slits after λ deposition	3
# of conducting slits after λ deposition	11
# of slits on the substrates with conduction	15
# slits where DNA molecules could be observed with the AFM in Orsay	1
# of slits on the control sample	14
# of conducting slits after buffer	0

TAB. 3.3 – Success rates for the formation of conductive junctions by deposition of λ molecules.

3.8 Transport measurements on conducting DNA samples

Before performing transport measurements on the three substrates where conduction appeared after deposition of DNA molecules we had to connect the samples to a sample holder which can be mounted inside one of our dilution fridges. This connection can be realized through thin ($\simeq 20\ \mu m$ diameter) wires with ultrasound bonding or glued with silver paint. Ultrasound bonding on a sample with three conducting gaps, led to disappearance of conduction on three gaps. It is possible that an electrical discharge was created during the ultrasound bonding destroying the conduction across our samples. In order to avoid this discharge we have decided to contact the second sample using silver paint. Surprisingly with silver paint conduction was also destroyed on the five conducting gaps of the second sample. During the process of contacting the gaps we checked their conductivity under a test-probe several times. The resistance of a gap could change even when the silver paint drops were deposited on the contact pads of the other samples. For example the resistance across one of the gaps took the following values : 1.8 kΩ $\rightarrow$ 160 kΩ $\rightarrow>$ 1000 kΩ $\rightarrow$ 5 kΩ $\rightarrow \infty$. These observations suggested that our samples were sensible to the vapors of the silver paint solvent. Hence we decided to avoid silver paint for the contacts on the last sample. A possibility was to replace silver paint with indium paste however the latter did not stick to contact pads after the pentylamine discharge probably because of the presence of the organic layer. A. Kasumov then proposed to use a system of mechanical contacts with springs that we fabricated specially to fit the geometric parameters of the last remaining sample (see Fig. 3.17).

This allowed us to contact 5 conducting gaps which we measured at low temperature. Their resistance at room temperature is listed in Tab. 3.4

To our surprise all four samples with room temperature resistance $\leq$ 10 kΩ exhibited superconducting behavior at low temperature. Indeed contrarily to the experiment [11] where superconducting electrodes where used to contact the DNA molecules, our platinum/carbon contacts are in a normal state. The dependence on temperature for different magnetic fields is shown for two samples on Figs. (3.18,3.19). Superconductivity appeared

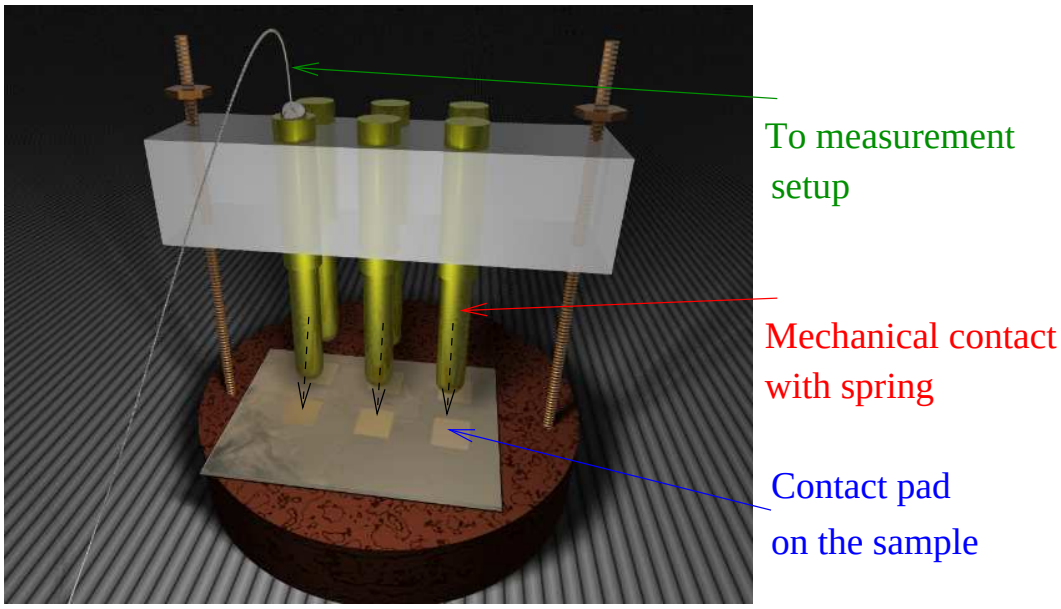

FIG. 3.17 – Three dimensional model of the mechanical connection system we used to contact our DNA sample to the dilution fridge.

measured at low temperature	3 kΩ	4.8 kΩ	6.1 kΩ	10 kΩ	10 MΩ
measured only at room temperature	4.0 kΩ	8.2 kΩ	∞	∞	

TAB. 3.4 – Room temperature resistances of the gaps at room temperature after deposition of DNA molecules on the sample measured at low temperature.

below 4 K and results in a drop of resistance that saturates at low temperature because of the finite resistance of the normal contacts. The 10 kΩ sample displayed a very smooth transition as a function of temperature (see Fig. 3.18) and the drop of resistance saturated at $T \simeq 200$ mK. In contrast less resistive samples had a sharper transition (see for e.g. Fig. 3.19) with a saturation temperature around 2 K. The smooth transition observed in the 10 kΩ sample has some similarities to smooth transitions observed in Superconductor-Normal-Superconductor (SNS) junctions in the intermediate regime between a long and a short junction. A long SNS junctions is characterized by the presence of two transitions. The transition at the highest temperature, stems from the transition of the superconducting contacts while at a lower temperature proximity induced superconductivity sets-in in the normal region [36]. When the length of the normal part is decreased the two transitions merge into a single smoother transition [37, 38]. Since in our samples only a single transition is observed, this suggests that we have created an SNS junction in this intermediate regime.

A possible origin of the superconductivity is the Gallium contamination deposited by the FIB. An insight on the size of the superconducting contamination islands is provided

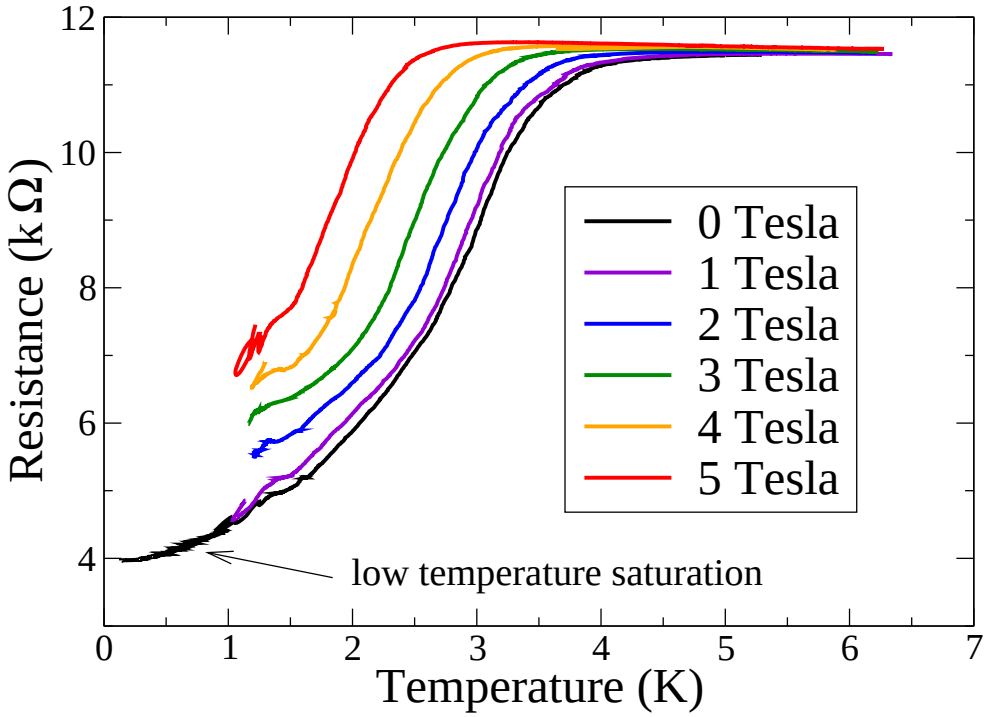

FIG. 3.18 – Temperature dependence of resistance for the 10 kΩ junction (see Tab. 3.4) at several magnetic fields.

by the dependence on magnetic field. Under a magnetic field the resistance of the samples increased, however the maximal magnetic field available in our setup (5 Tesla) was not sufficient to completely destroy superconductivity at low temperature indicating a critical magnetic field of the order of 10 Tesla (see Figs. 3.18 and 3.19). Assuming the presence of superconducting nanoparticles we can also understand the origin of this relatively high critical field. The magnetic field destroys superconductivity in a nanoparticle when it creates a flux of the order of the flux quantum through the nanoparticle surface πR^2 where R is the nanoparticle radius. This criterion gives a typical nanoparticle radius of the order of $R \simeq 10$ nm. Through extensive AFM/SEM characterization of the measured sample (see Chap. 3.9) we were able to establish that these nanoparticles were deposited by FIB. Gallium is superconducting with transition temperature $\simeq 1$ K, the presence of carbon impurities may increase this transition temperature to $\simeq 4$ K. Indeed tungsten wires deposited with FIB containing Gallium and carbon have critical temperature $T \simeq 4$ K whereas the pure tungsten has critical temperature around < 50 mK [39]. Thus it is probable that the source of superconductivity are superconducting nanoparticles inside (and even outside!) the gap cut by the FIB. The nanoparticles themselves can not give rise to ohmic resistances of a few kOhms, hence the large amplitude of the resistance (drop for e.g. from 10 kΩ to 3 kΩ) between the normal and the superconducting states, indicates a configuration where a normal nanowire connecting the contacts is rendered superconducting by proximity effect from the nanoparticles. To conclude on the dependence on magnetic

field, one of the samples displayed SQUID like modulation in the magnetoresistance with a period of 0.5 Tesla at temperature $T \simeq 2$ K. These oscillations disappeared at lower and higher temperatures $T < 1$ K and $T > 3$ K suggesting a complex geometry with several SNS junctions connected in series and/or in parallel.

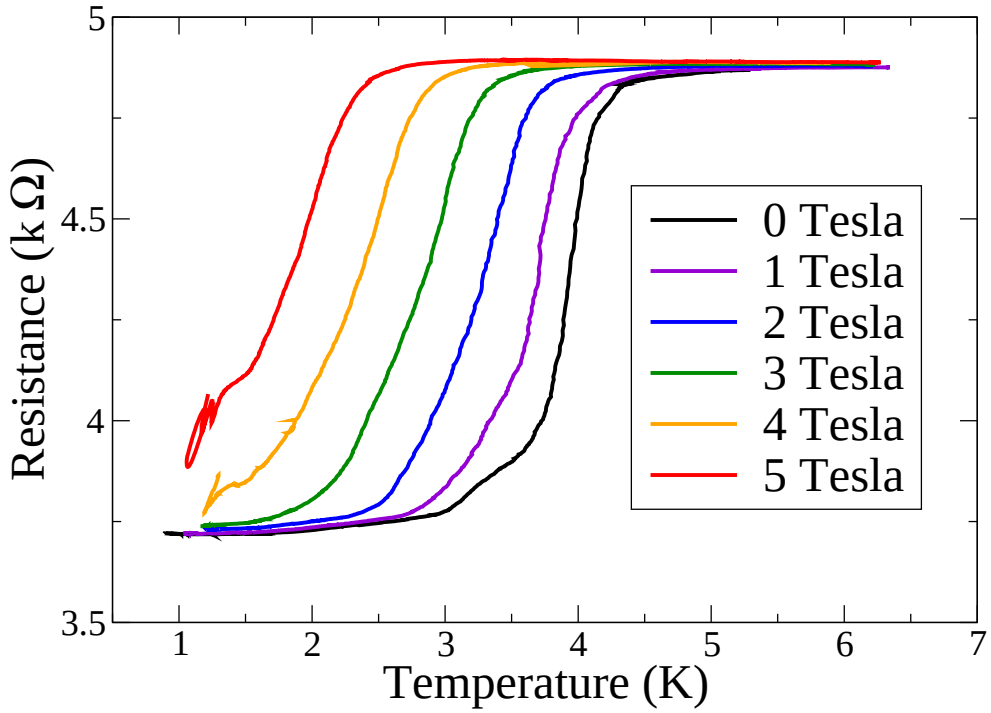

FIG. 3.19 – Temperature dependence of resistance for the 4.8 kΩ junction (see Tab. 3.4) at several magnetic fields.

We have also measured the differential resistance of the sample as a function of a DC current. The results for the 10 kΩ sample are shown on Fig. 3.20 and resemble the data obtained from Ref. [11] on DNA samples with superconducting Rhenium contacts. At zero magnetic field the differential resistance exhibits a large drop in the current interval -250 nA $\leq i \leq 250$ nA. Inside the gap the resistance drops smoothly but does not vanish probably because of the contact resistance of the normal electrodes. In our interpretation the large peak at $i \simeq \pm 250$ nA corresponds to the critical current of a nanoparticle. The smaller peaks may appear due to other nanoparticles weakly connected in series or in parallel in our conducting junction. As suggested by the colorscale diagram, the gap shrinks when a magnetic field is applied. At the maximal available magnetic field $H \simeq 5$ Tesla, the critical current is $i \simeq 130$ nA since as stressed above our magnetic fields are not strong enough to completely suppress superconductivity. The three other less resistive junctions give similar dV/di dependence (see Fig. 3.21). In these other samples more peaks are apparent and one of the junctions was hysteric. Figure 3.21 also presents the low temperature differential conductance of the resistive junction with room temperature resistance of 10 MΩ. At low temperature this sample becomes insulating at low bias voltage. When the bias

exceeds 100 mV the conductance starts to increase following a cone shape typical for graphite but a priori unexpected in our samples. An hysteric singularity appears when the bias reaches a value around −3 V. Although it is hard to determine with certitude the origin of this hysteresis we note that −3 V is close to the estimated HOMO-LUMO gap in DNA and that similar singularities were observed at room temperature in the conduction of DNA/lipid films confined between nanogaps [40]. In this respect this is the only sample whose DC transport characteristics can hardly be mimicked by a metallic short-circuit of very small dimensions.

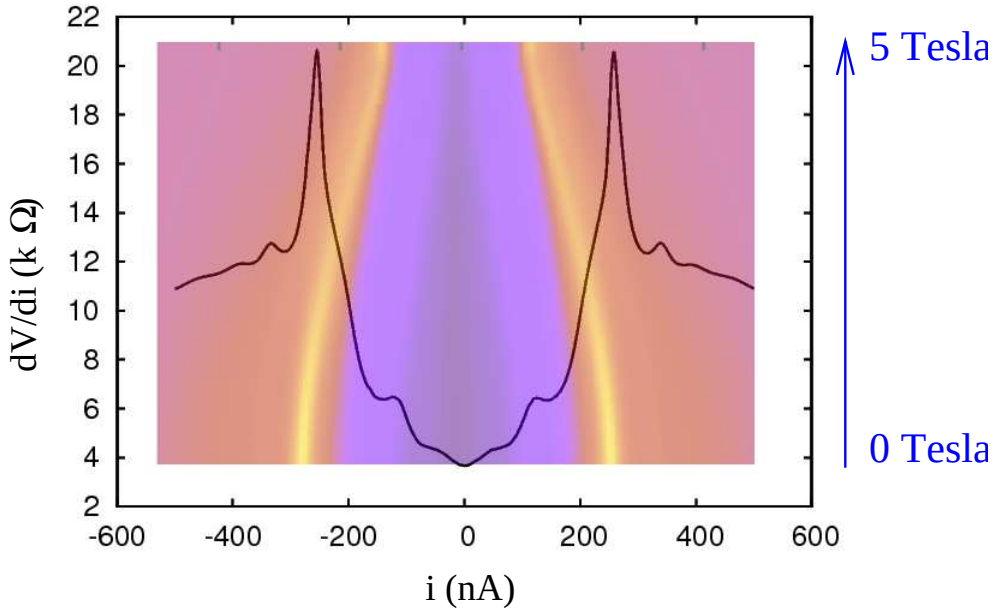

FIG. 3.20 – The black curve represents the differential resistance dV/di as a function of DC current through the 10 kΩ sample at 100 mK. The color inset in the background shows the evolution of the differential resistance encoded as a color scale with yellow/violet representing maximal/minimal differential resistance. The x axis represents the DC-current as in the main figure, and the y axis indicates the magnetic field ranging from 0 to 5 Teslas.

In order to search for sample characteristics which might be specific of DNA molecules we have irradiated our samples with microwaves. Our idea was that the helix structure of the molecule could induce special magnetic field asymmetry in the out of equilibrium transport across the molecule. This expectation was not confirmed experimentally since the $R(B)$ dependence under irradiation remained rather symmetrical. However the DC-magnetoresistance of our samples could become unstable under microwave irradiation (see Fig. 3.22). Interestingly instabilities were observed mainly at rather low frequencies $f <$ 1 GHz. A possible (although science fiction like) interpretation is that the microwave field excites a mechanical transition between two possible equilibrium positions for a DNA molecule suspended across the peaks created on both sides of the gap by the FIB etching ; in this scenario the superconductivity just enhances the sensibility to these mechanical

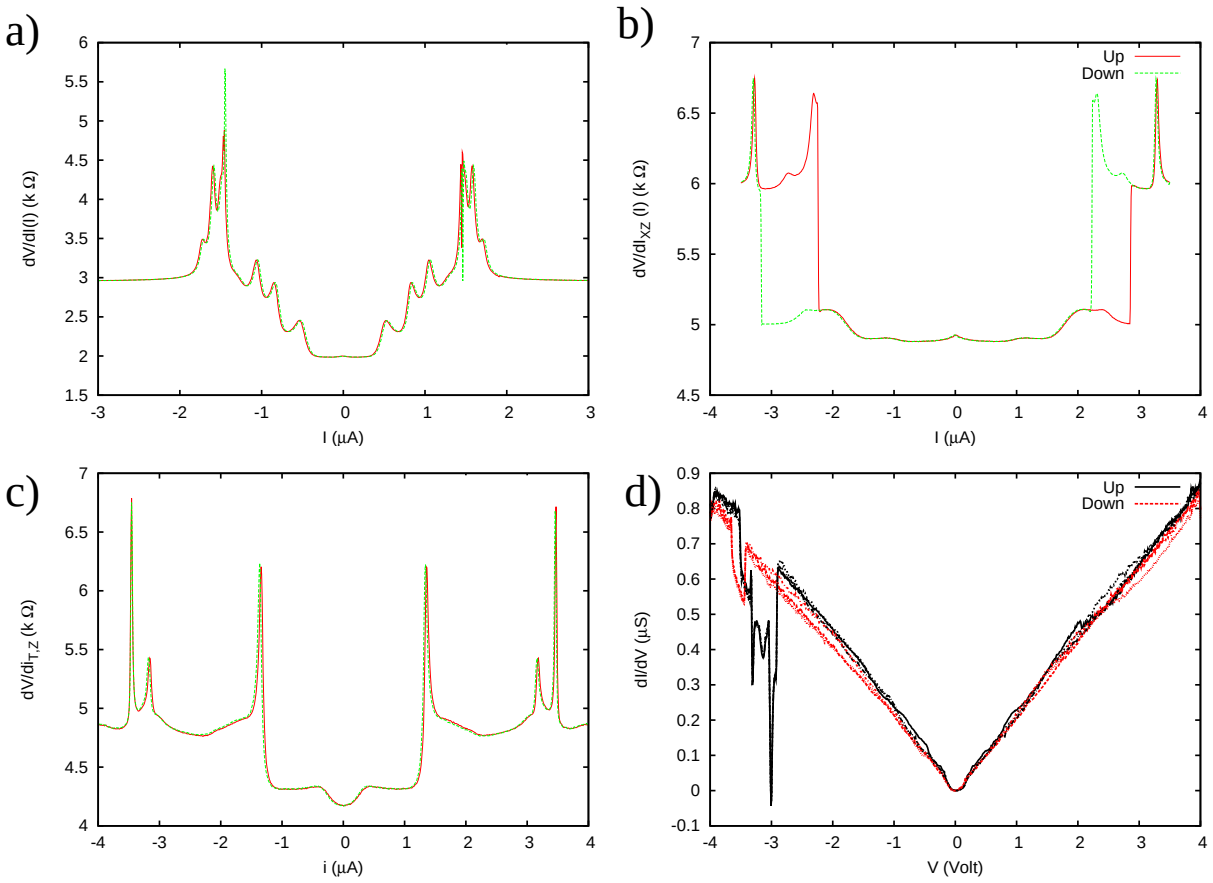

FIG. 3.21 – The panels a,b,c. show the differential resistance of the 3 $k\Omega$, 4.8 $k\Omega$ and 6.1 kΩ samples which have a superconducting behavior. The panel d. displays the differential conductance of the resistive 10 MΩ sample. Temperature was 100 mK.

vibrations. However one must take into account that the response to microwave may be very complicated in superconducting weak links where the switching may become chaotic. In particular magnetic field anti-symmetric photovoltaic effect was observed in such systems by [41]. Hence the presence of a magnetic field asymmetry does not allow to discriminate between a chiral molecule like DNA and an array of superconducting weak links.

In the above experiments we have assumed that superconductivity was induced by superconducting nanoparticles because of the high critical magnetic fields. Yet it is not the only possibility since FIB irradiation can induce superconductivity in materials with otherwise very small critical temperatures. For example the tungsten deposited under FIB has critical temperatures around 4 K and a high critical magnetic field of 4 Tesla. Hence there is also a possibility that the pics observed on the edges of the gap (see Fig. 3.16) could become superconducting due to a high concentration of incorporated Gallium atoms. In order to check experimentally if this is indeed the case we have deliberately prepared a short-circuit across a clean Pt film by stopping the FIB etching before the gap became completely insulating (this may be compared with Fig. 3.15 where the metallic film was

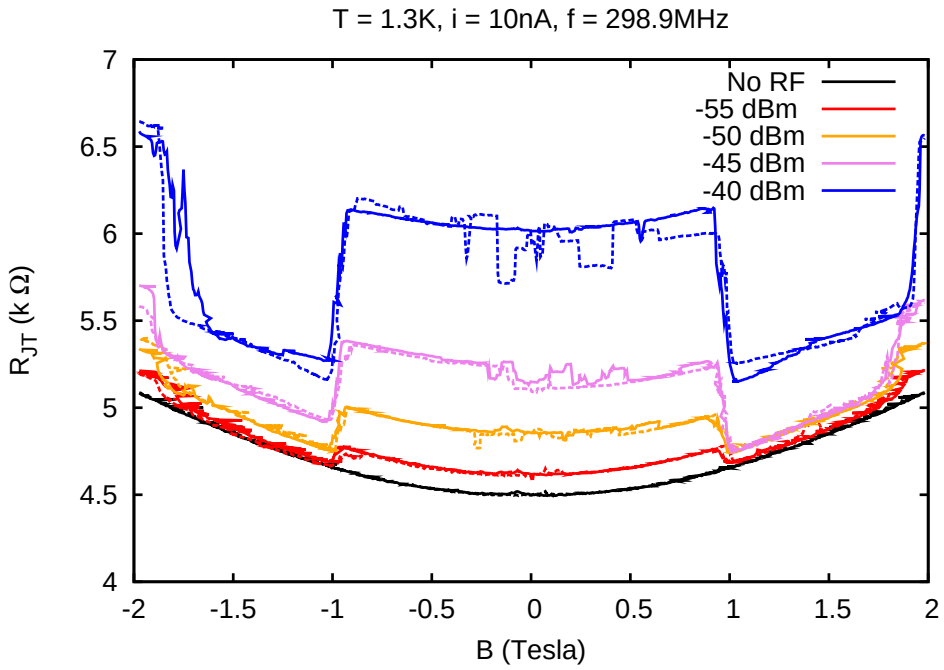

FIG. 3.22 – Magnetoresistance of the 10 $k\Omega$ sample for several microwave powers. Microwave frequency was $f = 298$ MHz.

etched until the gap became insulating). In this control sample superconductivity was absent, but low temperature measurements revealed a low bias differential resistance peak which grow at low temperature (see Fig. 3.23) in a behavior reminiscent of dynamical Coulomb blockade [12]. The effect in Fig. 3.23 is smaller by an order of magnitude compared to Ref. [12]. This is probably because we measured a short-circuit much more conductive than conductance quantum, however short-circuits formed by FIB can be more resistive see for e.g. Fig. 3.15. Hence FIB etching can create quasi-one dimensional filaments inside the gap capable of producing dynamical coulomb blockade behavior. However it does not induce superconductivity on the edges of the gap and the origin of superconductivity can only be attributed to the presence of superconducting nanoparticles inside the insulating gap.

In general these superconducting nanoparticles are unlikely to induce superconductivity in a normal metal because of the inverse proximity effect. Direct proximity effect is possible in this regime only if the density of states in the normal metal is very low. For example it was recently proposed that nanoparticles could induce superconductivity in graphene [42]. Since DNA molecules have a very low density of states they are good candidates for forming the normal region of our SNS junctions. The image that then comes to mind (see Fig. 3.23) is that of a DNA molecule connecting several nanoparticles and connected to the normal PtC contacts.

However it is also possible that the nano-filaments created by FIB can be small enough

for the direct proximity effect to be possible. Indeed, even if the gaps were insulating before deposition of DNA, one can imagine that the metallic residues inside the gap could have been displaced by the DNA molecules creating a leak. Note that the absence of superconductivity in the control sample from Fig. 3.23 does not rule out this scenario. Indeed we will show in the next chapter that the deposition of nanoparticle is not a reproducible phenomena and a single control short-circuit sample may not be representative. It is actually hard to discriminate between these two possibilities. Our samples do not have a backgate since they are prepared on mica, heating up to the denaturation temperature of DNA is not possible since pure Gallium melts at low temperature of $\simeq 30$ °C and experiments in liquid may simply break the device by removing the pentylamine layer. As a result we have chosen ultraviolet (UV) irradiation as the most distinctive experiment, indeed it is well established that UV can damage the DNA molecules whereas it is not harmful for a metallic film provided that there is no heating from the UV lamp. We tried to irradiate one of the samples with an UV irradiation with wavelength $\lambda = 233$ nm. The electrical conduction disappeared immediately (on the scale of seconds) after the UV lamp was switched, whereas the resistivity of a platinum film of a few nanometers thickness did not change after an hour of irradiation. Even if this experiment is spectacular it is not necessarily conclusive because an electrical discharge could have occurred when the lamp was switched on (the lamp and resistance measuring equipment are connected through a common connection to the ground). Probably in future experiments UV must be attenuated to observe a more progressive transition. In our case we had to spare samples for more detailed AFM studies and these experiments have not yet been performed.

If our interpretation in term of proximity-induced superconductivity in DNA molecules is valid, the number of peaks in the differential resistance measurements (see Fig. 3.20 and Figs. 3.21.a,b,c) gives an estimation of the number of nanoparticles connected to the DNA molecules that transit to the superconducting state. Two limiting cases may occur depending on the number of connected DNA molecules that exhibit proximity induced superconductivity :

- **1.** It is possible that only a single molecule transits into the superconducting state. In this case each peak in the differential resistance should correspond to the critical current of a superconducting nanoparticle connected to the superconducting DNA molecule and the number of peaks should give the number of nanoparticles connected to the superconducting DNA molecule. In our samples the number of peaks varies from 3 to 6 (sample from Fig. 3.21.b and Fig. 3.21.a respectively). By dividing the average length of the gap by the number of connected nanoparticles, we can estimate the typical length of the individual DNA segments that connect neighboring nanoparticles (see Fig. 3.24 for a sketch of the geometry). For a gap width of approximately 100 nm, we find that this length scale varies from 15 nm to 30 nm.
- **2.** In the opposite limit, we can assume that there is only a single connected nanoparticle per superconducting molecule. Under this assumption the number of peaks gives the number of superconducting molecules. The transport in DNA molecules in this configuration is typically probed on a length scale corresponding to half of the gap width : 50 nm.

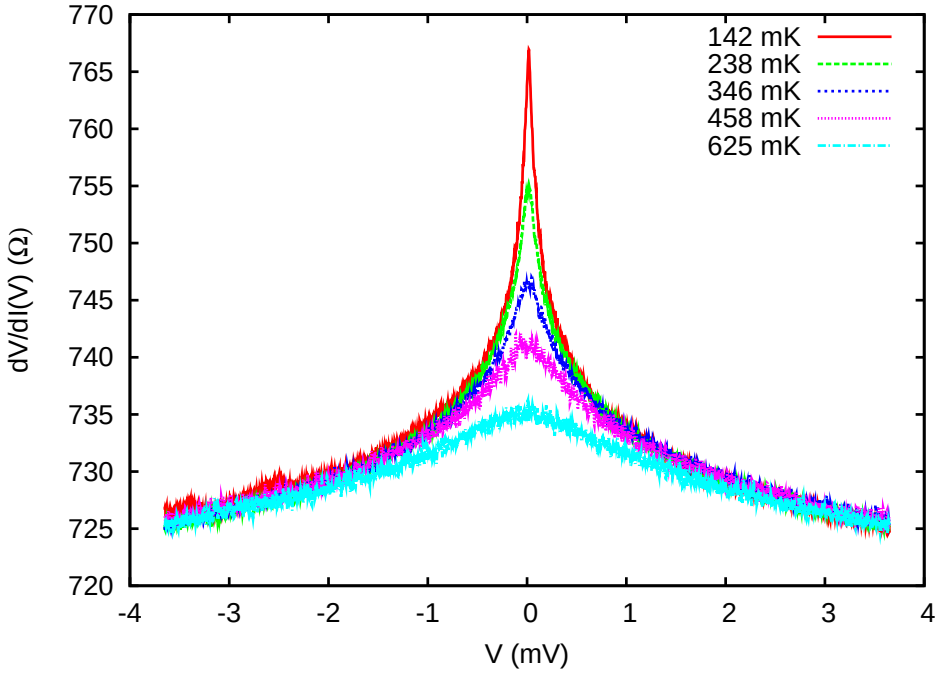

FIG. 3.23 – Differential resistance at several temperatures as a function of applied voltage for the control short-circuit sample without DNA. During the FIB etching the sample resistance was increased from 1.2 kΩ to 1.9 kΩ.

In conclusion the conductivity of DNA molecules is probed on a length scale between 10 and 50 nm which is smaller than width of the insulating gap which is around 100 nm wide. We note that transport in DNA on a 10 nm scale was reported by several independent groups for e.g. [10, 21].

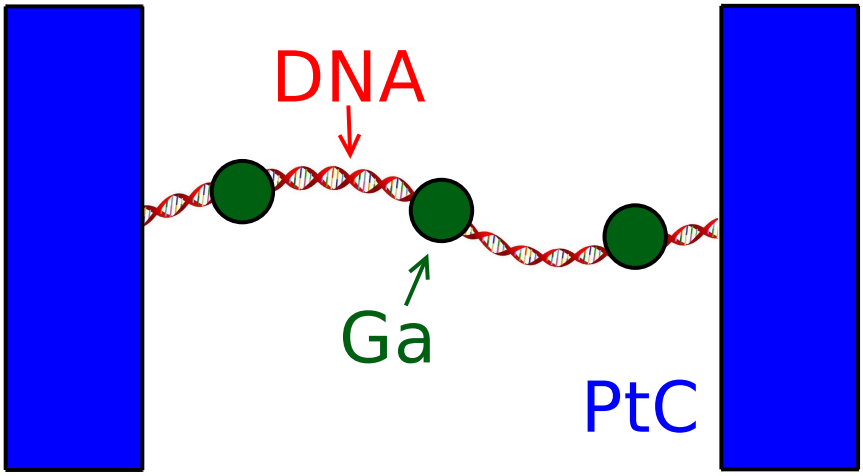

FIG. 3.24 – Schematic representation of a conducting DNA molecule contacting the normal PtC electrodes and superconducting Gallium nanoparticles.

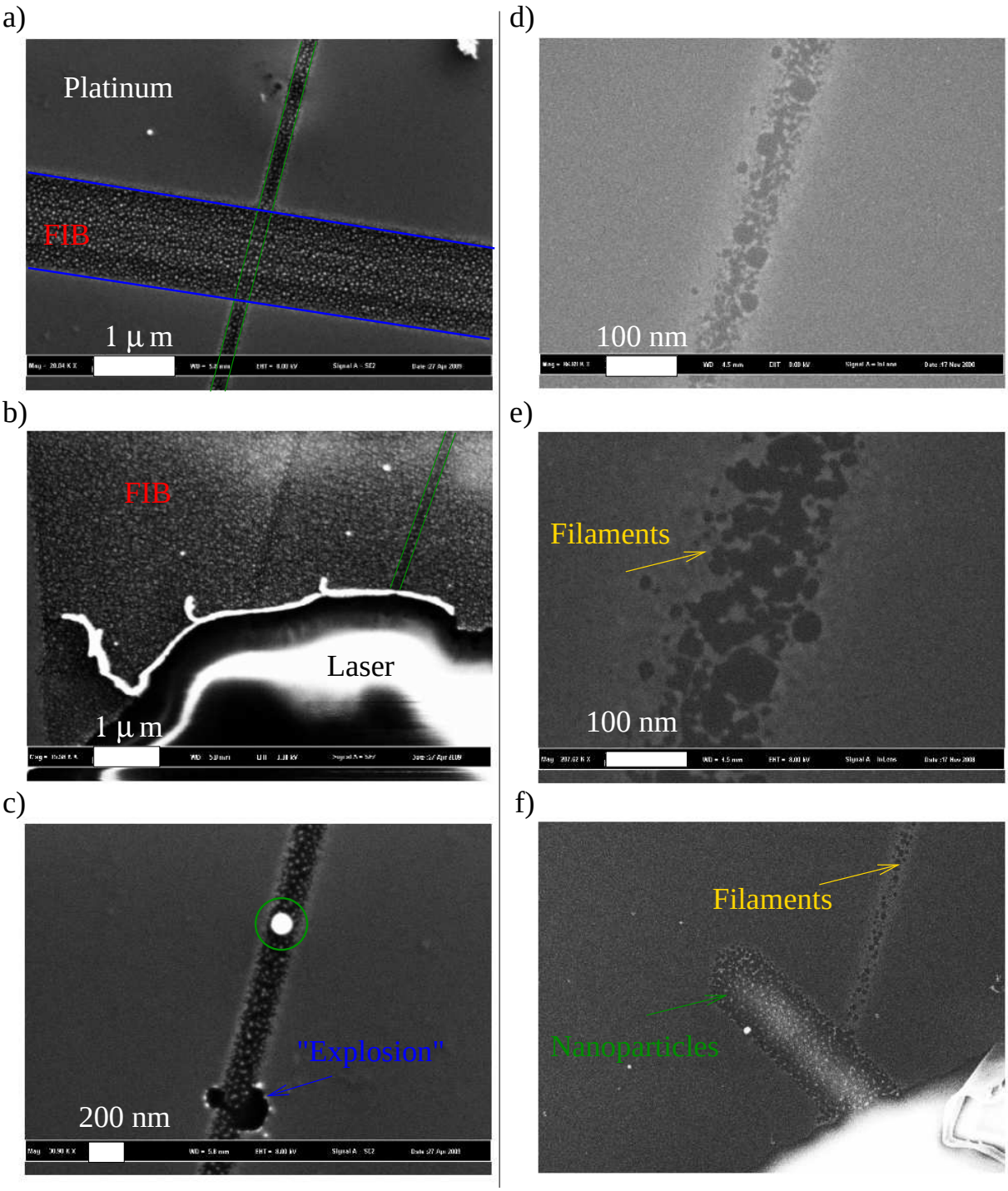

FIG. 3.25 – (left) SEM images of the gaps from our experiment. Images a,b and c were taken on the control sample from Fig. 3.23. Even if we know that a short-circuit was present we could not find it under SEM, probably because the slit is long and the short-circuit is very narrow. (right) The SEM images d,e and f where taken from a sample used for deposition of DNA molecules.

3.9 Characterization of the gaps from our transport experiments

The topography characterization of the gaps etched by FIB was already exposed in Chap. 3.7 and I will start this characterization chapter by describing the scanning electron microscope (SEM) images of our gaps. SEM provides a strong contrast between insulators and metals, whereas AFM in tapping mode is only sensible to topography. Hence SEM is a good technique to detect metallic residues inside the gap where the topography is rough after FIB etching. Note that no careful SEM analysis of the gaps was done in the previous experiments [11, 12], however it is very likely that the gaps used in these experiments had a similar structure specially in [12] where they were also fabricated by FIB.

Several SEM images of the FIB gaps are displayed on Fig. 3.25, intriguingly in all the images metallic contamination is present in the gap after etching. Two possible limit situations seem to emerge from our observations. In the case where the FIB dose is weak the metallic residues take the form of filaments (Fig. 3.25 right panel) whereas after a stronger dose the residues seem to form an ordered network of nanoparticles (Fig. 3.25 left panel). This transition may be inferred from Fig. 3.25.f, where two neighbor regions were etched with different FIB doses under the same beam conditions. In the narrow trench filaments can be clearly distinguished (see also Figs. 3.25.d,e) while in the wider trench where the dose was stronger residues form individual nanoparticles. Naturally one can expect the residues to disappear after a sufficient FIB dose. This dose however seems difficult to attain in practice. This difficulty is illustrated on Figs. 3.25.a,b. In the first figure two intersecting regions were etched with FIB (they are highlighted by blue and green lines). Both regions were exposed to a dose sufficient to etch most of the metallic film leaving isolated nanoparticles inside the gap. Surprisingly the density of nanoparticles does not decrease in the intersection between these two regions (parallelogram with edges formed by blue and green lines) even if the intersection area received a dose about two times larger than the other regions. A similar situation is observed on Fig. 3.25.b, where a large area was etched by FIB irradiation around a slit cut by FIB (delimited by the parallel green lines). The region inside the slit still contains nanoparticle even if it received twice an irradiation dose capable of etching most of the platinum film. As a result the dose needed to completely etch all metallic residues, is certainly much larger than the minimal dose required to create an insulating slit.

The presence of nanoparticles has two possible origins, an instability of the gallium tip that can start to emit small nanoparticles instead of individual gallium ions and the recombination of the gallium atoms on the mica surface (the latter mechanism is then specific to mica since it is not observed on Si/SiO_2). Our observations suggests that both mechanisms are possible. On one sample we have detected nanoparticles everywhere inside a large square area corresponding to the scan size of the FIB (see Fig. 3.26). This proves that in some uncontrolled regime FIB is capable of disseminating small nanoparticle instead of individual gallium ions. The above behavior was observed on only a single sample, however this was the sample that we studied at low temperature in Chap. 3.8, hence this rather

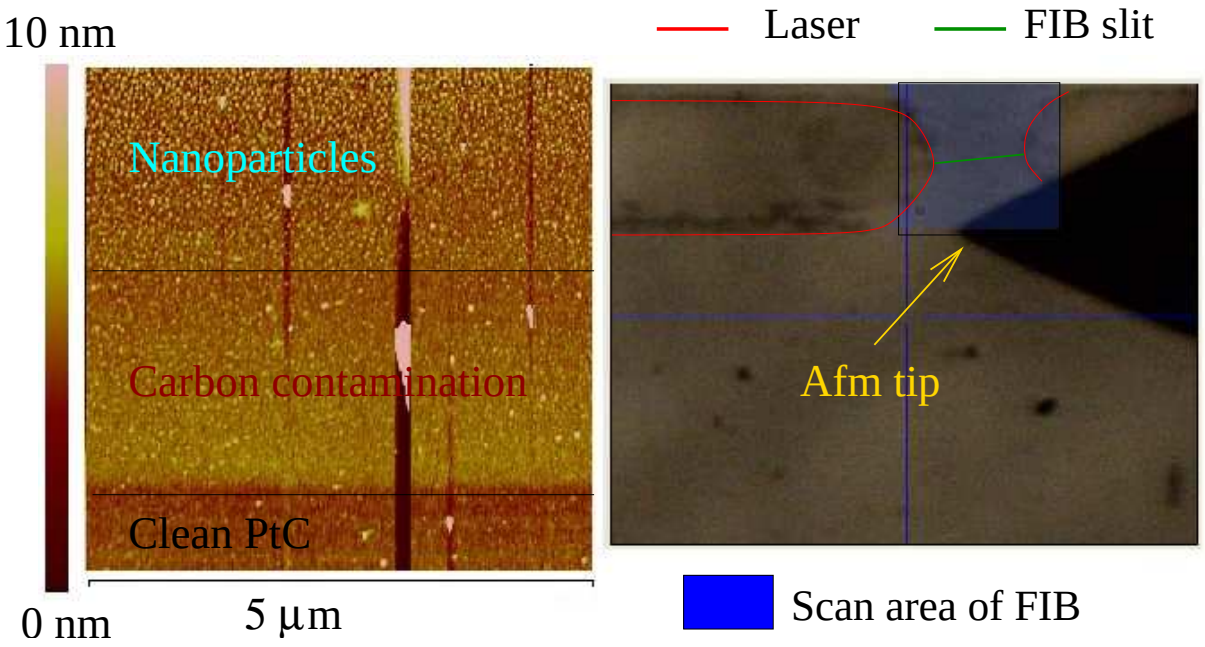

FIG. 3.26 – (left) AFM image showing the boundary of the area contaminated by nanoparticle, it almost coincides with the border of the contamination layer deposited by FIB. This image was taken on the sample measured at low temperature in Chap. 3.8 and is representative of the other slits on that substrate. The typical height of the nanoparticle is between 5 and 7 nm which is compatible with the estimates from Chap. 3.8. (right) The position of the AFM tip is shown on an optical microscope photograph and coincides with the border of the FIB scan windows with size $\simeq 100\ \mu\text{m} \times 100\ \mu\text{m}$).

special case is very important for the interpretation of our transport measurements. In other samples nanoparticles were observed only inside the gap indicating a different origin. It may be possible that Gallium atoms recombine on the mica surface to form nanoparticles. Note that a similar behavior has been observed on GaAs substrates [43] and the presence of Aluminum atoms in mica substrate may play a role.

The atomic force microscopy measurements on the edge of the FIB scan window depicted on Fig. 3.26, revealed another source of contamination. A step of $1-2$ nm height systematically surrounded the FIB scan window, this contamination layer is probably composed of carbon deposited during FIB imaging of the gaps (similarly to a contamination layer deposited under SEM). This is actually very discouraging because the FIB technology was chosen because it supposedly limited contamination. In reality the electrodes are covered by a poorly characterized carbon contamination layer. As a side consequence this makes the debate on platinum versus platinum carbon electrodes not pertinent near the slits.

I will now summarize the different contamination sources that were revealed through SEM and tapping mode AFM microscopy. On mica substrate it seems that metal residues are always present inside the gap (at least for practically reasonable FIB doses). They can

take the form of narrow filaments for low FIB doses or a net of nanoparticles at high doses. An exceptional regime can also occur where the gallium tip of the FIB becomes unstable and starts to stew nanoparticles everywhere in its scan area. From our experiments this case seems rather improbable however it occurred at least once, on the sample that we measured at low temperatures. Finally a carbon contamination layer is deposited near the gap during the imaging inside the FIB microscope. Keeping in mind the above information, I will now focus on the detection of DNA molecules across the gaps where conduction was observed after deposition of DNA molecules.

In previous experiments [11, 12] DNA molecules crossing FIB slits could be detected with tapping mode AFM. However AFM and low temperature transport measurements were done independently, and probably on different samples while we know that fluctuations are very strong from one sample to another. Thus the correlation between the presence of DNA molecule and the appearance of electronic transport was supported only by a statistical argument (absence of conduction on control samples when a buffer solution without DNA was deposited). Here we tried to detect DNA molecules on the three samples where conduction was induced after the deposition of DNA molecules with the pentylamine technique was attempted.

We will start with two samples where conduction was destroyed during the attempts to contact the samples electrically (see Chap.3.8). In one of the samples DNA molecules could be observed both in the region far from the gaps where PtC was clean and inside the area covered by the carbon contamination film near the gap as illustrated on Fig. 3.27. On this sample we could confirm the presence of DNA on some of the conducting slits. It was however impossible to make a complete statistic because after the electrical conduction was destroyed we tried to recover the conduction by keeping the sample in a humid atmosphere for a couple of days. This procedure did not restore the conductivity but it led to the formation of unidentified "contamination pancakes" on the sample surface which impeded further AFM characterization.

In the next samples (DnaBox3A) were taken after silver paint and ultrasound bonding that destroyed conductivity across the slits. The experiments were done in this order because priority was given to transport measurements over AFM characterization and we were afraid that the AFM tip could damage conducting DNA molecules when scanning. Hence only the previous sample (Fig. 3.27, DnaBox3B), was well characterized before transport measurements. We then (misleadingly) assumed some homogeneity between the samples. Actually the AFM pictures from Fig. 3.28 reveal a different behavior from sample DnaBox3B. Many combed λ molecules could be observed far from the thin FIB slits outside the carbon contamination layer. Near the slits however the surface was very different, it included small holes around 3 nanometers deep and no visible DNA molecules.

The absence of DNA molecules near the gap inside the carbon contamination layer, was observed for at least two other samples, including the sample DnaBox2B where electron transport was investigated in Chap. 3.8. The situation on this sample is depicted on Fig. 3.29, far from the gap the surface is clean. The region near the slit is covered with nanoparticles (see also Fig. 3.26) but the apparent density of DNA molecules seems very low. Indeed after scanning across the entire length of a conducting FIB slit at most a single

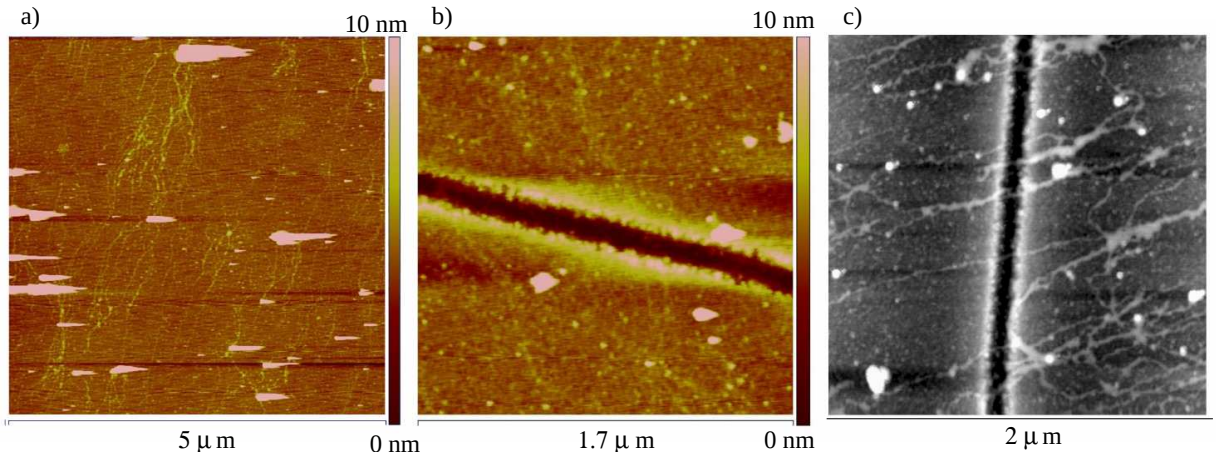

FIG. 3.27 – (Sample DnaBox3B) AFM microscopy images of a sample where conduction was observed after deposition of DNA. DNA molecules can be observed far from the gap on the clean PtC surface (panel a) and near the gaps. Some molecules crossing the slits were also observed on this same sample (panel b). The gap shown on panel b was conducting after deposition of DNA and took the following resistances 1.8 kΩ → 160 kΩ →> 1000 kΩ → 5 kΩ → ∞ while we tried to make contacts with silver paint on the sample. Panel c. shows an image of DNA molecules crossing a slit obtained by D.Klinov, most likely on the same sample.

molecules could be seen near the gap (Fig. 3.26.c). On the one hand the fact that we do not observe DNA molecules does not prove that they are completely absent in the gap. Imaging conditions could be spoiled because of the presence of nanoparticles/holes in the contamination layer. We note that further AFM characterization, performed by Dmitry Klinov using a sharper tip revealed some molecules crossing the FIB slits (see Fig. 3.30), which supports this hypothesis. On the other hand, it is also possible that the presence of a FIB contamination layer reduces significantly the efficiency of the pentylamine plasma. This claim may seem strange since the experiments described in Chap. 3.6 demonstrate that pentylamine is a reliable technique to attach DNA on metallic electrodes with a sufficient quantity of carbon atoms on the surface. The above description apriori apply to the FIB contamination layer. A hint on why this argument can fail, is provided by the insitu transport measurements inside the FIB chamber. As mentioned in Chap. 3.7 the resistance generally decreased slightly at the beginning of the FIB etching. Probably during this time the deposition of contamination prevailed over etching, the drop of resistivity then indicates that the carbon contamination layer is rather conducting and probably locally graphitic. This claim is supported by the fact that platinum can be used as a chemical vapor deposition (CVD) catalyst for the growth of single wall carbon nanotube [44]. A last argument in this direction comes from the differential conductance of the resistive sample on Fig. 3.21 which has a cone structure very similar to the density of states in graphene ; it is possible that accidentally the current passed through a flake of few layer graphene in this sample. Since graphite is very stable the available number of carbon atoms that can serve

to anchor the pentylamine plasma can be greatly reduced compared to the situation where for example, the surface is covered with amorphous carbon. This can make the pentylamine film less stable on the surface so that sometimes it is removed when the sample is dried in a scenario similar to that described for mica in Chap. 3.6. The holes observed on Fig. 3.28 give a cue in this direction since they show that a layer at least 3 nm thick was partially removed from the surface.

To summarize even if DNA molecules were detected across some conducting slits, it was not possible to establish a clear correlation between conductivity and the presence of DNA molecules on the basis of our AFM measurements. The major obstacle comes from the contamination layer deposited by FIB around the slits. Due to this layer DNA deposition near the gap does not take place in the same conditions as everywhere else on the clean PtC surface and the density of DNA molecules seems reduced near the gap on several samples. We have argued that the pentylamine layer may not be stable enough because the carbon layer deposited by FIB is partially graphitic and provides few fixation points. This hypothesis also gives an interpretation for the transport data on the resistive sample from Chap. 3.8 (Fig. 3.21.d) where a graphene/DNA junction may incidentally have been formed.

We now turn our attention to the last characterization issue of this chapter. The pentylamine plasma creates a positively charged organic layer that allows to bind DNA molecules onto the electrodes. This layer is believed to permit a favorable interaction regime between molecules and the substrate where DNA can be conducting [12]. However if this layer is continuous it forms an insulating separation between DNA on top of the layer and electrodes at the bottom. In a few samples we have noticed holes after deposition of DNA on the pentylamine treated surface. Nevertheless in the majority of cases the surface remained smooth even after deposition of pentylamine and DNA molecules with a roughness similar to that of the clean Platinum/Carbon surface. We suspect that holes appear when pentylamine is not stable enough on the surface and partially desorbs in the buffer during the deposition of DNA. From this point of view the depth of the holes gives an estimation of the pentylamine film thickness. In the two cases displayed on Fig. 3.28.d and Fig. 3.28.f this depth is respectively 3 and 1 nm. These values support the picture of a continuous insulating layer and cast doubt on the possibility of an electrical contact between DNA and electrodes in presence of pentylamine. Note that these values in the range of a few nanometers, are even smaller than those measured in Ref. [45] where a different plasma functionalization was used to deposit a positively charged organic layer. Plasma discharges are even used industrially to grow silicon nitrate when both ammonia and silane are present in the discharge chamber with a typical growth rate of $20 - 50$ nm/s [46, 47]. In view of the above data, our estimates for the thickness of the pentlyamine film are very plausible.

In order to determine experimentally whether electrical contact between DNA and electrodes is possible in our samples we have carried on conducting AFM experiments at the Institute for Electronics, Microelectronics and Nanotechnology (Lille, France) in the group of D. Vuillaume. When we performed conducting AFM scans over the PtC electrodes no current was detected between the tip with a typical bias of 100 mV and the grounded sample electrodes. The absence of current is probably due to the insulating pentylamine

layer between the tip and the electrode surface. To check whether the absence of conduction was due to the insulating pentylamine layer, we scratched the surface in contact mode until conduction appeared probably removing the pentylamine on top of the electrode surface. Once a finite current appeared we switched back to tapping AFM mode and scanned the surface over a wider area. An AFM image obtained during the described experiment is presented on Fig. 3.31.b. A hole roughly 1.5 nm deep was drilled in the region where the substrate was scratched until conductivity appeared. Probably this value provides a measurement of the pentylamine film thickness which in this case also is in the range of a few nanometers.

Conducting AFM data in the bulk of the electrodes indicate that it is very difficult to establish an electrical contact between DNA molecules and the electrodes beneath probably because of the presence of the pentylamine layer. On the edge of the FIB slits however the situation is different. A comparison between conduction (Fig. 3.31.c) and topography (Fig. 3.31.d) images in the region of a slit shows that the edge of the gap are not covered by the insulating film and contact is possible in this region. The above images were recorded on a slit from the sample where low temperature conduction properties were investigated in Chap. 3.8. They also give a clue on why inverse proximity effect does not occur in the conduction model from Fig. 3.24 where DNA becomes superconducting due to nanoparticles of diameter 10 nm although it is deposited on normal electrodes. Indeed even if the molecule rests almost entirely over the normal electrodes, electrical contact can be established only in a region of a few nanometers near the gap.

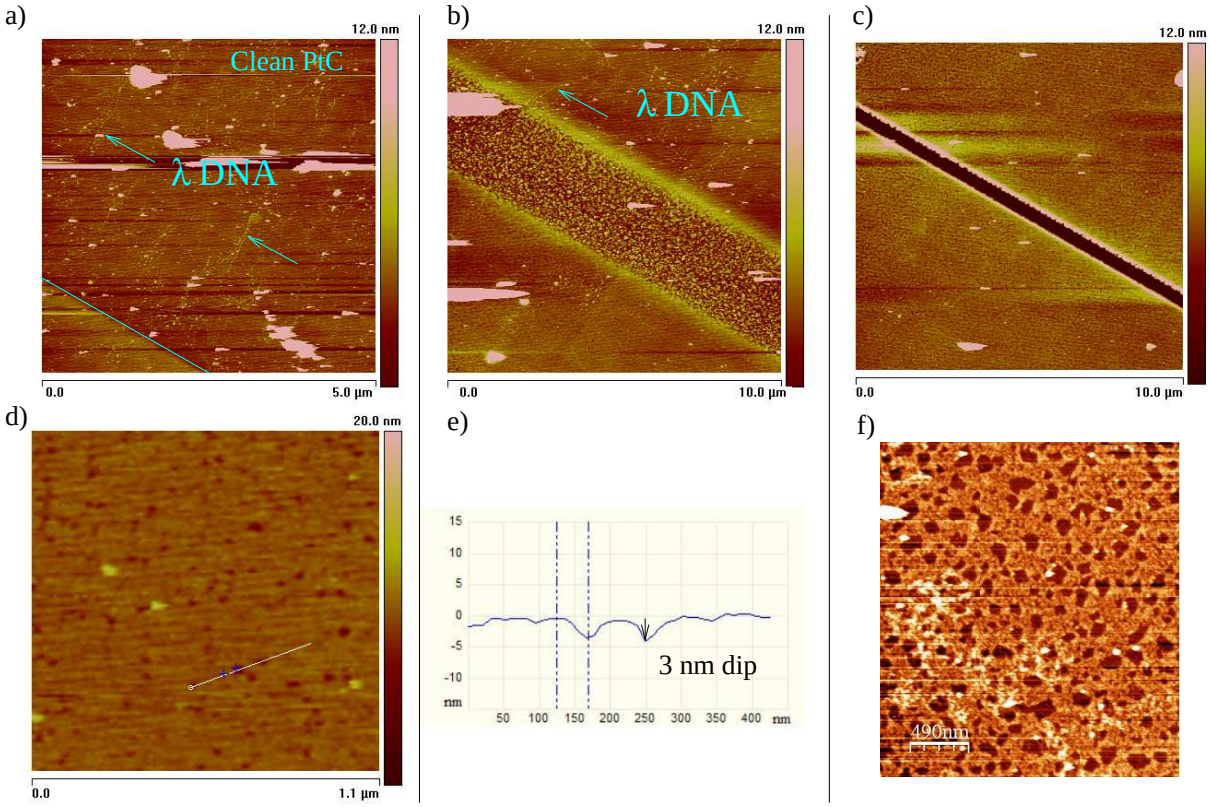

FIG. 3.28 – (Sample DnaBox3A) AFM microscopy images of one of a sample where conduction was observed after deposition of DNA molecules. As on Fig. 3.27 DNA molecules can be observed far from the gap on the clean PtC surface (panel a). some DNA molecules cross the border of the carbon contamination. On panel b) the λ molecules cross a large trench (not connected electrically) cut by FIB inside the carbon contamination layer. The λ concentration seems to drop on the bottom side of the trench, one can notice small holes in the substrate in this region. Panel c) is an AFM scan around the narrow FIB slit that is connected electrically. No DNA molecules could be seen in this region, although we were able to resolve many DNA molecules on the same scale on panels a) and b). Panel d) shows in more detail the small dips in the surface. The depth of these holes is measured on panel e) and is approximately $\simeq$ 3 nm. Panel f) displays another sample where holes appeared after deposition of DNA on a PtC substrate using pentylamine functionalization (hole depth was $\simeq$ 1 nm). The formation of holes was not observed on other samples.

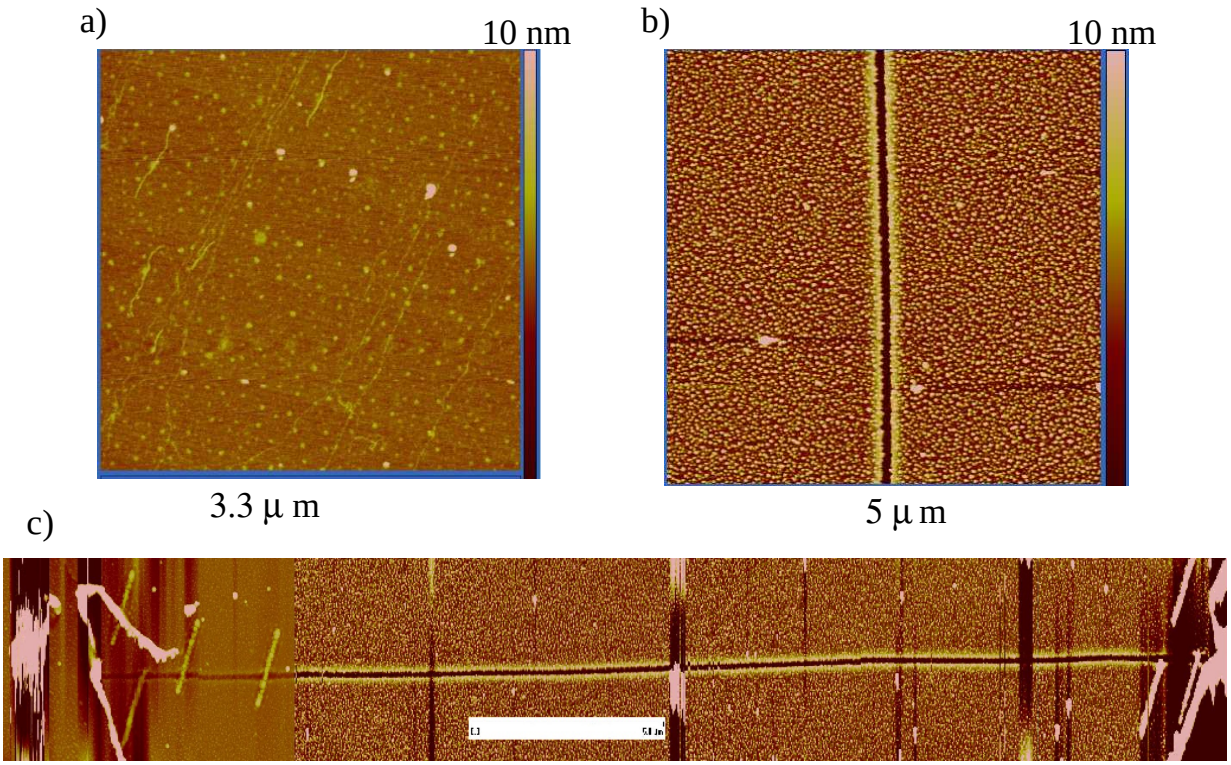

FIG. 3.29 – (Sample DnaBox2B) AFM microscopy images from the sample where low temperature transport was investigated in Chap. 3.8. Panel a) shows DNA molecules observed far from the slit, panel b) shows a 5 μmm $\times$ 5 μm image of a slit that became conducting after deposition of λ-DNA molecules whereas panel c) displays several $5\mu \times 5\mu$ scans merged together to form a complete AFM image of a gap. Figure Fig 3.30 obtained by Dmitry Klinov using an ultrasharp AFM tip, shows at least one DNA molecule that crosses the insulting gap cut by FIB.

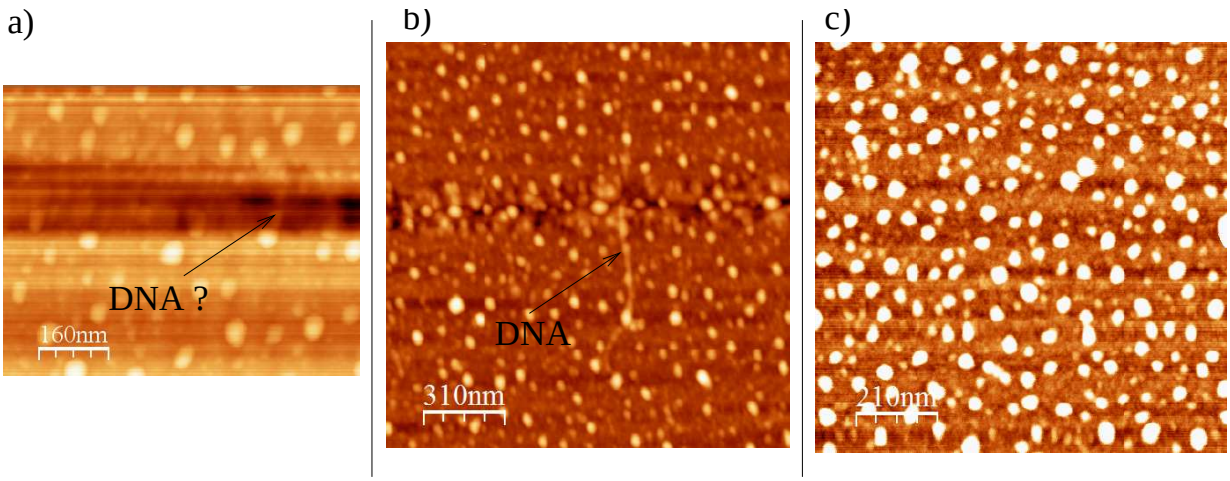

FIG. 3.30 – (Sample DnaBox2B) AFM microscopy images from the sample where low temperature transport was investigated in Chap. 3.8. These images were taken by Dmitry Klinov using an ultrasharp AFM tip, some images show the presence of DNA molecules close to the insulating gaps (panel a) and b)). However on typical images DNA molecules seem absent (see panel c of this figure, or Fig. 3.29 which was obtained in Orsay).

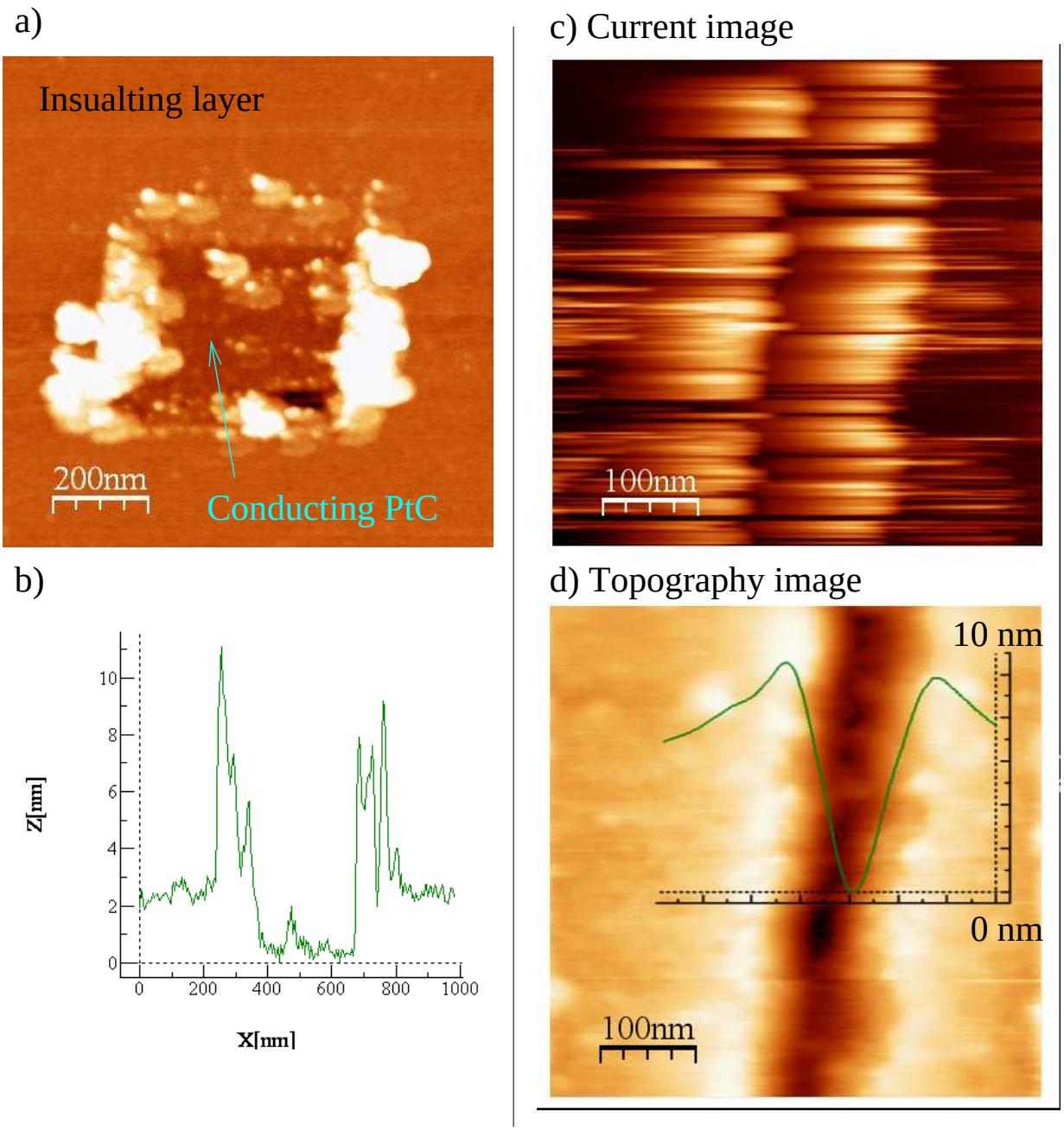

FIG. 3.31 – a) The sample is PtC with deposited pentylamine and DNA. A small square region was scratched with the AFM tip until conduction was observed. This image is a tapping mode picture of the hole formed after this procedure (see cross section on panel b). c) Conducting AFM image of a conducting slit from Chap. 3.8 where low temperature transport was studied (see also Fig. 3.29). d) Contact mode topography image of the same slit.

3.10 Conclusions on DNA transport experiments

I will first summarize the experimental results obtained in the previous chapters.

- **Chap. 3.3** describes the λ DNA solution that was used in all our DNA deposition experiments and showed that it yields satisfactory deposition onto mica.
- **Chap. 3.4** shows that binding through DNA extremities allows to deposit molecules on a metallic platinum substrate. No conduction was observed in this case, in agreement with most of other works.
- **Chap. 3.5** describes the pentylamine plasma functionalization for the adsorption of DNA molecules. We argued that this technique is reliable only on carbon coated surfaces. When it is applied on mica the pentylamine layer is probably removed at the last step when the sample is dried explaining the absence of DNA molecules on the surface.
- **Chap. 3.6** we demonstrated that reliable combing of DNA molecules across insulating slits can be achieved combining pentylamine and rinsing in a steady flow of water. However the samples we prepared with this technique exhibited insulating behavior for both samples prepared by electron beam lithography and ion beam etching. A possible reason for the absence of conductivity may be that a thin layer of amorphous carbon was evaporated at the last step just before deposition of pentylamine and DNA molecules. While it ensured a good adhesion of pentylamine it could render the edges of the gap insulating by stabilizing the pentylamine even there (see Chap.3.9). Conducting atomic force microscopy (AFM) measurements could have shown if this explanation is true.
- **Chap. 3.7** explains how the gaps for deposition of DNA were fabricated using in situ resistance measurements inside the focused ion beam microscope (FIB). AFM topography of the gaps is also discussed. Starting from this chapter deposition of DNA molecules was done by D. Klinov.
- **Chap. 3.8** describes electrical transport measurements in the low temperature regime on samples where conduction was established after the deposition of DNA molecules. On four samples superconductivity was observed whereas a last resistive sample had a differential conductance similar to graphene. Due to high critical magnetic fields around 10 Tesla we interpreted the observed superconductivity as proximity effect from superconducting nanoparticles inside the FIB slit. On a control sample where a short circuit was formed by stopping FIB etching before the sample became insulating no superconductivity was observed. However a zero bias anomaly was observed, possibly due to the formation of conducting nanofilaments in the gap during the FIB etching. Scanning electron microscope images of the filaments that may be formed are shown on Fig. 3.25.
- **Chap. 3.9** showed scanning electron microscope (SEM) and AFM images of the gaps. Metallic nanoparticles were identified on the sample from Chap. 3.8, they appeared because FIB worked in a special regime on this sample where it disseminated Ga nanoparticles everywhere. On other samples, both metallic filaments and nanoparticles were observed inside the gap. AFM characterization revealed that a carbon

contamination layer was deposited by FIB around the gap. We conjectured that this contamination layer was partially graphitic, this probably explains the poor reproducibility of deposition near the slits while good reproducibility was achieved in Chap. 3.6. This conjecture also gives insight on the origin of the "graphitic" sample that we measured in Chap. 3.8. Due to the limits of AFM resolution on the rough surface of the electrodes, we could not reach a definite conclusion on the presence of DNA molecules around the gaps. Figure 3.30 shows a few molecules in this region, however DNA was absent in most of our AFM images. Finally both tapping and conducting mode AFM indicate that pentylamine forms an insulating film of a few nanometers on top of the electrode surface. The electrical contact between DNA and electrodes seem possible only at the edges of the slit were conduction was observed in conducting mode AFM.

I will now focus on the conclusions that can be drawn from our experiments concerning the possibility of electrical transport across DNA.

- **Arguments in favor of DNA conduction.** Two main arguments can be retained to prove that transport was due to DNA molecules in our experiments. The first argument is statistical, for transport was not observed after deposition of a buffer solution without DNA. However one must be cautious with statistical arguments in these systems where sample to sample fluctuations are large. The destruction of conductance by UV irradiation with wavelength 233 nm is much more encouraging since it is hard to imagine how UV may destroy metallic nano-filaments. However the experiment was performed on only a single sample and more statistics and better control of irradiation doses are needed.

  Concerning the conduction data the observed proximity effect suggests that transport takes place across a nanowire with a very small density of states. It is tempting to conclude that only DNA molecules can match this criteria. However here also caution is required since we have shown that FIB can create narrow conducting filaments inside the slits whose properties are not well characterized (for e.g. they seem to exhibit dynamical coulomb blockade). Note that the resistive sample with hysteric behavior of differential conductance is in this respect an exception since transport is strongly non ohmic and suggests transport across a molecule. Ultimately one must keep in mind that even if the gaps are about 100 nm wide, transport may actually be probed on a much shorter length-scales around 10 nm due to the presence of metallic residues. The possibility of electron transport in DNA for very short fragments has now been reported by several independent groups, thus our results may be consistent with other experimental findings.
- **Strategies for future experiments.** Concerning the fabrication of samples with pentylamine plasma, it is probably better to replace mica by silicon. This will make possible the implementation of an electrostatic backgate, that could discriminate between DNA and a metallic short circuit. Another important aspect is to improve the reliability of the pentylamine plasma near the slits. Probably the best option is to limit as far as possible FIB imaging, technologically this may be achieved by cutting the FIB slits in the first stage when no alignment is needed (i.e. before laser

etching). Another alternative is to renounce using the FIB etching, and prepare a thin metallic film bellow the percolation threshold. Our experiments suggest that it would be possible to render this film conducting by depositing DNA molecules. From the measurement point of view experiments using UV/blue light irradiation at room temperature are most promising, alongside more detailed conducting-mode AFM characterization.

In the next chapter I will describe an experimental technique that we developed to probe phototransport in nanowires without direct electrical contacts that we plan to apply to DNA in the near future. In the last Chapter 3.12 we will discuss in more detail counterion condensation that played some role in the DNA deposition experiments from Chap. 3.6.

3.11 Contactless photoconductivity measurements on (Si) nanowires

Conduction properties of DNA are extremely hard to probe due to contact problems between electrodes and molecules. In this chapter we develop a technique to measure electronic transport in nanowires from the loss in a highly sensitive electromagnetic resonator. We implement this technique by investigating phototransport in both bulk silicon and silicon nanowires using a superconducting multimode resonator operating at frequencies between 0.3 and 3 GHz. We find that whereas the bulk Si response is mainly dissipative, the nanowires exhibit a large dielectric polarizability. This technique is contactless and can be applied to many other semiconducting nanowires and molecules. Our approach also allows to investigate the coupling of electron transport to surface acoustic waves in bulk Si and to electro-mechanical resonances in the nanowires.

In recent years transport properties of conducting nanowires attracted a considerable interest. Synthesis of carbon nanotubes and semiconducting nanowires opened the possibility of new mechanical, electronic and optical applications. For example carbon nanotubes allowed to fabricate single electron transistors operating at room temperatures [48], and very high quality nano-electromechanical resonators in suspended nanotube samples [49]. Numerous photonics applications were achieved with Si nanowires including microcavities and waveguides [50]. Despite these successes, our understanding of transport properties of nanowires is limited by our ability to make good ohmic contacts at low temperatures. Thus for carbon nanotubes the nature of electronic transport at low temperatures is still unknown (possibilities include formation of a Luttinger liquid or dynamical coulomb blockade) [51]. For more exotic nanowires like DNA, even qualitative information on whether the molecule is conducting or insulating is not reliable [2]. Measurements of DNA conductivity using a contactless microwave technique have already been reported [52], however the observed signal could also originate from ionic conduction inside the buffer or inside the hydration layer around DNA. Note that vitreous materials may also contribute to microwave loss even if they are insulating.

In this chapter, we propose a generic experiment to probe photoconductivity without direct contacts. To this end, we couple nanowires to a multimode electromagnetic (EM) resonator. Light irradiation is used to excite carriers in the nanowires which interact with the EM field of the resonator and change the resonance parameters. This allows us to discriminate clearly between the background signal (insensitive to light irradiation) and the signal from the (photoconductive) sample. We demonstrate this technique in practice, by measuring photo-transport in bulk silicon and Si nanowires.

Our probe is a multimode EM resonator formed by two superconducting meanders of total length $L_R \simeq 25$ cm (see Fig. 3.32.a). This structure has regularly spaced resonant frequencies given by $f \simeq f_n = nf_1$ where $f_1 \simeq 365$ MHz and n is an integer. The meanders were fabricated by etching a 1 μm thick niobium film with SF_6 reactive ion etching. During this procedure the meanders were protected by an aluminum mask patterned using optical lithography. In a last step Al was dissolved in a KOH solution [53, 54]. Two types

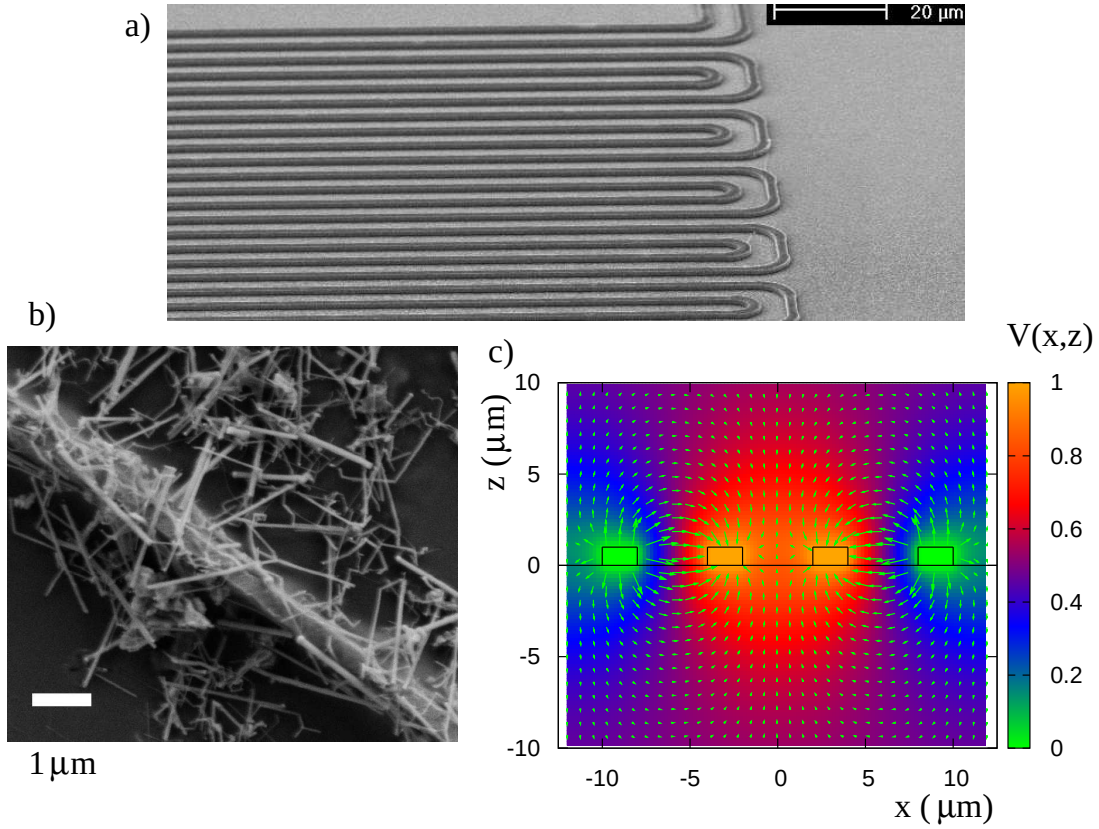

FIG. 3.32 – (Color online) a) Scanning electron microscope (SEM) image of the superconducting niobium meanders that form a multimode resonator. The substrate in this samples is Si/SiO_2. b) SEM image of a resonator after deposition of undoped Si nanowires, for this experiment the substrate is sapphire. c) FEM calculation of the electric field far from the meander boundaries. The color/gray scale indicates the value of the scalar potential $V(x, z)$ while the arrows show the direction and amplitude of the electric field $\mathbf{E} = -\nabla V$.

of dielectric substrates were used. In a first experiment the resonator was prepared on top of a Si/SiO_2 substrate (the oxide layer was $\simeq$ 500nm thick), which allowed us to probe conductivity of bulk Si under light irradiation (see Fig. 3.32.a). In a second experiment we used sapphire as dielectric substrate and we deposited vapour-liquid-solid grown Si nanowires [55] on top of the resonator (see Fig. 3.32.b). Note that sapphire remains insulating under blue irradiation (energy 2.5 eV) due to its high band gap of 9.9 eV.

The coupling between the resonator and the Si-nanowires is greatly enhanced by the resonator's meander structure which strongly confines the EM field near the substrate interface where the nanowires are deposited. We have checked this using a finite element (FEM) calculation of the potential and of the electric field. The results of the simulation are shown on Fig. 3.32.c, and clearly indicate that the electric field vanishes for $|z| \leq 5$ μm where $|z|$ is the distance to the substrate interface (distance between meanders is $D = 7$ μm). The FEM simulations also show that the electric field is mainly oriented along the interface for $z = 0$.

During the measurements the resonators are immersed in liquid He^4 at 4.2 K. The shape and position of the resonances are determined by measuring the reflection along a coaxial cable capacitively coupled to the resonator. At resonant frequencies more power is absorbed by the resonator, and a dip in reflected power is observed (incident microwave power was -60 dBm). The resonators were then irradiated with a blue light provided by a commercial diode operating at low temperature. For samples on bulk Si the resonances are strongly broadened under irradiation, a typical behavior is shown in Fig. 3.33.b for the first harmonic of the resonator while no broadening was observed for a control resonator on a sapphire substrate.

This drop of the resonance quality factor under irradiation can be understood in terms of photoinduced conductivity in Si. Indeed the photon energy of $\hbar\omega \simeq 2.5$ eV is much larger than the Si gap $\Delta \simeq 1.2$ eV. Thus the adsorption of photons creates a stationary population of electron/holes pairs, and a finite photo-conductivity $\sigma(2\pi f)$ where f is the microwave frequency. In the regime of a weak conductor with $\sigma \ll \epsilon\ 2\pi f$ the screening is negligible and the associated drop in the resonator quality factor is well described by the relation [56] :

$$\text{Re}\ \sigma(2\pi f) = \epsilon\ 2\pi f\ \delta Q^{-1} = \frac{\sigma_0}{1 + (2\pi f \tau)^2} \tag{3.1}$$

Here ϵ is dielectric constant in Si, and the last equality in Eq. (3.1) is a Drude approximation to $\sigma(2\pi f)$ with elastic relaxation time τ. The quantity δQ^{-1} is the difference between Q^{-1} with and without irradiation. The experimental values for $\epsilon\ 2\pi f\ \delta Q^{-1}$ are shown on Fig. 3.33, the quality factors are determined using both amplitude and phase of the reflection coefficient to remove the artificial broadening of the resonance induced by the coupling to the transmission line. Since the excited carrier concentration is proportional to light intensity, we rescale the data of Fig. 3.33 by the electrical power absorbed by the diode.

A good agreement with Eq. (3.1) is found for a relaxation time of $\tau = 90$ ps that corresponds to a mobility $\mu \simeq e\tau/m \simeq 10^5$ cm^2/(Vs) (here m is the electron mass).

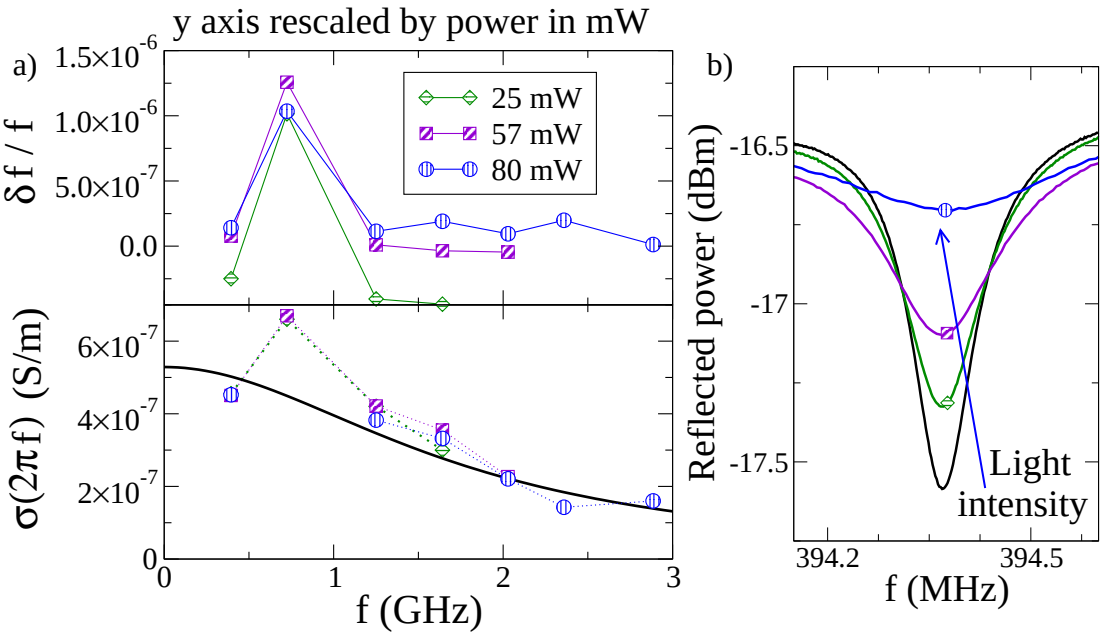

FIG. 3.33 – (Color online) Measurements on a bulk Si sample (see Fig. 3.32.a). a) Top panel : relative shift of resonance frequencies under light irradiation as a function of microwave frequency, symbol abscissa correspond to resonance positions. Bottom panel : photo-conductivity $\sigma(2\pi f)$ as obtained from the drop of resonance quality factor Q using Eq. (3.1). The smooth black curve represents a Drude fit with a relaxation time of $\tau = 90$ ps. In both panels symbol shape indicates electrical power provided to the diode. The values of $\delta f/f$ and σ are divided by the power value in mW and collapse on a single curve (at highest power data must be rescaled by 190mW to coincide with other curves, we attribute this to nonlinear dependence of light intensity on electrical power). b) Broadening of the fundamental resonance under light irradiation (drop of Q factor). Temperature is 4.2 K.

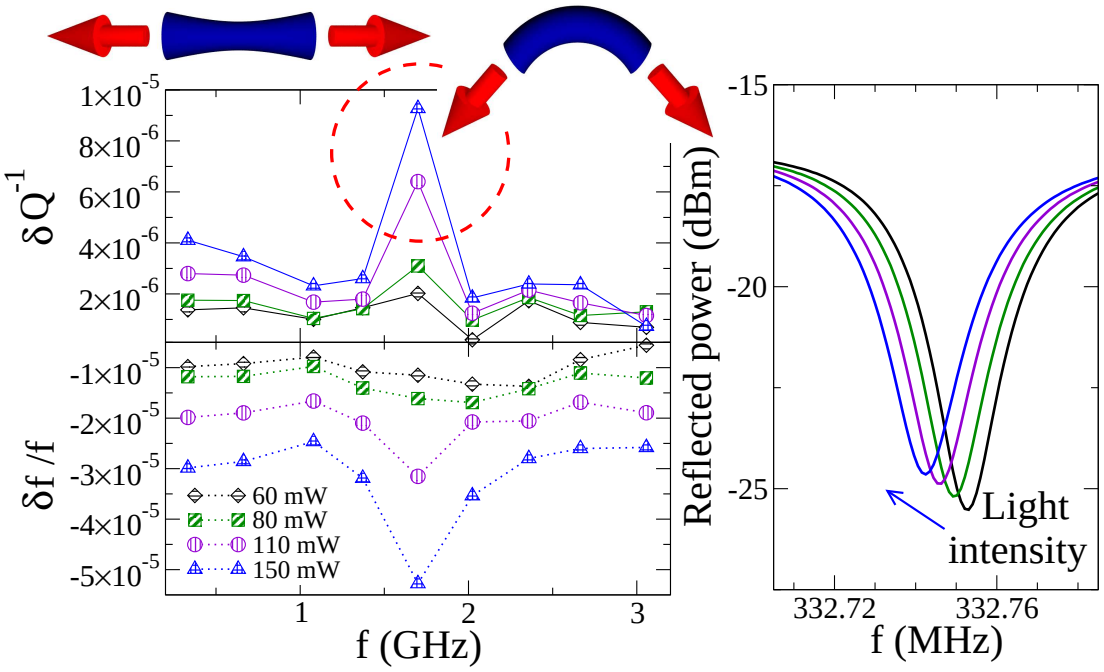

FIG. 3.34 – (Color online) Measurements on the sample with Si nanowires (see also Fig. 3.32.b) : a) δQ^{-1} and $\delta f/f$ as a function of frequency for several light intensities, b) Shift and broadening of the fundamental resonance under light irradiation. On control sample without Si nanowires typical $|\delta f/f| \leq 2 \times 10^{-6}$ and $|\delta Q^{-1}| \leq 10^{-6}$ at maximum light power.

From this value the effective carrier temperature $T_{eff} \simeq 20$ K can be determined using the mobility dependence on temperature in high purity Si [58]. This effective temperature is determined by the energy transferred by a photon $\hbar\omega - \Delta$ to an electron-hole pair and energy dissipation mechanisms in Si. It does not depend on light power as long as the carrier density n_+ remains small (from conductivity data on Fig. 3.33 we estimate $n_+ \simeq 10^8$ cm^{-3}). The Drude approximation works for all frequencies except for the second resonance at $f = f_2 \simeq 725$ MHz. The relative frequency shift under irradiation $\delta f/f$ has also a peak at $f \simeq f_2$. The origin of this resonant frequency can be understood in terms of emission of surface acoustic waves (SAW) in the Si substrate. Indeed the periodic structure of the meanders also creates a resonance for SAW. The corresponding frequency is determined by the distance between meanders $D \simeq 7\ \mu m$ and the transverse sound velocity in Si : $V_T \simeq 5500$ m/s [57], giving a resonant frequency of $f_{SAW} = V_T/D \simeq 785$ MHz close to the frequency f_2 of the EM resonator. The blue irradiation intensity is also modulated with a period D by the presence of the resonator and the continuous excitation of electron-hole pairs can create a charge density wave with period D strongly increasing the coupling between the acoustic and EM modes. This would explain why SAW resonance appears very clearly in the photoconduction data.

We also used this technique to probe phototransport in Si nanowires (see sample on Fig. 3.32.b). The typical behavior under irradiation is shown for the first resonance on Fig. 3.34. Contrarily to samples on bulk Si where only a broadening of the resonance was observed, a shift of the resonance position is clearly visible. In the bulk the charges were not confined in the direction parallel to the Si interface hence only dissipative photoconductive response $\propto \delta Q^{-1}$ could be observed. In the nanowires, photo-induced charges are confined and can be polarized, creating a photopolarizability $\propto \delta f/f$. In order to compare the magnitude of these two effects we assume that we excite at most one electron-hole pair in a nanowire, and we call n_{Si^+} the surface density of the excited nanowires. The polarization P of an excited nanowire is determined from an equilibrium Boltzmann distribution in presence of the resonator electric field E : $P \simeq \int_{-L/2}^{L/2} qx \exp\left(\frac{qEx}{T_{eff}}\right) \frac{dx}{L} \simeq q^2L^2E/T_{eff}$. Here L is the nanowire length, q is the carrier charge and T_{eff} is the effective carrier temperature. This polarization creates a shift of the resonant frequencies :

$$\frac{\delta f}{f} \simeq -\frac{q^2L^2}{\epsilon T_{eff}} \frac{n_{Si^+}}{D}. \tag{3.2}$$

where the factor $1/D$ originates from the confinement of the EM field. Photoconductivity is determined by Eq. (3.1), the unknown conductivity σ_0 can be estimated with a Drude approximation : $\sigma_0 \simeq \frac{q^2\tau_{Si}n_{Si^+}}{mD}$ where n_{Si^+}/D is the effective carrier concentration. The relaxation time τ_{Si} is determined by the collisions with the nanowire walls $\tau_{Si} \simeq R\sqrt{m/T_{eff}}$ where R is the nanowire radius and m is the electron mass. Combining these results with Eq. (3.2) yields the dimensionless ratio Γ :

$$\Gamma = \delta Q^{-1}/(\delta f/f) \simeq -\frac{R}{2\pi f L^2}\sqrt{\frac{T_{eff}}{m}} \tag{3.3}$$

The quantity Γ does not depend on n_{Si^+} and thus on light power. This is confirmed by extracting Γ from the data of Fig. 3.34 which gives typical $\Gamma \simeq 10^{-1}$. After injecting this value in Eq. (3.3) together with $R \simeq 50$ nm, $L \simeq 2.5$ μm and $f \simeq 400$ MHz we find an effective temperature $T_{eff} \simeq 65$ K of the same order of magnitude as in bulk Si.

The frequency dependence in Fig. 3.34 is characterized by a peak at $f_R \simeq 1.7$ GHz. The origin of this peak can be related to mechanical resonances in the nanowires, similarly to interaction with SAW for bulk Si. Possible excited modes are shown on top of Fig. 3.34. The bending mode resonance occurs at frequency $f_R \simeq V_T/L \simeq 2.2$ GHz where $L \simeq 2.5\mu$m is the average nanowire length (length fluctuations are around 1 μm), whereas for the stretching mode the frequency reads $f_R \simeq V_L/(2L) \simeq 1.8$ GHz, where $V_L \simeq 9000$ m/s is the longitudinal sound velocity in Si [57]. In our experiments the dispersion in nanowire radius, length and orientation does not allow to discriminate between these two excited modes.

In conclusion we have shown that using a high Q multimode resonator we can probe effectively low temperature photo-transport in bulk Si and Si nanowires. For bulk Si, photo-induced carriers induce a dissipative response which broadens the resonances. The drop of

quality factor allows to deduce the relaxation time and the carrier effective temperature. At a special frequency resonant interaction with surface acoustic waves is observed. In Si nanowires, photo-induced carriers can polarize the nanowires and thereby induce a dominant non dissipative response absent in the bulk. We showed that the ratio between dissipative and non-dissipative responses determines the effective carrier temperature in the nanowires. For some special resonant frequencies mechanical resonances in the nanowire could be excited. We stress that this technique is very generic and can be applied to many other systems where photoconductivity is expected, possible examples include DNA and photochromic molecular switches. Coupled with optical spectroscopy, it could provide valuable transport data on nanowires with embedded quantum dots.

3.12 Counterion condensation around (hydrophobic) poly-electrolytes

In order to perform the DNA combing experiments described in Chap. 3.6, it was important to gain an understanding of the electrostatic properties of the DNA molecules that play an important role in their adhesion properties. For this purpose, I worked on a related theoretical problem concerning the behavior of hydrophobic polyelectrolytes under the direction of Prof. E. Raphaël. It has been proposed that this system adopts a pearl-necklace structure reminiscent of the Rayleigh instability of a charged droplet. Using a Poisson-Boltzmann approach, we calculate the counterion distribution around a given pearl assuming the latter to be penetrable for the counterions. This allows us to calculate the effective electric charge of the pearl as a function of the chemical charge. Our predictions are in good agreement with the recent experimental measurements of the effective charge by Essafi *et al.* (Europhys. Lett. **71**, 938 (2005)). Our results allow to understand the large deviation from the Manning law observed in these experiments.

The study of polyelectrolytes has attracted an increased attention in the scientific community over the last decades. This interest is motivated by technological applications including viscosity modifiers, or leak protectors and by the hope that advances in this domain will allow to unravel the structure of complex biological macromolecules. In these systems, the Coulomb interactions leads to many remarkable and counterintuitive phenomena [59, 60, 61, 62, 63]. A celebrated example is the Manning-Oosawa counterion condensation. In his classical work [59], Manning showed that a charged rod-like polymer can create such a strong attractive force on its counterions, that a finite fraction condenses onto the polymer backbone. This condensation-phenomenon was also described by Oosawa within a two state model [60]. It leads to an effective decrease of the polymer charge, and the macroscopic properties of the polyelectrolyte, like migration in an electrophoresis experiment, are not determined by its bare charge, but by an effective charge that accounts for the Manning-Oosawa counterion condensation. It is now well-established that counterion condensation is a fundamental phenomenon, and that it occurs in many important systems including DNA in both its double-stranded and single-stranded form [64]. It was

predicted in [59] that condensation occurs whenever the average distance l between co-ions on the polymer backbone is smaller than the Bjerrum length $\ell_B = q^2/(4\pi\epsilon\epsilon_0 k_B T)$, where q is the co-ion charge, $k_B T$ the thermal energy and ϵ the (relative) dielectric constant of the solvent. This condensation is expected to lead to an average charge density of q/ℓ_B on the polymer backbone. Since the original prediction by Manning, important efforts have been devoted to a description of the Manning-Oosawa condensation within the Poisson-Boltzmann theory and beyond [65, 66, 67, 68, 69], establishing the influence of salt, the thickness of the condensed counterion layer and the corrections induced by short range correlation.

While the conformation of many polyelectrolytes is well described by the rod-like model, many proteins organize into complex self-assembled structures [70]. A challenging and important topic is the extent to which the structural complexity of biological enzymes can be understood from simple physical models. Polyelectrolytes with an hydrophobic backbone may provide an interesting system, that achieves a certain degree of self-organization while the relevant interactions remain relatively simple. Indeed, it has been predicted in a seminal paper by Dobrynin and Rubinstein that hydrophobic polyelectrolytes should fold into an organized pearl-necklace structure where regions of high and low monomer density coexist [71]. Therefore both theoretical and experimental studies of the hydrophobic polyelectrolytes have shown a growing activity in the past few years [72, 73, 62, 74, 75, 76, 77, 78, 63, 79].

The question of the validity of the Manning condensation model for hydrophobic polyelectrolytes has been addressed experimentally by W. Essafi *et al.* [80]. The authors have measured the effective charge fraction of a highly charged hydrophobic polyelectrolyte (poly(styrene)-co-styrene sulphonate) by osmotic-pressure and cryoscopy measurements. Their findings, which are recalled on Fig. 3.38, showed that the measured effective charge is significantly smaller than that predicted by the Manning-Oosawa theory. The aim of the present article is to provide a theoretical explanation of the counterion condensation in this system, where the hydrophobicity of the backbone strongly influences its conformation. This problem was first addressed theoretically by Dobrynin, and Rubinstein [75], who analyzed the phase diagram of a solution of hydrophobic polyelectrolytes as a function of solvent quality and polymer concentration. However, the question of the effective charge of the chains was not directly investigated by the authors.

Let us first recall for completeness the pearl-necklace theory of hydrophobic polyelectrolytes (for a more complete review, see [79]). The polyelectrolyte solution is parameterized by its degree of polymerization N, its monomer size b (for the polyelectrolytes used by W. Essafi *et. al*, one has $b \approx 0.25$nm), the charge fraction along the chain f, and the reduced temperature $\tau \equiv 1 - \frac{\Theta}{T}$, where Θ and T denote the theta temperature of the polyelectrolyte and the temperature of the system, respectively. We note that in a bad solvent, the reduced temperature is negative $\tau < 0$. Let us denote by C the average monomer concentration in the solution.

In a poor solvent, an uncharged polymer forms a globule in order to decrease its surface energy. In a similar way, a drop of water adopts a spherical configuration in a hydrophobic environment.

To estimate the gyration radius R_g of the polymer, we divide the polymer into smaller units, in such a way that inside each unit the thermal fluctuations dominate and the chain has Gaussian behavior. These units are usually called thermal blobs in the literature and the typical radius of the blobs is denoted by ξ_T. It can be shown that they contain about $1/\tau^2$ monomers, and have a typical size of $\xi_T \simeq b/|\tau|$. At larger scales, the polymer tends to collapse onto itself in order to minimize its surface of contact with the liquid. This can happen by forming a dense packing of thermal blobs. A polymer of polymerization degree N can be split into $\tau^2 N$ thermal blobs and the volume occupied by the polymer is proportional to the number of subunits. Therefore one can estimate the gyration radius of the polymer as

$$R_g^3 \simeq \tau^2 N \xi_T^3 \simeq \frac{N b^3}{|\tau|}. \tag{3.4}$$

The surface energy E_S associated with this configuration is given by $k_B T$ times the number of thermal blobs in contact with the solvent. This leads to

$$\frac{E_S}{k_B T} \simeq \frac{\tau^2 R_g^2}{b^2}. \tag{3.5}$$

Upon charging, the electrostatic repulsion sets in, which results in a change of the globule shape. When the electrostatic repulsion energy becomes larger than the surface energy, the globule splits into several globules of smaller size consisting of N_g monomers. According to Eq. (3.4), the typical size of these globules is given by

$$R_g^3 \simeq \frac{N_g b^3}{|\tau|}. \tag{3.6}$$

This behavior is reminiscent of the Rayleigh instability of a charged droplet [81]. In this state, the polyelectrolyte forms a sequence of globules that are connected by strings made of thermal blobs (see Fig. 3.35). In the literature, this conformation is known as the "pearl-necklace" structure. The presence of counterions will screen the electrostatic repulsion. Therefore it is important to account for their role explicitly in the balance between the surface tension and the electrostatic repulsion that governs the equilibrium structure of the necklace.

For simplicity we assume that the main effect of the counterions is to reduce the charge of the pearls. Indeed, some counterions can be attracted inside the globules due to the attractive electrostatic forces. In the absence of any counterion condensation, the total electrostatic charge of a globule consisting of N_g monomers is simply given by qfN_g. If the counterions penetrate inside the globule, its effective charge is decreased and is given by $qf_{eff}N_g$, where f_{eff} denotes the effective charge fraction. We can understand this relation by noting that in the presence of counterion condensation the total charge of the pearl is the chemical charge of the pearl minus the charge of the counterions inside it. Therefore, the electrostatic energy E_{el} of a pearl can be estimated as

$$\frac{E_{el}}{k_B T} \simeq \frac{\ell_B \left(f_{eff} N_g\right)^2}{R_g}, \tag{3.7}$$

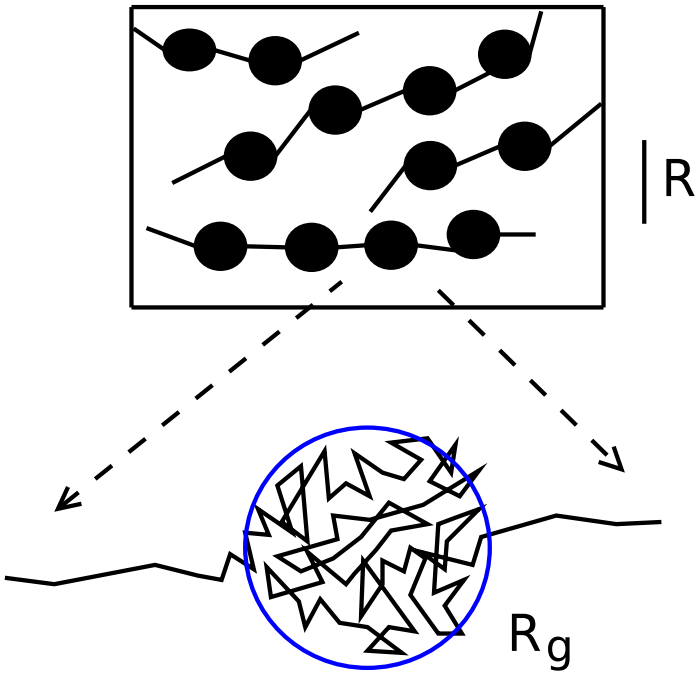

FIG. 3.35 – Schematic drawing of the pearl necklace structure of hydrophobic polyelectrolytes : Inside the blue (gray) circle the polymer backbone, represented by a continuous black line, is wrapped into a dense configuration of typical radius R_g, that we call pearl or globule in the text. The inset shows on a larger scale, that these pearls are connected by thin polymer strings, thus forming the pearl necklace structure. The average distance between the pearls is R (black vertical scale line).

where the Bjerrum length is defined as

$$\ell_B = \frac{q^2}{4\pi\epsilon\epsilon_0 k_B T}, \tag{3.8}$$

where ϵ is the dielectric constant of the medium and $k_B T$ denotes the thermal fluctuation energy. For example for water at room temperature ($T = 300\ K$, $\epsilon = 80$) the value of the Bjerrum length is $\ell_B \approx 0.7$nm. Using the relation between R_g and the N_g given in Eq. (3.6), the electrostatic energy of a pearl is simplified to

$$\frac{E_{el}}{k_B T} \simeq |\tau|^2 f_{eff}^2 \frac{\ell_B R_g^5}{b^6}. \tag{3.9}$$

In its equilibrium configuration the pearl-necklace tends to balance its electrostatic and surface energies $E_{el} \simeq E_S$. Inserting the results of Eq. (3.5) and Eq. (3.9) in this equality leads to an expression of the globule radius R_g as a function of the effective charge fraction f_{eff} :

$$R_g \simeq b \left(\frac{b}{\ell_B}\right)^{1/3} \frac{1}{f_{eff}^{2/3}}. \tag{3.10}$$

We stress that this relation between the typical pearl size and the effective charge has been verified experimentally by D. Baigl *et al.* in [82] with an X-ray diffraction technique. This suggests that the hydrophobic polyelectrolytes studied in the experiment of W. Essafi actually formed a pearl necklace structure.

The problem of the effective charge of spherical microion-permeable globules of size R_g surrounded by their own counterions can be solved in the mean-field approximation using the Poisson-Boltzmann theory. This problem was first studied numerically and analytically by Wall and Berkowitz [83]. It was shown that for such a globule, counterion condensation can occur (see e.g. Ref [84] for a general discussion of the condensation phenomenon). In this approach, a charged globule is modelled as a sphere with radius R_g and a uniform charge distribution inside it. Therefore, the charge density of the globule is given by

$$q\rho_0 \simeq q\frac{fN_g}{R_g^3}, \tag{3.11}$$

where ρ_0 denotes the mean density of charged monomers that are distributed inside the globule. Using Eq. (3.6), ρ_0 can be simplified to

$$\rho_0 \simeq \frac{f|\tau|}{b^3}. \tag{3.12}$$

In the solution, the mean monomer concentration is denoted by C. As far as the counterions are distributed inside an elementary cell of radius R (Wigner-Seitz approach), the average concentration of the counterions is given by

$$n_{av} = fC. \tag{3.13}$$

Using the electro-neutrality condition, one can find a relation between the radius of the elementary cell, R, and the density of the charged monomers inside the globule as

$$\rho_0 R_g^3 = n_{av} R^3. \tag{3.14}$$

Assuming a spherical symmetry for the charge distribution, all the quantities such as the electrostatic potential, the counterion concentration, *etc* depend only on the distance r to the center of the globule. Under the assumption of a Boltzmann-distribution, the concentration profile $n(r)$ of the counterions is related to the electrostatic potential $\phi(r)$ as

$$n(r) = n_{av} e^{\frac{q\phi(r)}{k_B T}}. \tag{3.15}$$

Inserting this expression into the Poisson equation $\nabla^2\phi = -\frac{1}{\epsilon\epsilon_0}(q\rho_0(r) - qn(r))$ leads to the well-known Poisson-Boltzmann (PB) equation :

$$\nabla^2\phi = \frac{1}{r^2}\frac{d}{dr}\left(r^2\frac{d\phi}{dr}\right) = -\frac{q\rho_0(r)}{\epsilon\epsilon_0} + \frac{qn_{av}}{\epsilon\epsilon_0}e^{\frac{q\phi}{k_B T}}, \tag{3.16}$$

where $\rho_0(r)$ is given by

$$\rho_0(r) = \begin{cases} \rho_0 \simeq \frac{fN_g}{R_g^3} & r \leq R_g, \\ 0 & r > R_g. \end{cases} \tag{3.17}$$

For our system with spherical symmetry in the charge distribution, the electric field is zero at $r = 0$. Electroneutrality also demands a vanishing electric field at the boundary $r = R$, so that the boundary conditions for the above PB equation read

$$\frac{d\phi(r=0)}{dr} = \frac{d\phi(r=R)}{dr} = 0. \tag{3.18}$$

In an elementary cell with the average counterion density n_{av}, the Debye screening length λ_D is given by

$$\frac{1}{\lambda_D^2} = 4\pi\ell_B n_{av}. \tag{3.19}$$

After defining the reduced electrostatic potential, $u \equiv q\phi/(k_B T)$, and $x \equiv r/\lambda_D$, PB equation can be written as

$$\frac{d^2u}{dx^2} + \frac{2}{x}\frac{du}{dx} = e^{u(x)} - A(x),\ \frac{du(0)}{dx} = \frac{du(X)}{dx} = 0, \tag{3.20}$$

where X denotes R/λ_D and $A(x)$ is defined as

$$A(x) \equiv \frac{\rho_0(x)}{n_{av}}. \tag{3.21}$$

The radius of the globule in the dimensionless form is denoted by $x_g \equiv R_g/\lambda_D$. We will set A as the value of $A(x)$ inside the globule : $A(x) = A$ for $x \leq x_g$. Using the aforementioned

reduced variables and the cell neutrality condition, Eq. (3.14), one can find the simple form of A as

$$A = \frac{\rho_0}{n_{av}} = \left(\frac{X}{x_g}\right)^3 \simeq \frac{|\tau|}{Cb^3}, \tag{3.22}$$

where in writing the last term, the explicit forms of ρ_0, Eq. (3.12), and n_{av}, Eq. (3.13), have been used. It appears that A does not depend on the chemical charge f. The quantity A may be seen as the inverse packing (or volume) fraction.

The fraction of counterions outside the globule, P, can be found as

$$P = \frac{\int_{r_g}^{R} n_{av}\, e^{q\phi(r)/k_BT} r^2\, dr}{\int_0^{R_g} \rho_0 r^2\, dr} = \frac{\int_{x_g}^{X} e^u x^2 dx}{\int_0^{x_g} A x^2 dx}, \tag{3.23}$$

where in writing the last term, the reduced variables and Eq. (3.22) have been used. Using Eq. (3.20), integration leads to a simpler form of the above equation :

$$P(x_g, A) = -\frac{3}{x_g A}\frac{du(x_g)}{dx}. \tag{3.24}$$

As far as the penetrated counterions inside the globule reduce its charge, the effective charge of the globule is proportional to the fraction of counterions outside the globule. Therefore, the effective charge of the globule can be written as

$$f_{eff} = P(x_g, A) f. \tag{3.25}$$

It has been shown in [83] that the potential $u(x)$ defined by the boundary problem, Eq. (3.20), is a decreasing function of x and the initial value of the potential satisfies $e^{u(0)} \leq A$. Physically, this inequality signifies the absence of over-screening (inside the globule $qn(r) \leq \rho_0$) as expected in a mean-field theory [85]. In order to estimate the lower limit of $e^{u(0)}$, we re-write Eq. (3.20) as

$$u(x) = u(0) + \int_0^x \left(y - \frac{y^2}{x}\right)\left[e^{u(y)} - A(y)\right] dy. \tag{3.26}$$

Since $u(x)$ is a decreasing function, it may be shown that

$$u(x) = u(0) + \frac{1}{6} min(x, x_g)^2 \left[e^{u(0)} - A\right], \tag{3.27}$$

where $min(x, x_g)$ yields the smallest quantity. After inserting this result in the cell neutrality condition, $\int_0^X x^2 \left[e^{u(x)} - A(x)\right] dx$, we find that $e^{u(0)}$ satisfies the following inequality relations :

$$1 - 2\frac{\ln\left(\widetilde{Z}_g/2\right)}{\widetilde{Z}_g} \leq \frac{e^{u(0)}}{A} \leq 1, \tag{3.28}$$

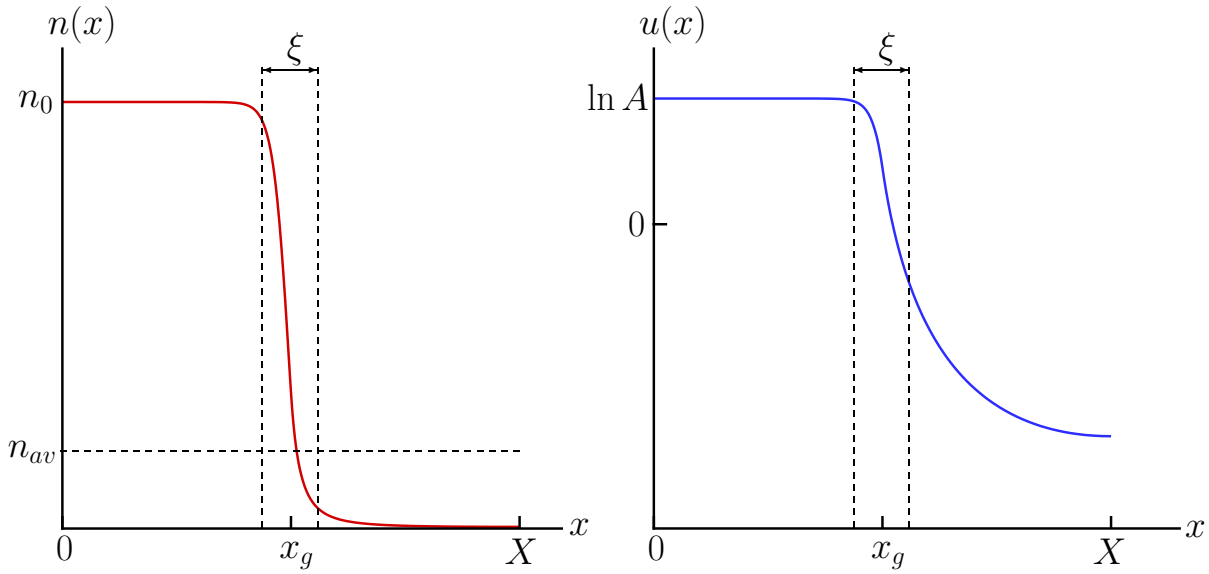

FIG. 3.36 – (Color online) Typical behavior of counterion charge distribution $n(x)$ and effective potential $u(x)$ in the cell. The dimensionless globule size is denoted by x_g and the cell size is denoted by X.

where we have set $\widetilde{Z}_g = Ax_g^2/3 > e$. The quantity $\widetilde{Z}_g$ has a simple interpretation as the total charge of the co-ions inside the globule $Z_g = \frac{4\pi}{3}\rho_0 R_g^3$ multiplied by the ratio between the Bjerrum length and the globule radius ℓ_B/R_g. Indeed, the following equality

$$\widetilde{Z}_g \equiv Z_g \frac{\ell_B}{R_g} = \frac{1}{3}x_g^2 A \tag{3.29}$$

can be checked using the relations $R_g = x_g\lambda_D$, $\rho_0 = n_{av}A$ and the expression of the Debye length λ_D from Eq. (3.19). In what follows, we will refer to $\widetilde{Z}_g$ as the reduced globule charge. With these notations the chain of inequalities in Eq. (3.28) implies that in the limit of large reduced globule charge $\widetilde{Z}_g \gg 1$, we have $e^{u(0)}/A \to 1$.

The behavior of a typical solution $u(x)$ is displayed in Fig. 3.36. It confirms that for large values of $\widetilde{Z}_g$, the counterion concentration at $x \simeq 0$ is very close to the concentration of charged monomers inside the globule : $e^{u(x)} \simeq A$. As the value of $\widetilde{Z}_g$ increases, the size of the neutral region where $u(x) \approx \ln A$ grows until it becomes of the order of globule size x_g. Therefore, to keep the system electrically neutral, the counterion concentration must fall down to values below n_{av} outside the globule.

The transition between these two regions occurs in a narrow layer of thickness ξ on the boundary of the globule, as shown in Fig. 3.36. In order to estimate the behavior of ξ in terms of the physical parameters of the problem, it is convenient to write the PB equation

for $x \gtrsim x_g$ in the following manner

$$\frac{d^2u}{dx^2}\left[1+\frac{2}{x}\frac{\frac{du}{dx}}{\frac{d^2u}{dx^2}}\right] = e^{u(x)}. \tag{3.30}$$

We note that d^2u/dx^2 and du/dx are of the order of $(\ln A)/\xi^2$ and $(\ln A)/\xi$, respectively. Putting these values in the above equation, we find

$$\frac{\ln A}{\xi^2}\left[1+2\frac{\xi}{x_g}\right] \simeq A. \tag{3.31}$$

We assume that we are in the regime where $\xi/x_g \ll 1$. Therefore, ξ scales as

$$\frac{\ln A}{\xi^2} \simeq A \implies \xi \simeq \frac{1}{\sqrt{A}}, \tag{3.32}$$

where we have neglected the logarithmic dependence on A. We note that for consistency, the requirement $\xi \ll x_g$ also implies $\widetilde{Z}_g \gg 1$.

We are now in a position to estimate the counterion concentration outside the globule. Using Eq. (3.24) in the limit of $\widetilde{Z}_g \gg 1$, the fraction of counterion outside the globule is found as

$$P(x_g, A) \simeq \frac{1}{x_g A}\frac{u}{\xi} \simeq \frac{6}{\sqrt{2e}}\frac{1}{x_g\sqrt{A}}. \tag{3.33}$$

Using Eq. (3.29) we find that in the asymptotic regime of $\widetilde{Z}_g \gg 1$, P depends only on the reduced globule charge $\widetilde{Z}_g$ through the simple equation

$$P = \sqrt{\frac{6}{e\widetilde{Z}_g}} \tag{3.34}$$

The proportionality constant in Eq. (3.33) was calculated by ignoring the first derivative term $\frac{1}{x}\frac{du}{dx}$ in Eq. (3.20). Fig. 3.37 shows that there is a very good agreement between the exact results and the analytical approximation in the limit $\widetilde{Z}_g \gg 1$ ($\xi \ll x_g$). We also see that for a wide range of A values, our analytical theory gives a good numerical approximation for P as far as $P \lesssim 0.4$. For example for $A = 500$, the relative error of our approximation is below 20% in this region. The exact numerical results were obtained using the method described in [83]. As a guide to the eye, we have marked the parameter range explored in the experiments of W. Essafi *et al.* with a black arrow on Fig. 3.37. This range was obtained from the experimental data as the ratio f_{eff}/f, and is well within the range of validity of Eq. (3.34).

In the regime explored experimentally by W. Essafi *et al.* [80], the value of the dimensionless parameter A can be estimated as follows. For $|\tau| \simeq 1$, monomer concentration $C = 0.1$ Mol L^{-1} and the bond length in the polymer $b = 0.25$ nm, the expected value of

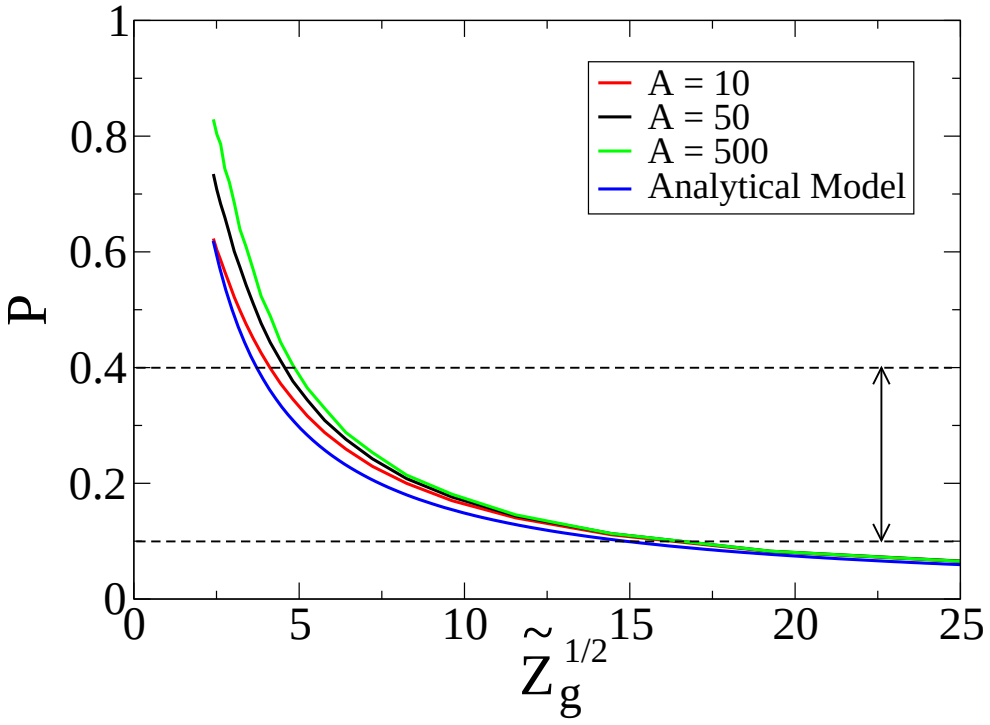

FIG. 3.37 – (Color online) Dependence of P on $\widetilde{Z}_g^{1/2}$ for different values of A. From top do bottom, $A = 500, 50, 10$ (green, black, red curves respectively), where A is the inverse volume fraction of the globules. The bottom (blue) curve is Eq. (3.33). The arrow shows the P range explored in the experiment. It is obtained by calculating the ratio f_{eff}/f from the experimental data on Fig. 3.38.

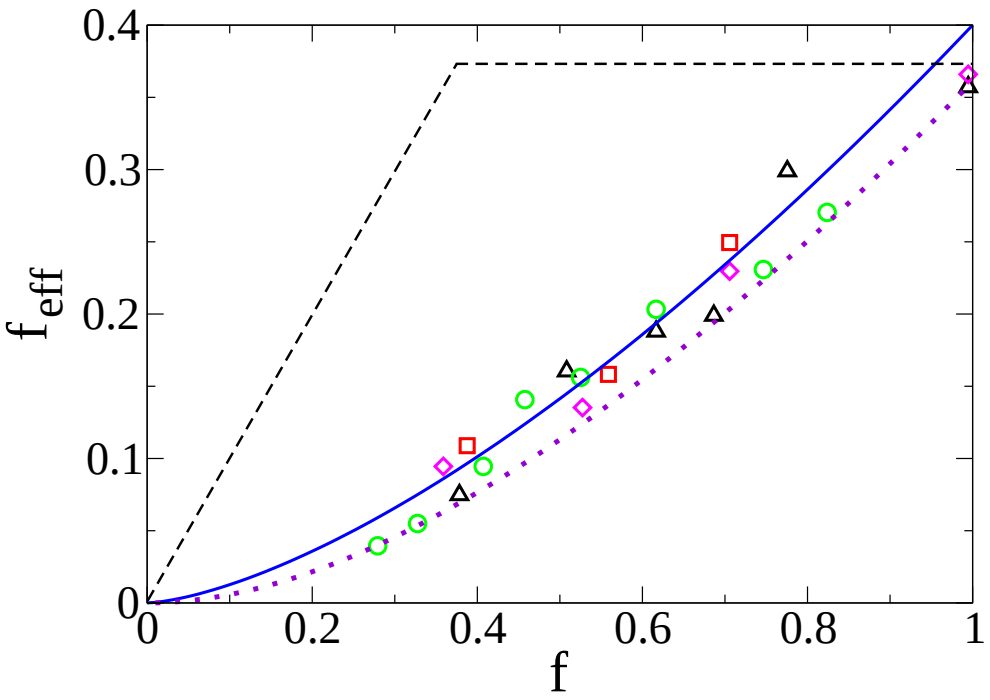

FIG. 3.38 – (Color online) Effective charge fraction f_{eff} versus the chemical charge fraction f. The experimental points were obtained in [80]. The red squares correspond to $N = 410$, green circles : $N = 930$, purple diamonds : $N = 1320$, and black deltas : $N = 2400$. The blue solid line corresponds to our theoretical model Eq. (3.36) with $\sqrt{b/\left(|\tau|^3 \ell_B\right)} = 0.4$. The dashed line corresponds to Manning's model. The dotted (violet) line includes additional counterion condensation outside the permeable globule. We note that this effect is a rather weak correction to the predictions of Eq. (3.36).

$A \simeq |\tau|/(Cb^3)$ is $A \simeq 10^3 \gg 1$. The value of x_g depends on both the chemical and effective charge fraction, f and f_{eff}, as

$$x_g = \frac{R_g}{\lambda_D} \simeq \frac{|\tau|^{1/2}}{A^{1/2}} \left(\frac{\ell_B}{b}\right)^{1/6} \frac{f^{1/2}}{f_{eff}^{2/3}}. \tag{3.35}$$

Using Eqs. (3.25), (3.33), and (3.35) the effective charge fraction f_{eff} is found as

$$f_{eff} \simeq \sqrt{\frac{b}{|\tau|^3 \ell_B}} f^{3/2}. \tag{3.36}$$

This result predicts that the effective charge fraction f_{eff} is proportional to $f^{3/2}$. We note that in this regime the effective charge does not depend on the average monomer concentration C and depends only on intrinsic properties of the polymer. The scaling law of Eq. (3.36) and the experimental data of Fig. 3.38 of [80] are shown in Fig. 3.38.

As one can see, there is a very good agreement between the predicted behavior and the experimental data. We stress that only one free coefficient of order one has been used to adjust the data. Thus, our theory can explain the origin of the difference between the effective charge predicted by the Manning-law recalled on Fig. 3.38 and that observed in experiments. Furthermore, using Eqs. (3.6), (3.10), and (3.36) the globule radius R_g and the number of monomers inside the globule N_g are found as $R_g \propto |\tau| b/f$, and $N_g \propto |\tau|^4/f^3$. Assuming $|\tau| \sim 1$ and f varying in the range $(0.2, 1)$, the above estimation for R_g allows to convert $\widetilde{Z}_g$ into Z_g. The experimentally relevant range shown on the x-axis in Figure 3.37 is $\widetilde{Z}_g \in (25, 225)$, which corresponds to Z_g in the range $(8, 225)$.

It is important to mention that in the experiments of [80], only samples with relatively high chemical charge fraction $f \geq 0.3$ were prepared, thereby limiting the range where our theory can be checked. This is related to the difficulty to stabilize solutions of hydrophobic polyelectrolytes with low chemical charge because the polyelectrolytes can form a macroscopic phase that is not soluble in the solvent. We expect that the formation of a macroscopic phase can occur if the number of monomers inside a globule N_g becomes larger than the polymerization degree of the polymer N. In this case the polymer chains must stick together to form globules of size $N_g \approx |\tau|^4/f^3 > N$, which may lead to form an entangled polymer network that is not soluble in the solvent anymore. More detailed theoretical studies are needed on this problem. We note that a detailed analysis of the possible phases and their stability range has been done in [86]. As mentioned above, the dimensionless factors are of order one and if we set $N = 1000$ this condition for phase separation reads $f_{eff} < 1/\sqrt{N} \simeq 0.03$. This result is in a reasonable agreement with the results displayed in Fig. 3.38. It is worth to mention that in the experiments no point could be obtained below this limit. We also emphasize that in our theory, when a stable pearl-necklace structure forms, the effective charge depends on N_g and not on polymerization degree N. This property has been verified in the experiment, where N has been varied from $N = 410$ to $N = 2400$ without apparent change of the measured values of f_{eff}.

In the above treatment, we have assumed that the polyelectrolyte chain in a dilute regime forms a necklace structure in the solvent. Liao *et al.* [87] have studied the necklace formation in polyelectrolyte solutions using both theory and molecular dynamics simulations. They have shown that partially charged chains form necklace-like structures of globules and strings in dilute solutions. For the dilute regime the phase diagram of hydrophobic polyelectrolytes was obtained in [87]. It has been shown that when the effective charge of the chain is larger than a threshold $\sqrt{b|\tau|/(\ell_B N)}$, the necklace structure is the dominant feature of the polyelectrolytes in a bad solvent. Using Eq. (3.36) and the mentioned criterion, we find that for chains consisting of more than $1/(|\tau|^2 f^3)$ monomers, the necklace-structure is formed in the system. For the experimental condition explained in [80], $|\tau| \simeq 1$ and $f > 0.2$, gives $1/(|\tau|^2 f^3) \simeq 150$. All the chains that have been used in the experiment [80] have more than 410 monomers on a chain, which means that our model considering necklace structure for the hydrophobic polyelectrolyte in the solution is reasonable. We note that our scaling approach does not allow to predict accurately the phase diagram of the polyelectrolyte chains. A consistent minimization of the free energy would

require to properly account for the logarithmic dependence of the counterion entropic and electrostatic energy as a function of the pearl radius [88]. The origin of such logarithmic terms can be seen by estimating the entropy of the counterions, since the condensed counterions explore only a phase volume of R_g^3 out of the total volume. In our analysis this dependence is ignored because the available phase volume is limited to the size of the Wigner-Seitz cell in a periodic system. Furthermore, the correlation induced effects like the nonmonotonic dependence of the solution osmotic coefficient on the polymer concentration have been observed in computer simulation analysis [87], which cannot be described in our model.

As we explained before, Eq. (3.36) is based on the validity of Eq. (3.33). It is justified provided that $P \ll 1$; our numerical calculations suggest that reasonable agreement is already achieved for $P \lesssim 0.4$ for the experimental value of $A \simeq 10^3$. For the parameters used in Fig. 3.38, the mentioned criterion is always satisfied. Furthermore, by placing the pearls inside neutral Wigner-Seitz cells, we have ignored the effect of the interaction between neighboring pearls on the counterion distribution. However the sharp decrease of the counterion concentration on the boundary of the globule (see Fig. 3.36) suggests that these interactions should not affect significantly the counterion distribution. We have also ignored the effect of the ions along the strings that connect adjacent pearls. This assumption can be checked by estimating the fraction s of the charged monomers present inside the pearls. It can be shown that

$$s \simeq \frac{1}{1 + f_{eff}\sqrt{\frac{\ell_B}{|\tau|^3 b}}} \simeq \frac{1}{1 + f_{eff}}, \tag{3.37}$$

where we have assumed that both the parameter $\sqrt{\frac{\ell_B}{|\tau|^3 b}}$ and intermediate scaling constants are of order one. These assumptions are consistent with the parameters used in Fig. 3.38. Our theory holds as long as $s \simeq 1$, that is when the effective charge f_{eff} is be small. While this is clearly the case in the range of small chemical charge f, the contribution of the strings may become important when $f \simeq 1$. Physically, we expect that around the strings the counterions will follow the usual Manning-condensation behavior. Therefore, the effect of the strings will be mainly to keep the effective charge f_{eff} below the Manning limit b/ℓ_B. In Fig. 3.38, the effective charge reaches this limit only at $f \simeq 1$; as a result the effect of the strings is not visible and our prediction holds even up to $f \simeq 1$.

Finally we have not taken into account additional counterion condensation outside the permeable globule. A popular criterion for counterion condensation in this setting, was proposed by Alexander *et al.* [89]. The renormalized charge Z_g^* of an impermeable globule of internal charge Z_{eff}, is determined from a linearization of the PB equation that ensures the best possible matching between the exact and linearized solution at the boundary of the Wigner-Seitz cell. In our case, the globule is permeable and Z_{eff} is smaller than the charge of the co-ions inside the globule, and is given by $Z_{eff} = PZ_g$. (We remind that P stands for the counterion fraction outside the globule.) The dependence of the ratio Z_g^*/Z_{eff} on the system parameters, is governed by the dimensionless parameter $\widetilde{Z}_{eff} = Z_{eff}\ell_B/R_g$,

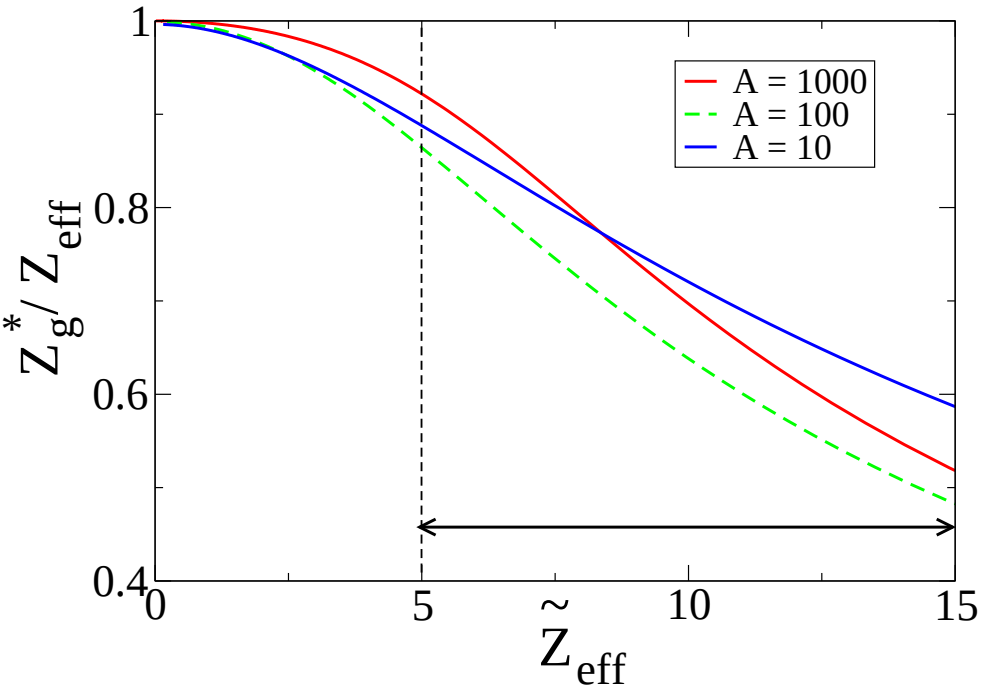

FIG. 3.39 – (Color online) Ratio between the Alexander charge of the globule Z_g^* and the total charge inside the globule $Z_{eff} = PZ_g$ as a function of $\widetilde{Z}_{eff} = Z_{eff}\ell_B/R_g$ for different values of the inverse volume fraction A. ($A \approx 10^3$ in the experimental conditions). The black arrow indicates the parameter range explored experimentally by Essafi *et al.* estimated from Eq. (3.38).

where R_g is the globule radius [89, 90]. This parameter can be estimated as follows for the case of our permeable pearl model : $\widetilde{Z}_{eff} = PZ_g\ell_B/R_g = P\widetilde{Z}_g$. Inserting the expression of P from Eq. (3.34) leads to

$$\widetilde{Z}_{eff} = \sqrt{\frac{6\widetilde{Z}_g}{e}} = \frac{6}{eP} \tag{3.38}$$

Since the range explored by P is $(0.15, 0.4)$, the above expression allows us to conclude that $\widetilde{Z}_{eff} \in (5, 15)$. We have calculated the ratio Z^*/Z_{eff} in this parameter range using the semi-analytical method proposed in [91] and our numerical procedure. The results obtained are presented in Fig. 3.39, and do not show significant renormalization in our regime. By combining the numerical results for inverse volume fraction $A = 1000$ and the analytical results from Eq. (3.36) we can calculate the effective charge of the globules including condensation outside the globule. Indeed the renormalized Alexander charge of the globule is given by $Z^*/Z_{eff}Pf$ where the product Pf gives as usually the charge inside the globule. The behavior of the Alexander charge for this problem is shown on Fig. 3.38 on the dotted line, which is the continuous line of equation $f_{eff} = Pf$ scaled down by a factor Z^*/Z_{eff}. The comparison between these two curves confirms that Eq. (3.36) is a very good approximation for the effective charge of the globule. For example in the region explored experimentally, the difference between these two curves lies within the experimental uncertainty range.

It is interesting to compare our results with the results of Dobrynin and Rubinstein [75]. These authors considered for the first time the problem of counterion-condensation around an hydrophobic polyelectrolyte using a two-state model. They determined the fraction P by using trial counterion densities of the form $n(r) = (1-P)n_{av}\frac{R^3}{R_g^3}$ inside the globule (for $r < R_g$), and $n(r) = Pn_{av}\frac{R^3}{R^3-R_g^3}$ in the outer region. This family of density is parameterized only by the parameter P. Therefore by minimizing the counterion free-energy density functional on this trial set, they could deduce an expression of P as a function of the system parameters [92]. However for reasonable values of $|\tau|\left(\frac{b}{\ell_B}\right)^{1/3} \simeq 1$, and for the experimental value of $A \simeq 10^3$, the value of f_{eff} predicted from the equations of ref. [75] is very close to f in most of the parameter range in contradiction with the experimental results of [80]. We attribute the difference between our model and the results of [75] to the two-state model used to estimate the fraction of dissociated counterions P. Indeed in the two state model the charge density is constant in the two regions inside and outside the globule. The Poisson equation then implies that in the two-state approximation, the graph of the electric field ($-\frac{du}{dx}$ in our dimensionless units) as a function of x has a typical angle shape for all values of P as illustrated in Fig. 3.40. In this figure, we have also compared this approximation, to the exact numerical behavior of $-\frac{du}{dx}$, for the typical parameters $A = 500, x_g = 1$. Since the charged monomers at the center of the globule are neutralized by the counterions, the true electric field distribution takes the form of a narrow peak centered at x_g. Because of its reduced family of trial functions, the two-state model can not reproduce the true behavior of the electric field. However the determination of the effective charge requires an

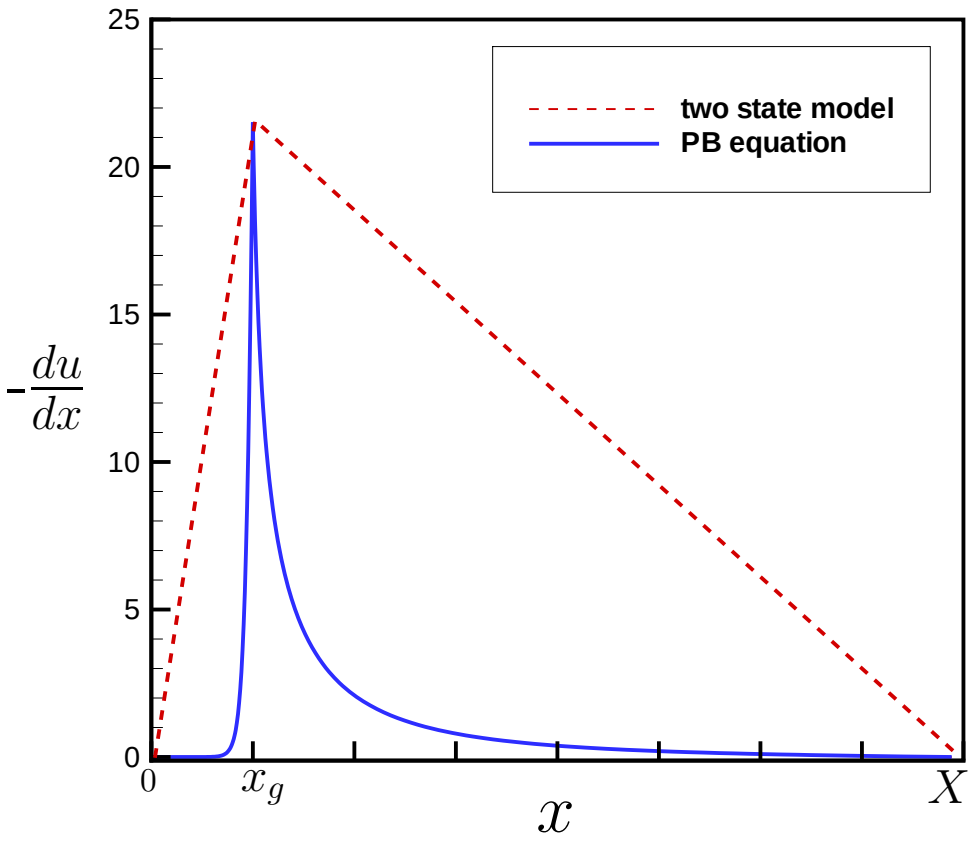

FIG. 3.40 – (Color online) Typical behavior of the dimensionless electric field $-\frac{du}{dx}$ using either the two state model (dashed line) or our PB model (solid line). The solid line corresponds to $x_g = 1$ and $A = 500$.

accurate knowledge of the electric-field in the whole cell. Therefore, we believe that the two state model is not accurate enough for the determination of the effective charge. Indeed it was shown in [93] that at least a three state model is necessary in the case of a permeable droplet.

In conclusion, we have developed a theory of counterion condensation around hydrophobic polyelectrolytes. Our theory is based on the pearl-necklace model for the polyelectrolyte backbone. We assumed that the pearls are permeable to the counterions, and use analytic results on the Poisson-Boltzmann equation to establish the fraction of counterions condensed inside the pearls. It allows us to establish a power law dependence of the effective charge f_{eff} on the chemical charge f as $f_{eff} \propto f^{3/2}$. This prediction is in very good agreement with recent experimental results by W. Essafi *et al.* [80] and explains the large deviation from the Manning law observed in these experiments. While our main results concern the effective charge of hydrophobic polyelectrolytes, the scaling laws that we derived may also apply to other areas of physics and chemistry where the Poisson-Boltzmann equation plays an important role.

Bibliographie

[1] B. Alberts, D. Bray, A. Johnson, J. Lewis, M. Raff, K. Roberts, P. Walter "Essential Cell Biology" Garland Publishing (1998)

[2] R.G. Endres, D.L. Cox and R.R.P. Singh, Rev. Mod. Phys. **76**, 195 (2004)

[3] N.C. Seeman, "An overview of structural DNA nanotechnology", Mol. Biotechnol. **37**, 246 (2007)

[4] P.W.K. Rothemund, Nature **440**, 297 (16 March 2006)

[5] Yu He, Tao Ye, Min Su, Chuan Zhang, Alexander E. Ribbe, Wen Jiang and Chengde Mao, Nature **198**, 198 (2008)

[6] E.S. Andersen, M. Dong, M.M. Nielsen, K. Jahn, R. Subramani, W. Mamdouh, M.M. Golas, B. Sander, H. Stark, C.L.P. Oliveira, J.S. Pendersen, V. Birkedal, F. Besenbacher, K.V. Gothelf and J. Kjems, Nature **459**, 73 (2009)

[7] H.-W Fink and C. Schönenberger, Nature **398** 407 (1999)

[8] M. R. Arkin, E. D. A. Stemp, R. E. Holmlin, J. K. Barton, A. Hoermann, E. J. C. Olson, and P. F. Barbara Science **273**, 475 (1996)

[9] D. B. Hall, R. E. Holmlin, and J. K. Barton, Nature, **382**, 731 (1996).

[10] D. Porath, A. Bezryadin, S. de Vries and C. Dekker, Nature **403** 635 (2000)

[11] A. Yu. Kasumov, M. Kociak, S. Guéron, B. Reulet, V. T. Volkov, D. V. Klinov and H. Bouchiat, Science **291** 280 (2001).

[12] A. Yu. Kasumov, D. V. Klinov, P.-E. Roche, S. Guéron, and H. Bouchiat, App. Phys. Let. **84** 1007 (2004) ;

[13] P.J. de Pablo, F. Moreno-Herrero, J. Colchero, J. Gómez Herrero, P. Herrero, A.M. Baró, Pablo Ordejón, José M. Soler and Emilio Artacho, PRL **85**, 4992 (2000)

[14] A. J. Storm, S. J. T. van Noort, S. de Vries, and C. Dekker, Appl. Phys. Lett. **79**, 3881 (2001)

[15] Y. Zhang, R. H. Austin, J. Kraeft, E. C. Cox and N. P. Ong, PRL **89**, 198102 (2002)

[16] C. Gomez-Navarro, F. Moreno-Herrero, P. J. de Pablo, J. Colchero, J. Gomez-Herrero and A. M. Baro, PNAS **99**, 8484 (2002)

[17] T. Heim, D. Deresmes, and D. Vuillaume, Appl. Phys. Lett. **85**, 2637 (2004)

[18] T. Heim, D. Deresmes, and D. Vuillaume, J. Appl. Phys. **96**, 2927 (2004)

[19] Bingqian Xu, Peiming Zhang, Xiulan Li,and Nongjian Tao, Nano. Let. **4**, 1105 (2004)

[20] Errez Shapir, Hezy Cohen, Arrigo Calzolari, Carlo Cavazzoni, Dmitry A. Ryndyk, Gianaurelio Cuniberti, Alexander Kotlyar, Rosa Di Felice and Danny Porath, Nature Materials **7**, 68 (2008)

[21] Xuefeng Guo, Alon A. Gorodetsky, James Hone, Jacqueline K. Barton and Colin Nuckolls, Nature Nanotechnology **3**, 163 (2008)

[22] M.D. Stoeckenius, J. Biophys. and Biochem. Cytol., **11**, 297 (1961)

[23] P. K. Hansma, J. P. Cleveland, M. Radmacher, D. A. Walters, P. E. Hillner, M. Bezanilla, M. Fritz, D. Vie, H. G. Hansma, C. B. Prater, J. Massie, L. Fukunaga, J. Gurley, and V. Elings, Appl. Phys. Lett. **64**, 1738 (1994)

[24] L. Gross, F. Mohn, N. Moll, P. Liljeroth, G. Meyer, Science **325** 1110 (2009)

[25] D. Pastré, O. Piétrement, S. Fusil, F. Landousy, J. Jeusset, M-O David, L. Hamon, E-L. Cam and A. Zozime Biophys. Jour. **85**, 2507 (2003)

[26] *Biological Electron Microscopy*, Michael J. Dykstra and Laura E. Reuss, Springer (2003) ISBN : 978-0306477492

[27] J. M. Vargason, K. Henderson and P. Shing Ho, PNAS **98** 7265 (2001)

[28] J. F. Allemand, D. Bensimon, R. Lavery and V. Croquette, PNAS **95** 14152 (1998)

[29] J.F. Allemand, D. Bensimon, L. Jullien, A. Bensimon and V. Croquette Biophis. J. **73** 2064 (1997)

[30] J. Dubochet, M. Ducommun, M. Zollinger and E. Kellenberger J. Ultrastruct. Res. **35** 147 (1971)

[31] M. A. Liberman and A. J. Lichtenberg, "Principles of plasma discharges and materials processing", A-Wiley interscience publication (1994)

[32] D. R. Lide, "Handbook of chemistry and physics", CRC Press 84-th edition (2003), chapters 9-67 and 10-187

[33] A. Podestà, M. Indrieri, D. Brogioli, G. S. Manning, P. Milani, R. Guerra, L. Finzi and D. Dunlap, Biophysical Journal **89**, 2558 (2005)

[34] A. Bensimon, A. Simon, A. Chiffaudel, V. Croquette, F. Heslot and D. Bensimon, Science **265** 2096 (1994)

[35] P. S. Doyle, B. Ladoux and J.-L. Viovy, Phys. Rev. Lett. **84** 4769 (2000)

[36] L. Angers, F. Chiodi, J. C. Cuevas, G. Montambaux, M. Ferrier, S. Gueron and H. Bouchiat, Phys. Rev. B **77**, 165408 (2008)

[37] A. Yu. Kasumov, R. Deblock, M. Kociak, B. Reulet, H. Bouchiat, I. I. Khodos, Yu. B. Gorbatov, V. T. Volkov, C. Journet and M. Burghard Science **284**, 1508 (1999)

[38] A. Kasumov, M. Kociak, M. Ferrier, R. Deblock, S. Guéron, B. Reulet, I. Khodos, O. Stéphan, and H. Bouchiat Phys. Rev. B **68**, 214521 (2003)

[39] A.Yu. Kasumov, K. Tsukagoshi, M. Kawamura, T. Kobayashi, Y. Aoyagi, K. Senba, T. Kodama, H. Nishikawa, I. Ikemoto, K. Kikuchi, V.T. Volkov, Yu.A. Kasumov, R. Deblock, S. Gueron, and H. Bouchiat Phys. Rev. B **72**, 033414 (2005)

[40] A.Yu. Kasumov, S. Nakamae, M. Cazayous, T. Kawasaki, Y. Okahata Research Letters in Nanotechnology, Article ID 540257 (2009)

[41] R. E. Bartolo and N. Giordano, Phys. Rev. B **54** 3571 (1996)

[42] M.V. Feigel'man, M.A. Skvortsov and K.S. Tikhonov, Solid State Comun. **149** 1101 (2009)

[43] Orsay physics, private communications

[44] Jae-Hee Hana, Sun Hong Choia, Tae Young Leea, Ji-Beom Yoo, Chong-Yun Parka, Taewon Jungb, SeGi Yub, Whikun Yic, In Taek Hanb and Jong Min Kimb, Diamond and Related Materials **12**, 878 (2003)

[45] Yuri Lvov, Heinrich Haas, Gero Decher, Helmuth Moehwald and Alexei Kalachev J. Phys. Chem.,**97** 12835 (1993)

[46] S. M. Rossnagel, J.J. Cuomo and W.D. Westwood "Handbook of plasma processing technology", Noyes Publications, Park Ridge U.S.A (1990)

[47] A. Nabok "Organic and inorganic nanostructures", Artech House (2005) p. 39

[48] H. W. Ch. Postma, T. Teepen, Z. Yao, M. Grifoni and C. Dekker, Science **293**, 76 (2001)

[49] A.K. Huettel, G.A. Steele, B. Witkamp, M. Poot, L.P. Kouwenhoven and H.S.J. van der Zant, Nano Let. **9**, 2547 (2009)

[50] N. Koshida, "Device Applications of Silicon Nanocrystals and Nanostructures", Series : Nanostructure Science and Technology, Springer (2009).

[51] A. Bachtold, M. de Jonge, K.G-Rasmussen, P.L McEulen, M. Buitelaar and C. Schönenberger, PRL **87** 166801 (2001)

[52] P. Tran, B. Alavi and G. Gruner, PRL **85** 1564 (2000)

[53] B. Reulet, M. Ramin, H. Bouchiat and D. Mailly, PRL **75** 124 (1995)

[54] Y. Noat, H. Bouchiat, B. Reulet and D. Mailly, PRL **80**, 4955 (1998)

[55] L. Latu-Romain, C. Mouchet, C. Cayron, E. Rouviere and J-P Simonato J. of Nano-Particle Research **10**, 1287 (2008)

[56] L.D. Landau and E.M. Lifshitz "Electrodynamics of continuous media", Addison-Wesley (1966).

[57] J.J. Wortman, R.A. Evans, J. Appl. Phys. **36** 153 (1965)

[58] C. Canali, C. Jacoboni, F. Nava, G. Ottaviani, and A. Alberigi-Quaranta, Phys. Rev. B **12**, 2265 (1975)

[59] G. S. Manning, J. Chem. Phys. **51**, 924 (1969).

[60] F. Oosawa, *Polyelectrolytes* (Marcel Dekker, New York, 1971).

[61] Y. Kantor, H. Li, and M. Kardar Phys. Rev. Lett. **69**, 61 (1992).

[62] J.-L. Barrat and J.-F. Joanny, Adv. Polym. Sci. **94**, 1 (1996).

[63] C. Holm, J.-F. Joanny, K. Kremer, R. R. Netz, P. Reineker, C. Seidel, T. A. Vilgis, and R. G. Winkler, Adv. Polym. Sci. **166**, 67 (2004).

[64] V. A. Bloomfield, D. M. Crothers and I. Tinoco, *Nucleic Acids Structures, Properties and Functions* (University Science Books, Sausalito, CA, 2000).

[65] J. R. Philif and R. A. Wooding, J. Chem. Phys. **52**, 953 (1970).

[66] B. O'Shaughnessy and Q. Yang, Phys. Rev. Lett. **94**, 048302 (2005).

[67] E. Trizac and G. Téllez, Phys. Rev. Lett. **96**, 038302 (2006).

[68] P. Gonzalez-Mozuelos and M. Olvera de la Cruz, J. Chem. Phys **103**, 22 (1995).

[69] A. Naji and R. R. Netz, Phys. Rev. Lett. **95**, 185703 (2005) ; Phys. Rev. E **73**, 056105 (2006).

[70] B. Alberts, D. Bray, A. Johnson, J. Lewis, M. Raff, K. Roberts, and P. Walter, *Essential Cell Biology* (Garland Publishing, New York, 1998).

[71] A. V. Dobrynin, M. Rubinstein, and S. P. Obukhov, Macromolecules **29**, 2974 (1996).

[72] E. Raphael and J.-F. Joanny, Europhys. Lett. **13**, 623 (1990)

[73] P. G. Higgs and E. Raphael, J. Phys. I France **1**, 1(1991).

[74] M. D. Carbajal-Tinoco and C. E. Willliams, Europhys. Lett. **52**, 284 (2000).

[75] A. V. Dobrynin and M. Rubinstein, Macromolecules **34**, 1964 (2001).

[76] M.-J. Lee, M. M. Green, F. Mikes, and H. Morawetz, Macromolecules **35**, 4216 (2002).

[77] A. Kyriy, G. Gorodyska, S. Minko, W. Jaeger, P. Stepanek, and M. Stamm, J. Am. Chem. Soc. **124**, 13454 (2002).

[78] H. J. Limbach and C. Holm, J. Phys. Chem. B **107**, 8041 (2003).

[79] A. V. Dobrynin and M. Rubinstein, Prog. Polym. Sci. **30**, 1049 (2005).

[80] W. Essafi, F. Lafuma, D. Baigl, and C. E. Williams, Europhys. Lett. **71**, 938 (2005).

[81] L. Rayleigh, Philos. Mag. **14**, 184 (1882).

[82] D. Baigl, R. Ober, D. Qu, A. Fery and C. E. Williams, Europhys. Lett. **62** 588 (2003).

[83] F. T. Wall and J. Berkowitz, J. Chem. Phys. **26**, 114 (1957).

[84] L. Belloni, Colloids Surf. A, 227, **140** (1998).

[85] E. Trizac, Phys. Rev. E **62**, R1465 (2000).

[86] H. Schiessel, and P. Pincus, Macromolecules **31**, 7953 (1998).

[87] Q. Liao, A. V. Dobrynin, and M. Rubinstein, Macromolecules **39**, 1920 (2006).

[88] A. V. Dobrynin, and M. Rubinstein, Macromolecules **32**, 915 (1999).

[89] S. Alexander, P. M. Chaikin, P. Grant, G. J. Morales, P. Pincus, and D. Hone, J. Chem. Phys. **80**, 5776 (1984).

[90] L. Belloni , M. Drifford, and P. Turq, Chem. Phys. **83**, 147 (1984).

[91] E. Trizac, L. Bocquet, M. Aubouy, and H. H. von Grunberg, Langmuir **19**, 4027 (2003).

[92] The final result is given in Eq. (21) of [75] where $P = x$.

[93] M. Deserno, Eur. Phys. J. E **6**, 163 (2001).

Acknowledgments

The work on two dimensional electron gas (2DEG) was made possible by the enthusiasm of Hélène Bouchiat, whose help was crucial at all stages starting from the conception of the experiments, including their real-life implementation, and continuing with their interpretation. Sophie Guéron introduced me to world of device fabrication, her insights were precious to solve experimental and conceptual problems and she often shed a pragmatic light on otherwise ethereal debates. I warmly thank Lionel Angers and Richard Deblock who supervised my bachelor thesis on rectification in Aharonov/Bohm rings where I first met the mesoscopic physics group, fruitful discussions with R. Deblock continued afterward during my thesis.

The 2DEG hetero-structures were grown at Laboratoire de photonique et nanosciences, by Ulf Gennser, Antonella Cavanna and Bernard Etienne who kindly gave us access to high mobility samples. The realization of the Ohmic contacts was made possible due to the help of Fédéric Pierre and Antonella Cavanna. The design of the microwave setup in my experiments was greatly improved thanks to advices by Julien Gabelli and Bertrand Reulet. Francesca Chiodi was an invaluable support during my years in Paris, and I will warmly remember the joyfulness she brought to my years as a Ph.D.

The theoretical aspects of nonlinear dynamics in 2DEG that I described, were inspired and ofter first put forward by my father Dima L. Shepelyansky. He always insisted on the importance of simple physical arguments and firmly believed that the explanation of zero resistance states was still an open problem in spite of the many existing theoretical proposals. Gilles Montambaux encouraged me for the finite frequency universal conductance fluctuation calculations, and was always open to discussion on theoretical issues in mesoscopic physics. I will greatly miss the cheerful discussions with Mikhail Polianski showed who great interest for the experiments on photo-magnetism. These discussions were highly stimulating and allowed to reach a deeper understanding of our observations.

The research on DNA was very demanding experimentally, hence I warmly thank (again) Sophie Guéron and Hélène Bouchiat who kindly helped me to perform these experiments and to understand, as far as possible, their results. Alik Kasumov's enthusiasm made enjoyable the long hours before the focused ion beam microscope and ensured that the fabrication of insulating slits was successful. During our experiments, we learned that the focused ion beam microscope was a capricious instrument : I am grateful to Franck Fortuna who always manged to fix the microscope even when all hope seemed lost. The collaboration with Dimitri Klinov was key in reproducing conductive samples, I thank him

for sustaining animated discussions and I hope that communication between our groups (hindered by spatial and linguistic barriers) will improve in the future.

Olivier Pietrement kindly helped us during our experiments on DNA deposition onto electrodes, his experience with DNA adsorption onto surfaces allowed us to understand the magic behind the pentylamine technique. More generally I am grateful to all the group "Microscopie moléculaire" for their warm welcome during our visits. Finally I want to compliment Sebastien Lyonnais for his great progress on the synthesis on G-wires. Our conducting AFM measurements were made possible by Dominique Vuillaume and Dominique Deresmes from IEMN in Lille who gave our access to their conducting AFM setup and spent precious time analyzing our samples. I also want to express my gratitude to Emmanuelle Rouvière who provided us with silicon nanowires for our contactless photoconductivity measurements.

The theoretical investigations in soft-matter physics that accompanied our experiments, were made possible by Elie Raphaël who was always ready to discuss the problems I encountered and propose new ideas. Finally during my Ph. D I was happy to collaborate with Frédéric Chevy, Farshid Mohammad Rafiee, Emmanuel Trizac, Michael Schindler and Fabien Closa on diverse and exciting problems.

I am grateful to Marcus Bütikker and Bernard Plaçais for their careful review of this thesis, and to D. Vuillaume and G. Rikken for their cheerful participation to the jury.

I wish to thank all my family for their kind support and care ; my parents, my sister Olga and my grand-parents Tamara and Lev. Finally I want to express my deep gratitude to my late grand-mother Larissa, who stimulated my interest for science and who was very happy that I decided to write this thesis.

Publications

- Phototransport in two dimensional electron gas [19,18,17,11,7]
- Molecular electronics (DNA, Graphene, Carbon nanotubes) [20,16,14,13]
- Ratchets in asymmetric nanostructures [15,8,6,5,2,1]
- Counter-ion condensation and capillarity gravity waves [22,21,12,9]
- Classical and Quantum Information theory [23,4,3]

[Pub23] A.D. Chepelianskii, "Towards physical laws for software architecture", http ://arxiv.org/abs/1003.5455

[Pub22] F. Closa, A.D. Chepelianskii and E. Raphaël "Capillary-Gravity waves generated by a sudden object motion", accepted to Physics of Fluids (2010)

[Pub21] A. D. Chepelianskii, M. Schindler, F. Chevy, E. Raphaël "Self-consistent theory of capillarity-wave generation by small moving objects", Phys. Rev. E **81**, 016306 (2010)

[Pub20] A.D. Chepelianskii, F. Chiodi, M. Ferrier, S. Gueron, E. Rouviere, H. Bouchiat "Contactless photoconductivity measurements on (Si) nanowires", to be published in Appl. Phys. Let. **96** (2010), arXiv :0909.4401

[Pub19] A.D. Chepelianskii, D.L. Shepelyansky "Microwave stabilization of edge transport and zero-resistance states", Phys. Rev. B 80, 241308(R) (2009), arXiv :0905.0593

[Pub18] A.D. Chepelianskii, H. Bouchiat "Hall detection of time-reversal symmetry breaking under AC electric driving", Phys. Rev. Lett. 102, 086810 (2009), arXiv :0811.4108

[Pub17] A. D. Chepelianskii, S. Gueron, F. Pierre, A. Cavanna, B. Etienne, H. Bouchiat "Magnetic field anti-symmetry of photovoltaic voltage in evanescent microwave fields", Phys. Rev. B 79, 195309 (2009) arXiv :0811.4108

[Pub16] A. Chepelianskii, P. Delplace, A. Shailos, A. Kasumov, R. Deblock, M. Monteverde, C. Ojeda-Aristizabal, M. Ferrier, S. Guéron, and H. Bouchiat "Phonon assisted dynamical Coulomb blockade in a thin suspended graphite sheet", Phys. Rev. B 79, 235418 (2009) arXiv :0807.1961

[Pub15] A. D. Chepelianskii, M. V. Entin, L. I. Magarill and D. L. Shepelyansky "Ratchet transport of interacting particles" Phys. Rev. E. v.78 , 041127 (2008)

[Pub14] S Lyonnais, O Piétrement, A Chepelianski, S Gueron, L Lacroix, E Le Cam, JL Mergny, "Functionalization of DNA G-Wires for patterning and nanofabrication." Nucleic acids symposium series (2004), No. 52. (2008), pp. 689-690.

[Pub13] M. Ferrier, A. Chepelianskii, S. Guéron, H. Bouchiat "Disorder induced transverse delocalisation in ropes of carbon nanotubes", Phys. Rev. B. v.77, 195420 (2008)

[Pub12] A. Chepelianskii, F. Mohammad-Rafiee, E. Raphael "On the effective charge of hydrophobic polyelectrolytes",
Journal of Physical Chemistry B 113, 3743 (2009) ; arXiv :0710.2471

[Pub11] L. Angers, A. Chepelianski, R. Deblock, B. Reulet, H. Bouchiat "Mesoscopic photovoltaic effect in GaAs/GaAlAs Aharonov Bohm rings", Phys. Rev. B 76, 075331 (2007).

[Pub10] A.D.Chepelianskii, A.S.Pikovsky, D.L.Shepelyansky "Synchnonization, zero-resistance states and rotating Wigner crystal",
Eur. Phys. J. B 60, 225-229 (2007) arXiv :0707.2694

[Pub9] A.D. Chepelianskii, F. Chevy, E. Raphael "On capillary-gravity waves generated by a slow moving object", Phys. Rev. Lett. 100, 074504 (2008), arXiv :0704.3990

[Pub8] A.D.Chepelianskii, M.V.Entin, L.I.Magarill, D.L.Shepelyansky "Photogalvanic current in artificial asymmetric nanostructures", Eur. Phys. J. B v.56, p.323-333 (2007), cond-mat/0701128

[Pub7] A.D.Chepelianskii and D.L.Shepelyansky "Magnetization of ballistic quantum dots induced by a linear-polarized microwave field", Eur. Phys. J. B v.55, p.261 (2007)

[Pub6] A.D.Chepelianskii "Microwave control of directed transport in asymmetric antidot structures", Eur. Phys. J. B 52, 389-396 (2006)

[Pub5] A.D.Chepelianskii and D.L.Shepelyansky, "Directing transport by polarized radiation in the presence of chaos and dissipation", Phys. Rev. B v.71, 052508 (2005)

[Pub4] W.Lee, A.D.Chepelianskii and D.L. Shepelyansky, "Treatment of sound on quantum computers", Proceedings of ERATO Conference on Quantum Information Science 2004, Tokyo, pp. 91-92 (2004), arXiv :quant-ph/0309018

[Pub3] A.D.Chepelianskii and D.L.Shepelyansky, "Simulation of chaos-assisted tunneling in a semiclassical regime on existing quantum computers" Phys. Rev. A v.66 (2002)

[Pub2] A.D.Chepelianskii and D.L.Shepelyansky, "Dynamical turbulent flow on the Galton board with friction", Phys. Rev. Lett. v.87 (2001)

[Pub1] A.D.Chepelianskii and D.L.Shepelyansky, "Repulsive trap for two electrons in a magnetic field", Phys. Rev. B v.63 (2001) p. 165310